ASSESSMENT AND OPTIMIZATION OF THE CANADIAN SCWR REACTIVITY CONTROL SYSTEMS THROUGH REACTOR PHYSICS AND THERMAL-HYDRAULICS COUPLING

ASSESSMENT AND OPTIMIZATION OF THE CANADIAN SCWR REACTIVITY CONTROL SYSTEMS THROUGH REACTOR PHYSICS AND THERMAL-HYDRAULICS COUPLING

BY FREDERIC SALAUN, M.ENG

A Thesis

Submitted to the School of Graduate Studies

in Partial Fulfillment of the Requirements for the Degree

Doctor of Philosophy

DOCTOR OF PHILOSOPHY (2017) McMaster University

(Department of Engineering Physics) Hamilton, Ontario

TITLE : ASSESSMENT AND OPTIMIZATION OF THE CANADIAN SCWR REACTIVITY CONTROL SYSTEMS THROUGH REACTOR PHYSICS AND THERMAL-HYDRAULICS COUPLING

AUTHOR : Frederic Salaun, B.Eng, M.Eng
(PHELMA - Grenoble Institute of Technology)

SUPERVISOR: Professor David R. Novog

NUMBER OF PAGES : xvi, 180

ABSTRACT

Canadian Nuclear Laboratories conceptualized a new reactor design to fulfill the goals set forth by the Generation IV International Forum. Unlike the traditional CANDU™, the Canadian Supercritical Water-cooled Reactor (SCWR) stands vertically and uses the batch fueling technique. Despite the CANDU-like assembly design, the traditional code system is not adequate to model this concept. Moreover, the current design lacks reactivity control mechanisms to remove the initial excess reactivity and manage the core power distribution.

Fuel-integrated burnable absorber and cruciform control rods were designed for the Canadian SCWR as part of this work. A new genetic algorithm technique has been applied to optimize the control rod pattern by trying to minimize the maximum cladding surface temperature (MCST) and the maximum fuel centerline temperature (MFCLT) through the use of unique surface responses.

The results of the study showed that the MCST and MFCLT did not meet the safety margins during normal operation. Therefore, the concept was enhanced by optimizing the fuel enrichment and burnable absorber concentration along the fuel assembly, shortening the cycle length, reducing the reactivity worth of the individual control rod, and finally lowering the core thermal power. The control rod pattern was re-evaluated and considerably improved the results.

PARCS and RELAP5/SCDAPSIM/MOD4 were coupled through a series of external scripts to simulate 3D neutron kinetics/thermal-hydraulics control rod drop accidents. Every assembly was individually modeled in the coupling to accurately represent the evolution of these localized transients. Fuel melting occurred when the reactor SCRAM was not available. On the contrary, the safety margins were largely met when the reactor tripped on the overpower signal. However, this detection method demonstrated its limitation when one power pulse did not reach the SCRAM signal and led to fuel melting. A local neutron overpower signal could be implemented to ensure the reactor SCRAM in every control rod drop accident.

ACKNOWLEDGMENTS

First and foremost, I want to thank my supervisor Dr. David Novog for giving me this Ph.D. opportunity. He has been everything I could hope for as a supervisor through his advice, knowledge, and support. He always encouraged me to get out of my comfort zone to gain experiences and learn from them. He has been a great mentor and I will be forever grateful. I would also like to thank my supervisory members: Dr Adriaan Buijs, Dr. Laurence Leung, and Dr. John Luxat. Their input and advice on my research project were of great help to bring this thesis to completion.

My friends and colleagues played an important role, each one in its own way. Whether it was brainstorming, coffee breaking, debating, WEBing or simply hanging out together, they all deserve my gratitude. I name Jason, Kendall, Matt, Haley, Brian, Ivan, Rachel, Hummel, Dave, Paul, Vanja, Monica, Zack, Abdul, Tim, Feng, Ali, Emily, Marion, Jon, Vicky, Sam, Salma, Shlomi, Liz, Travis, Sylwia, Simon, Pedro, Julie, Darryl, Bertha, Carrie, James, Michel and all the ones I forgot to mention. You brought my Ph.D. experience to the next level and I am so grateful to all of you for it.

Of that list, Hummel and Jason deserve a little extra recognition. Firstly, Hummel, now Dr. Hummel, has been my second mentor. His helpfulness and knowledge are off the charts and I can't even describe how much I learned from him. Jason Ray Sharpe was my office mate, my friend, my best friend, my "English" teacher (at least he likes to think that!), and probably became family. We spent a lot of time together, maybe too much, but it was undoubtedly quality time. He was always there for me and I could not have asked for a better friend. Thank you, Jay.

My childhood friends, while far away, are a pillar of my life. Flavien, Célie, Matthieu, Cindy, Manue, Mailys, Bleuenn, and Justine are some good old solid friends. Thank you for visiting me, keeping in touch and your moral support throughout those years. You all mean a lot to me and I wish we were geographically closer.

Last but not least, I would like to thank my family - particularly my parents. They always supported my decisions and choices, especially the one of living abroad. I have this immense privilege to know that they will always be there for me no matter what happens. That is also why I was able to pursue my dreams and I owe them everything I accomplished. Thank you Mom, Dad, Mamie, Papy, and Grandma.

Enfin et surtout, je voudrais remercier ma famille - tout particulièrement mes parents. Ils m'ont toujours supporté dans mes choix et decisions, surtout dans celui de vivre à l'étranger. J'ai cet immense privilège de savoir qu'ils seront toujours là pour moi peu importe ce qui arrive. C'est aussi la raison pour laquelle j'ai pu poursuivre mes rêves et je leur dois tout ce que j'ai accompli. Merci Maman, Papa, Mamie, Papy et Grand-mère.

To my family and friends

Table of Contents

List of Figures

List of Tables

List of Acronyms

BOC	Beginning Of Cycle
BWR	Boiling Water Reactor
CANDU	CANada Deuterium Uranium
CFD	Computational Fluid Dynamics
CNL	Canadian Nuclear Laboratories
CR	Control Rod
CVR	Coolant Void Reactivity
DF	Dancoff Factor
ENDF	Evaluated Nuclear Data Library
EOC	End Of Cycle
FIBA	Fuel-Integrated Burnable Absorber
GA	Genetic Algorithm
GFR	Gas-cooled Fast Reactor
GIF	Generation IV International Forum
GHG	GreenHouse Gas
HERC	High Efficiency Re-entrant Channel
IPCC	International Panel on Climate Change
IR	Inner Ring
LER	Linear Element Rating
LFR	Lead-cooled Fast Reactor
LWR	Light Water Reactor
MCDANCOFF	Monte-Carlo Dancoff
MCST	Maximum Cladding Surface Temperature
MeV	Mega Electron Volt
MFCLT	Maximum Fuel CenterLine Temperature
MPa	Mega Pascal

MSR	Molten Salt Reactor
MW	Mega Watt
NTE	Neutron Transport Equation
OR	Outer Ring
PHTS	Primary Heat Transport System
PWR	Pressurized Water Reactor
SFR	Sodium Fast Reactor
RSM4	RELAP5/SCDAPSIM/MOD4
SCWR	SuperCritical Water-cooled Reactor
TH	Thermal-hydraulic
VHTR	Very-High Temperature Reactor

List of Symbols

A	Surface area
A	Flow area
C	Precursor concentration
c_p	Specific heat
CO_2	Carbon dioxide
D	Diffusion coefficient
D	Hydraulic diameter
E	Energy
g	Gravitational constant
Gd	Gadolinium
h	Convective heat transfer coefficient
$\vec{J}$	Neutron current
k	Multiplication constant
k	Thermal conductivity
$\bar{l}$	Mean chord length
L	Length
n	Neutron density
N	Number density
N_A	Avogadro's Number
Nu	Nusselt number
p	Wetted perimeter
P	Pressure
Pr	Prandtl number
Pu	Plutonium
q''	Heat flux
q'''	Volumetric heat generation

r	Radius
Re	Reynolds number
S	Surface
S	Neutron source
t	Time
T	Temperature
$T_{1/2}$	Half-life
Th	Thorium
u	Internal and kinetic energy
U	Uranium
v	Neutron speed
v	Fluid velocity
V	Volume
x,y,z	Cartesian spatial coordinates
Y_{lm}	Spherical harmonics
σ_0	Background cross-section
σ_e	Escape probability
$\overline{\mu_0}$	Average scattering angle

Greek Letters

β	Delayed neutron fraction
ε	Surface roughness
θ	Polar angle
λ	Decay constant
λ	Darcy factor
μ	Scattering angle
μ	Dynamic viscosity
ν	Average number of neutrons generated per fission reaction

ρ	Density
ρ	Reactivity
σ	Microscopic cross-section
τ	Shear stress
$\emptyset$	Angular neutron flux
χ	Fission spectrum distribution
ψ	Azimuthal angle
ω	Quadrature weighting factor
Σ	Macroscopic cross-section
$\vec{\Omega}$	Neutron direction

Subscripts and superscripts

∞	infinity
1	fast energy group
2	thermal energy group
a	absorption
d	delayed
eff	effective
f	fission
g	energy group
in	inlet
k	delayed neutron group
out	outlet
p	prompt
s	scattering
t	total
tr	transport

Declaration of Academic Achievement

This thesis was primarily supervised by Dr. David Novog who was regularly consulted for guidance and expertise since September 2013. Three other members also provided insight throughout this work as part of my supervisory committee: Dr. Adriaan Buijs, Dr. Laurence Leung, and Dr. John Luxat. The author performed all the work presented in this sandwich thesis; this includes the background research, preparation of codes' input, simulations, data analysis, generation of the scripts, and redaction of the three publications.

The author designed the reactivity control systems for the Canadian Supercritical Water-cooled Reactor (SCWR). A new optimization technique based on genetic algorithms was utilized to find a control rod pattern for the equilibrium cycle. The maximum cladding temperature (MCST) was minimized using a unique response surface. Then, the core design was enhanced to reduce the MCST and maximum fuel centerline temperature (MFCLT). Finally, PARCS and RELAP5/SCDAPSIM/MOD4 were coupled using a new thermal-hydraulic feedback database to perform transient analysis. Moreover, high spatial resolution was achieved through the individual modeling of the 336 fuel assemblies. For the first time, the impact of control rod drop accidents was assessed for the Canadian SCWR.

Chapter 1

Introduction

1.1 Background

Nuclear power currently provides 11% of the world's electricity needs [1]. While it has been reliable and low-cost for many decades, other technologies have emerged or improved over the recent years and are now challenging the attractiveness of nuclear power. In 2000, a group of experts from nine countries gathered to enhance international collaboration for the future generation of nuclear reactors. They shortlisted six reactor concepts: the Very High-Temperature Reactor (VHTR), the Gas-cooled Fast Reactor (GFR), the Sodium-cooled Fast Reactor (SFR), the Lead-cooled Fast Reactor (LFR), the Molten Salt Reactor (MSR), and the SuperCritical Water-cooled Reactor (SCWR). These most promising concepts were selected based on the several key areas [2]:

- Sustainability: the need for fuel resources and nuclear waste has to be minimized while increasing the fuel utilization. Life expectancy of the nuclear plant has to be maximized to provide long-term clean energy.
- Economics: the concept should be financially competitive with future energy sources. Therefore, the most important factor would be to reduce the capital costs associated with reactor licensing, construction and decommissioning.
- Safety and reliability: the probability of core damage should be reduced by one order of magnitude compared to the current fleet of reactors and the offsite emergency response should not be necessary for any scenario.
- Proliferation resistance and physical protection: the technology should be undesirable to the production of weapons-grade material and safe from ill-intentioned people.

In addition, the current threat of climate change due to the constant increase of carbon dioxide (CO_2) emissions in the atmosphere makes us rethink our vision

of power generation. In a talk [3], Bill Gates illustrated CO_2 production through a rather straightforward equation:

$$CO_2 = P \times S \times E \times C$$

where:

- P is the World population
- S is the number of services per person
- E is the energy used per service
- C is the amount of CO_2 put out per unit of energy

He then claimed that: "One of these numbers is going to have to get pretty near to zero" [to not produce CO_2 emissions]. While "E" tends to decrease, "P" and "S" are continually rising; therefore, the only viable option is to have carbon-free energy sources (i.e., reduce C to zero). Nuclear power is one option.

A few years later, in 2015, 195 countries signed the Paris Agreement, in which the main goals are to minimize the global temperature increase and foster low greenhouse gas (GHG) emissions technologies [4]. In addition, the Intergovernmental Panel on Climate Change (IPCC) published a report in 2014 [5] stating that:

"Scenarios that are likely to maintain warming at below 2°C include more rapid improvements in energy efficiency and a tripling to nearly a quadrupling of the share of zero- and low-carbon energy supply from renewable energy, nuclear energy and fossil energy with carbon dioxide capture and storage (CCS) or BECCS by the year 2050"

Despite the reduced interest in nuclear power after the Fukushima accident in 2011, the future of nuclear energy seems rather promising as long as the safety issues from that accident are addressed. One or more of the six reactor concepts could help fight global warming while providing the energy needed to sustain a thriving world.

The SCWR concept uses water above the thermodynamic critical point (374°C, 22.1 MPa). Many advantages ensue from it such as higher efficiency, direct cycle and a lower mass flow rate. The latter improves the economics by reducing the Primary Heat Transport System (PHTS) inventory. In this work, the SCWR concept developed in Canada – which could represent the future of nuclear power in the country - was investigated. The author worked on issues which arose from earlier studies and are introduced in the following section.

1.2 Motivation

The Canadian SCWR has been subjected to many modifications, particularly at the assembly level by, for instance, decreasing the linear element rating (LER) or obtaining a negative coolant void reactivity (CVR) [6, 7]. Canadian Nuclear Laboratories (CNL) carried out the only study on the implementation of reactivity control systems; however, the batch cycle dramatically decreased by 35-40% (280 days) leading to a lower average fuel exit burnup as well [8].

In addition, the maximum cladding surface temperature (MCST) is a very challenging safety limit due to the high temperatures in the core. The current concept (as of this writing) already exceeds the 850°C limit set by CNL without reactivity hold-down systems [9].

The unique assembly design contains two separate coolants leading to two very different reactivity feedback mechanisms which surpass the capability of the available simulation codes. Moreover, the change in cross-sections due to the variation of a thermal-hydraulic parameter is rather linear for the existing reactors. Therefore, a simple linear interpolation for each reactivity feedback is deemed acceptable; however, the validity of the linear approach has to be demonstrated for the Canadian SCWR to ensure the reactor kinetics is accurately modeled.

Finally, no reactivity initiated accidents have been simulated for the Canadian SCWR thus far. Scenarios involving an accidental movement of a control rod can lead to asymmetrical transients with a localized power excursion. Therefore, a fine spatial treatment of the assembly powers and thermal-hydraulic conditions changes is required. PARCS and RELAP5/SCDAPSIM/ MOD4 were externally coupled to investigate control rod drop accidents and evaluate the Canadian SCWR response.

1.3 Outline of the thesis

After this introductory chapter, this sandwich thesis contains six more chapters. Chapter 2 introduces the relevant theory for the work performed. It includes the fundamentals of neutron interactions, the neutron transport equation, reactor physics calculations, and thermal-hydraulic simulations. Chapter 3 aims to support chapters 4, 5, and 6 by providing the reader with more details on the use of the simulation codes and modeling choices which were not included in the journal manuscripts. Chapter 4 presents the first journal publication. The work was published in the *Canadian Nuclear Laboratories Nuclear Review* (CNLNR) as part of a special issue related to the Canadian SCWR. Prior to the article, the author performed a literature review on optimization techniques used in nuclear reactors and described the novelty

of the work. The article introduces a new optimization technique to find the position of the control rods throughout the batch cycle. The models built for neutron physics and thermal-hydraulics simulations are described before the optimization itself. The work performed in Chapter 5 directly follows the results from Chapter 4. The article was published in the *Nuclear Engineering and Radiation Science* (NERS) journal and proposed many design changes to improve the Canadian SCWR concept. Chapter 6 introduces the last journal article which was submitted and accepted to *Science and Technology of Nuclear Installations* (STNI). The simulated Canadian SCWR incorporates all the design changes made in the second publication as well as the optimized control rod pattern. The manuscript evaluates the impact of control rod drop accidents in the Canadian SCWR. It has to be noted that each publication introduces the modeling of the reactor and can be a little redundant for the reader. Finally, Chapter 7 concludes on the work performed and proposes some suggestions for future research.

Chapter 2

Relevant theoretical background

This chapter introduces the relevant concepts for the work performed in this study. From the fundamental neutron interactions to the evaluation of the three-dimensional neutron flux distribution in the reactor core, this section first introduces the fundamental concepts and modeling techniques related to reactor physics. The thermal-hydraulic conditions heavily influence the power distribution and are evaluated by solving a different set of equations presented in a second section of this chapter.

2.1 Reactor physics

The production of neutrons and their interactions are fundamental principles of reactor physics and are described below. The equation governing the neutron population in a reactor core is then derived from those principles. Finally, the complexity of the transport equation, the numerical methods used to solve it and assumptions are discussed.

2.1.1 Neutron interactions

The neutron is an elementary particle and is unstable when not bound to a nucleus. An unbound neutron undergoes a beta decay to produce a proton, an electron, and an antineutrino with a half-life of approximately 12 minutes [10]. However, in a nuclear reactor, the neutron is absorbed or leaks out of the core on a sub-milliseconds timescale and is therefore considered stable for the purposes of nuclear reactor analysis. The collision of two neutrons in a nuclear reactor can also be neglected in this discussion as the density of neutrons is on the order of 10^8 n.cm^{-3}, while the medium is on the order of 10^{22} molecules.cm^{-3} or higher [11]. When a neutron does interact with a nucleus, it can be absorbed to form a compound nucleus or it may undergo scattering. In the case of absorption, the nucleus is transformed into an excited state, which can lead to:

- Radiative capture: The target nucleus emits one or several γ-rays to reach a stable ground state. This interaction represents a neutron loss for the system.
- Fission reaction: The target nucleus splits into two lighter elements while producing between two and three neutrons, on average, and emitting a number of γ-rays. Heavy nuclides can be categorized into two groups: fissile or fissionable. If the binding energy of the incident neutron is sufficient to overcome the fission barrier, the nucleus is classified as fissile, such as U-233, U-235, Pu-239, and Pu-241. In other words, absorption of a neutron with little or no kinetic energy can induce fission in these nuclides. Alternatively, nuclides such as U-238, Th-232, and Pu-240 are considered to be fissionable since some minimum kinetic energy is needed in addition to the binding energy to induce fission. The energy released from one fission reaction varies with the target nucleus but is approximately 200 MeV. The majority of the liberated energy goes towards the two fission products in the form of kinetic energy (see Table [12]).

Table 2-1 Energy released per fission for Plutonium 239

Thermal fission of Pu-239	Average energy released (MeV)
Kinetic energy of fission fragments	175.8
Kinetic energy of prompt neutrons	5.9
Energy carried by prompt γ-rays	7.8
Total instantaneous energy	189.5
Energy of β- particles	5.3
Energy of anti-neutrinos	7.1
Energy of delayed γ-rays	5.2
Total from decaying fission products	17.6
Total heat released in a thermal spectrum reactor	200

The probability of obtaining a specific isotope from a fission reaction is called the fission product yield. The distribution is weakly sensitive to the target nucleus but notably changes with the energy of the incident neutron. As most of the fission reactions are induced by thermal (or “slow”) neutrons in the SCWR, the fission product yield for Pu-239 when struck by a thermal neutron is shown in Figure 2-1 [13].

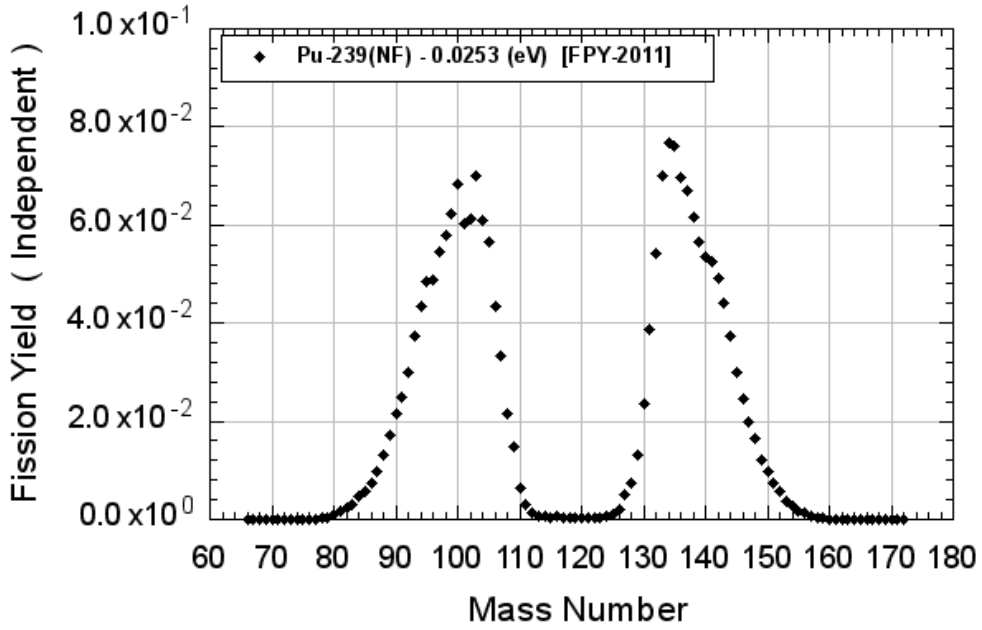

Figure 2-1 Pu-239 Neutron-induced Fission Yield

The fission fragments are generally unstable or in an excited state. They will eventually emit a series of γ-rays to reach their ground state or undergo β-decay with time scales ranging from seconds to millions of years. An alternative way to reach stability is for the nucleus to eject a neutron. Because these neutrons are produced after the initial fission, they are called delayed neutrons and play a major role in reactor kinetics.

- Inelastic scattering: The absorbed neutron is re-emitted, but part of the neutron energy is used to leave the nucleus in an excited state. The nucleus later de-excites by emitting one or more γ-rays.
- Threshold reactions: While these types of reactions occur less frequently than those discussed above, absorption of a high energy neutron can eject two or more neutrons or an alpha particle, for instance.

Finally, the neutron can be subjected to elastic or potential scattering. While the nucleus is left in its ground state in both cases, the two interactions differ slightly. In elastic scattering, the neutron is absorbed by the nucleus before being re-emitted. In potential scattering, the neutron "bounces off" of the nucleus without being absorbed. The neutron loses energy to the target nucleus which recoils and the neutron changes direction.

2.1.2 Neutron production

Neutrons are generated in fission reactions. As mentioned above, the fission of a nucleus releases a number of neutrons, typically between 0 and 5. These neutrons are considered prompt neutrons, as they are produced nearly instantaneously after a fission event. The average number of neutrons, denoted by ν_p, mostly varies with the fissioning nuclide, but also as a function of the incident neutron's energy. For instance, ν_p is approximately equal to 2.867 for Pu-239 when hit by a thermal neutron [10]. The energy distribution of the prompt neutrons can be represented by the Watt Fission spectrum function (1) [14] and is illustrated in Figure 2-2.

$$\chi(E) = C\, e^{(-\frac{a}{E})\times} \sinh(bE) \qquad (1)$$

where 'a' is equal to 0.966, 'b' to 2.842 and 'C' to 0.3568 for a thermal neutron inducing a fission in Pu-239 and E is the prompt neutron energy in MeV. More generally, a, b, and C are determined as a function of the parent nucleus and incident neutron energy.

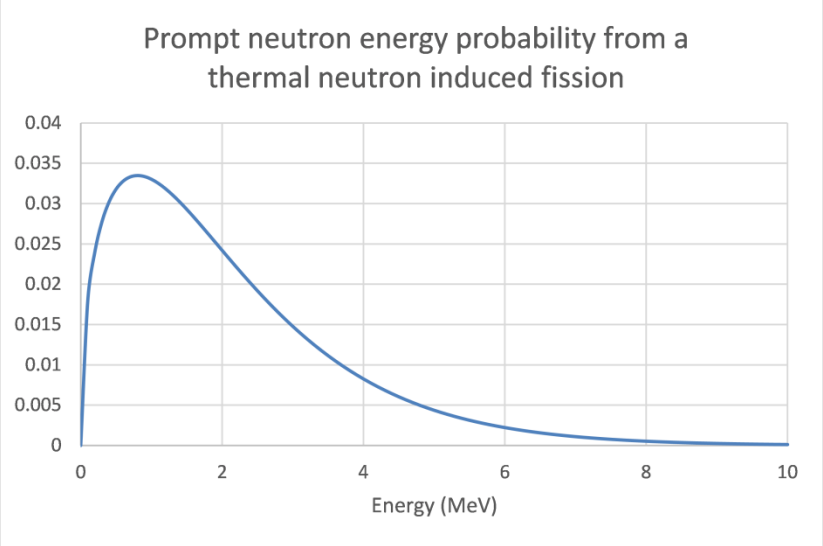

Figure 2-2 Prompt neutron energy distribution for a thermal neutron induced fission in Pu-239

The unstable daughter products can also emit delayed neutrons, as mentioned in section II.1.1. The fission fragments can undergo one or more β- decays before emitting a neutron, and as such, are called delayed neutrons precursors. As the neutron is emitted in 10^{-14}s [10], the time delay is entirely due to the decay constant of the fission products. Many precursors exist, and for the purpose of nuclear reactor analysis, it was found adequate to group them in six groups [11] based on their half-lives (see Table 2-2).

Table 2-2 Half-life and fraction of delayed neutrons for Pu-239

Pu-239			
Group	$T_{1/2}$ (sec)	Relative Yield (β_i/β)	β_i (%)
1	53.75	0.038	0.00854
2	22.29	0.28	0.06293
3	5.19	0.216	0.04854
4	2.09	0.328	0.07371
5	0.549	0.103	0.02315
6	0.216	0.035	0.00787

The number of delayed neutrons, denoted by ν_d, varies considerably with the nuclide of interest because of the fission products the parent produces. The delayed neutron fraction β is used to describe the fraction of neutrons that are delayed in the core (2). Table 2-3 gives the β for the most common nuclides [10].

$$\beta = \frac{delayed\ neutrons}{prompt\ neutrons + delayed\ neutrons} \quad (2)$$

Table 2-3 Fraction of delayed neutrons for different fuels

Group	U-235	Pu-239	Pu-241	U-238
1	0.0251	0.0087	0.0066	0.0206
2	0.1545	0.0639	0.1234	0.2174
3	0.1476	0.0493	0.0932	0.257
4	0.2663	0.0747	0.2102	0.6156
5	0.0756	0.0235	0.0981	0.357
6	0.0293	0.008	0.0086	0.119
Total β	0.6984	0.2281	0.5401	1.5866

2.1.3 Neutron life cycle

By producing two to three neutrons from a single neutron absorption, a sustained chain reaction is possible. The reactor design has to ensure that only one of the produced neutrons will induce a new fission reaction to maintain a steady population of neutrons. Figure 2-3 describes the neutron life cycle [15]. Starting from a population of N_1 fast neutrons, they can first undergo a fast fission or leak out of the system. Any surviving neutrons, if not absorbed in fuel resonances as they slow down or leak out of the system, reach thermal energies. Once the neutrons have been thermalized, they can still leak out of the system, be absorbed in non-fuel materials, be absorbed in the fuel without producing a fission (radiative capture), or undergo a thermal fission in order to

generate N_2 new fast neutrons. The effective multiplication constant k_{eff} is defined by:

$$k_{eff} = \frac{Number\ of\ neutrons\ \ in\ the\ new\ population\ (N_2)}{Number\ of\ neutrons\ in\ the\ previous\ population\ (N_1)} \quad (3)$$

k_{eff} must equal unity to obtain a steady population of neutrons over time. If k > 1, the reactor is supercritical and the neutron population will increase; conversely, if k < 1, it is subcritical and the neutron population will decrease.

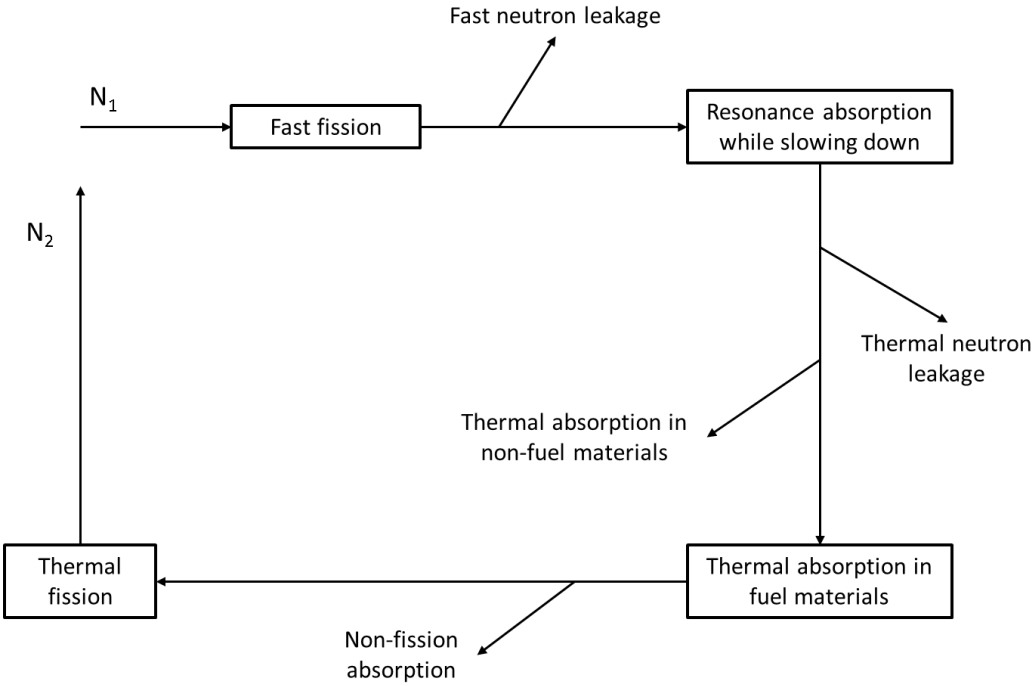

Figure 2-3 Neutron life cycle in a thermal reactor

2.1.4 Neutron cross-sections

The nuclear cross-section is the probability of a neutron to interact with a nucleus. Two types of cross-sections can be defined:

- Microscopic cross-sections: To define this quantity, let us consider a uniform mono-energetic and unidirectional beam of neutrons impinging upon an atom-thick target so that no nuclei are shielded (Figure 2-4). Equation (4) shows that the rate of neutron interactions 'R' with the target (interactions.cm^{-2}.s^{-1}) is proportional to the incident beam flux 'I' (neutrons.cm^{-2}.s^{-1}) and the number of atoms per unit area 'N_A' (cm^{-2}). The proportionality constant is called the microscopic cross-section 'σ' (cm^2) and is usually given in barns (1 barn = 10^{-24} cm^2). This cross-section depends on the relative energy of the incident neutron to the target nucleus, the target nuclide itself, and the type of

interaction (fission, capture, scattering, etc.). All these cross-sections have been evaluated experimentally over the past few decades and stored in Evaluated Nuclear Data Files (ENDF) [16]. Figure 2-5 illustrates the fission and absorption cross-section of Pu-239 [16]. Generally speaking, the cross-section varies in 1/E for E < 100 keV, except for very specific energies called resonances due to quantum effects.

$$R = \sigma \times I \times N_A \tag{4}$$

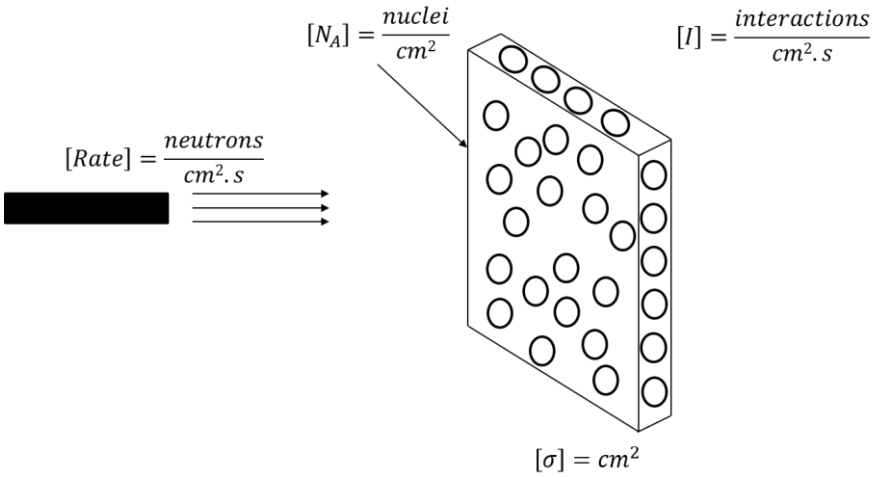

Figure 2-4 Mono-energetic neutron beam impinging upon a one-atom thick target

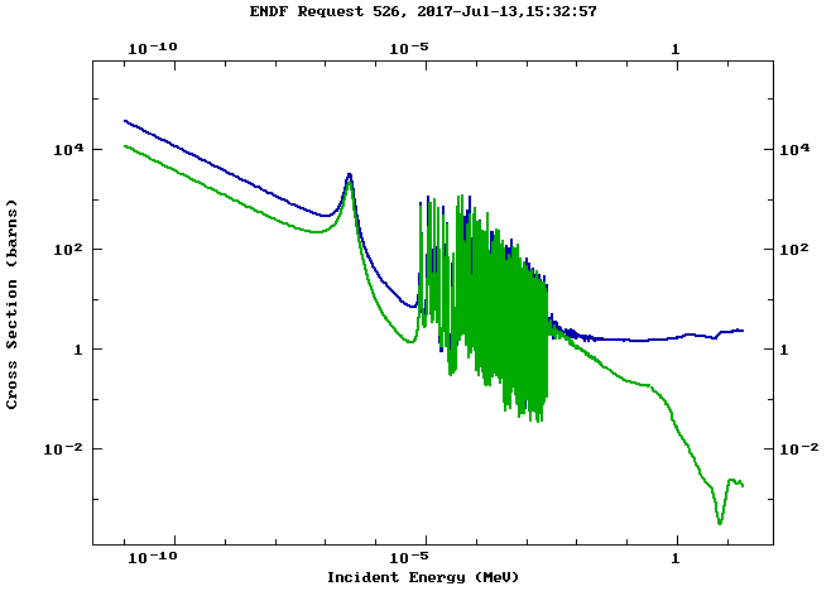

Figure 2-5 Fission (blue) and absorption (green) cross-section for Pu-239

- Macroscopic cross-sections: Since materials are not one-atom thick, let us now consider a target with N nuclei per unit volume. There is a certain density of neutrons "n" per unit volume traveling isotropically at speed "v". The rate of interactions per unit volume can be expressed as:

$$R = N \times \sigma \times n \times v = \Sigma \times \emptyset \quad (5)$$

The constant of proportionality Σ is called the macroscopic cross-section, and its units are cm^{-1}. If the medium contains many types of nuclides, the cross-section will be the sum of the macroscopic cross-section of each nuclide. Finally, the cross-section is defined for each type of interaction: absorption or scattering[1]. The absorption cross-section includes fission, radiative capture, n-2n, etc.

Like the microscopic cross-section, the macroscopic cross-section is also dependent upon energy, as is shown in equation (6). Nuclear interactions have a weak angular dependence except for scattering interactions, as the outgoing neutrons will have a angular distribution. Furthermore, in an inhomogeneous reactor, the number density N can vary in space and time, and therefore the macroscopic cross-section can be written:

$$\Sigma(r, E, t) = N(r, t)\sigma(E) \quad (6)$$

2.2 Neutron transport equation

The neutron distribution in a reactor core is exactly described by the neutron transport equation. This equation can be derived from an elementary volume by evaluating the neutron balance within this volume (Figure 2-6).

The angular neutron density is defined such that $n(r, E, \vec{\Omega}, t)d^3r d\vec{\Omega} dE$ is the number of neutrons in an elementary volume d^3r around r, energy dE about E, moving in direction $\vec{\Omega}$ in solid angle $d\vec{\Omega}$, at time "t". The angular neutron flux Φ and the angular current density $\vec{j}$ are defined in (7) and (8), respectively.

$$\emptyset(r, E, \vec{\Omega}, t) = n(r, E, \vec{\Omega}, t).v \quad (7)$$

[1] It must be noted that, in reactor physics analysis, the scattering cross-section includes elastic and inelastic scattering even though absorption happens in the case of the latter.

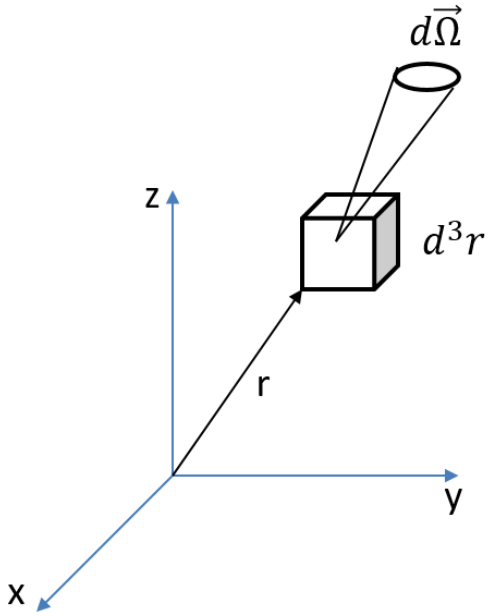

Figure 2-6 Elementary volume with neutron density

$$\vec{j}(r,E,\vec{\Omega},t) = \vec{\Omega}.\emptyset(r,E,\vec{\Omega},t) = \vec{\Omega}.v.n(r,E,\vec{\Omega},t). \quad (8)$$

The neutron transport equation simply describes that the rate of change of the neutron population is equal to the number of neutrons created minus the number of neutrons lost in a volume V:

$$\frac{\partial n}{\partial t} = neutrons\ gained - neutrons\ lost \quad (9)$$

Neutrons are gained firstly through the fission process, and if neutrons are assumed to be emitted isotropically, the rate of neutrons born through fission reactions can be expressed as follow:

$$\int_V d^3r \frac{\chi_p(E)}{4\pi} \int_{4\pi} d\overrightarrow{\Omega'} \int_0^\infty dE'\, \nu_p(E')\Sigma_f(r,E',t)\emptyset(r,E',\overrightarrow{\Omega'},t) \quad (10)$$

Neutrons with an energy E' and direction $\overrightarrow{\Omega'}$ can scatter into the energy E and direction $\vec{\Omega}$ of interest leading to a gain of neutrons. The rate of neutrons generated by scattering interactions is described by:

$$\int_V d^3r \int_{4\pi} d\vec{\Omega}' \int_0^\infty dE'\, \Sigma_s(r,\ E' \to E, \overrightarrow{\Omega'} \to \vec{\Omega}, t)\emptyset'(r,E',\overrightarrow{\Omega'},t) \quad (11)$$

Delayed neutrons are considered as an independent source of neutrons 'S_d' due to their delayed production and offer a means to provide better control over the reactor, and will be described in more details in section 2.3.3. For time-independent studies, the rate of delayed neutron production is, however, typically included in the fission source term. The term ν_p is simply replaced by $\nu = \nu_p + \nu_d$,

which assumes that the delayed neutrons are generated as prompt neutrons in steady-state analyses.

$$\int_V d^3r\, S_d\left(r, E, \vec{\Omega}, t\right) \tag{12}$$

The neutrons can be removed from the volume by absorption or by scattering from energy E and direction Ω into energy E' and direction Ω'. These two interactions represent all the possible interactions that neutrons can have and is expressed through the total cross-section Σ_t. The neutron loss rate can then be written as follows:

$$\int_V \Sigma_t(r, E, t)\emptyset\left(r, E, \vec{\Omega}, t\right) \tag{13}$$

Finally, the neutron can enter or leave the volume of interest. This net quantity can either add or remove neutrons to the volume and is referred to as the leakage term. The angular current density $\vec{j}\left(r, E, \vec{\Omega}, t\right)$ is commonly used to describe the rate at which neutrons leak through the surface S:

$$\oint_S dS.\vec{\Omega}\emptyset(r, E, \vec{\Omega}, t) \tag{14}$$

And by using Gauss's theorem of the divergence:

$$\int_V d^3r\vec{\Omega}\nabla\emptyset(r, E, \vec{\Omega}, t) \tag{15}$$

The neutron transport equation (NTE) can finally be written by combining equations (10), (11), (12), (13), and (15) together. The only way for the volume integral to be equal to zero is for its integrand to be equal to zero, leading to the balance equation:

$$\begin{aligned}&\frac{\partial n(r,E,\vec{\Omega},t)}{\partial t}+\vec{\Omega}.\nabla\emptyset(r,E,\vec{\Omega},t)+\Sigma_t(r,E,t)\emptyset(r,E,\vec{\Omega},t)\\&=\int_{4\pi}d\vec{\Omega}\int_0^{\infty}dE'\,\Sigma_s(r,E'\rightarrow E,\overrightarrow{\Omega'}\rightarrow\vec{\Omega},t)\emptyset'(r,E',\overrightarrow{\Omega'},t)\\&+\frac{\chi_p(E)}{4\pi}\int_{4\pi}d\vec{\Omega}\int_0^{\infty}dE'\,\nu_p(E')\Sigma_f(r,E',t)\emptyset(r,E',\overrightarrow{\Omega'},t)\\&+S_d(r,E,t)\end{aligned}\qquad(16)$$

2.3 Reactor Physics Calculations

The goal of neutronic calculations is to obtain the neutron flux distribution within the reactor core. The core is typically dynamic, three dimensional, large, and very heterogeneous and a solution of the NTE would require a prohibitively large amount of time, even with today's most advanced computers. Even assuming steady-state conditions does not easily allow for a rapid solution. In order to overcome the computational challenges, the problem is segmented and solved using appropriate assumptions. As the core is composed of a regular pattern of fuel assemblies, the first step consists of getting an accurate flux distribution by solving the NTE in a two-dimensional fuel lattice cell (section 2.3.1). Such an accurate solution for a single lattice with suitable boundary conditions (typically reflective) allows some knowledge of the space-energy neutron flux. Using this information, it is possible to obtain homogenous macroscopic cross-sections over the entire lattice cell, which can effectively replicate important reaction rates and represent the bulk behavior of a single lattice cell. The next stage of analyses then uses these homogenous cell cross-sections to solve a diffusion approximation for the full core (section 2.3.2).

2.3.1 Deterministic lattice cell calculations

2.3.1.1 NTE solver techniques

The integrodifferential form of the NTE (16) remains intractable to solve exactly. Therefore, the system variables are discretized to obtain a set of coupled algebraic equations to be solved for the spatial and energy dependent neutron flux. Lattice physics codes numerically solve the steady-state NTE ($\frac{\partial n}{\partial t}=0$) within a fuel lattice shown in Figure 2-7. A wide selection of codes is available, including SCALE/NEWT [17] (used in this work), DRAGON [18], and HELIOS [19].

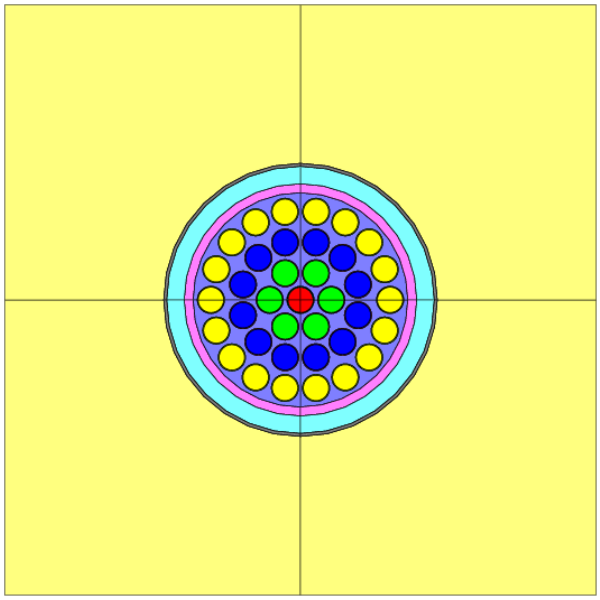

Figure 2-7 CANDU 37-element fuel lattice cell

Spatial discretization of a geometry is rather straightforward and uses relatively fine mesh spacing (Figure 2-8) such that the derivatives can be replaced by finite difference equations. The integrations in the NTE are replaced with suitable approximate numerical integrations over the mesh points.

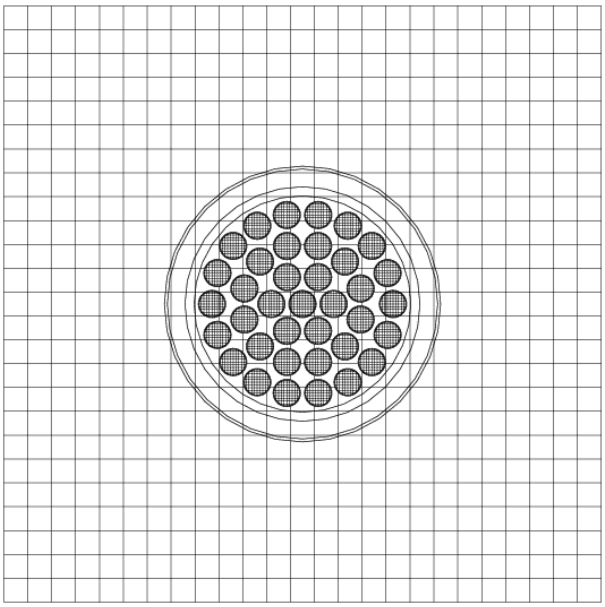

Figure 2-8 Example of a spatial meshing for a CANDU 37-element bundle

The angular variable Ω can be discretized using a discrete ordinate approach (used by NEWT) or functional expansions [11]. In the case of the discrete ordinates technique, a set of angular directions is selected and the integral of the angular neutron flux turns into a summation over all the chosen directions:

$$\int_{4\pi} \emptyset(r, E, \vec{\Omega}) d\vec{\Omega} \cong \sum_{i=1}^{N} w_i \emptyset_i(r, E) \tag{17}$$

where the ω_i are the quadrature weights which add up to the surface integral of a sphere (4π). The NTE becomes a set of coupled equations referred to as the S_N equations.

The functional expansions use a finite series of spherical harmonics $Y_{lm}(\Omega) = Y_{lm}(\theta,\psi)$ [11]. The lattice geometry only uses a two-dimensional space; therefore, the expansion of the spherical harmonics corresponds to an expansion in Legendre polynomials [11]:

$$\emptyset(r, E, \mu) = \sum_{i=0}^{N} \left(\frac{2i+1}{4\pi}\right) \emptyset_i(r, E) P_i(\mu) \quad ; \quad \mu = \cos(\theta) \tag{18}$$

The solution becomes more accurate with a higher N value at the expense of additional equations in the system to be solved, commonly named the P_N equations.

The energy variable also uses a discrete approach where the energy range (usually 10^{-5} eV to 20 MeV) is divided into a discrete number of energy groups. The continuous cross-sections have to be averaged over each energy group using (19) to remove the fine energy structure of the cross-sections within each energy bin. The NTE becomes the multi-group NTE.

$$\Sigma_{i_g} = \frac{\int_{E_g}^{E_{g-1}} dE \; \Sigma_i(E) \emptyset(E)}{\int_{E_g}^{E_{g-1}} dE \; \emptyset(E)} \tag{19}$$

The presence of the flux in equation (19) poses a problem since it is the variable sought in the solution of the NTE. To overcome this initial difficulty and generate multi-group discrete cross sections an intermediate code such as NJOY will discretize the continuous spectra in ENDF libraries using a typical flux solution where:

- High energy neutrons assume a fission spectrum (similar to Figure 2-2)
- Intermediate energy neutrons assume a 1/E flux shape
- Low energy neutrons assume a Maxwell-Boltzmann distribution as they are in thermal equilibrium with the medium [11]

The assumption of an inversely proportional flux variation with neutron energy for intermediate neutron energies is however only satisfied far from resonance peaks. In fact, these resonances represent a sharp increase in cross-

section leading to a high probability of the neutron to be absorbed in this energy range. Figure 2-9 and Figure 2-10 illustrate the Pu-239 fission cross-section over the entire energy spectrum and a zoom-in over part of the resonance region, respectively. As a consequence, the neutron flux is highly depressed within the resonance energy range and assuming a 1/E flux variation as a weighting function for the cross-section is not a good approximation (see Figure 2-11 [20]). The flux depression in the vicinity of the resonance is called resonance self-shielding. This phenomenon is important because fuel material may have many isotopes with strong resonances and hence the flux spectrum becomes significantly perturbed.

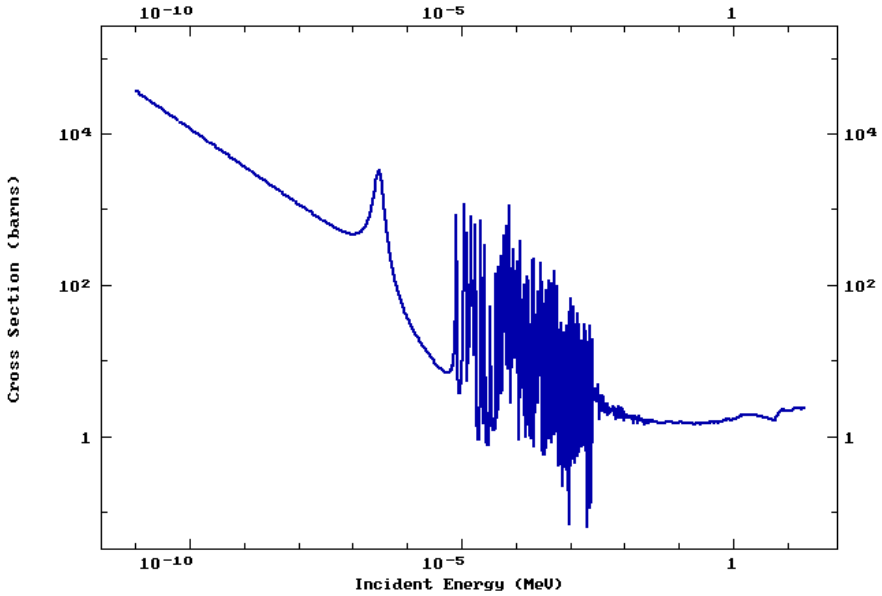

Figure 2-9 Pu-239 fission cross-section [16]

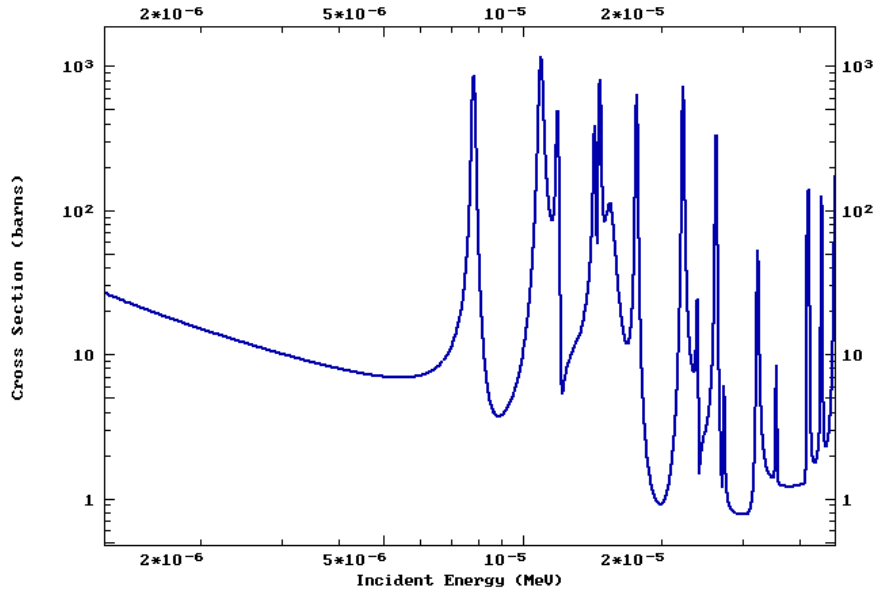

Figure 2-10 Resonance region of Pu-239 fission cross-section [16]

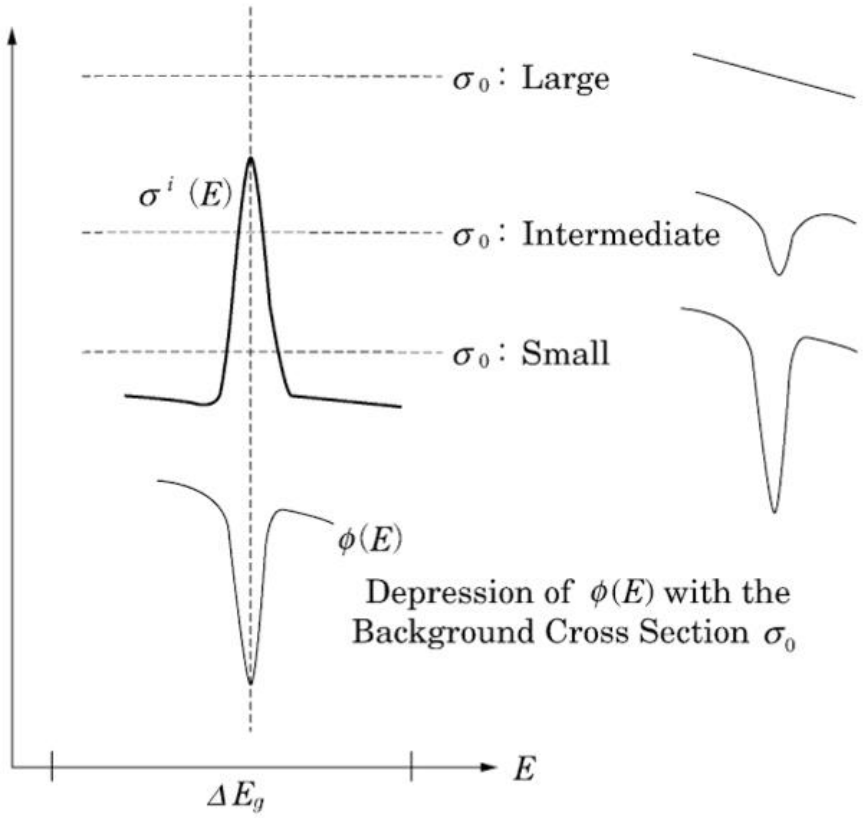

Figure 2-11 Flux depression in the vicinity of a cross-section resonance

One method used to treat the resonances occurring from multiple isotopes in a mixture is to examine the relative dilution of each isotope. This dilution is used to evaluate the importance of the nuclide's resonances and is used to generate the background cross-section. As it can be observed in Figure 2-11, if the nuclide is highly diluted the impact of its resonances will have a negligible effect on the flux as very few neutrons will encounter it; conversely, if the nuclide has a low dilution, the neutron flux will be more affected by its resonances. In other words, it is a weighting function for the resonance impact on the neutron flux.

Multi-group nuclear libraries contain tabulated values of the group-averaged cross-sections based on a nuclide's dilution (or background cross-section) and temperature in order to account for resonance broadening. They are commonly called "Bondarenko factors" or "f-factors" [21]. The lattice code has to evaluate the nuclide dilution to interpolate a problem-specific cross-section and the process iterates on each nuclide in the system as the self-shielding modifies the background cross-sections that is applied to a nuclide. Such calculations are commonly referred to as self-shielding calculations.

The background cross-section does not take into account geometric effects such as leakage nor the presence of other fuel elements around it. Therefore,

an escape (or heterogeneous) cross-sections is added to the background cross-section. The Wigner rational approximation is commonly used to calculate the escape microscopic cross-section [22]:

$$\sigma_e = \frac{1}{\bar{l} \times N_i} \tag{20}$$

where:

- $\bar{l}$ is the mean chord length in the body (four times the volume over the surface area)
- N_i is the number density of the nuclide being evaluated

In order to compute self-shielding effects SCALE uses a square-lattice arrangement of fuel rods and a moderating fluid. For non-square fuel element arrangements SCALE uses Dancoff factors to account for heterogeneous effects of a lattice of fuel elements. Dancoff factors modify the value of $\bar{l}$ and represent the "probability of a neutron emitted isotropically from the surface of one absorber lump will pass through the external media and enter a nearby absorber lump" [23]. A Dancoff factor of zero implies a single fuel element surrounded by an infinite moderator; conversely, a value of one would signify an infinite medium of absorber without moderator in the geometry.

The absorption resonances discussed above drive the design of reactor cores (fuel lumping) since it is advantageous to moderate a neutron through the resonance energy region in a moderating fluid where no fuel exists. Thermalized neutrons can then re-enter the fuel (see Figure 2-9) without being captured in the resonance region.

2.3.1.2 Fuel depletion calculation

The fuel composition is constantly changing due to fission reactions producing fission products, nuclear transmutations, and radioactive decay of unstable nuclei. Equation 21, commonly known as the Bateman equation, is used to calculate the new fuel composition later in time by assuming a constant flux solution over the depletion period. It is then very important to ensure that the flux distribution remains fairly constant over a depletion step.

$$\frac{dN_i}{dt} = \sum_{j=1}^{m} l_{ij}\lambda_j N_j + \overline{\Phi}\sum_{k=1}^{m} f_{ik}\,\sigma_k N_k - \left(\lambda_i + \overline{\Phi}\sigma_i\right)N_i, \qquad (i = 1, \ldots, m) \tag{21}$$

where

N_i is the atom density of nuclide i

λ_i is the radioactive disintegration constant of nuclide i

σ_i is the spectrum-averaged neutron absorption cross-section of nuclide i

$\overline{\Phi}$ is the space- and energy-averaged neutron flux

l_{ij} are the branching fractions of radioactive disintegrations from nuclides j

f_{ik} are the branching fractions for neutron absorption by other nuclides k that lead to the formation of species i

2.3.1.3 Outputs of the lattice physics calculation

Most fuel lattice calculations typically assume a reflective outer boundary condition thus the solution represents that of an infinite number of identical cells and is therefore referenced as an infinite lattice calculation. As there is no leakage in such an arrangement, the steady-state multi-group NTE becomes only a balance between the neutron production and removal. Therefore, equation (16) reduces to an eigenvalue problem (see equation (22)) where the eigenvalue is 1/k where k is the multiplication constant of the system.

$$\begin{aligned}&\Sigma_t(r,E)\emptyset\left(r,E,\vec{\Omega},t\right)\\&=\int_{4\pi}d\vec{\Omega}\int_0^{\infty}dE'\,\Sigma_s(r,E'\rightarrow E,\overrightarrow{\Omega'}\rightarrow\vec{\Omega})\emptyset'(r,E',\overrightarrow{\Omega'},t)\\&+\frac{\chi_p(E)}{4\pi k}\int_{4\pi}d\vec{\Omega}\int_0^{\infty}dE'\,\nu_p(r,E')\Sigma_f(E')\emptyset\left(r,E',\overrightarrow{\Omega'},t\right)\end{aligned}\qquad(22)$$

The fuel composition is also changing as a function of time due to the fissile depletion, creation of fission products, and nuclear transmutation. The flux solution of the problem is fed into the Bateman equations over a user-defined time step to evaluate the new fuel isotopic composition (ORIGEN module [24]). The steady-state NTE is solved again to obtain a new flux distribution before depleting the fuel another time. This process is repeated for a selected number of depletion steps, also called burnup steps. The infinite multiplication constant, k_{inf}, is then obtained as a function of fuel burnup as illustrated in Figure 2-12 for a CANDU infinite lattice cell.

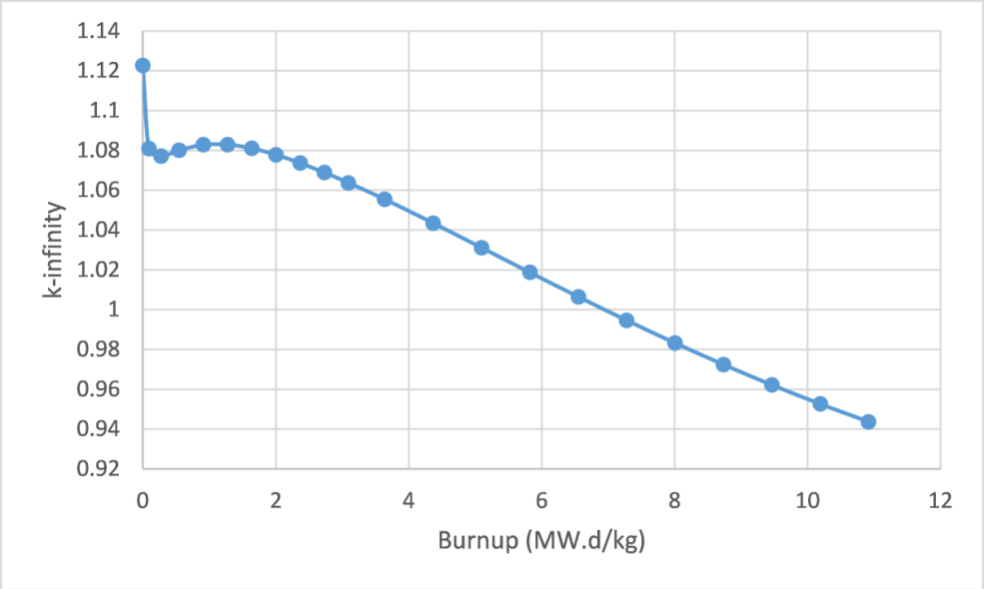

Figure 2-12 k-infinity as a function of fuel burnup in a CANDU lattice cell

The spatially heterogeneous and multi-group cross-sections are furthermore spatially averaged and condensed in few energy groups (usually two) at each depletion step. The procedure involves a flux weighted calculation to conserve the reaction rate within the lattice cell:

$$\overline{\Sigma_g} = \frac{\int_{E_g}^{E_{g-1}} dE \int_V d^3r\, \Sigma(r,E)\emptyset(r,E)}{\int_{E_g}^{E_{g-1}} dE \int_V d^3r\, \emptyset(r,E)} \tag{23}$$

The lattice physics calculation stores these cross-sections tabulated with fuel burnup in a file to be further utilized by a full-core diffusion model.

These few-group cross-sections are at their expected thermal-hydraulic reference conditions (i.e., reference coolant densities, moderator temperatures, coolant temperatures and fuel temperatures). However, the reactor core can be subjected to a wide range of thermal-hydraulic variations both during normal operation and accident conditions. The impact of such changes can be evaluated by modifying the thermal-hydraulic properties parametrically at each depletion step and re-solving the multi-group NTE. Each thermal-hydraulic variable that undergoes a perturbation is referred to as a "branch". Note that the cell is depleted at the reference state conditions only. Figure 2-13 illustrates the process in a flow diagram. Finally, another dimension representing the different thermal-hydraulic conditions is added to the burnup tabulated cross-sections table as shown in Figure 2-14.

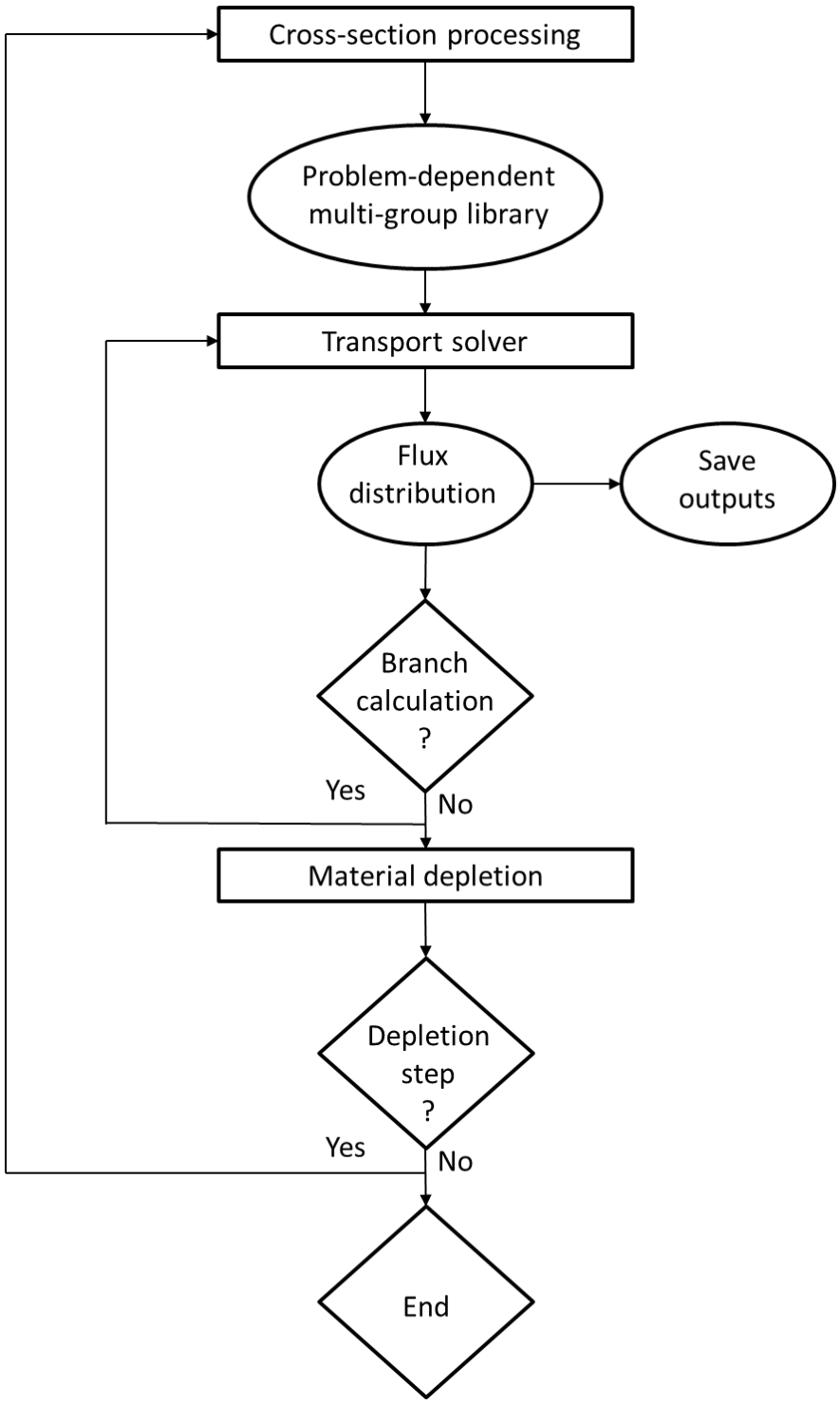

Figure 2-13 Cross-sections generation for subsequent full-core diffusion analysis

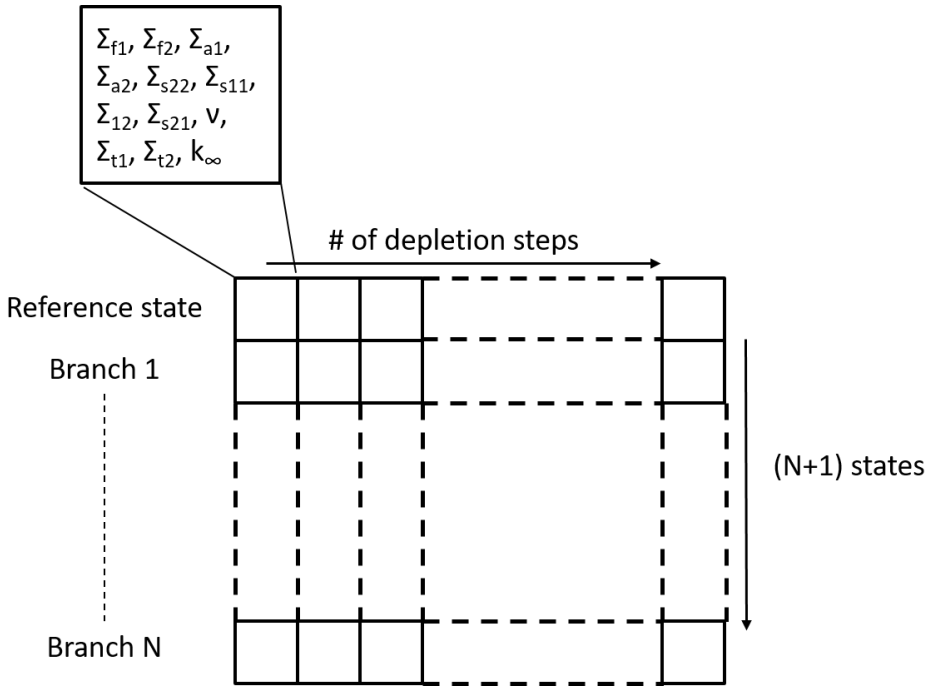

Figure 2-14 Lattice cross-sections tabulated as a function of fuel burnup and thermal-hydraulic conditions

2.3.2 The neutron diffusion approximation for simplified core calculations

The NTE is here simplified through the use of few carefully chosen assumptions. The neutron flux is first assumed to be weakly dependent on angle. The angular dependence is removed by integrating (16) over all directions leading to the neutron continuity equation:

$$\begin{aligned}\frac{\partial n(r,E,t)}{\partial t} + \nabla J(r,E,t) + \Sigma_t(r,E,t)\emptyset(r,E,t) \\ = \int_0^\infty dE'\, \Sigma_s(r,E'\to E,t)\emptyset'(r,E',t) \\ + \chi(E)\int_0^\infty dE'\, \nu_p(E')\Sigma_f(r,E',t)\emptyset(r,E',t) \\ + S_d(r,E,t)\end{aligned} \tag{24}$$

Fick's law [11] can then be applied to relate the currents to fluxes using:

$$J(r,E,t) = -D(r,E,t)\nabla\emptyset(r,E,t) \tag{25}$$

which simply expresses the idea that neutrons tend to travel from high to low neutron density regions. However, this assumption is only valid if the medium is highly diffusive which can be observed to be generally true for reactors except in the vicinity of strongly absorbing materials, sources, and boundaries. The diffusion coefficient can also be proven to be written as [11]:

$$D(r,E,t) = \frac{1}{3\Sigma_{tr}(r,E,t)} = \frac{1}{3\left(\Sigma_t(r,E,t) - \overline{\mu_0}\,\Sigma_s(r,E,t)\right)} \tag{26}$$

where $\overline{\mu_0}$ is the average scattering cosine.

These assumptions finally lead to the neutron diffusion equation:

$$\begin{aligned}\frac{\partial n(r,E,t)}{\partial t} + \nabla D(r,E)\nabla\emptyset(r,E,t) + \Sigma_t(r,E)\emptyset(r,E,t) \\ = \int_0^\infty dE'\,\Sigma_s(r,E'\to E,t)\emptyset'(r,E',t) \\ + \chi_p(E)\int_0^\infty dE'\,\nu_p(E')\Sigma_f(r,E',t)\emptyset(r,E',t) \\ + S_d(r,E,t)\end{aligned} \tag{27}$$

For static reactor physics calculations, the time-dependence disappears and the delayed neutron source is merged with the prompt neutron source. For time-dependent solutions a suitable time marching numerical scheme can be used. The three-dimensional core is divided in coarse meshes where the cross-sections are constant over each individual mesh and condensed in two (or more) energy groups obtained from the lattice calculations. The cross-sections at each location in the core are interpolated from the lattice level simulations using the table shown in Figure 2-14 based on the mesh fuel burnup, the presence of a control rod, and the thermal-hydraulic conditions, if needed. Boundary conditions are also applied at all core boundaries, and a system of coupled algebraic equations is iteratively solved for the neutron flux.

2.3.3 Reactor kinetics: time involvement

The use of the diffusion equation as presented in equation (27) is only adequate to evaluate the core power distribution when the neutron population is constant over time. As soon as a perturbation affects the core, this equilibrium is disturbed and the time-dependence of the neutron population needs to be taken into consideration.

To properly account for the time-dependence of the neutron population, the neutron production term needs to differentiate the neutrons born from fission

(prompt neutrons) and the neutrons emitted by the six groups of precursors (delayed neutrons) as seen in section 2.1.2.

$$\begin{aligned}\frac{\partial n(r,E,t)}{\partial t} + \nabla D(r,E,t)\nabla\emptyset(r,E,t) + \Sigma_t(r,E,t)\emptyset(r,E,t) \\ = \int_0^\infty dE'\, \Sigma_s(r,E' \to E,t)\emptyset'(r,E',t) \\ + \chi_p(E)\int_0^\infty dE'\, \nu_p(E')\Sigma_f(r,E',t)\emptyset(r,E',t) \\ + \sum_k \chi_{dk}(E)\lambda_k C_k(r,t)\end{aligned} \quad (28)$$

where χ_{dk} is the delayed neutron spectrum of group k, λ_k is decay constant of group k, and C_k is the precursors concentration of group k.

The concentration of the precursors C(r,t) evolves with time, and an additional six coupled ordinary differential equations are added to the system to calculate their evolution. The precursors are generated by the decay of certain fission products but can also be consumed through neutron capture.

$$\frac{dC_k(r,t)}{dt} = -\lambda_k C_k(r,t) + \nu_d \Sigma_f(E)\emptyset(r,E,t) \quad ; \quad k = 1,\dots,6 \quad (29)$$

The set of seven coupled equations is then solved to obtain the evolution of the neutron population in the reactor core. For many perturbations, the flux shape is assumed constant and only the amplitude varies with time. This approximation is referred to as the point kinetics approximation and is often sufficient to obtain the time behavior of the neutron population. However, local perturbations lead to a substantial flux distortion and the point kinetics equations cannot be applied. Therefore, as space and time cannot be decoupled, spatial kinetics is needed to model the evolution of the flux distribution accurately.

The thermal-hydraulic conditions are also changing during a transient and hence additional information is required and can be obtained by separate time-dependent thermal hydraulic calculations. Such information is used with the above described branch perturbations to update the relevant cross sections within the physics simulations at each time step.

2.4 Thermal-hydraulics calculations

Thermal-hydraulic conditions are tightly coupled to the power distribution, and vice-versa. The evaluation of fluid properties due to the heat generated through fission reactions was therefore carried out with a one-dimensional code: RELAP5/SCDAPSIM/MOD4 (RSM4) [25]. While CATHENA [26], SCTRAN [27], and TRACE [28] are similar codes, RSM4 was subjected to many modifications to accommodate supercritical conditions [29, 30] hence the decision to perform the analyses with it.

The primary heat transport system, or part of it, can be approximated with one-dimensional pipes and junctions. The conservation of mass, momentum, and energy has to be ensured in each control volume of the system and is therefore presented in this section. Numerous constitutive relationships and equations of state are also required, and a selected number will be introduced here.

It is important to notice that the water at supercritical conditions is always considered as a single phase fluid (non-phasic transformations). The field equations, as a consequence, will be described for single phase fluids.

2.4.1 Conservation equations for a single phase fluid

The three field equations are introduced in turn in a one dimensionalized simple rectangular control volume of length Δz and cross-sectional area A. The idea is to write a balance equation for each variable in the control volume:

$$\begin{aligned}\{Rate\ of\ change\} \\ = \{What\ is\ leaving\} - \{what\ is\ entering\} \\ + \{what\ is\ stored\}\end{aligned} \tag{30}$$

- Mass continuity

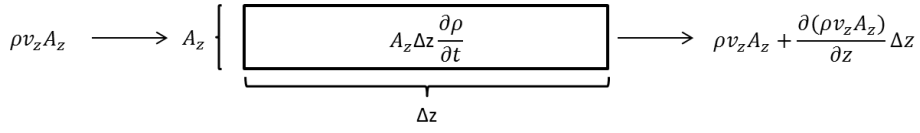

Figure 2-15 Rate of change for the mass continuity

The balance equation for the mass continuity, where no mass is stored, can be written as:

$$A\frac{\partial \rho}{\partial t} + \frac{\partial}{\partial z}(\rho \vec{v} A) = 0 \tag{31}$$

where ρ is the fluid density in kg.m^{-3}, t the time, z the spatial variable, and $\vec{v}$ is the fluid velocity in m.s^{-1}.

- Momentum conservation

The momentum flow rate can change due to external forces. These forces can be defined as a body force such as gravity or surface forces. The shear stress is a tangential surface force trying to rotate the fluid element by internal friction. The normal surface forces such as pressure and internal friction effect tend to elongate the fluid element in the direction of interest. Figure 2-16 illustrates the different forces applied on the control volume. Note that the forces in the y-direction are not represented for simplicity.

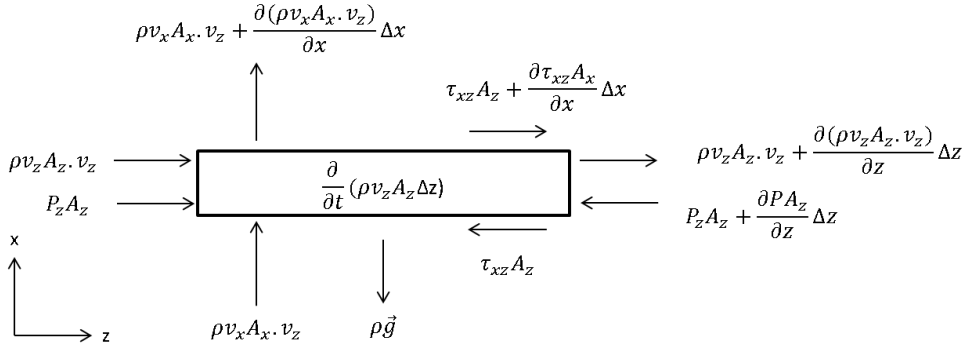

Figure 2-16 Forces involved in the conservation of momentum on a control volume

$$\frac{\partial(\rho v_z)}{\partial t} + \frac{\partial(\rho v_z . v_z)}{\partial z} + \frac{\partial(\rho v_z . v_x)}{\partial x} + \frac{\partial(\rho v_z . v_y)}{\partial y} = -\frac{\partial P}{\partial z} - \rho g cos\theta + \frac{\partial \tau_{zz}}{\partial z} + \frac{\partial \tau_{xz}}{\partial x} + \frac{\partial \tau_{yz}}{\partial y} \quad (32)$$

where θ is the angle between the gravity vector and the flow direction, P is the pressure in Pa, τ is the shear stress in Pa.

The shear forces (terms including a tensor τ) are usually represented as a friction force in the thermal-hydraulics codes mentioned earlier, referred as "$F_{friction}$" in equation (33). This term is determined with a closure relationship presented further in this section.

$$\frac{\partial(\rho v_z A_z \Delta_z)}{\partial t} + \frac{\partial(\rho v_z A_z \Delta_z . v_z)}{\partial z} + \frac{\partial(\rho v_z A_x \Delta_x . v_x)}{\partial x} + \frac{\partial(\rho v_z A_y \Delta_y . v_y)}{\partial y} = -\frac{\partial P A_z}{\partial z} - \rho g A_x sin\theta + F_{friction} \quad (33)$$

- Energy conservation

The energy "u" is defined as the sum of the internal energy and the kinetic energy. By keeping the previous notation, the balance equation for the fluid energy can be written as [31]:

$$\frac{\partial(\rho u)}{\partial t} = -\frac{\partial(\rho u v_z)}{\partial z} - \frac{\partial q_z''}{\partial z} + q''' - \frac{\partial(p v_z)}{\partial z} + \frac{\partial}{\partial z}\left(\tau_{zz} v_z + \tau_{xz} v_x + \tau_{yz} v_y\right) + v_z \rho g cos\theta \quad (34)$$

The first term on the right-hand side represents the rate of change in energy due to convection in the control volume. The second term is the net heat transport rate due to conduction. q''' is the internal heat production due to eventual energy sources. The last three terms represent the rate of work done on the fluid by the pressure, viscous forces, and body forces, respectively [31].

2.4.2 Constitutive relationship

2.4.2.1 Wall friction evaluation

The wall friction forces in the momentum equation (33) were simplified by inserting the $F_{friction}$ term. This term only includes the losses due to the shear stress. Complicated geometries losses are taken into account using either energy-loss coefficients or mechanical form-loss models [32].

It is shown that $F_{friction}$ can be written as follow [32]:

$$F_{friction} = \tau p = \lambda(Re)\frac{\rho v^2}{2} p \quad (35)$$

where:

- 'p' is the wetted perimeter
- 'v' is the fluid velocity
- '$\lambda(Re)$' is the Darcy friction factor

- $Re = \frac{\rho v D}{\mu}$ is the Reynolds number
- $D = \frac{4A}{p}$ is the hydraulic perimeter
- 'A' is the flow area
- 'μ' is the dynamic viscosity of the fluid

The determination of the Darcy friction factor in RELAP5 depends on the flow regime which is based on the Reynolds number.

- Laminar flow (Re ≤ 2200):

$$\lambda(Re) = \frac{64}{Re.\emptyset_s} \tag{36}$$

with $\emptyset_s$being a user-input shape factor for non-cylindrical geometries.

- Turbulent flow (Re ≥ 3000):

$$\lambda(Re) = \frac{1}{\left[-2\log_{10}\left(\frac{\varepsilon}{3.7D} + \frac{2.51}{Re}\left(1.14 - 2\log_{10}\left(\frac{\varepsilon}{D} - \frac{21.25}{Re^{0.9}}\right)\right)\right)\right]^2} \tag{37}$$

This equation comes from the Zigrang-Sylvester approximation to the Colebrook-White correlation [32] where 'ε' is the surface roughness.

- Transition regime (2200 < Re < 3000):

$$\lambda(Re) = \lambda(2200) + (\lambda(3000) - \lambda(2200))\left(3.75 - \frac{8250}{Re}\right) \tag{38}$$

The transition zone simply uses an interpolation between the friction factor at the upper range of the laminar flow and the lower range of the turbulent flow. While there may be some differences in super-critical water friction factor as compared to sub-critical conditions, these differences are still a topic of research and not included in the analysis within this thesis.

2.4.2.2 Conductive heat transfer calculation

Conduction is the heat transfer in a medium due to the presence of a temperature gradient. The heat transferred through conduction is calculated using the heat equation in one dimension (39). As the location of interest is usually a fuel pin, cylindrical coordinates are used.

$$\rho C_p \frac{\partial T}{\partial t} = \frac{1}{r}\left[\frac{\partial}{\partial r}\left(rk\frac{\partial T}{\partial r}\right)\right] + q''' \quad (39)$$

where 'ρ' is the material density, 'C_p' is the specific heat capacity, 'r' is the radius, T is the temperature, 'k' is the material thermal conductivity, and q''' is the internal heat source.

The internal heat source would usually be the energy generated through fission in the fuel material. The heat would then be conducted through the fuel, gap, and the cladding before being transferred to the coolant. The heat exchange from the cladding to the coolant is dominated by a different heat transfer mechanism referred as "convective heat transfer" presented in the following section.

2.4.2.3 Convective heat transfer calculation

Convection is the heat transfer by movement of fluids. The convective heat transfer is modeled using (40):

$$\mathrm{Q} = hA\left(T_w - T_f\right) \quad (40)$$

where Q is the heat transferred, 'h' is the heat transfer coefficient, 'A' is the area of heat exchange, 'T_w' is the wall temperature, and 'T_f' is the bulk fluid temperature.

While the relationship seems rather simple, the determination of the heat transfer coefficient can be quite challenging, especially in the vicinity of the pseudo-critical point where the water properties undergo abrupt changes. Water in the supercritical phase has been the subject of extensive studies with the objective of determining an empirical correlation for the heat transfer coefficient. Fortunately, the famous Dittus-Boelter correlation, given below in equation (41), for single-phase water was proven quite appropriate. Therefore, in RELAP5, the supercritical water is considered as a single-phase liquid for the purpose of convective heat transfer. The heat transfer coefficient is evaluated through the use of:

$$Nu = \frac{hD_e}{k} = 0.023Re^{0.8}Pr^{0.4} \quad (41)$$

where:

- Nu is the Nusselt number representing the ratio of convective over conductive forces
- Pr is the Prandtl number representing the ratio of the viscous and thermal diffusion rates

$$\mathrm{Pr} = \frac{viscous\ diffusion\ rate}{thermal\ diffusion\ rate} = \frac{c_p \mu}{k} \tag{42}$$

- D_e is the heated equivalent diameter
- k is the thermal conductivity

There is significant ongoing research related to the behavior of the convective heat transfer coefficient under SCWR conditions including normal heat transfer (like that modeled in equation (41)), enhanced heat transfer, and deteriorated heat transfer. Since there is no consensus on the latter two mechanisms, they are not modelled in this thesis. Given that such phenomena usually occur near the pseudocritical temperature and that this location is usually much further upstream from the location of peak clad temperature, the impact on the results is small.

Chapter 3

Modeling and Optimization

A combination of lattice physics, full-core diffusion and thermal-hydraulic simulations were utilized to model, optimize, and study the Canadian SCWR. This section aims at providing a more detailed description of the different models built for this work and should be seen as a support of the three journal publications presented in Chapter 4, Chapter 5, and Chapter 6.

3.1 Reactor physics

One of the main goals of reactor physics modelling is to obtain the three-dimensional power distribution in the reactor core. A common practice uses a two-step approach. First, neutron transport simulations are performed over a representative portion of core, typically for a single lattice cell with reflective boundary conditions. The flux and reaction rate information from these lattice level simulations are then used to spatially homogenize a cell and condense the number of energy groups. Such calculations are performed at fresh and burnt fuel conditions as well as for each branch condition and the results form a database of potential cross section information. The second step of the analysis uses these condensed and homogenized cross-sections to generate a full core model. With this information the flux/power distribution is calculated for the entire core by solving the diffusion equation. This section describes in details the models built for simulating the Canadian SCWR.

3.1.1 Lattice physics calculations

3.1.1.1 The original Canadian SCWR lattice cell: a CNL design

The fuel lattice cell design has evolved over the past decade to improve its performance. The initial CANFLEX geometry contained 43 fuel elements arranged in four rings similar to a CANDU lattice geometry [33] but quickly changed to a 54-element geometry organized in three concentric rings to improve the fuel burnup and coolant void reactivity [7]. The linear element

rating (LER) was later found to be excessively high, and the concept was adjusted [6]. The next year, a 78-element concept was created to reduce the LER while maintaining the performance criteria [34] and at that time a code-to-code benchmark comparison was performed [35]. Finally, a lattice with 62 fuel elements arranged in two concentric rings was developed [36] which rapidly evolved into an optimized 64-element geometry [37]. The Canadian SCWR fuel lattice cell evolution is summarized in [38] and the latest design was used as a starting point for this work. A two-dimensional slice of the 64-element fuel assembly was modeled in SCALE [22] (Figure 3-1) according to the specifications provided by Canadian Nuclear Laboratories (CNL) as listed in Table 3-2 and Table 3-3 [37].

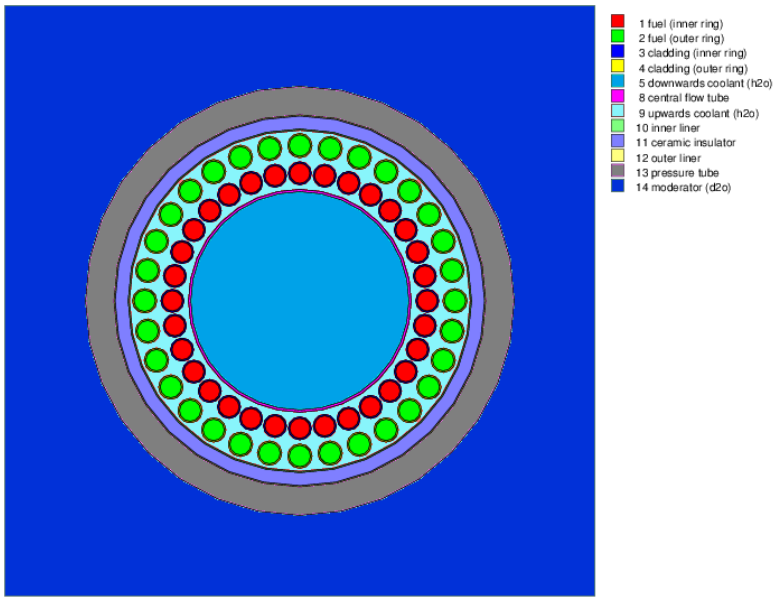

Figure 3-1 Original CNL fuel lattice cell design

As described in Section 2.3.1.1, NEWT uses a discrete ordinates method to solve the neutron transport equation for the flux. The lattice was discretized (1) in space by using a meshing, (2) in energy by using a 238 energy group library based on ENDF/B.VII.0, and finally (3) in angular direction by considering a certain number of discrete angular quadrature (S_n). Reflective boundary conditions were applied on the edge of the cell which is equivalent to say that the lattice cell is surrounded by an infinite number of identical cells.

The light water coolant is subjected to a large density change, while heating up along the fuel channel (Figure 3-2), which significantly impacts the lattice physics phenomena. Harrisson and Marleau [39] demonstrated that a minimum of 14 isovolumetric axial nodes should be used to properly model the fuel assembly in 3D. The fuel assembly was therefore divided into 20 nodes along the channel axis to obtain isometric nodes (25x25x25 cm^3). Thus the two-dimensional fuel lattice calculations were performed at each axial position with averaged material temperatures and densities (Table 3-2 and

Table 3-3 [9]). This results in 20 separate fuel tables, each with its own depletion and branch calculations.

Table 3-1 Geometry specifications of CNL's Canadian SCWR lattice cell

Component	Dimension	Material	Composition [wt%]	Density [g.cm^{-3}]
Centre Tube Coolant	4.6 cm radius	Light Water	100% H_2O	Variable
Centre Flow Tube	4.60 cm inner radius ; 0.1 cm thick	Zr-modified 310 Stainless Steel	C: 0.034; Si: 0.51; Mn: 0.74; P: 0.016; S: 0.002; Ni: 20.82; Cr: 25.04; Fe: 51.738; Mo: 0.51; Zr: 0.59	7.9
Inner Fuel Pins (32)	0.415 cm radius; 5.4 cm pitch radius	15 wt% PuO_2 in ThO_2	Pu: 13.23; Th: 74.7; O: 12.07	9.91
Outer Fuel Pins (32)	0.44 cm radius; 6.575 cm pitch radius	12 wt% PuO_2 in ThO_2	Pu: 10.59; Th: 77.34; O: 12.08	9.87
Cladding	0.06 cm thick	Zr-modified 310 Stainless Steel	As above	7.9
Coolant		Light Water	100% H_2O	Variable
Liner Tube	7.2 cm inner radius; 0.05 cm thick	Zr-modified 310 Stainless Steel	As above	7.9
Insulator	7.25 cm inner radius; 0.55 cm thick	Yttria Stabilized Zirconia	Zr: 66.63; Y: 7.87; O: 25.5	5.37
Outer Liner Tube	7.8 cm inner radius; 0.05 cm thick	Excel Alloy	Sn: 3.5; Mo: 0.8; Nb: 0.8; Zr 94.9	6.52
Pressure Tube	7.85 cm inner radius; 1.2 cm thick	Excel Alloy	As above	6.52
Moderator	25 cm square lattice pitch	Heavy Water	99.833 D_2O; 0.167 H_2O	1.0851
Plutonium Isotopics		Reactor Grade Plutonium	Pu238: 2.75; Pu239: 51.96; Pu240: 22.96; Pu241: 15.23; Pu242: 7.10	

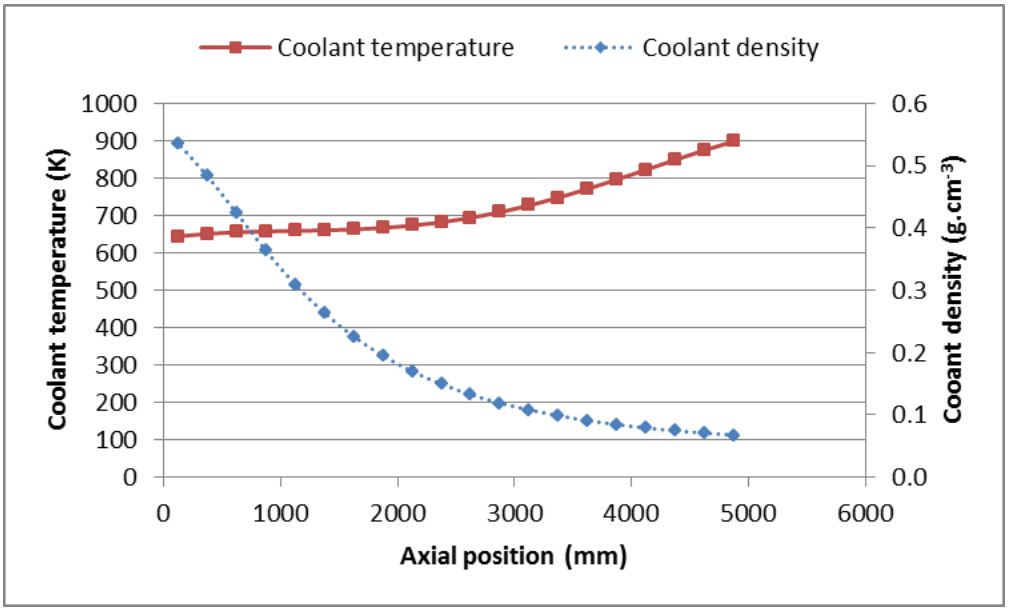

Figure 3-2 Coolant temperature and density variation along the fuel channel

Table 3-2 Thermal-hydraulic conditions of the fuel lattice cell's materials

Position (mm)	Upward Coolant Density ($g.cm^{-3}$)	Upward Coolant Temperature (K)	Cladding Temperature (K)	Liner Temperature (K)	Insulator Temperature (K)
4875	0.0677	898.22	1027.86	868.77	678.80
4625	0.0707	874.76	1015.29	846.94	665.38
4375	0.0744	849.19	995.60	822.77	650.51
4125	0.0789	822.58	969.50	797.80	635.14
3875	0.0843	796.23	940.27	773.34	620.04
3625	0.0908	771.03	909.17	750.17	605.84
3375	0.0985	747.67	877.38	729.00	592.80
3125	0.1080	726.72	845.01	710.29	581.20
2875	0.1190	708.63	813.50	694.45	571.33
2625	0.1327	693.64	783.80	681.62	563.33
2375	0.1493	681.79	756.30	671.80	557.17
2125	0.1697	672.97	732.66	664.82	552.79
1875	0.1948	666.80	712.63	660.28	549.94
1625	0.2257	662.80	696.70	657.67	548.31
1375	0.2634	660.35	685.40	656.27	547.43
1125	0.3093	658.78	678.51	655.37	546.87
875	0.3637	657.34	679.99	653.71	545.82
625	0.4238	655.07	684.69	650.74	543.96
375	0.4834	650.88	689.28	645.52	540.68
125	0.5358	644.19	684.35	637.83	535.83

Table 3-3 Thermal-hydraulic conditions of the fuel lattice cell's materials

Position (mm)	Pressure Tube Temperature (K)	Downward Coolant Temperature (K)	Downward Coolant Density ($g.cm^{-3}$)	Average Fuel Temperature (K)	Center Tube Temperature (K)
4875	453.89	624.65	0.6211	1625.88	761.44
4625	449.98	626.29	0.6156	1676.94	750.53
4375	445.60	627.74	0.6105	1700.69	738.47
4125	441.01	629.00	0.6060	1691.88	725.79
3875	436.44	630.08	0.6021	1666.43	713.15
3625	432.10	631.00	0.5986	1631.85	701.01
3375	428.05	631.77	0.5956	1594.48	689.72
3125	424.40	632.42	0.5931	1551.57	679.57
2875	421.27	632.96	0.5909	1507.90	670.79
2625	418.72	633.41	0.5891	1465.39	663.53
2375	416.74	633.79	0.5876	1420.62	657.79
2125	415.32	634.11	0.5862	1381.78	653.54
1875	414.40	634.40	0.5851	1345.72	650.60
1625	413.86	634.66	0.5840	1312.25	648.73
1375	413.58	634.90	0.5829	1285.71	647.62
1125	413.40	635.13	0.5820	1262.89	646.96
875	413.06	635.34	0.5811	1249.20	646.34
625	412.45	635.52	0.5803	1234.12	645.30
375	411.37	635.66	0.5797	1201.29	643.27
125	409.77	635.73	0.5794	1136.85	639.96

NEWT requires the evaluation of Dancoff factors (DF) to perform the energy self-shielding calculation. The MCDANCOFF module [40] was initially developed to evaluate DFs in irregular geometries such as water holes in BWR lattices and was later extended to CANDU-type geometries [41] as explain in Section 2.3.1.1 above.

The DFs were calculated for each fuel pin. However, they were found to be extremely similar in fuel pins within the same ring (standard deviation < 1%). As a consequence, the DFs were averaged over each fuel ring. Moreover, the coolant density variations considerably affect the DFs, so they were evaluated at each axial position as recommended in [22] (see Appendix A).

As mentioned above, a combination of Cartesian spatial meshing and angular meshing was used within a lattice cell. On the one hand, a very fine meshing would produce accurate results; yet, it would require a considerable amount of time. On the other hand, a very coarse meshing would be time efficient but could produce very inaccurate results. A balance between accuracy and simulation time needed to be found; thus a sensitivity study was performed to minimize the running time while maintaining acceptably accurate results. For each case, the infinite multiplication constant (k_{inf}) was chosen as an element of comparison due to its integral nature.

Firstly, the sensitivity to the angular discretization, represented by the "Sn" variable, was evaluated (Table 3-4) with a very fine meshing. As expected, the maximum error is observed with the lowest angular quadrature (S_n=4); however, the discrepancy remains small (28 pcm) so the choice was made to carry on with an angular quadrature of four to reduce the computational burden.

The spatial meshing sensitivity was performed for three variables:

- global Cartesian meshing
- concentric radial meshes in the central tube
- concentric radial meshes in the coolant between the fuel pins

While the other components (liners, insulator, and pressure tube) also utilize radial meshing, lattice calculations are relatively insensitive to it in these more transparent materials. Therefore the focus of the mesh sensitivity study was on Cartesian mesh and radial mesh in the coolant regions.

While refining one mesh type generally increases the computational time, the k_{inf} may or may not improve relative to the reference. The parametric study of the spatial meshing requires more attention due to the overlapping of a Cartesian-type meshing with a radial-type meshing. In fact, anytime the two mesh types intercept, a new mesh is created in SCALE for the flux calculation. The parametric study is presented in Table 3-5, and the discrepancy was calculated relative to the reference case in Table 3-4. The computation time

clearly increased with the refinement of the meshing (Cartesian or radial), but while the discrepancy tended to decrease with an increasing number of radial meshes, the most coarse Cartesian meshing (16x16) displayed more accurate results. The bolded case (Cartesian=16x16, central tube=25, and Outer coolant=10) in Table 3-5 displays a 4 pcm discrepancy relative to the reference case and was deemed a good compromise between accuracy and computational time and was used throughout this work.

Table 3-4 Angular quadrature sensitivity study

S_n	Cartesian	Radial meshing		Discrepancy (pcm)	Time (min)
	Cell	Central tube	Outer coolant		
16	48x48	25	25	0.00	72
14				0.16	57
12				0.48	43
10				0.12	30
8				1.56	21
6				6.63	12
4				28.15	6

Table 3-5 Parametric study on the fuel lattice cell meshing

S_n	Cartesian	Radial meshing		Discrepancy (pcm)	Time (min)
	Cell	Central tube	Outer coolant		
4	**16x16**	15	10	29	2.5
			15	20	2.9
			20	22	3.3
		20	10	13	2.5
			15	4	3.0
			20	6	3.5
		25	**10**	**4**	**2.7**
			15	5	3.0
			20	3	3.5
	20x20	15	10	33	4.2
			15	32	4.2
			20	32	4.7
		20	10	18	4.3
			15	16	4.7
			20	16	5.3
		25	10	9	4.2
			15	8	5.0
			20	7	5.6
	24x24	15	10	53	38.9
			15	51	46.1
			20	49	52.1
		20	10	39	35.0
			15	36	40.3
			20	34	46.5
		25	10	32	36.4
			15	29	41.6
			20	27	45.3
	28x28	15	10	52	45.2
			15	51	51.6
			20	51	58.6
		20	10	41	46.7
			15	40	53.2
			20	40	60.0
		25	10	34	49.4
			15	33	54.0
			20	33	60.7

3.1.1.2 Control rod design

The inlet and outlet plena are located above the reactor core making it very difficult for the control systems to be inserted from the top of the core. Raouafi and Marleau [42] investigated inclined reactivity control rods inserted at the top of the core while CNL designed control rods entering from the side of the core perpendicular to the fuel assemblies (similar to a CANDU reactor) [8]. In this work, the author opted for cruciform control rods which were designed to enter from the bottom of the core between four fuel assemblies in the low-pressure moderator (Figure 3-3). This control rod design was proposed within the work performed in this thesis because (1) due to the alignment with the fuel channels it provides superior individual channel power control, (2) mimics existing and well-proven BWR blade designs and (3) the increase in negative reactivity towards the edge of the blades minimizes the impact on assembly radial power tilt in the vicinity of an inserted rod. Table 3-6 summarizes the control rod specifications proposed in this work.

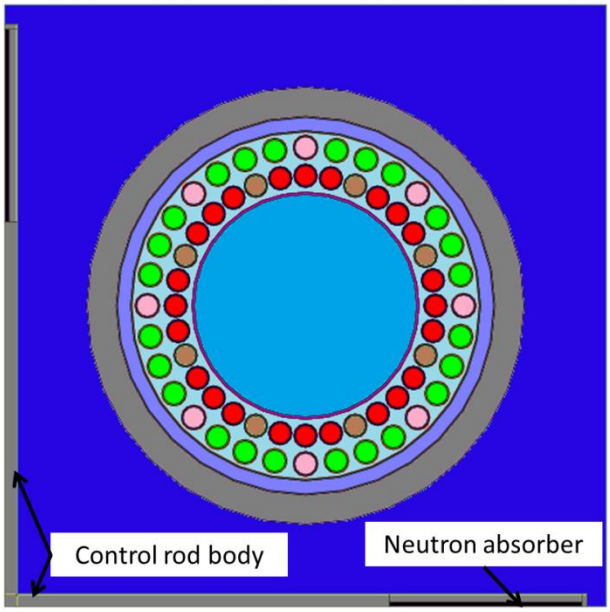

Figure 3-3 Fuel lattice cell with control rod.

Table 3-6 Control rod specifications

	Dimension	Material	Composition	Density
Body	Half span: 24.2 cm ; Thickness: 0.5 cm	Excel Alloy	Sn: 3.5; Mo: 0.8; Nb: 0.8; Zr: 94.9	6.52
Neutron absorber	16 cm from the center; 8 cm long; 0.4 cm thick	Stainless Steel 304	-	7.94

The amount of absorber and its location on the blade were determined as part of the work performed in the first publication (Chapter 4). The neutron absorber was initially occupying more space on the blade (9 cm from the center and 15 cm long) but was later shortened in the second publication (Chapter 5), as shown in Figure 3-3, to obtain a finer control over the channel powers.

3.1.1.3 Fuel-integrated burnable absorbers and depletion steps sensitivity

The design of the fuel-integrated burnable absorber (FIBA) and the parametric study on the number of depletion steps had to be done in parallel due to their interdependence [43]. On the one hand, not only the FIBA has to remove the desired amount of reactivity at beginning of cycle (BOC) but also, they have to burn out at the desired rate. On the other hand, the number of depletion steps has to be carefully selected to simulate the FIBA (and fuel) burnout correctly.

The location and absorber type of the FIBA were largely inspired by earlier studies performed at CNL [8, 44]. Each ring of fuel elements contains 32 fuel pins of which eight contain three weight percent (wt%) gadolinia (Gd_2O_3) in $(Th,Pu)O_2$. By concentrating the gadolinia in fewer fuel pins, the spatial self-shielding was increased allowing for a slower burnout rate of the FIBA. While the power ratio between the inner and outer ring of fuel pins remained similar (blue and black curves in Figure 3-4), the power distribution within a ring was no longer uniform, especially at low burnup due to the high concentration of gadolinia in the selected fuel pins. Indeed, the fuel elements with burnable poison have a lower power; conversely, the power tends to increase in fuel pins without gadolinia to maintain the same power output. Figure 3-5 and Figure 3-6 illustrate the pin power tilt that occurred in each ring of fuel pins at the bottom and top of the core, and with and without the presence of the control[2]. As the fuel ages, the poison is consumed and the pin power tilt becomes negligible.

[2] The control rod mainly affects the neutron flux in the moderator region; therefore, the outer ring is more sensitive to its presence. When inserted, the control rod increases the overall power generated in the inner ring (decreases the power generated in the outer ring) as observed in Figure 3-4. In addition, the tilt is increased by 12% in the outer ring of fuel pins (2% in the inner ring) when comparing Figure 3-5 and Figure 3-6

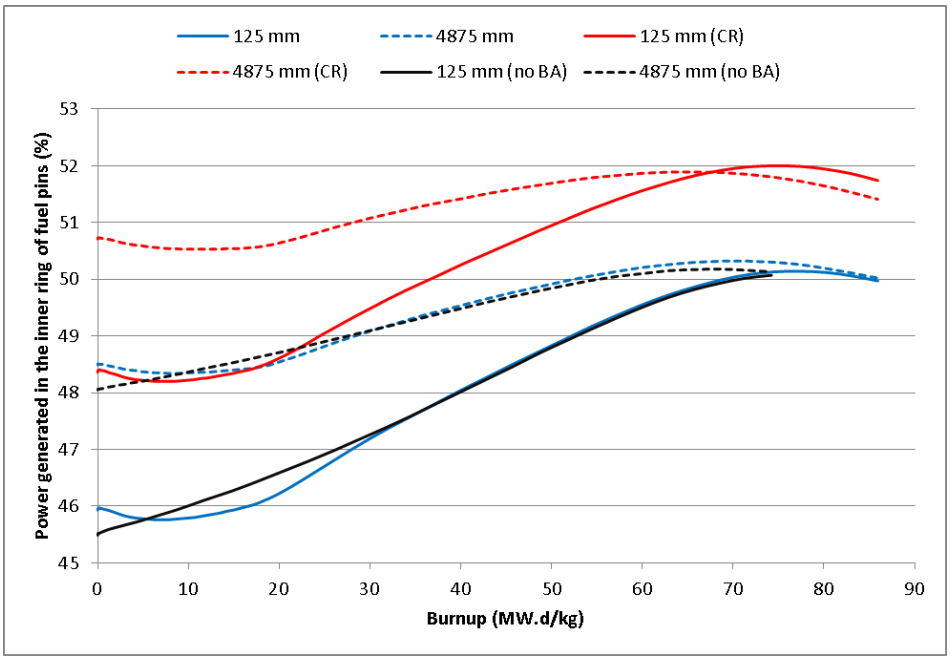

Figure 3-4 Amount of power generated in the inner ring of fuel pins as a function of fuel burnup for 3 cases: no FIBA (no BA), with FIBA, and with FIBA and control rod (CR) inserted

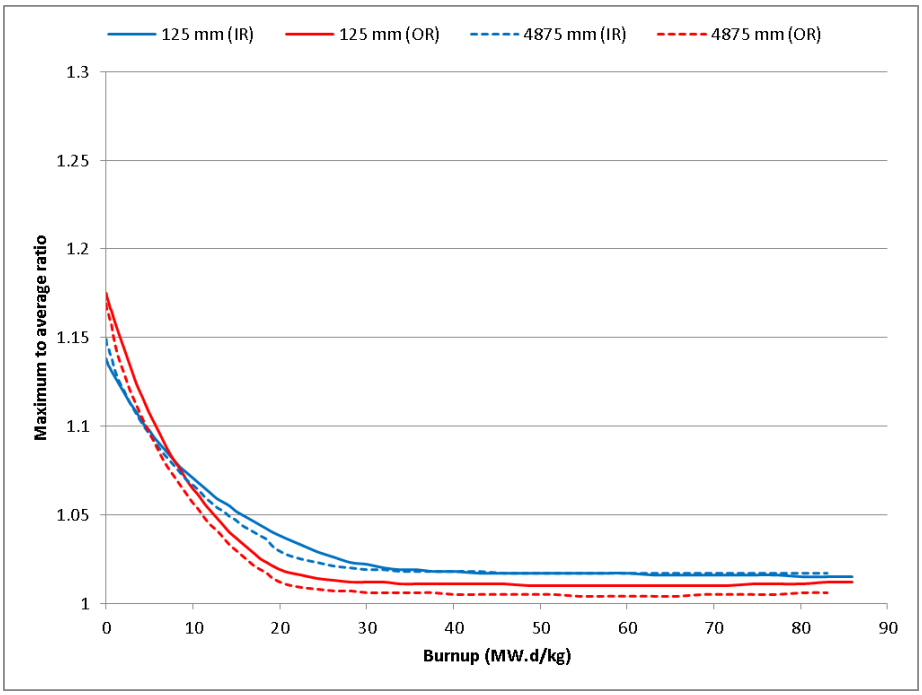

Figure 3-5 Ratio of the maximum pin power over the average ring power for the inner ring (IR) and outer ring (OR) at the bottom (125 mm) and top (4875 mm) of the core <u>without the control rod</u>

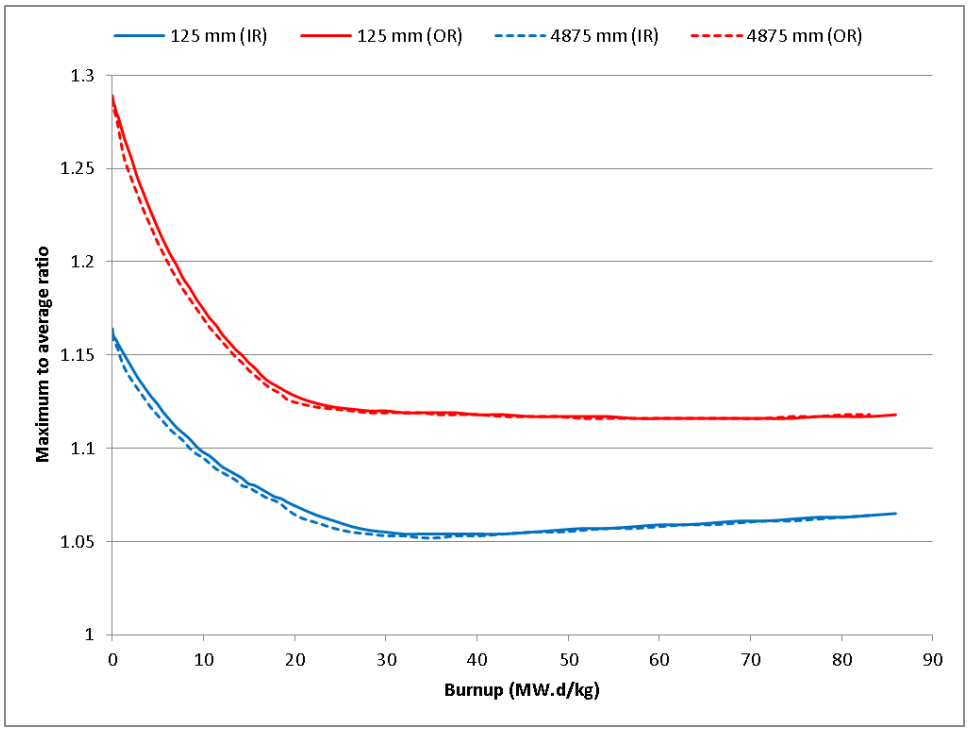

Figure 3-6 Ratio of the maximum pin power over the average ring power for the inner ring (IR) and outer ring (OR) at the bottom (125 mm) and top (4875 mm) of the core with the control rod

When simulating the FIBA depletion, an appropriate radial meshing within the fuel pin needs to be used to model the spatial self-shielding accurately [43]; therefore 12 radial meshes were chosen as a reference and sensitivity studies were used to assess the effect of radial meshing. The fuel material in each mesh was independently depleted based on the flux solution within the mesh. The number of depletion steps for the reference case (93) used very small time steps for the first 20 days to account for the fission products build-up and small time steps until exhaustion of the FIBA (see Table 3-7) [43].

The multiplication constant as a function of fuel burnup is plotted in Figure 3-7 for three FIBA concentrations; namely 2.5, 3.0 and 3.5 wt% gadolinia in $(Th,Pu)O_2$, using the reference number of depletion steps (93) and radial meshes (12) within pins containing FIBA. 3.0 wt% gadolinia in $(Th,Pu)O_2$ was deemed satisfactory as (i) the initial excess reactivity was considerably reduced, (ii) the reactivity swing throughout the FIBA burnout is acceptable compared to a previous study [8], and (iii) the impact of the FIBA on the lattice reactivity at the end of a batch length (~420 days) is small.

The depletion calculation was successively run with 5, 8, and 12 (reference) radial zones of equal volume using three wt% gadolinia in $(Th,Pu)O_2$ for the reference number of depletion steps. A maximum of 0.5 mk was observed for 8 radial zones (1.72 mk for 5 zones) with an averaged discrepancy of 0.21 mk (0.7 mk for 5 zones). Therefore, k_{inf} is weakly sensitive to the number of radial

meshes above eight radial zones. Eight concentric meshes were then deemed sufficient and used in all subsequent cases (Figure 3-8). Figure 3-9 illustrates the number density of Gd-157 as a function of fuel burnup in each radial zone. The outermost zone depletes Gd-157 faster due to the higher thermal neutron flux. The innermost zone has the lowest thermal neutron flux due to spatial shielding (thermal absorptions) in the outer regions.

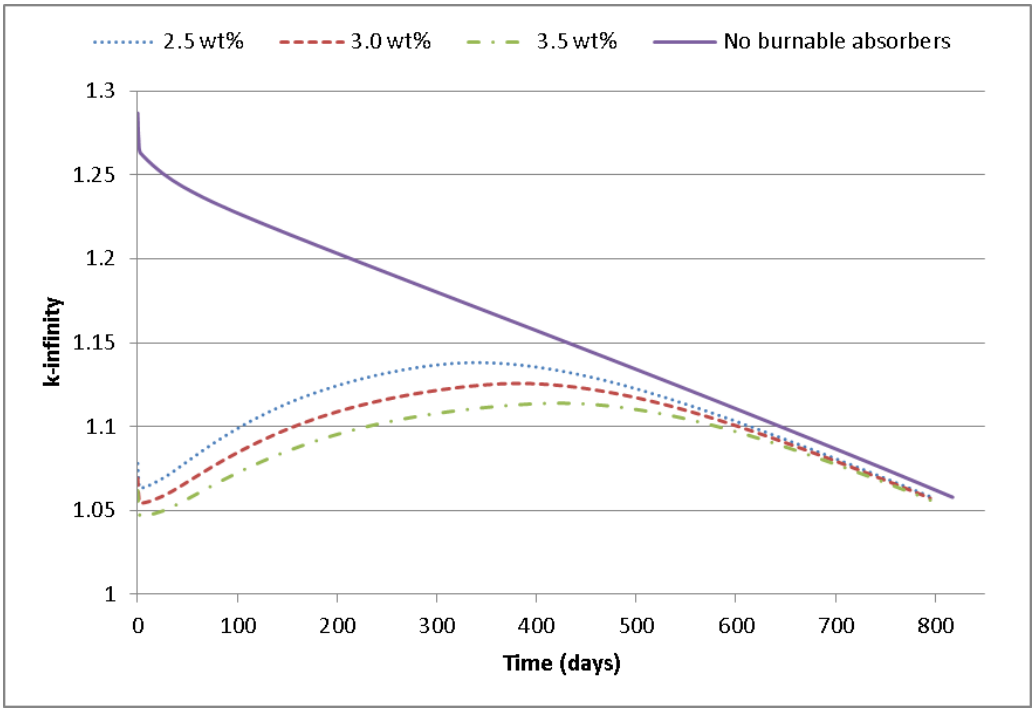

Figure 3-7 k-infinity as a function of time for three FIBA concentrations

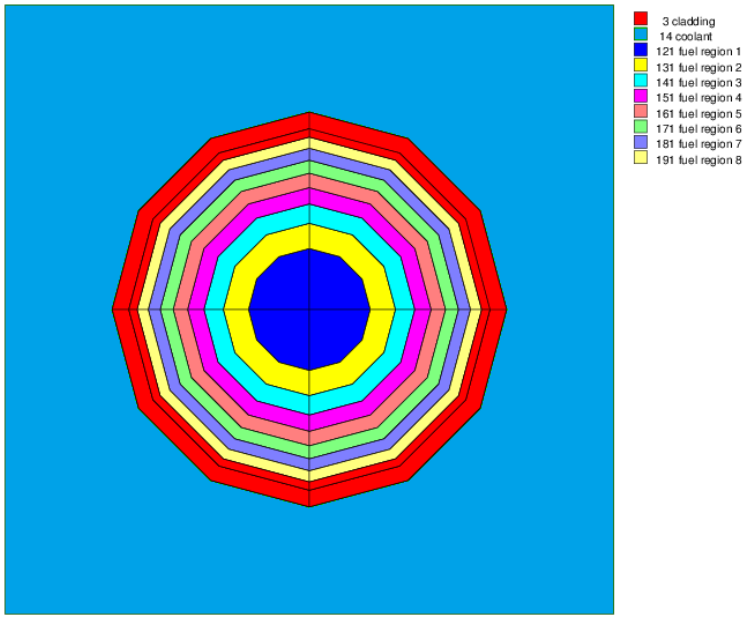

Figure 3-8 Radial meshing in a fuel pin with gadolinia

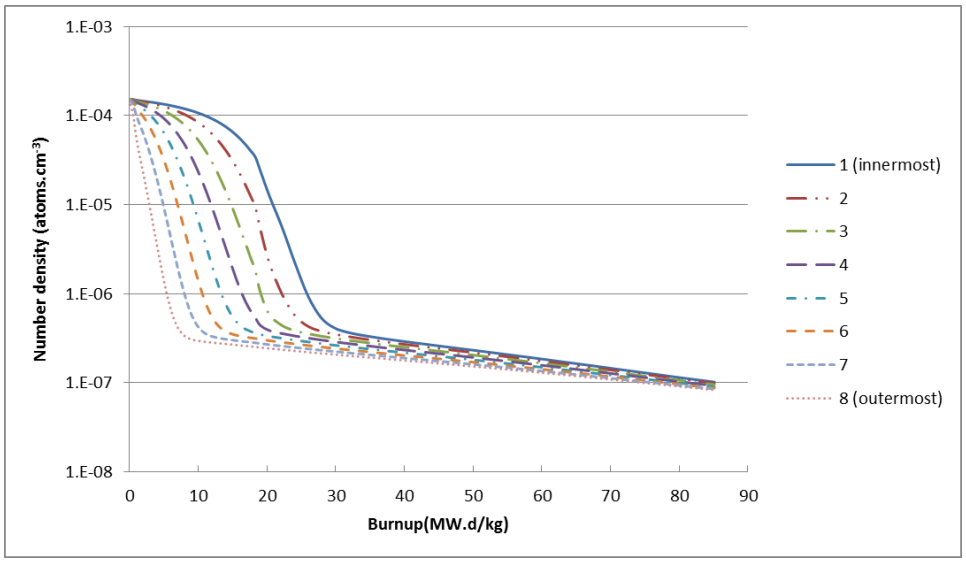

Figure 3-9 Gd-157 number density in each ring as a function of burnup

SCALE uses the ORIGEN module to perform fuel depletion calculations [24], which has a computational time that is directly related to the number of depletion steps. Again, to optimize accuracy and time, a parametric study on the number of depletion steps was performed. A reference case was created for the evolution of k_{inf} when a high number of depletion steps were used until the FIBA were depleted. k_{inf} was then evaluated as a function of fuel burnup with fewer depletion steps. Table 3-7 summarizes the results obtained for several cases. Case 3 (42 depletion steps) showed a maximum discrepancy of 0.89 mk with an average error of 0.293 mk and was chosen to perform depletion calculations. Figure 3-10 illustrates the evolution of k_{inf} for cases 3, 6, and the reference case in Table 3-7. When the FIBA was depleted, the fuel materials were depleted with steps of approximately 3 MW.d/kg (equivalent to approximately 60 days at 100% full power), as recommended in [43], up to 75 MW.d/kg. A larger depletion step is acceptable as the flux solution does not vary quickly anymore and the k_{inf} decrease becomes fairly linear as a function of burnup due to the fissile depletion/fission products buildup.

The condensed and homogenized cross-sections were generated at each depletion step following the technique described in section 2.3.1.3 using the 238 energy group flux solution of the neutron transport equation. The cross-sections were condensed in two energy groups with an energy cut-off of 2.57 eV due to higher core temperatures, which is higher than that used in thermal reactors and reflects the higher coolant temperatures in the SCWR core. Indeed, the literature suggests an energy cutoff between 2 and 3 eV [11, 45] but a recent study demonstrated the potential need for more energy groups [46]. Finally, the kinetics parameters (neutron velocity, 6-group delayed neutron fractions and lambdas) were generated, and all the data was saved into a file for subsequent use in the diffusion model. These cross-sections are called the “reference” or “unperturbed” cross-sections.

Table 3-7 Parametric study on the number of depletion steps

	From day	To day	Number of steps	Total steps	Max discrepancy (mk)	Averaged discrepancy (mk)
Reference	0	10	10	93	-	-
	10	20	5			
	20	800	78			
1	0	3	3	46	0.89	0.293
	3	10	2			
	10	20	2			
	20	410	26			
	410	800	13			
2	0	1	1	45	1.56	0.523
	1	10	3			
	10	20	2			
	20	800	39			
3	0	1	1	42	0.89	0.268
	1	10	3			
	10	20	2			
	20	410	26			
	410	810	10			
4	0	1	1	35	1.56	0.516
	1	10	3			
	10	20	2			
	20	400	19			
	400	800	10			
5	0	1	2	27	3.82	1.53
	1	10	1			
	10	810	25			
6	0	1	1	22	5.45	2.33
	1	10	1			
	10	810	20			

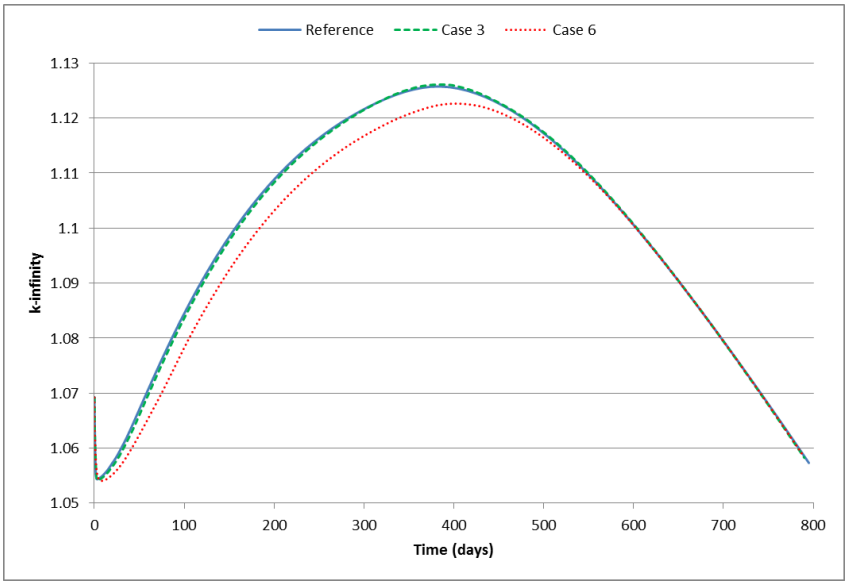

Figure 3-10 k_{inf} as a function of burnup for three different depletion scenarios

3.1.1.4 Reflector cross-sections generation

The Canadian SCWR reactor core is surrounded by a low-pressure heavy water reflector. The radial and axial reflectors are 100 cm and 75 cm thick, respectively [9]. NEWT [17] cannot simply simulate a reflector cell as there are no neutron sources in the geometry. Figure 3-11 depicts a 6x6 multi-cell geometry built in NEWT which includes four fuel lattice cells (used as a neutron source) and 22 reflector cells arranged in a similar pattern as the actual core. Figure 3-12 shows the spatial meshing used in the multi-cell geometry. The fuel cells had the same meshing as the infinite lattice fuel cell described in section 3.1.1.1, and the reflector cells used a 32x32 Cartesian meshing.

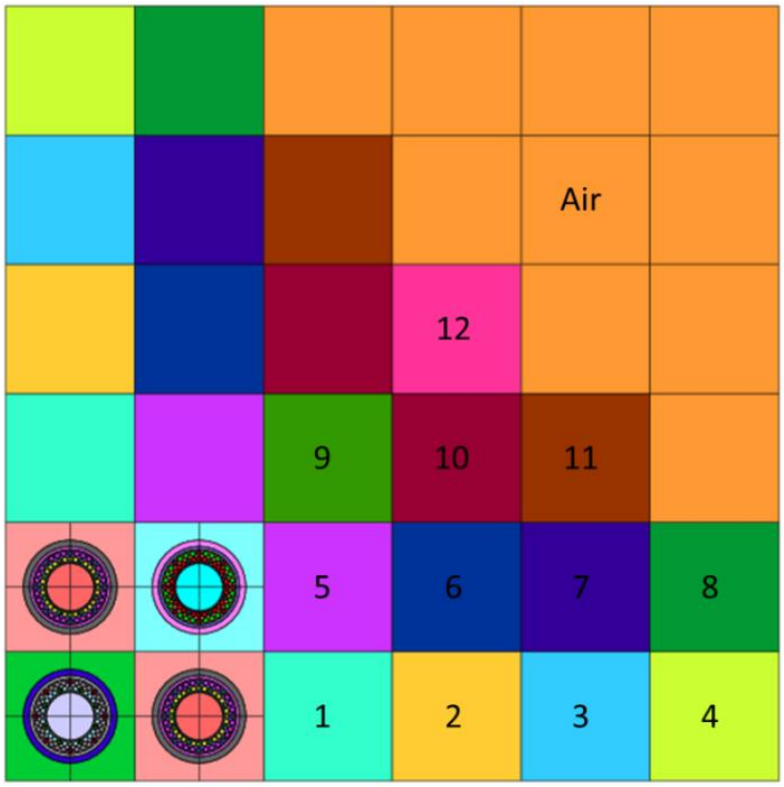

Figure 3-11 Multi-cell geometry in NEWT for reflector cross-sections evaluation

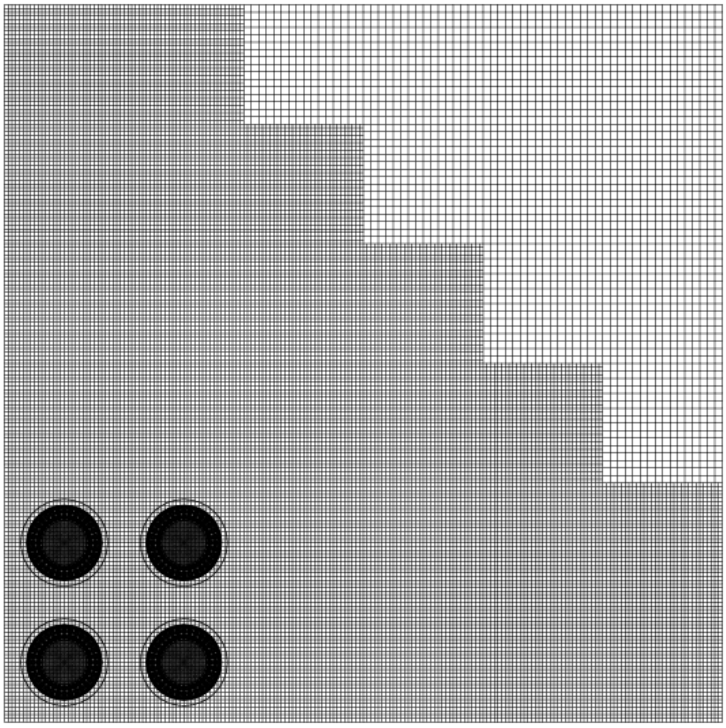

Figure 3-12 Spatial meshing of the multi-cell geometry

The neutrons exiting the reflector through the North or East side represent leakage out of the core. Therefore a reflective boundary condition would not be considered appropriate and a void boundary condition was applied to these two faces.

In the analysis of the simulation results used to determine the homogenized cross sections for the moderator cells, it was observed that even the fuel cells near the edge of the core differed in characteristics as compared to that in the infinite lattice. Earlier studies also demonstrated that errors resulted from the use of infinite lattice cross sections in place of more accurately homogenized fuel cells when they are adjacent to the reflector [47, 48]. The implementation of side/corner cells in the full-core diffusion model, as in Hummel's work [49], or the use of mean reference discontinuity factors (R_mDFs) like in Sharpe's work [50] should be performed in future studies to obtain a more accurate core power distribution. For the purposes of core optimization (Chapter 4 and Chapter 5) and rod drop analyses (Chapter 6), such improvements were not considered practical and were omitted but should be incorporated in future analyses.

3.1.2 Full-core diffusion model

The Purdue Advanced Reactor Core Simulator (PARCS) was used to model the reactor core in three dimensions [51]. The cross-sections generated at the lattice level were processed by a separate code named GENPMAXS [52]

which converts the TRITON output file into a PMAXS file readable by PARCS.

3.1.2.1 PARCS model

The Canadian SCWR core specifications are listed in Table 3-8. The core is quarter symmetric; therefore, only 84 fuel assemblies were modeled for steady-state simulations. Each 5-meter long fuel channel was divided into 20 axial slices creating 1680 isovolumetric fuel nodes. Infinite fuel lattice cell cross-sections were used in each fuel node but each of the 20 axial elevations has its own set of cross-sections. The fuel assemblies are radially surrounded by a 1-meter thick reflector and a 75 cm thick reflector at the top and bottom of the channel.

Table 3-8 Canadian SCWR core specifications [8]

Power (thermal)	2540 MW
Power (electric)	1200 MW
Coolant inlet temperature	350°C
Coolant outlet temperature	625°C
Number of assemblies	336
Assemby pitch	25 cm
Core diameter	710 cm
Core height	650 cm
Active length	500 cm
Axial reflector (top and bottom)	75 cm
Radial reflector	105 cm
Fuel batches	3

3.1.2.2 Equilibrium core calculations

The Canadian SCWR is batch fueled similar to PWRs and BWRs. The core is depleted by steps of 5 days starting from an initial fuel burnup distribution, until the effective multiplication constant (k_{eff}) reaches 1.01 (or approximately 10 mk) similar to previous studies [36]. The fuel assemblies are then shuffled according to a fueling scheme. The process is repeated until the initial burnup (i.e., isotopic concentrations) in each fuel node has not changed by more than 0.1% from one cycle to the next. At this point, the equilibrium cycle is considered to have been reached. The evolution of the equilibrium cycle throughout the work performed is introduced here, step by step:

- Reference design (0.625 eV thermal cut-off, 3-batches) - These simulations were used to benchmark the modeling of the Canadian SCWR core with SCALE, GenPMAXS, and PARCS by comparing the results to the available literature. In addition to the consistency checks with previous simulations using alternative codes, a study was also

performed to choose an appropriate set of cross-sections for the reflector region.

- Implementation of FIBA (0.625 eV cut-off, new 3-batch) - The burnable poison has a significant impact on the power distribution in the core as it reduces the power in the fresh assemblies. The purpose of this analysis stage was to develop a new fueling scheme including FIBA to obtain a similar cycle length and acceptable power distributions during a fueling cycle.
- Axially graded fuel enrichment and FIBA concentration (2.57 eV cut-off, 4-batch cycle,) - In this optimization stage the thermal power of the core was reduced which led to a reduction in overall fuel enrichment to maintain a similar cycle length. In addition, the impact of the new thermal energy barrier on the radial power distribution was investigated. The final design is extensively discussed in Chapter 5.

Each of these analysis stages is discussed below.

3.1.2.3 Reference core results

Hummel's work [9] involved calculating the equilibrium cycle using DRAGON [18] and DONJON [53] for the 64-element fuel assembly design [37]. The 3-batch refueling scheme was taken from [36], and the radial power distribution obtained in PARCS was plotted at BOC and EOC in Figure 3-13 and Figure 3-14 with the absolute difference relative to Hummel's results using DONJON.

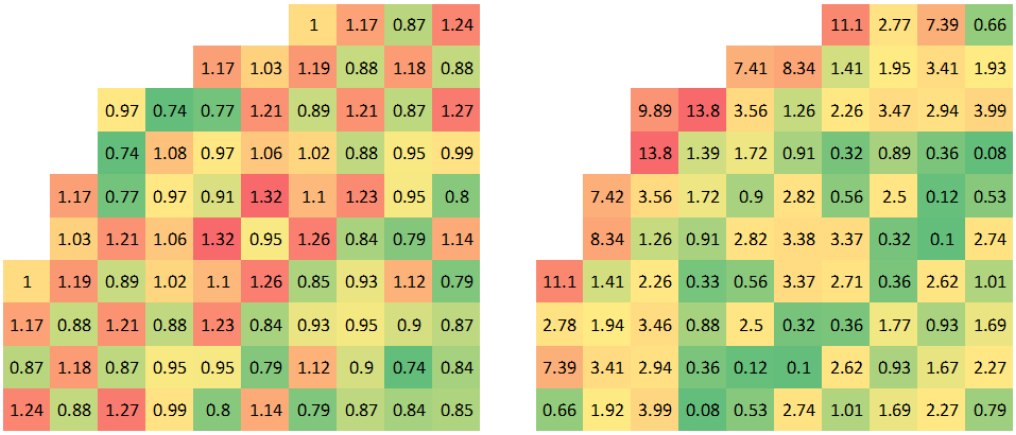

Figure 3-13 Normalized radial power distribution in PARCS at BOC (left) and discrepancy from Hummel's work (%) (right)

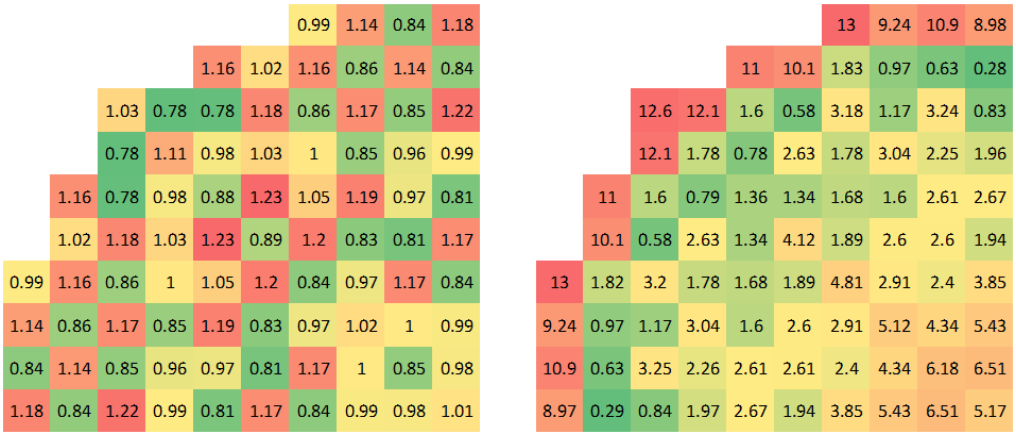

Figure 3-14 Normalized radial power distribution in PARCS at EOC (left) and discrepancy from Hummel's work (%) (right)

Table 3-9 Comparison of the calculated equilibrium cycle to the literature

	Hummel	Current work
Cycle length (days)	447	450
Excess reactivity at BOC (mk)	116	111.6
Average exit fuel burnup (MW.d/kg)	63.401	64.78
Average assembly power discrepancy BOC/EOC (%)	-	2.74 / 3.98

Table 3-9 demonstrates that the equilibrium cycle calculated in this work is very similar to Hummel's work. An average discrepancy of 2.75% (BOC) and 3.98% (EOC) with Hummel's work confirms the proper use of SCALE and PARCS and their capability of modeling the Canadian SCWR. However it should be noted that Hummel's work used eight energy groups and utilized different cross-sections for the assemblies in contact with the reflector which explains the higher discrepancy for the assemblies on the edge of the core.

3.1.2.4 Reflector cross-sections

The multi-cell geometry introduced in section 3.1.1.4 was used to generate several sets of 2-group cross-sections for the reflector region. Three types of multi-cell were built to evaluate the impact of the four fuel cells used on the reflector cross-sections:

- the four fuel cells had no FIBA and used the thermal-hydraulic conditions at the bottom of the core (125 mm)
- the four fuel cells included FIBA and used the thermal-hydraulic conditions at the bottom of the core (125 mm)
- the four fuel cells had no FIBA and used the thermal-hydraulic conditions at the top of the core (4875 mm)

For each of the three cases, 13 sets of cross-sections were generated. The 12 first ones correspond to the 12 different reflector cells numbered in Figure 3-11 and the thirteenth set of cross-sections merged the 12 previous cells into one. Therefore, this study generated six types of reflectors (3 cases producing 12 plus 1 set(s) of cross-sections) which will be compared to evaluate their impact on the 3D core power distribution.

The equilibrium core was then evaluated for each type of reflector. If 12 sets of reflector cross-sections were chosen for the diffusion model, they were applied similar to the multi-cell's. If the averaged set of cross-sections was utilized, every single reflector cell in PARCS used the same set of cross-sections. The three-dimensional core power distribution (84 assemblies x 20 axial positions = 1640 nodes) at beginning of cycle (BOC) and end of cycle (EOC) were compared relative to an arbitrary chosen case. The maximum and average local power difference of the 1640 nodes were evaluated and summarized in Table 3-10. By looking at case 1, it was concluded that the number of reflector cell types had a minor impact on the power distribution. The location of the fuel cells used in the multi-cell geometry (bottom of top of the core) had a maximum error of 0.082% at BOC with an average of 0.015% which is considered negligible. Finally, the presence of burnable poison had the most effect but remained, however, insignificant (0.13% and 0.022% on average at BOC and EOC, respectively).

Table 3-10 Impact of the reflector cross-sections on the core power distribution

	Location of the fuell cells used (mm)	Number of reflector XS sets	FIBA	Maximum local power difference (%)		Average local power difference (%)	
				BOC	EOC	BOC	EOC
Ref	125	12	no	-	-	-	-
1	125	1	no	0.2	0.075	0.072	0.0099
2	125	12	yes	0.17	0.08	0.052	0.014
3	125	1	yes	0.33	0.13	0.088	0.022
4	4875	12	no	0.082	0.041	0.015	0.0065
5	4875	1	no	0.2	0.038	0.072	0.0062

Therefore, the reflector cross-sections were evaluated at only one axial position (bottom of the core) and only used one set of cross-sections applied to every reflector cell in the diffusion model. Case 1 was chosen for consistency to compare this work to the literature in Section 3.1.2.3 (no burnable poison in the four fuel cells). The remaining of this work used the model with burnable poison in the fuel cell (Case 3).

3.1.2.5 Implementation of the FIBA

The implementation of the fuel-integrated gadolinia significantly alters the 2-group cross-sections as a function of burnup, and the equilibrium core had to be re-evaluated. The normalized radial power distribution at BOC and EOC

was re-calculated using the same fueling scheme as in Section 3.1.2.3, and the results are shown in Figure 3-15. Many assemblies reach an unacceptably high power, especially towards BOC. Consequently, a new fueling scheme was proposed (Figure 3-16) and the new radial power distribution is presented in Figure 3-17.

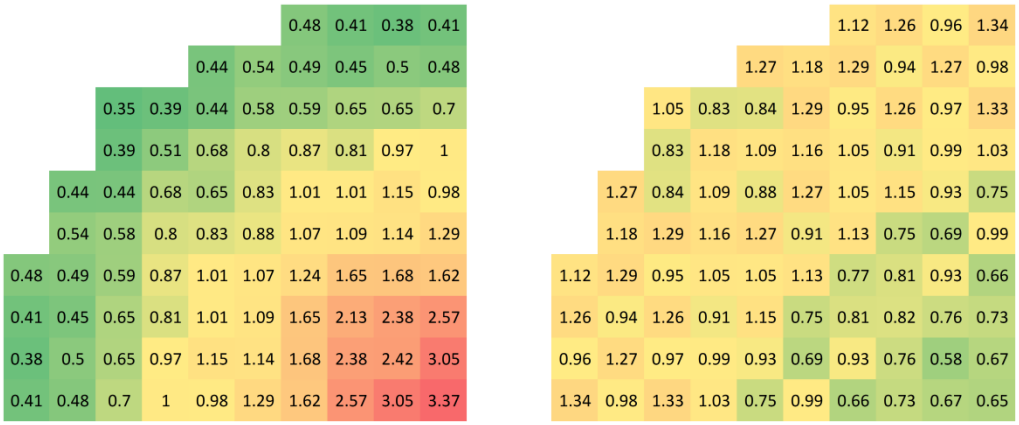

Figure 3-15 Normalized radial power distribution with FIBA and CNL's fueling scheme at BOC (left) and EOC (right)

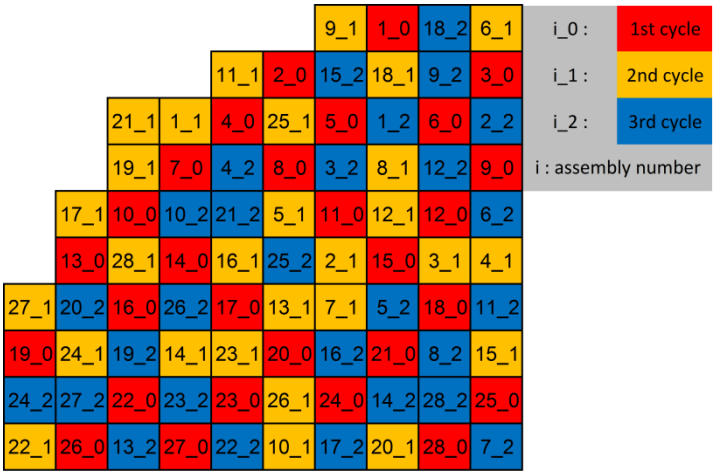

Figure 3-16 New fueling scheme to the FIBA

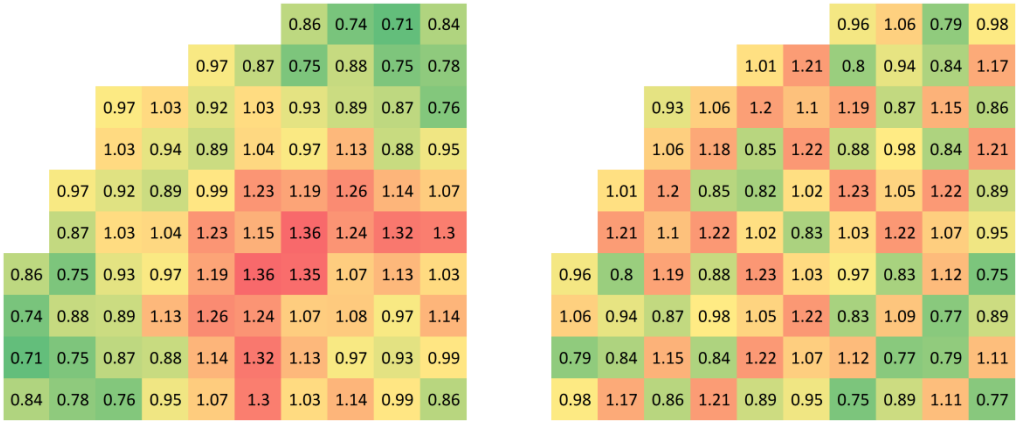

Figure 3-17 Normalized radial power distribution with the FIBA

The addition of the burnable poison reduced the initial excess reactivity from 111.6 mk to 49.2 mk while keeping a similar cycle length (435 days) and average exit fuel burnup (63.49 MW.d/kg).

3.1.2.6 Axially graded fuel enrichment and FIBA concentration

In the previous section, the maximum cladding surface temperature (MCST) and the maximum fuel centerline temperature (MFCLT) were found to exceed the safety limits (see Chapter 4). In this stage of the analysis the core thermal power was reduced by 20% and the overall fuel enrichment was decreased to keep a similar cycle length. In addition, the fuel enrichment and the FIBA concentration were axially graded to lower the power generated towards the top of the assembly throughout the fuel cycle which, in turn, helps to improve the MCST. The energy cut-off between the fast and thermal group was also increased from 0.625 eV to 2.57 eV due to suggestions found in the literature [11, 46].

The impact of the new energy cut-off is demonstrated in Figure 3-18 and Figure 3-19. While the axial power distribution is weakly sensitive to the new energy barrier, the radial power distribution shows a difference up to 12.5 %. This demonstrates the importance of the energy cut-off when using 2-group condensed and homogenized cross-sections.

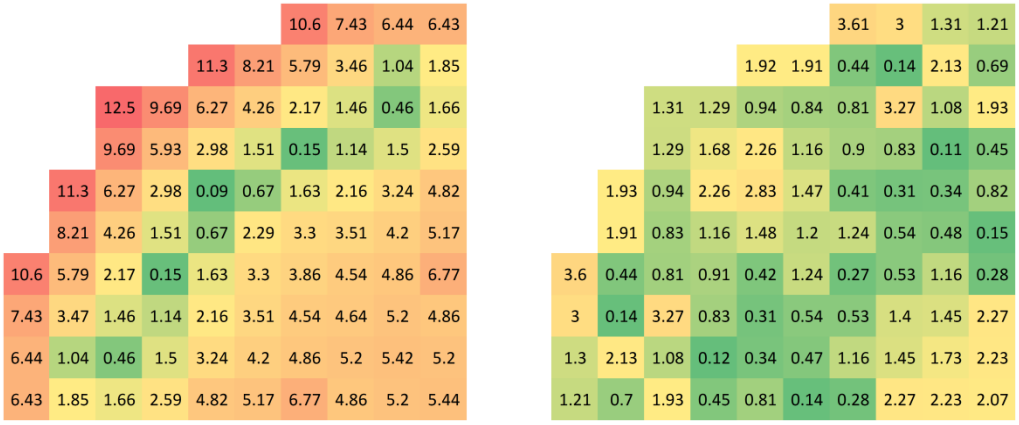

Figure 3-18 Absolute difference (%) in radial power distribution at BOC (left) and EOC (right) for the equilibrium cycle using an energy cut-off of 2.57 eV instead of 0.625 eV

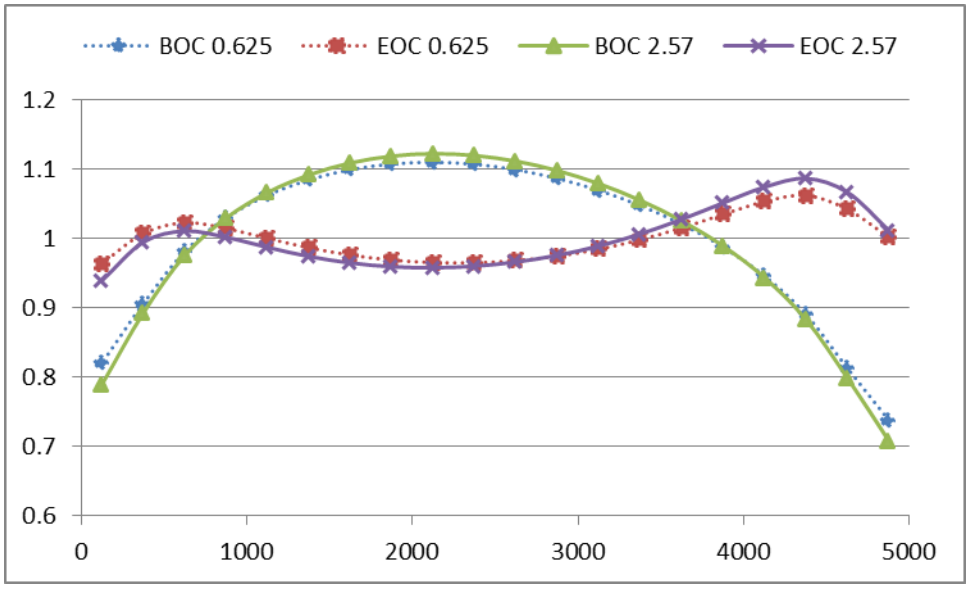

Figure 3-19 Axial power distribution at BOC and EOC for the equilibrium cycle using an energy cut-off of 2.57 eV and 0.625 eV

Then, the assembly was divided into three distinct zones where different fuel enrichments and FIBA concentrations were applied (see Chapter 5). The goal was to demonstrate the potential for MCST improvement by lowering the power towards the end of the channel. Three zones were deemed sufficient for the study but the assembly could be further divided in the future. The same ratio of enrichment between the inner and outer ring of fuel pins was maintained to keep a similar ratio of power generated between the two rings of fuel pins.

3.2 Thermal-hydraulics model

In this work, the thermal-hydraulics code RELAP5/SCDAPSIM/MOD4 (RSM4) developed by Innovative Software System in Idaho National Engineering and Environmental Laboratory (INEEL) was used to simulate the Canadian SCWR [25]. RSM4 calculates the reactor coolant system thermal-hydraulics and control systems interactions with the capability of evaluating the eventual structural changes during severe accidents. This latter capability was not used in this work but could be investigated in future works when extreme core conditions are expected.

The original version of RSM4 was modified by Lou [30] as the thermal conductivity of water was falsely assumed constant above the thermodynamic critical point. The latest publication of the International Association for the Properties of Steam and Water (IAPWS) was adopted and verified against National Institute of Standards and Technology. Special techniques to cope with the transition through the pseudo-critical point were also implemented in the code [29].

3.2.1 Quarter core model

The Canadian SCWR is $1/8^{th}$ symmetric; therefore, a total of 46 channels was sufficient to obtain the equilibrium thermal-hydraulic conditions of the core. The primary loop was simulated from the exit of the pump, through the reactor internals, and to the inlet of the turbine consistent with previous thermal-hydraulic studies [9, 30, 54]. The pump discharge is modeled through a fixed inlet boundary condition: 25.8 MPa and 350°C. The outlet pressure was maintained constant at 25.0 MPa, and channel-specific static orifices were used to obtain a uniform coolant outlet temperature of 625°C in each channel. It has to be understood that for one orifice size, there is only one channel power that will output a coolant temperature of 625°C. Therefore, the radial power distribution has to be kept as close as possible to its reference throughout the fuel cycle to minimize the coolant outlet temperature deviation.

3.2.1.1 Hydraulic components

The coolant first passes through the cold leg pipe to enter the inlet plenum. The coolant is then split into 46 parallel channels with different mass flow rates due to the channel-specific orifices. The coolant travels downwards through the central tube to the bottom of the assembly where the coolant reverses direction to travel upwards to cool the 64 fuel pins. The flow reversal was modeled using two single volumes with vertically opposed direction. The forward and reverse flow resistance factors were assigned the value of 1.16 and 1.36, respectively, consistent with [30]. Both pipes describing the fuel assemblies were sliced in 20 equal volumes consistent with the PARCS diffusion model described in section 3.1.2.1. The coolant from the 46 channels

flows through the riser before reaching the outlet plenum and finally the hot leg pipe leading to the high-pressure turbine. Figure 3-20 depicts the arrangement of the hydraulic components and Table 3-11 lists their specifications which were either calculated with the fuel lattice cell dimensions (Table 3-1) or taken from the literature [9, 30].

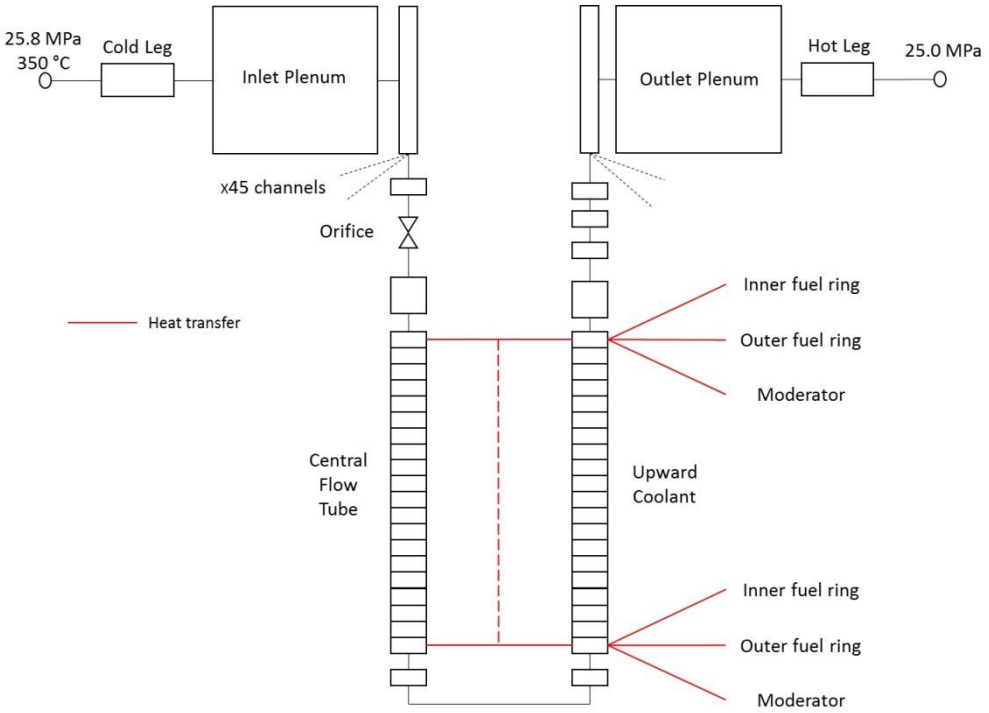

Figure 3-20 RELAP5/SCDAPSIM/MOD4 model of the Canadian SCWR

Table 3-11 Hydraulic components specification

	Component type	Area (m^2)	Length (m)	Orientation (°)	Hydraulic diameter (m)
Cold Leg	Pipe	0.2761	1	0	0.5929
Inlet Plenum	Pipe	38.485	1	-90	7
Orifice	Servo valve	0.0066476 (fully open)	-	-	-
Central tube	Pipe	0.0066476	5	-90	0.092
Reversal 1	Single volume	0.0066476	0.125	-90	0.092
Reversal 2	Single volume	0.0093462	0.125	90	0.05
Between fuel pins	Pipe	0.0093462	5	90	0.0067425
Outlet Plenum	Pipe	33.183	1	90	6.5
Hot Leg	Pipe	0.50265	1	0	0.8

The moderator system was represented in a different loop with a fixed 0.336 MPa inlet pressure and 55°C inlet temperature boundary conditions. A constant mass flow rate of 1550 kg/s was applied through the system to circulate the moderator [30]. The moderator tank was divided into 20 axial positions to be consistent with the fuel assemblies to facilitate the heat transfer between them as presented in the next section.

3.2.1.2 Heat transfer structures

Each channel possesses four ways to exchange heat within the system:

- Inner ring of fuel elements to upward coolant
- Outer ring of fuel elements to upward coolant
- Central tube between downward and upward coolant
- From upward coolant to moderator through the liners, insulator, and pressure tube

While quite similar, the inner and outer ring of fuel pins differ in dimensions, power generated, and material properties, therefore, they were modeled as two separate heat structures. Each ring of fuel pins was modeled as a single pipe with 20 axial nodes matching PARCS's nodalization. They are both composed of the fuel material within a 6 mm thick stainless steel cladding. The thermal conductivity and volumetric heat capacity of the fuels were provided by CNL (Table 3-12) while the RELAP internal properties were used for the cladding material (stainless steel).

Table 3-12 Thermophysical properties of the fuels

	Inner ring of fuel pins		Outer ring of fuel pins	
Temperature (K)	Thermal conductivity ($W.m^{-1}.K^{-1}$)	Volumetric heat capacity ($J.m^{-3}.K^{-1}$)	Thermal conductivity ($W.m^{-1}.K^{-1}$)	Volumetric heat capacity ($J.m^{-3}.K^{-1}$)
300	3.8	2.18E+06	4.77	2.17E+06
400	3.42	2.39E+06	4.2	2.38E+06
500	3.11	2.51E+06	3.75	2.50E+06
600	2.86	2.60E+06	3.39	2.59E+06
700	2.64	2.66E+06	3.1	2.64E+06
800	2.45	2.70E+06	2.85	2.69E+06
900	2.29	2.72E+06	2.63	2.71E+06
1000	2.15	2.74E+06	2.45	2.73E+06
1100	2.02	2.75E+06	2.29	2.74E+06
1200	1.91	2.75E+06	2.15	2.74E+06
1300	1.81	2.75E+06	2.03	2.74E+06
1400	1.72	2.75E+06	1.92	2.74E+06
1500	1.64	2.75E+06	1.82	2.74E+06
1600	1.57	2.76E+06	1.73	2.75E+06
1700	1.5	2.76E+06	1.65	2.75E+06
1800	1.44	2.78E+06	1.58	2.77E+06
1900	1.38	2.79E+06	1.51	2.79E+06
2000	1.33	2.82E+06	1.45	2.82E+06
2100	1.28	2.86E+06	1.39	2.86E+06
2200	1.23	2.91E+06	1.34	2.91E+06
2300	1.19	2.98E+06	1.29	2.98E+06
2400	1.15	3.06E+06	1.24	3.06E+06
2500	1.11	3.15E+06	1.2	3.16E+06
2600	1.08	3.26E+06	1.16	3.27E+06
2700	1.05	3.40E+06	1.12	3.41E+06
2800	1.01	3.55E+06	1.09	3.57E+06
2900	0.99	3.73E+06	1.06	3.75E+06
3000	0.96	3.93E+06	1.03	3.96E+06

The power in each axial node was determined by PARCS; however, the ratio of power between the inner and outer ring varies with axial position, fuel

burnup, and the presence of the control rod. This ratio was evaluated based on fuel lattice calculations (section 3.1.1.3). For each thermal-hydraulic node, a single value of 53%/47% for the inner/outer ring of fuel pins was chosen independently of the axial position, fuel burnup, and presence of the control rod as it is the most conservative ratio relative to the cladding and fuel centerline temperature. To show this, a single channel was built in RELAP to show the variation of the MCST and MFCLT with the span of ratios observed at the lattice level (from 45%/55% until 53%/47% for the inner/outer ring) (see Figure 3-21 and Figure 3-22).

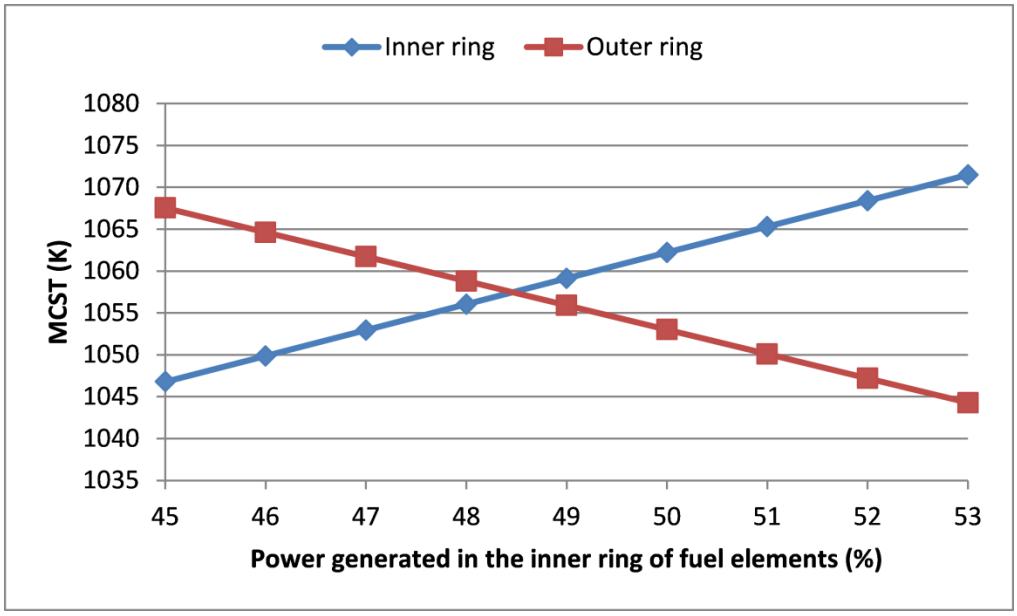

Figure 3-21 MCST in the inner and outer fuel ring with variable power ratio

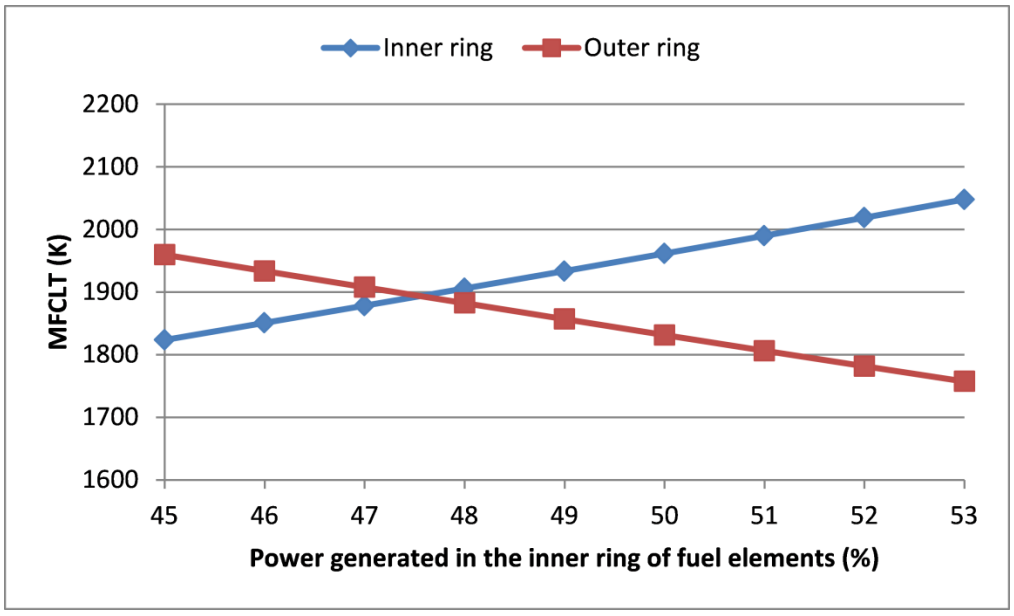

Figure 3-22 MFCLT in the inner and outer fuel ring with variable power ratio

The central flow tube was modeled as a cylinder with built-in stainless steel thermal properties similar to the fuel cladding material. The cylinder was vertically sliced into 20 nodes and coupled to the corresponding 20 nodes representing the upward coolant.

Finally, the heat transfer to the moderator from the coolant through the inner liner, insulator, outer liner, and the pressure tube. The thermal properties of the inner liner are the stainless steel reference properties included in RSM4 while the insulator properties were taken from [9] and are listed in Table 3-13. The outer liner and pressure tube are primarily made of zirconium (94.9 wt%) so the RSM4 default zirconium thermal properties were utilized.

Table 3-13 Thermophysical properties of the ceramic insulator

Temperature (K)	Thermal conductivity ($W.m^{-1}.K^{-1}$)	Volumetric heat capacity ($J.m^{-3}.K^{-1}$)
323.15	2.51	2.75E+06
373.15	2.52	2.90E+06
423.15	2.47	3.05E+06
473.15	2.39	3.18E+06
523.15	2.31	3.28E+06
573.15	2.22	3.35E+06
623.15	2.15	3.43E+06
673.15	2.09	3.51E+06
723.15	2.03	3.55E+06
773.15	1.99	3.56E+06
823.15	1.96	3.58E+06
873.15	1.93	3.64E+06
923.15	1.91	3.67E+06
973.15	1.9	3.70E+06
1023.15	1.9	3.72E+06
1073.15	1.92	3.77E+06
1123.15	1.94	3.76E+06
1173.15	1.97	3.81E+06
1223.15	2	3.84E+06
1273.15	2.06	3.86E+06

There is no consensus in literature on correlations for supercritical water heat transfer or pressure drop. The strong variation of the water properties in the vicinity of the pseudo-critical point makes it difficult to evaluate the convective heat transfer coefficient but many experiments and CFD studies have come up with new empirical correlations for SCWR applications [55]. However, the Dittus-Boelter correlation for single phase liquid was proven to agree fairly well as long as the temperature is 20°C away from the pseudocritical temperature. Since the pseudo critical transition is located at the bottom of the channel, while the parameters of interests, namely the maximum cladding surface and maximum fuel centerline temperature, are located toward the top of the assembly, the prediction of heat transfer at the

downstream end of the channel with the Dittus-Boelter correlation is adequate for conceptual design studies.

3.3 Feedback database for PARCS-RSM4 coupling

To integrate the physics and thermal-hydraulic codes a set of relationships was needed to relate changes in cross sections to changes in thermal-hydraulic phenomena. This information is available from the branch calculations performed at the lattice level. The information from each branch calculation was used to generate a feedback database which contains information on how each few-group cross section changes with a given change in thermal-hydraulic conditions. The procedure to create the feedback database is described in this section.

In addition to the control rod insertion, a total of five TH variables were considered in the feedback database:

- Fuel temperature (TF)
- Central tube coolant density (DM)
- Central tube coolant temperature (TM)
- Coolant density between fuel pins (DC)
- Coolant temperature between fuel pins (TC)

A branch was always evaluated using a suitable perturbation from the reference TH conditions (Table 3-2 and Table 3-3). Since the modification of a TH variable can affect the Dancoff factors, the Dancoff factors have been re-calculated for every branch type. The transport solution is then re-calculated and the cross-sections are condensed and homogenized in two energy groups. This operation is performed for the 21 branches listed in Table 3-14 for the 20 axial positions and at seven fuel burnups. Each calculation generates a "txtfile" containing the perturbed cross-sections.

Table 3-14 Branches evaluated in SCALE/NEWT

	Control Rod	Central Tube		Fuel	Coolant around fuel pins	
Branches	0 = out 1 = in	Density ($g.cm^{-3}$)	Temperature (K)	Temperature (K)	Density ($g.cm^{-3}$)	Temperature (K)
0 (reference)	0	ρ_{ref_cool1}	T_{ref_cool1}	T_{ref_fuel}	ρ_{ref_cool2}	T_{ref_cool2}
1	1	-	-	-	-	-
2	0	0.02	-	-	-	-
3	0	0.70	-	-	-	-
4	0	-	600	-	-	-
5	0	-	1000	-	-	-
6	0	-	-	600	-	-
7	0	-	-	2000	-	-
8	0	-	-	-	0.02	-
9	0	-	-	-	0.70	-
10	0	-	-	-	-	650
11	0	-	-	-	-	1000
12	1	0.02	-	-	-	-
13	1	0.70	-	-	-	-
14	1	-	600	-	-	-
15	1	-	1000	-	-	-
16	1	-	-	600	-	-
17	1	-	-	2000	-	-
18	1	-	-	-	0.02	-
19	1	-	-	-	0.70	-
20	1	-	-	-	-	650
21	1	-	-	-	-	1000

For each axial position, a single "txtfile" is reconstructed with the reference and perturbed cross-sections. GENPMAXS [52] transforms each of the 20 "txtfiles" into 20 PMAXS files containing the reference cross-sections and the first order derivatives for each branch at each fuel burnup. PARCS is then able to interpolate the cross-sections according to the local TH conditions based on the branches performed.

PARCS can read up to 12 branches [52]:

1 Control rod
2 Coolant density
3 Coolant poison
4 Fuel temperature
5 Coolant temperature
6 Coolant impurity
7 Moderator density
8 Moderator poison
9 Moderator temperature
10 Moderator impurity
11 Density difference between current assembly and neighbors
12 Burnup difference between current assembly and neighbors

Not all of the available branches were used in this study. The local conditions were read from a separate file named "TH.dep" here for simplicity. During a steady-state calculation, PARCS read this file and interpolated the local cross-sections based on the given TH conditions to calculate the power distribution. During a transient calculation, the "TH.dep" file had to be updated at each time step and PARCS needed to re-evaluate the local cross-sections according to the altered TH conditions. However, PARCS was developed to natively couple with specific USNRC versions of RELAP or TRACE, and not with the version of RELAP used in this thesis. At the source code level, PARCS acquires information related to feedbacks 2, 3, 4, 5 from memory transfers, not from a file and such a feature cannot be bypassed. Therefore, branches 1, 6, 7, 8, 9, and 10 were used for the control rod, TF, DM, DC, TM, and TC, respectively, in the PMAXS file to perform the cross-sections interpolation. The proper implementation of each feedback mechanism was verified and is presented in Chapter 6.

The validity of the interpolation method used by PARCS was also verified independently. The k_{inf} of the lattice was calculated in NEWT [17] for several values of each TH variables. The k_{inf} for the same TH conditions were calculated through interpolation to assess the accuracy of the PARCS method. The interpolation technique is explained in Chapter 6 and more details can be found in [52]. This study was performed with and without a control rod inserted in the lattice cell and are shown in Figure 3-23 and Figure 11 of the second journal publication (Chapter 5), respectively. Each study was performed for two fuel burnups as well as at the bottom and top of the channel. The black boxes show the range of interest for the control rod drop accident and show the interpolation scheme performs well in those regions. However, it does not perform as well for some variables such as "DC" or "DM" away from the target areas of application. Therefore, it is recommended to evaluate more branches for these TH variables or improve the interpolation technique if the simulated transient is expecting more extreme TH conditions, such as in fully voided coolants. Figure 3-23's legend is composed of three variables in the following form: X_Y_Z. "X" represents the TH variable studied, "Y" is the fuel burnup (in MW.d/kg), and "Z" can either be "c" for "Calculated" (meaning it is the exact value calculated by NEWT) or "i" for "Interpolated".

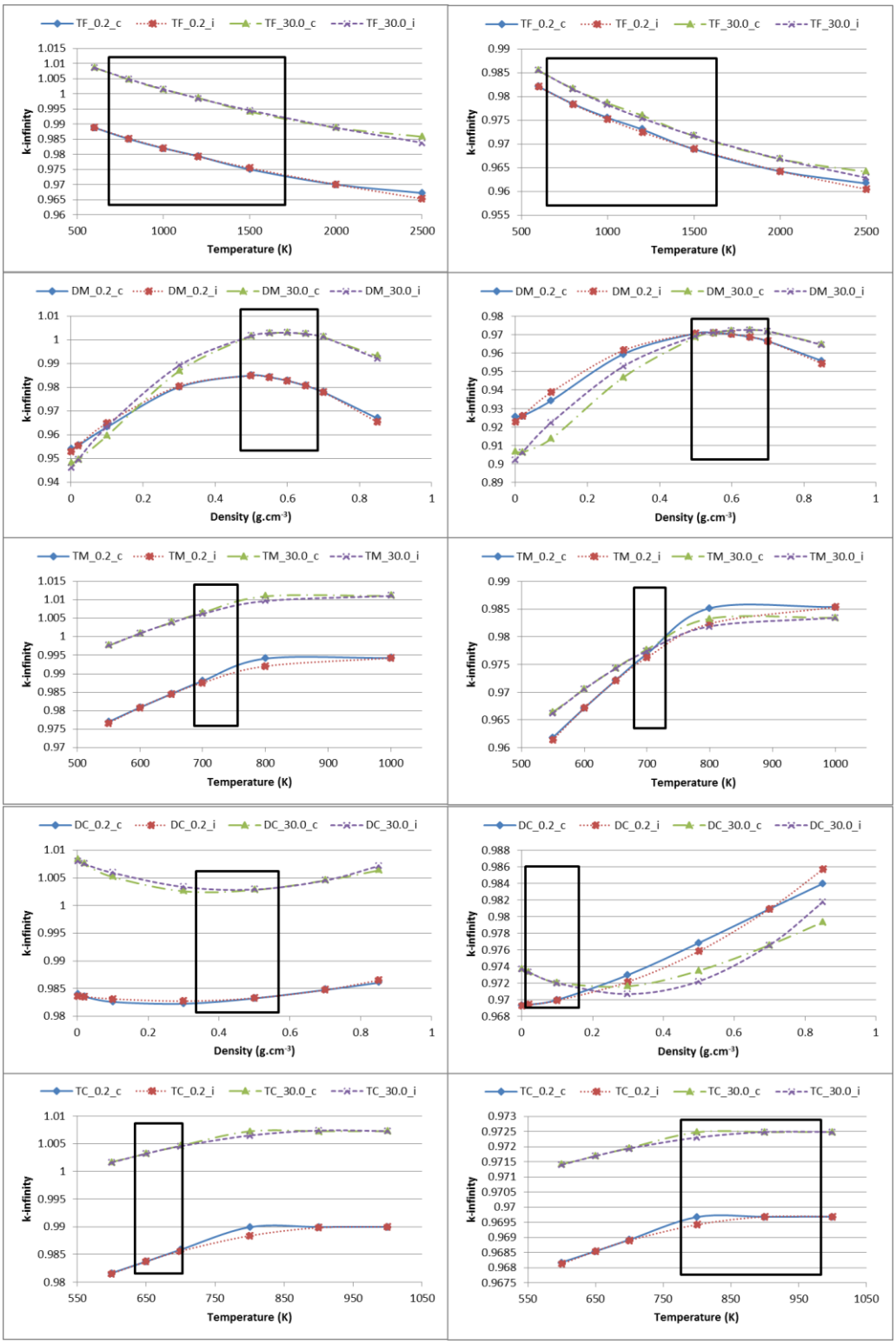

Figure 3-23 Fuel lattice's k_{inf} variations as a function of five thermalhydraulic conditions and two fuel burnups at the bottom (left) and top (right) of the core with a control rod inserted

3.4 Genetic Algorithm Optimization technique

Genetic algorithms (GAs) are based on Darwin's theory of evolution [56] and were first introduced by J.K. Holland [57]. The principle states that an individual who is more fit for a specific environment has a higher chance of survival and therefore, to reproduce. This metaheuristic technique is of particular interest when it comes to solving non-linear optimization problems over a large solution space where gradient methods may fail to find global maximum/minimums. The Design Analysis Kit for Optimization and Terascale Applications (DAKOTA) software was developed at Sandia National Laboratories in Albuquerque, New Mexico. DAKOTA was designed for engineers to perform analyses such as optimizations, uncertainty quantifications, parametric studies, and the design of experiments. DAKOTA can interface with any external simulation codes in a "black-box" fashion where it modifies the input files, executes a simulation, and collects results. The genetic algorithm used in DAKOTA [58, 59] is introduced in this section.

The GA is a population-based method, and the first step is to initialize the population from a random seed. Each individual in a generation in this case corresponds to a unique set of input parameters for a simulation that may potentially give rise to an optimal solution. The size of the initial population can vary but is generally chosen to be around 50 individuals. Too small of a population would not generate enough diversity while too large of a population would significantly increase the computational burden within a generation (and noting that the solution only improves over generations). The fitness of each individual is evaluated based on one or more objective function(s) and any other constraint(s). DAKOTA calls a set of simulation codes and obtains the results of the simulations for a given individual within a generation. It then extracts the relevant output from the simulation code and uses it to assess the objective function(s) and other criteria (if imposed). If a single objective function is used, the ranking is simple as the individuals are ranked based on their actual fitness. When a multi-objective GA is employed a trade-off between the objective functions, called the Pareto front [58], is created. The GA tries to minimize both objective functions by shifting the Pareto front towards the lowest possible value (for all objective functions). The individuals are ranked regarding this two-dimensional front (or higher dimension if more objective functions were to be used).
Once the fitness of each individual in a generation is assessed then new individuals are generated by crossover from two (or more) parents selected from the current population. The crossovers in this case involve exchanging certain variables within the input files of two initial individuals who were ranked higher in previous generations. Individuals with a higher fitness have a higher probability to be chosen as parents as they are more likely to give birth to a better individual. The number of new individuals generated from

crossover is based on a fixed rate chosen by the user. This rate is multiplied by the population size to calculate the total number to be created.

Mutations are also applied to the new individuals based on a separate fixed rate chosen by the user. A mutation is equivalent to a random change of a variable of a randomly chosen individual. The mutation rate is multiplied by the population size to calculate the number of mutations to be performed. Mutations allow exploring other areas of the solution space in hopes to find better individuals.

Once all the new individuals have been generated from crossovers and mutations, their fitness is evaluated and they are added to the population. The individuals with the lowest fitness are discarded and a new set of crossovers and mutations is applied to generate a subsequent generation. The optimization is terminated when the progress of the population over a certain number of generations is below a used defined threshold.

A sensitivity study was carried out to observe the impact of several parameters on the outcome of the optimization, namely the MCST, MFCLT, and the number of evaluations (directly linked to the computational time). Table 3-15 displays the simulations performed and shows that a population of 56 individuals performs well. A high crossover rate produces better results with comparable computational time; however the choice of the mutation rate is less obvious. The higher the mutation rate, the longer the optimization takes but no correlations with the objective functions can be observed. Finally, a new seed seems to be a good way to potentially improve the solution. Therefore, this technique was used in this work if a solution was not satisfying in order to maybe find a better solution.

Table 3-15 Parametric study of the genetic algorithm

Case	Seed	Population Size	Crossover Rate	Mutation Rate	Shrinkage percentage	Below limit	Mutation type	XO parents	XO offsprings	Best MCST	Best MFCLT	Nb of evaluations
ref	10973	56	0.95	0.5	0.99	4	bit_random	3	3	1161.1	2396.2	6269
1	**10976**	56	0.95	0.5	0.99	4	bit_random	3	3	1144.1	2495.5	5179
2	10973	**20**	0.95	0.5	0.99	4	bit_random	3	3	1197.3	2565.6	14065
3	10973	**200**	0.95	0.5	0.99	4	bit_random	3	3	1157.9	2335.3	13592
4	10973	56	**0.8**	0.5	0.99	4	bit_random	3	3	1177.3	2527.6	5619
5	10973	56	**0.5**	0.5	0.99	4	bit_random	3	3	1182.8	2506.0	7704
6	10973	56	0.8	**0.8**	0.99	4	bit_random	3	3	1152.9	2354.4	10295
7	10973	56	0.95	**0.3**	0.99	4	bit_random	3	3	1173.3	2446.7	7823
8	10973	56	0.95	**0.1**	0.99	4	bit_random	3	3	1155.8	2500.6	3840
9	10973	56	0.95	**0**	0.99	4	bit_random	3	3	1190.7	2595.5	2430
10	10973	56	0.95	0.5	**1**	4	bit_random	3	3	1164.9	2358.1	9553
11	10973	56	0.95	0.5	**0.5**	4	bit_random	3	3	1151.4	2386.5	3105
12	10973	56	0.95	0.5	0.99	**6**	bit_random	3	3	1163.6	2461.3	21928
13	10973	56	0.95	0.5	0.99	4	bit_random	**2**	**2**	1162.4	2505.4	6062
14	10973	56	0.95	0.5	0.99	4	bit_random	**4**	**4**	1164.9	2527.3	5575
15	10973	56	0.95	0.5	0.99	4	**replace_uniform**	3	3	1166.8	2489.9	5786

Chapter 4

Spatial and bulk reactivity systems design and optimization for the Canadian Supercritical Water Reactor

4.1 Preface

Nuclear fuel management commonly refers to the optimization of four main problems:

- Lattice fuel cell design
- Axial fuel assembly design
- Fueling scheme
- Control rods pattern

Each of these optimization areas has a very large, if not infinite, space solution. Moreover, the nonlinearity of the space solutions requires advanced optimization techniques such as metaheuristic algorithms [57, 60, 61, 62, 63] (e.g. tabu search, simulating annealing or genetic algorithm).While these techniques might not find the most optimal solution, they can rapidly find a near optimal solution.

The best way to deal with nuclear fuel management would be to optimize the four optimization areas altogether due to their interdependency; however, this would be an extremely large problem to be solved. For example, each small change in lattice design will require a re-simulation of the entire fueling sequence and rod pattern, while a change in the axial assembly design or core layout will require a change in all lattice physics, burnup and rod patterns etc…). Given that the computational costs of generating a new lattice, core

and fueling scheme is on the order of weeks, a continuous optimization is prohibitively lengthy. Each optimization problem is therefore decoupled from the others to obtain a solution in a reasonable time frame. Moreover, metaheuristic algorithms have been increasingly utilized due to the large space of each problem as well as the large improvement of computer resources over the past decades. The four areas of nuclear fuel management and their optimization techniques are presented below based on the open literature.

Lattice level cell optimization

The optimization of the fuel lattice cell has been widely studied. The main goal is to improve the economics of the reactor (i.e. minimize fuel enrichment) or increase the safety margins by lowering the local power peaking factor, for instance.

Metaheuristic techniques such as TABU search [64], swarm optimization and local search [65], ant colony system [66], and artificial neural network [66] have been used to achieve the previously mentioned goals. The most common optimized variables are the enrichment distribution and the location/concentration of burnable absorber. Depending on the goal of the study, the objective function includes the minimization of the local power peaking factor (LPPF) [65, 66, 67, 68, 69, 70, 71], the minimization of the average fuel enrichment [64, 66, 72, 73, 74, 75], the maximization of the end of cycle reactivity [76], the maximization of the plutonium destruction [77] [78], the minimization of minor actinides at the end of cycle [78], the maximization of the plutonium loading [79] or the maximization of the fuel exit burnup [80]. Constraints are also applied to most optimizations and include LPPF [64, 73, 75, 77, 81], lattice reactivity [64, 65, 67, 68, 69, 70, 73, 75, 81], linear element rating (LER) [80] and shutdown margins [77]. All these optimization studies were primarily performed on BWRs but a few of them targeted PWRs, the AP1000 or the Canadian SCWR.

Axial fuel assembly design

The optimization of the axial fuel assembly has been subjected to fewer studies. A TABU search [72] and a genetic algorithm [82] were used to minimize the fuel assembly mean fuel enrichment while constraining the cycle length and several safety limits. The fuel assembly is axially divided into slices. A predefined number of fuel lattices can then be used by each slice. In [83], the fuel enrichment of several axial segments is optimized by minimizing an objective function which includes safety limits, cold shutdown margin, hot excess reactivity and effective multiplication constant. A parametric study on the number of axial layers (seed and blanket), the fuel rod diameter, pitch to diameter radio and the duct wall clearance was performed in [84] to improve the neutronic and thermal-hydraulic performances of the SCWR with mixed neutron spectrum (SCWR-M) assembly. Finally, [85] used a multi objective

genetic algorithm to optimize the shape of the wires wrapped around fuel pins. The wire-spacer diameter to fuel rod diameter ratio and the wire-wrap pitch to fuel rod diameter ratio were varied to find a compromise between heat transfer enhancement and friction loss reduction.

Fueling scheme

Metaheuristic algorithms have been extensively used to come up with improved fueling schemes. The common goal of these optimizations is to extend the length of the cycle (improve economics) while respecting the safety limits. A biogeography based algorithm [86], a genetic algorithm [87], a variant of a firefly algorithm [88], and a particle swarm optimization were used to maximize the reactivity at BOC while flattening the power distribution. A genetic algorithm was utilized in [89] to maximize the k_{eff} at EOC, minimize the power peaking factor, and ensure an appropriate cold shutdown margin at BOC of a BWR. Another study combined two evolutionary algorithms to optimize a PWR loading scheme. Cycle length, maximum discharge burnup, liner element rating, moderator temperature coefficient, and shutdown margins at EOC were evaluated during the process [90]. A parallel computing adaptive simulated annealing technique was used to maximize the EOC critical soluble boron concentration while constraining the maximum radial pin power and fuel assembly discharge burnup [91]. The maximization of the fertile conversion into fissile isotopes was the focus of [92]. An ant system colony and modified particle swarm techniques optimized the fueling scheme while constraining the power peak factor and void coefficient.

Control rod pattern

Very few research groups investigated control rod pattern (CRP) optimizations. A BWR's CRP was optimized using a rank-based ant system in [93] and a particle swarm optimization and local search in [94]. An optimization of the Laguna Verde Nuclear Power Plant's CRP was also performed by using an ant colony system in [95], a genetic algorithm [96], and a fuzzy logic system [97]. These studies took into consideration the axial power distribution, k_{eff}, the shutdown margin and thermal limits.

The particular interest in the axial power distribution resides in the spectral shift at the beginning of cycle. This means that the core would have a power distribution peaked towards the bottom of the core early on to increase the void fraction at the top of the core. The breeding of fertile isotopes (e.g. U-238) into fissile isotopes (e.g. Pu-239) will then be increased at the top of the core which can fission later on and extend the fuel cycle. This effect can also be observed by reducing the mass flow rate in the core [93, 96]. The insertion of the control rods must, however, maintain a core close to criticality while ensuring the respect of the safety limits.

Every aspect of nuclear fuel management has been individually studied through optimization techniques. However, few studies have attempted to combine two or more areas. In [98], the authors optimized the axial fuel assembly and the lattice fuel. They iteratively solved each problem to minimize the overall fuel enrichment while fulfilling the energy requirements. In [99], the fueling scheme and control rod pattern were optimized in a coupled way. The method goes back and forth between the optimization of the fueling scheme and control rod pattern. If the control rod pattern is being optimized, the most recent optimized result for the fueling scheme is used and vice versa. In [100], the fueling scheme and the control rod pattern are sequentially optimized, and a feedback mechanism is used to improve the solution. Finally, the optimization of the four areas of nuclear fuel management was attempted in [101]. Each phase of the nuclear fuel management can only take tabulated configurations and the optimization tries to find the best combination to maximize the objective function.

Previous control rod pattern optimizations have been performed for existing nuclear reactors such as a typical BWR-6 [93, 94], the Kuosheng Nuclear Power Plant Unit 1 [100] and the Laguna Verde Nuclear Power Plant (BWR-5) [95, 96, 97]. Therefore, data regarding the initial conditions of the core (burnup distribution) can be obtained since these are established a priori through operations. The control rods' insertion can then be determined at day zero knowing that this initial core fuel load is fixed. Once the control rods' position has been evaluated, the core can be burned for a chosen period. An optimization is performed to find a new optimal control rods' arrangement and the process is repeated until the end of the cycle is reached. This technique can be referred to as a multi-step procedure.

The Canadian SCWR is at the conceptual stage and, as a consequence, no actual data is available. The only initial conditions that can be obtained are from the equilibrium cycle without the use of the control rods. Once a control rod pattern is found for the cycle, the new equilibrium cycle is calculated. The initial burnup distribution is now different and a new control rod pattern optimization has to be performed. Therefore, the optimization is a multi-cycle, multi-step process. Despite the cumbersomeness, more realistic results are produced. If the results are not satisfying, any phase of the nuclear fuel management can be re-designed to improve the Canadian SCWR conceptual design.

This journal article presents one of the first Canadian SCWR fuel lattice cell built in SCALE/TRITON. A parametric study on the meshing and the evaluation of the Dancoff factors were performed to ensure accurate modeling

(see section 3.1.1.1). Burnable poison was incorporated into a selected number of fuel pins to remove part of the excess reactivity at beginning of cycle. While their location is identical to [37], their concentration was reduced to increase their consumption by the end of the cycle and therefore reduces the penalty on the cycle length. A unique treatment of the fuel pins with gadolinia was performed to model the spatial self-shielding (see section 3.1.1.3). The depletion steps were also closely optimized to accurately simulate the fuel and poison burnout (see section 3.1.1.3).

The Canadian SCWR utilizes channel specific static orifices. Each channel has a "reference" power and the orifice was sized to regulate the coolant mass flow rate to obtain a 625°C coolant outlet temperature. It also means that if a channel deviates from its reference power, so will the exit coolant temperature and the cladding temperature. The assembly powers must be controlled to minimize the deviation of the channel power throughout each batch cycle and a control rod configuration parallel to the channels would provide optimal spatial control in this regard. Since the top of the core contains the inlet and outlet plenum the control rods could not be inserted from the top. Therefore cruciform control rods were then designed which penetrate from the bottom of the core similar to a BWR. Unlike a BWR these rods are inserted into a low-pressure and temperature calandria vessel, thereby avoiding large ejection driving forces.

A full-core model of the Canadian SCWR was built in the diffusion code PARCS for the first time in open literature. To begin with, the base core (with no reactivity devices) was modeled and compared to the literature to benchmark the PARCS/SCALE computational tools for the Canadian SCWR (see section 3.1.2.3). A model of the core was also built in RELAP5/SCDAPSIM/MOD4 where every channel was represented to obtain the exact thermal-hydraulic conditions.

A genetic algorithm - included in DAKOTA - was used to find the insertion of the control rods throughout the cycle which optimizes several key metrics. The innovative method uses a multi-step, multi-cycle process and evaluates power-related criteria (k-eff, LER) as well as a thermal limit (cladding temperature). The latter was performed through a novel response surface generated prior to the optimization. Such a response surface method was necessary since the RELAP5/SCDAPSIM/MOD4 simulations are too slow and proved to be inconvenient for optimization purposes. Three main factors were found to be influencing the cladding temperature. Therefore, a three-dimensional look-up table was generated, and the cladding temperature can be estimated solely based on the PARCS output. The response surface was validated against several hundred cases and demonstrated a very good agreement between the real and interpolated cladding temperatures.

The DAKOTA results produced an optimal solution for the control rod pattern. Even with the optimal control rod sequence, the results presented in this paper did not meet the safety criteria. A few options were investigated at the end of the paper which showed improved results.

The modeling of the Canadian SCWR in SCALE, PARCS, and RSM4 was performed by the main author (F. Salaun). The design of the burnable absorbers was inspired by an early CNL design but the cruciform control rod design was entirely done by the main author. The author also came up with the idea of metaheuristic algorithms to optimize the control rods pattern. All the simulations, scripts, data analysis, and writing was performed by the main author. Dr. David Novog was consulted on several occasions for guidance and expertise.

Salaun, F. and Novog, D.R., 2016, "Spatial and bulk reactivity systems design an optimization for the Canadian Supercritical Water Reactor", Canadian Nuclear Laboratories Nuclear Review 5(2), pp.285-298, doi: 10.12943/CNR.2016.00037

4.2 Publication 1

SPATIAL AND BULK REACTIVITY SYSTEMS DESIGN AND OPTIMIZATION FOR THE CANADIAN SUPERCRITICAL WATER REACTOR

F. Salaun, D. R. Novog
McMaster University
1280 Main Street west, Hamilton, Ontario L8S4L8
salaunf@mcmaster.ca, novog@mcmaster.ca

Abstract

Keywords: Reactor physics, Thermal-hydraulic, Optimization, Reactivity control systems

A full-core reactor physics model of the Canadian SCWR concept was modeled, including proposed reactivity control devices. Fuel-integrated burnable absorbers and control blades, adjusted throughout the cycle, have been implemented in the fuel lattice cell to compensate for the excess reactivity. In addition to bulk reactivity control, the control blades provide radial flux shaping to minimize channel power fluctuations during the fuel cycle. As each channel has a static orifice at the inlet which imposes the coolant mass flow rate for a specific reference channel power, each channel

power has to be maintained as close as possible to its designed power so that deviations from the target exit coolant temperature are minimized. The combination of burnable absorbers and variable insertion control rods ensures that the bulk and spatial reactivity is managed as well as maintaining channel powers as close to the reference as possible throughout the cycle. The analysis was performed by coupling the reactor core physics code PARCS and the thermalhydraulics code RELAP5/MOD4/SCDAPSIM to DAKOTA. An automated process has been developed to find a control blade sequence that (1) maintains each channel power as close to its designed power as possible, (2) reduces the maximum sheath surface temperature (MSST), (3) keeps the core reactivity near criticality and, (4) maintains acceptable linear element rating (LER). The study demonstrates the potential for the combined use of fuel-integrated burnable absorbers and control blades to remove the excess reactivity, as well as using a genetic algorithm to find an optimal control blade sequence which minimizes channel power deviations. The results show that while the MSST shows near acceptable values at ideal steady-state conditions, the reactivity control functions are unable to maintain the limit over the length of the fuelling cycle even for the most optimized configurations. Design options are presented which provide more acceptable sheath temperatures and include possible reduction in the coolant exit temperature as well as advanced fuel design (graded enrichment, graded burnable poisons and partial length fuel rods).

Nomenclature

CNL	Canadian Nuclear Laboratories
SCWR	Supercritical Water-cooled Reactor
CANDU™	Canadian Deuterium Trade Mark
BWR	Boiling Water Reactor
PWR	Pressurized Water Reactor
BOC	Beginning Of Cycle
MOC	Middle Of Cycle
EOC	End Of Cycle
CB	Control Blade
BA	Burnable Absorber
APD	Axial Power Distributions
IAPWS	International Association for the Properties of Water and Steam
LER	Liner Element Rating
MSST	Maximum Sheath Surface Temperature
CP	Channel Power

1. Introduction

Canada is developing a SCWR as part of the Generation IV program. This concept draws its inspiration from the CANDU™ reactor and uses pressure-tubes for each channel and a low pressure heavy water moderator. Unlike traditional CANDU™ designs the reactor is vertically orientated and batch fuelled [1].

A total of 336 High-Efficiency Re-entrant Channels (HERC) house the fuel and provide the pressure boundary for the heat transport system coolant [2,3]. As depicted in Figure 1, the light water coolant enters the channel at the top of the core at 350°C and 25.8 MPa and travels downward in a central flow tube [4] within each channel. At the bottom of the channel the coolant direction reverses and passes to the outer flow tube traveling upward around the two fuel rings, where the flow then exits the top of the fuel channel assembly with an outlet temperature of approximately 625°C. Each fuel ring contains 32 $(Pu,Th)O_2$ fuel pins. The low pressure moderator (heavy water) is separated from the hot light water coolant by liner-tubes, a ceramic insulator and a pressure tube [5].

A core design was proposed by Canadian Nuclear Laboratories (CNL) but lacked mechanisms to compensate for the initial excess reactivity at beginning-of-cycle (BOC) [5]. Options for reactivity control include bulk moderator poison, carefully selected burnable neutron absorbers within the fuel, or movable control devices, such as control rods or blades. In the case of the latter, as fuel depletes during the cycle the positions of the control blades must be adjusted accordingly to maintain a critical core. A further advantage to using control blades is that they may also provide radial power shaping throughout the cycle. Bulk moderator poison has a negative effect on channel power peaking and cannot be used for spatial control, hence while such chemical moderator additives may be employed in operation, they are not considered further since bulk poison leads to radial power distribution issues since poison in the reflector region will cause higher interior core channel powers.

In the current reference design, static orifices at each channel inlet regulate the flow through the channels to be proportional to its reference power and ensure a uniform channel outlet temperature of 625°C. As a consequence each channel power has to remain as constant as possible or the outlet temperature will deviate from the target temperature. A study carried out by CNL [6] proposed fuel-integrated burnable absorbers as well as 25 horizontally orientated control rods. However, the design was limited to 280 days batch cycles and did not consider the use of cruciform blades which would reduce the fuel assembly flux asymmetries as compared to cylindrical rod designs. In this study, a set of BWR-like cruciform control blades and a modified version of fuel-integrated burnable absorbers have been proposed to compensate for the initial excess reactivity while keeping a cycle length above 400 days. The optimal positions of the control blades throughout the fuelling cycle are then determined such that the channel power changes anticipated with burnup, as well as the associated change in maximum sheath surface temperature (MSST) are minimized.

This paper describes the design of the burnable absorbers and control blades along with the lattice calculations using the SCALE 6.1.3 code [7]. The homogenized and condensed cross sections obtained from SCALE were then used in the PARCS model [8]. Finally, the DAKOTA optimization software, using a genetic algorithm, has been coupled to PARCS and RELAP5/MOD4

to find the control blade insertion sequence that maintains the channel powers as constant as possible while satisfying the desired constraints [9] [10].

2. Canadian SCWR core physics model

2.1. Lattice calculations: SCALE/TRITON

The SCALE 6.1 package was developed at the Oak Ridge National Laboratory (ORNL). Among other capabilities, SCALE uses the NEWT module to solve the multi-group transport equation and create problem-dependent few-group cross sections. Moreover, the ORIGEN module is used to predict the isotopic evolution as a function of burn-up. The major output from the SCALE package are the few-group homogenized cross sections as a function of burnup for subsequent full core calculations.

The 2D infinite lattice fuel cell, with a control blade and the burnable absorbers, was modelled in TRITON. Figure 2 and Figure 3 show the meshing used and the different materials, respectively. The geometry and material information are given in Table 1 [4]. The plutonium is called reactor-grade as its isotopic composition is derived from recycled light water reactor fuel. All simulations were performed using the 238 energy group library based on the ENDF/B-VII.0, which is included in SCALE 6.1. Moreover, the Dancoff factors were evaluated beforehand for each axial position in the core through the MCDancoff module due to the irregular pin distribution. Reflective boundary conditions were also applied on each side of the cell. The transport equation was solved for different stages of fuel burnup and is subsequently used to generate a set of 2-group homogenized cross sections indexed by burnup. At each burn-up step a branch calculation was performed with the control blade inserted.

In order to obtain the reflector cross-sections, a multi-cell geometry was created with several fuel and reflector cells. The collapsed two-group cross sections for the reflector are then extracted and used as input in the PARCS calculations.

In the SCWR design the coolant density changes significantly along the channel from ~ 0.62 $g.cm^{-3}$ to ~ 0.06 $g.cm^{-3}$. Thus the core was divided into twenty axial slices to account for the coolant density and temperature changes on the lattice physics. Therefore, the 2-group homogenized cross sections have been simulated in TRITON for those twenty positions using appropriate local averaged temperatures and densities for each material at each elevation (Table 2 and 3 [4]).

In this work, as in [6], burnable absorbers were used to eliminate some of the excess reactivity during the initial stages of each batch cycle. The number of pins, the neutron absorber concentration and the absorbing material were chosen to:

- remove approximately one-half of the excess reactivity at BOC
- burn out at the desired rate (by concentrating the absorber in few pins the spatial self-shielding was increased and the absorber life extended

as compared to more distributed but less lumped cases which would burnout faster),
- maintain the $1/8^{th}$ symmetry of the lattice

To accurately simulate the burnup of the fuel and BAs, 8 radial meshes of equal volume in each fuel pin with BA (Figure 4) and 61 burnup steps were used.

The control blade design is based on a typical BWR cruciform shape with the neutron absorbing material being located towards the tip of each blade in order to minimize the perturbation of the cell flux and pin powers when it is inserted. As compared to rod-based absorbers, the cruciform design distributes the absorbing material through a greater length along the edges of a lattice. The distribution of absorbing material towards the end of the arm of the cruciform produced a cell flux imbalance of 1.042 as compared to an imbalance of 1.067 for designs where the absorber was distributed towards the central portion of each arm. Therefore a cruciform design with the bulk of the absorbing material towards the end of each cruciform was adopted for this case.

The above mentioned lattice physics calculations were performed at all core elevations, with and without control blade, and for each burn-up step. As an example of the lattice-level physics results, the infinite lattice multiplication constant (k_{inf}) is plotted in Figure 5 to observe the impact of the burnable absorbers and the control blade as a function of burnup for the 10^{th} axial position (2.625 m). The specifications of the burnable absorbers and the control blade are given in Table 4 and 5, respectively.

2.2 Full-core model: PARCS

The Purdue Advanced Reactor Core Simulator (PARCS) is a three-dimensional reactor core simulator used by the US Nuclear Regulatory Commission (USNRC) for BWR and PWR analysis. PARCS solves the few-group neutron diffusion equation using, amongst others, the finite difference method for steady-state and time-dependent reactor physics phenomena. The output files from SCALE/TRITON are converted to the correct format for PARCS using GenPMAXS [11].

Through symmetry, only a quarter of the SCWR core (84 out of the 336 channels) was simulated in PARCS. Each assembly was divided into 20 axial positions each with unique two group cross sections for the reference case and the control blade branch. Heavy water radial and axial reflectors properties as determined by SCALE have also been included into the model and are 100 cm and 75 cm thick, respectively.

A refuelling scheme without control devices has been proposed by CNL [5]**.** However, with the addition of the burnable absorbers and the reactivity control systems, a new refuelling scheme (Figure 6) was necessary. While not optimized, the refuelling scheme represents an intuitive first approximation of the fuel movements, and further optimization of the scheme may produce some improvement in the core wide results. However, several fuelling schemes were tested with only modest changes in the MSST and other criteria.

Similar to typical BWR designs, the 89 control blades are inserted from the bottom of the core, however unlike a BWR, the rods are inserted into the low-pressure moderator and hence the mechanics of insertion as well as the likelihood of a rod ejection are significantly reduced. Their location in a quarter of the core is shown in Figure 7.
To establish an initial steady-state and reference core a series of repetitive batch fuelling process was simulated. Starting from a completely fresh core, a burnup cycle (in 1 full-power-day increments) was simulated using PARCS until the total core excess reactivity reached 10 mk. Throughout these initial simulations, the thermal-hydraulic conditions in the channel were assumed to be constant and at the reference conditions. The assemblies in the core were then shuffled and replaced as identified in the fuelling pattern given in Figure 6. The burnup simulations and subsequent refuelling were then repeated until such time that the current cycle showed a burnup distribution within a small tolerance to the previously simulated cycle. Convergence was achieved after roughly 25 iterations and all subsequent calculations are performed from this reference state.

3. Thermal-hydraulic model

The system is principally composed of a cold and hot leg, inlet and outlet plena, the channels' orifices and the fuel channels (Figure 8). Fixed boundary conditions are applied at the system's inlet and outlet (25.8 MPa/350°C and 25.0 MPa, respectively). The model also includes nodalization that represents the simplified heat removal to the moderator system.

Each assembly was divided into 20 equal volumes matching the PARCS meshing, and contains a static orifice at the inlet, a central flow tube, the inner and outer fuel ring, and the liners/insulator/pressure tube. Heat transfer was modelled from the two fuel rings to the upward coolant, from the upward coolant to the downward coolant in the central flow tube and finally from the upward coolant to the moderator through the liners, insulator and pressure tube. The channel's static orifice is used to match the channel's flow to its reference power in order to obtain an outlet temperature of 625°C in each channel.

A modified version of RELAP5/MOD4 was used to simulate the primary system since the current off-the-shelf version of RELAP5/MOD4 assumes a constant thermal conductivity value for liquid above the critical temperature (647 K) at any pressure which is innacurate. The thermal conductivity has then been updated in the source code using the most recently published IAPWS formulation 2011 (IF-2011) for ordinary substance in order to obtain the actual variation of thermal conductivity [12]. Comparing the predictions with the improved MOD4 to previous versions shows a sheath temperature increase of approximately 70°C in the equilibrium core predictions.

4. Control blade sequence optimization

The Design Analysis Kit for Optimization and Terascale Applications (DAKOTA), developed at Sandia National Laboratories, is a multilevel parallel object-oriented framework for design optimization, parameter estimation, uncertainty quantification and sensitivity analysis. It is a flexible tool which can be coupled with many simulation codes to solve engineering-based problems. Among others, DAKOTA possesses algorithms for optimization with non-gradient based methods which are of particular interest for this study. Since the number of potential control blade arrangements is very large (i.e., 16 control blade banks (Figure 7) each independently adjustable with 20 possible depths of insertion) and the reactor response may be non-linear to multiple control blade perturbations, DAKOTA was used to perform an optimization with regards to sequence and positioning. The details of the evolutionary algorithm in DAKOTA and used in this work can be found in Reference [9].

4.1 PARCS-RELAP5/MOD4-DAKOTA coupling

As mentioned earlier, the power of each assembly should remain as constant as possible over the entire cycle in order to minimize the deviation of the coolant outlet temperature from 625°C. DAKOTA was used to generate possible control blade configurations at each burn-up step and PARCS-RELAP were used to assess the acceptability of each configuration. As mentioned an evolutionary algorithm was employed to generate the optimal blade configuration at each burn-up step. Ideally, a control blade sequence is desired such that:

- The maximum sheath surface temperature has been minimized (and ideally below the target of 850°C [13])
- The instantaneous channel power at each point in the batch cycle has minimal deviation from the reference predefined channel power distribution. Thus, the variable "σ_{core}" (Equation (1)) - the standard deviation of the 84 channel powers, relative to their reference power – was minimized (P_{opti} is the vector containing the 84 channel powers obtained from a PARCS run with the control blades' position generated by DAKOTA. P_{target} is the vector containing the 84 targeted channel powers which are to be matched)

$$\boldsymbol{\sigma_{core}} = \sqrt{\frac{\sum_{i=1}^{84}(\boldsymbol{P_{opti}^{i}} - \boldsymbol{P_{target}^{i}})^{2}}{\mathbf{84}}} \qquad (1)$$

- Core reactivity has to be maintained close to 10 mk (value used in a previous study [14]),
- The ¼ core model has 84 fuel channels each with 20 axial positions, which gives a total of 1680 nodes. Each of the 1680 nodes has a

specific power and linear element rating (LER). The average LER of the Canadian SCWR can be evaluated using equation (2) where P_{tot} is the core total power (2540 MW), N_{ch} is the total number of fuel channels (336), L_{ch} is the length of a fuel channel (5 m), and N_{pins} is the number of pins per channel (64). Therefore, the average LER is equal to 23.6 $kW \cdot m^{-1}$. A maximum of 40 $kW \cdot m^{-1}$ has been suggested in early studies and was included as here as a constraint, thus the power in a given node should not exceed a normalized nodal power of 1.7 [14].

$$LER = \frac{P_{tot}}{N_{ch} L_{ch} N_{pins}} \quad (2)$$

In order to find an acceptable solution while respecting the above constraints, a total of 16 banks of control blades can be inserted into the core with discrete steps of 25 cm (the size of the steps could be reduced in a further optimization to refine the position of the control blades as fine motion control exists). Rods are assigned to banks according to core symmetry and position, and rod banks move simultaneously to identical positions in the simulations. As the core is five meters high, 21 positions can be occupied by each bank of control blades (20 in-core positions and 1 position corresponding to out of core). Therefore, the space to be searched contains approximately $21^{16} \approx 1.43 \times 10^{21}$ possible solutions.

Figure 9 presents the optimization process of the control blade sequence. For the first cycle, the initial nodal burnups and the target channel powers are extracted from the steady-state converged refuelling simulations without control blades. They are then updated during each stage of the optimization process. The positions of the control blades were searched at day 0, day 5 (to adjust for the quick power change in fresh fuel due to fission product generation) and every 50 days afterwards until day 405. At each discrete time step, DAKOTA's evolutionary algorithm searches for the control blade positions which best satisfy the criteria discussed above. Once the optimal configuration is determined, the time step is advanced and a new configuration search is initiated.

4.2 Maximum sheath surface temperature evaluation

The coupled simulation of the thermal-hydraulic conditions for every possible search configuration generated by DAKOTA was impractical since the thermal-hydraulic simulations take 10 to 20 times longer than the PARCS calculation. To circumvent these time constraints, the optimization was performed in three stages. During the first stage DAKOTA calls PARCS directly to calculate the multiplication constant (k_{eff}), the maximum LER and channel powers for a given position of the rods and time within the cycle. The second stage used the predicted channel powers and axial power distributions from PARCS to evaluate the MSST through a response surface methodology generated ahead of time. DAKOTA then compares the optimization criteria (MSST, k_{eff} and LER) and searches the space by adjusting rod positions

according to its evolutionary algorithm. The third stage involves confirmation of the MSST behaviour using full RELAP-PARCS simulations for the entire cycle according to the optimized sequence identified by DAKOTA.

The main factors influencing the maximum sheath surface temperature in each channel are the:

- ratio of the power in the two fuel rings
- axial power distribution,
- deviation of the channel power from its reference power (since the coolant flow and orifice size were unique selected based on its reference power),
- channel reference power .

Therefore, a response surface methodology was created which captures these effects. A two-channel group thermal-hydraulic model was created in RELAP5/MOD4 for the SCWR core. The first channel is a single channel containing the varying parameters (axial power distribution, channel reference power and channel actual power) while the other channel represents an average of the remaining 83 channels, with a fixed axial power distribution and a total power of 635 MW (= 2540 MW / 4) minus the power generated in the first channel-power group. Simulations are performed by varying the conditions in the first channel according to the conditions discussed below and recording the MSST predicted by RELAP.

4.2.1 Inner and outer fuel ring power production

The amount of power generated in each fuel ring depends on several factors, namely fuel burnup, axial position and presence of the control blade. However, the burnup and the presence of the control blade along the channel are unknown parameters at the outset of the optimization process. Therefore the most conservative value for the fuel-ring power imbalance was used in the optimization (Table 6 and 7). While this conservatively removes the dependency of the ring powers in the optimization process, its level of conservatism is unknown since the burnable absorbers will also impose pin specific tilts in the assembly which are not included here. Additional lattice physics and sub-channel thermal-hydraulics is required in the future to assess the impact of local pin power and ring power deviations on MSST.

4.2.2 List of axial power distributions (APDs)

The axial power distribution influences the sheath temperature as it affects the coolant enthalpy distribution in the channel. The first stage of response surface modelling was to capture the APDs used in PARCS and DAKOTA to optimize the blade positions without RELAP and based on minimizing "σ_{core}" (Equation (1)). Over 20000 DAKOTA-PARCS simulations were performed to obtain a pseudo-optimized blade sequence that only considers nodal power deviation as a criterion. From this initial set of simulations, the APDs (in the

form of 20 discrete values along the channel length) were extracted for each channel at each step and compared to one another. If the average deviation of the 20 values was less than 5%, the APDs were considered similar and only one was kept. In the end 1034 APDs were selected as a representative set of APD from the 10000s of simulations performed in the DAKOTA-PARCS standalone optimization.

4.2.3 Orifice size

The orifice size is directly dependent on the reference channel power. However, for the same channel power, two different APDs might produce two different orifice sizes in order to reach the same coolant outlet temperature, since the changes in fluid enthalpy and specific heat are highly non-linear in the pseudo-critical regime. To test this importance the orifice size was evaluated for the 1034 representative APDs for a range of typical channel powers (6.0, 7.0, 7.56, 8.0 and 9.0 MW). For each channel power, the orifice size and its standard deviation about its mean for each of the 1034 APDs were calculated (Table 8). Examining the standard deviation, it can be noted that the APD has very little impact on the orifice size and as a consequence the orifice size can be considered independent of the APD. The size, however, varies linearly with the reference channel power (Figure 10). In lieu of these results, the deviation in power from the reference channel power is viewed as the most significant variable influencing the MSST and is a main component of the response surface.

4.2.4 Surface response

Based on the above discussion the MSST surface response has three dimensions:

- Channel's reference power
  - 3 values: 6.0, 7.56 and 9.0 MW
- Power deviation from the reference power
  - 8 values: -2.5, -1.0, -0.5, 0.0, +0.5, +1.0, +1.5 and +2.5 MW
- Axial power distribution
  - 1034 shapes

RELAP5/MOD4 has been run for each combination of these three variables (3*8*1034 = 24,816 runs) and the MSSTs were stored in a three-dimensional look-up table for further interpolation.
The interpolation process is as follow. After a PARCS simulation, the information relative to the table (APD, channel reference power and channel actual power) are extracted from the PARCS output file and the closest APD (in terms of the minimum deviation between the 20 axial locations between the PARCS APD and that in the look-up table) is selected. For a given APD a 2-dimensional interpolation is performed using the results at the nearest reference channel powers and power deviations.
The functional response surface was tested for a few thousands cases against RELAP5/MOD4 simulations. The average discrepancy between the

RELAP5/MOD4 simulations and the functional response surface was approximately 12°C and is considered acceptably accurate based on the overall variation of MSST of 350°C over those same cases

5. Results and Discussion

The reference power distribution is shown in Figure 11. Figure 12 shows the standard deviation (in MW) for each channel over the entire cycle with respect to their targeted channel powers (Figure 11) utilizing the DAKOTA optimized control blade sequence. In general the optimized sequence provides less than 0.5 MW or approximately less than 10% variation in channel powers over the cycle. The deviation is greatly reduced when the worst-three channels (on the periphery of the core) are removed. In general some consideration of an additional control rod in the reflector region is needed, since the variation of outer channels tends to be larger than in the core interior.

Figure 13 and 14 display the effective multiplication constant (k_{eff}) and the maximum linear element rating (LER) of the core during the cycle with and without the use of control blades, respectively. By inserting control blades in the core, the initial excess reactivity has been reduced from 50 mk to about 15 mk and maintained around the targeted 10 mk throughout the cycle (value used in previous studies [14,15]). The suppression of reactivity is expected to cause some local power peaking in channels which are influenced by the inserted blades. As the blade sequence changes, local peaking moves to differing locations depending on the position and extent of insertion of each rod. Even though the maximum LER is overall higher than that without control rods, the limit of 40 kW/m was never reached. In Figure 15 the "MSST (interpolated)" curve is the maximum sheath surface temperature obtained by interpolation from the surface response during the optimization process and the "MSST (Exact)" curve is the actual MSST recalculated with the exact parameters for each optimized configuration. Looking at the latter, the optimization yields a MSST varying between 1150K and 1235K along the cycle while the target was 1123K. While the target temperature for the sheath is not met, the variation of MSST over the entire cycle was 85°C which is much better than case without blade spatial control which had an MSST variation of over 150°C.

To further investigate the MSST behaviour, the curve labelled "MSST (CPs = targeted CPs)" represents the MSST that would be obtained if the channel powers were perfectly maintained at the reference power over the entire cycle. Even in this unrealistic case, the target cladding temperatures cannot be met due to, but not only, the axial power distribution being too peaked at the top of the core.

Moreover, the MSST was calculated for the equilibrium cycle without control blades. A targeted power for each channel was evaluated by taking the average power of each channel over the cycle. The "MSST (Exact) – No control blades" curve simply represents the MSST evolution during the cycle without control blades (but including burnable absorbers). As there is no spatial reactivity control, the channel powers evolve freely with the cycle minimum

occurring at middle-of-cycle conditions – which confirms the results found in [16]. Such a result arises from the orifice sizing calculations which were performed at MOC conditions.

In order to explore the sensitivity of the MSST to the assumptions in this work, three options have been investigated which may lower the MSST. In order to isolate the effect of these improvements, the simulations are performed using RELAP for a fixed set control blade sequence from PARCS. While the lattice physics would also be impacted by the changes in the thermal-hydraulic properties (for example: fuel temperature and coolant density distributions), the different cases investigated were used to probe the most impactful options.

The first case consisted of reducing the core total power by 10% while maintaining the same inlet and outlet coolant conditions (i.e., the flow was lowered such that the enthalpy rise through each channel was the same). The change in MSST and fuel centreline temperature are shown in Figure 16 and 17, respectively. While the fuel centreline temperature has been reduced by about 300°C due to the lower power density, the MSST remained within 10°C of the previous results. While the heat flux would tend to decrease the sheath temperature in isolation, the effect of the lower mass flux partially compensates, making the net improvement in sheath temperature small. Therefore, the change in core total power has a very limited effect on the MSST. The fuel centreline temperature is however quite high for the reference case event though this study is using conservative assumptions. The power production in the inner and outer fuel ring should be kept around 48% and 52% respectively to obtain a balance fuel centreline temperature between the two rings. The thermal conductivity values used for each rings are taken from [12]. Further studies should examine whether a core power reduction is warranted.

The second sensitivity case examined the effect of APD on the MSST, mainly because the APD may be altered in the design by using a combination of graded enrichment/burnable absorber and/or partial-length fuel rods. Since core redesign with such features is beyond the scope of this work, the list of APD generated in the optimization was used as a surrogate. In the sensitivity cases the APD in every fuel channel is overwritten with each of the 1034 representative APDs developed in Section 4.2.2 and RELAP simulations are used to recalculate the MSST. Then the minimum MSST is determined based on these new simulations (Figure 18). Examining the minimum MSST over the range of possible APDs represents an unrealistic case where all the APDs would be peaked towards the bottom of the channel, however such a case gives an approximation of the best possible improvement from core power shaping using graded enrichment/absorbers and partial length rods. By examining Figure 18 the largest improvement over the 1034 APDs was approximately 100°C. While this case is unrealistic, the APDs could be moderately shifted towards the bottom of the core and hence some improvement (up to 100°C may be possible).

The third and last case investigated involved lowering the coolant outlet temperature from 625°C to 550°C, comparable to the outlet temperature used

in the European HPLWR design [17]. In this case the core power was kept constant while the orifice sizes were increased such as to provide an outlet temperature of 550°C. An improvement of about 100°C throughout the cycle can be observed in Figure 19. While this change would reduce the possible efficiency improvements of the SCWR design, the reduction in coolant outlet temperature alone would provide an MSST within the acceptable limit of 1123 K.
Considering these results, several recommendations can be made. In order to reduce the MSST below the 1123 K material property limit, reducing the coolant outlet temperature seems to be the best option. Moreover, an axially graded fuel enrichment and/or burnable absorber concentration along with partial length fuel-rods (similar to an ESBWR) would also reduce the MSST by shifting the power towards the bottom of the core where the coolant enthalpy is lowest. The effect of a core power reduction (and subsequent orifice size changes so that the same enthalpy rise is achieved) is insignificant as compared to the potential improvements discussed above.

6. Conclusions

The combined use of fuel-integrated burnable absorbers in a selected number of fuel pins and cruciform control blades inserted from the bottom of the core into the low pressure moderator has been investigated for the Canadian SCWR. These reactivity control mechanisms provide bulk and spatial power control during the entire batch cycle length. While the burnable absorbers have been designed to burn out as a desired rate, the control blade insertion sequence requires optimization so as to maintain the key core parameters within acceptable limits. Therefore, an evolutionary algorithm was used to find the position of the control blades during the cycle while minimizing the maximum sheath surface temperature as well as constraining k_{eff} and the linear element rating. Even for the optimized sequence, the MSST exceed the material limits for normal operation.

Three options were investigated to demonstrate the sensitivity of the MSST to core design assumptions. First the core power was reduced to 90% full power and while the maximum fuel centreline temperature was reduced by about 300°C, the MSST was not significantly reduced. The second option considered core flux shaping that would favorably alter the axial power distribution. An ideal case of APDs peaked towards the bottom of the core reduced the MSST by approximately 100°C. Therefore an axially graded fuel enrichment and/or burnable absorber concentration and/or partial length fuel rods could be further investigated to lower the MSST. Finally, the coolant outlet temperature was changed from 625°C to 550°C and an improvement of about 100°C has been observed.

This study demonstrates the need for design changes to be able to meet the 850°C sheath surface temperature limit. The best option seems to be reducing the coolant exit temperature by about 75°C coupled to core flux shaping. Such changes would likely result in normal operating sheath temperatures well

below the acceptance criteria, and hence provide margin to the material limits. An earlier study shows that the highest MSST obtained during the most limiting loss of coolant accident is below the thermal limit of stainless steel if the initial MSST is within acceptable values during normal operation [12]. The maximum fuel centreline temperature also appears to be quite high and further studies should make sure it remains within acceptable values. The reference fuelling scheme provided by CNL is no longer optimal for cases with reactivity control systems and hence it is recommended to re-evaluate the fueling scheme as part of a larger core optimization process.

Acknowledgements

This research on the Canadian GEN-IV program was funded by Natural Resources Canada (NRCAN) through the office of Energy Research and Development, Canadian Nuclear Laboratories (CNL) and Natural Sciences and Engineering Research Council of Canada (NSERC). The authors would also like to thank Innovative System Software (ISS) for providing RELAP/MOD4/SCDAPSIM.

References

[1] L. K. H. Leung, M. Yetisir, W. Diamond, D. Martin, J. Pencer, B. Hyland, H. Hamilton, D. Guzonas and R. Duffey, 2011, "A Next Generation Heavy Water Nuclear Reactor with Supercritical Water as Coolant", International Conference on Future of Heavy Water Reactors, Ottawa, Canada

[2] J. Pencer and A. Colton, 2013, "Progression of the Lattice Physics Concept for the Canadian Supercritical Water Reactor", 34th Annual Conference of the Canadian Nuclear Society, Toronto, Canada

[3] J. Pencer, B. Bromley, and A. Nava-Dominguez, "Fuel Channel Assembly and Fuel Bundle for a Nuclear Reactor", Canadian Patent CA 2881784 A1, June 13, 2012.

[4] D. W. Hummel and D. R. Novog, 2016, "Coupled 3D neutron kinetics and thermalhydraulics characteristics of the Canadian supercritical water reactor", Nuclear Engineering and Design 298, 78-89, DOI: 10.1016/j.engdes.2015.12.008

[5] J. Pencer, D, Watts, A. Colton, X. Wang, L. Blomeley, V. Anghel and S. Yue, 2013, "Core neutronics for the Canadian SCWR Conceptual Design", The 6th International Symposium on Supercritical Water-Cooled Reactors (ISSCWR-6), Shenzhen, China

[6] M. McDonald, A. Colton, J. Pencer, 2015, "Power Flattening and Reactivity Suppression Strategies for the Canadian Supercritical Water Reactor Concept", 39th Annual Conference of the Canadian Nuclear Society, Saint John, New-Brunswick, Canada

[7] Oak Ridge National Laboratory, SCALE: A comprehensive modelling and simulation suite for nuclear safety analysis and design, ORNL/TM-2005/39 Version 6.1, 2011

[8] T. Downar, Y. Xu and V.Seker, PARCS v3.0 U.S.NRC Core Neutronics Simulator, USER MANUAL draft (05/29/2013)

[9] Dakota, A Multilevel Parallel Object-Oriented Framework for Design Optimization, Parameter Estimation, Uncertainty Quantification and Sensitivity Analysis, Version 5.4 Reference Manual released December 2009 and updated November 2013, Sandia National Laboratories

[10] C. M. Allison and J. K. Hohorst. Role of RELAP5/SCDAPSIM in Nuclear Safety. Science and Technology of Nuclear Installations. Volume 2010, Article ID 425658.

[11] A. Ward, Y. Xu and T. Downar, GenPMAXS – v6.1.2dev, Code for Generating the PARCS Cross Section Interface File PMAXS, 2013

[12] C. Lou, 2016, "Loss of coolant accident simulation for the Canadian supercritical water-cooled reactor using RELAP5/MOD4", Master thesis, McMaster University, Hamilton, Ontario, Canada

[13] S. Xu, S. Amirkhiz, 2016, "Mechanical Properties of Fuel Cladding Candidate Alloys for Canadian SCWR Concept", JOM, Vol 68, Issue 2, pp. 469-474, DOI: 10.1007/s11837-015-1725-9

[14] M. H. McDonald, B. Hyland, H. Hamilton, L. K. H Leung, N. Onder, J. Pencer and R .Xu, 2011, "Pre-conceptual Fuel Design Concepts For The Canadian Super Critical Water-cooled Reactor", The 5th International Symposium on Supercritical Water-Cooled Reactors (ISSCWR-5), Vancouver, Canada

[15] J. Pencer, D. Watts, A. Colton, X. Wang, L. Blomeley, V. Anghel and S. Yue, 2013, "Core Neutronics for the Canadian SCWR Conceptual Design", The 6th International Symposium on Supercritical Water-Cooled Reactors (ISSCWR-6), Shenzhen, Guangdong, China

[16] D. W. Hummel, 2015, "Transient neutronic-thermalhydraulic coupling in a PT-SCWR", PhD thesis, McMaster University, Hamilton, Ontario, Canada

[17] T. Schulenberg, J. Starflinger, P. Marsault, D. Bitterman, C. Maraczy, E. Laurien, J. A. Lycklama a Nijeholt, H. Anglart, M. Andreani, M. Ruzickova, A. Toivonen, 2011, "European supercritical water cooled reactor", Nuclear Engineering and Design 241, p. 3505-3513, DOI 10.1016/j.nucengdes.2010.09.039

List of Figures

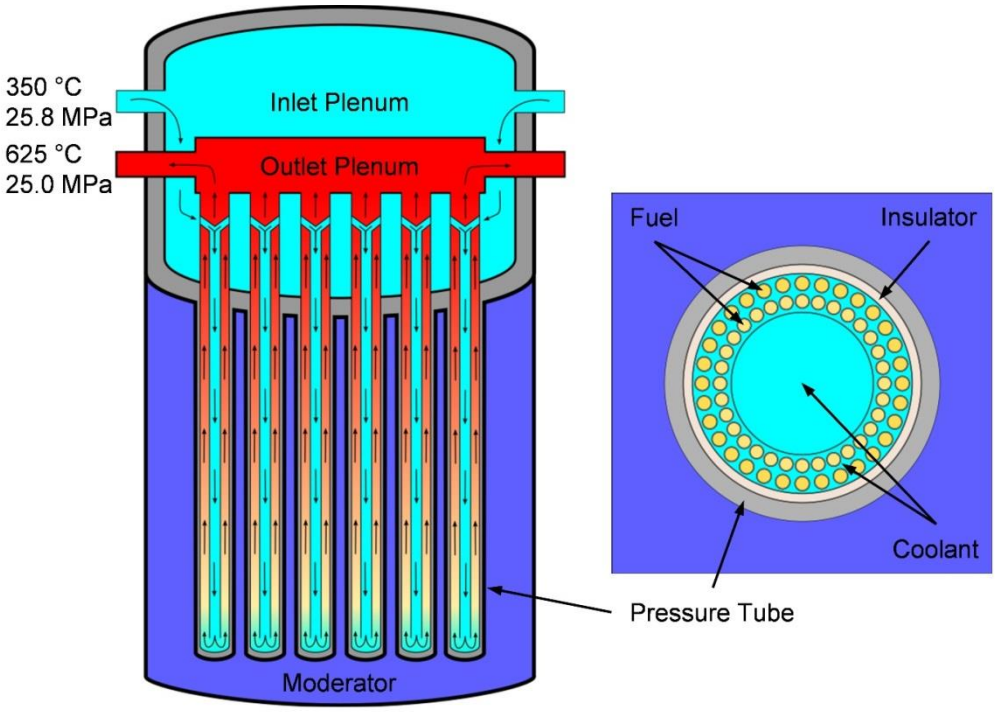

Figure 1 Canadian SCWR core concept and HERC concept

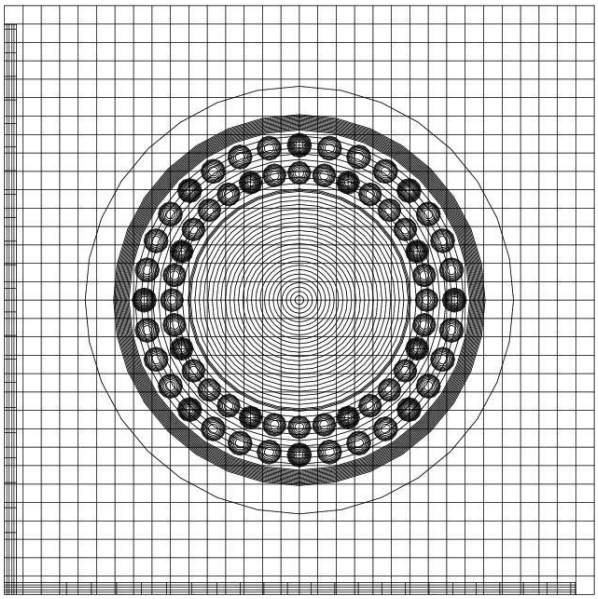

Figure 2 Meshing of the Canadian SCWR infinite lattice cell with fuel-integrated burnable absorber and a control blade inserted

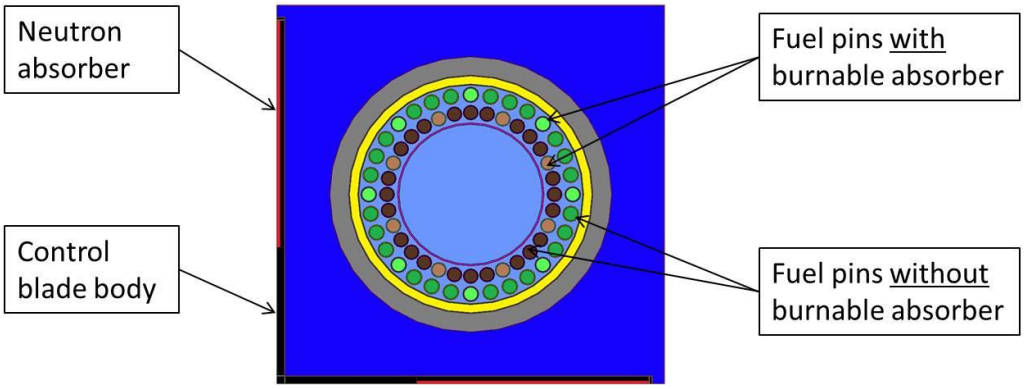

Figure 3 Materials in the Canadian SCWR infinite lattice cell with fuel-integrated burnable absorber and a control blade inserted

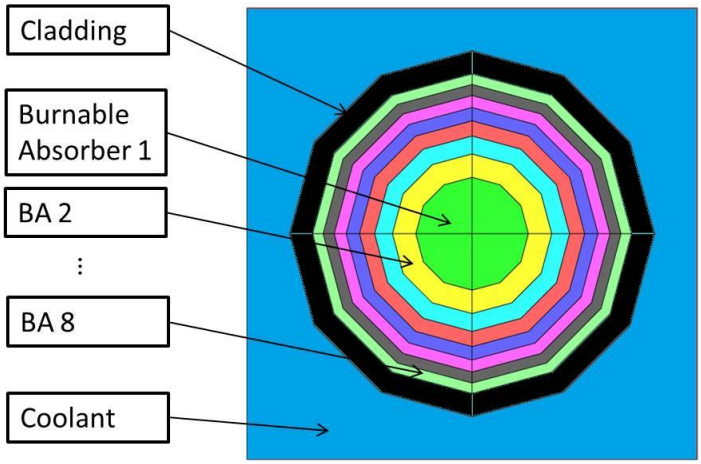

Figure 4 Radial meshing in fuel pins containing burnable absorbers

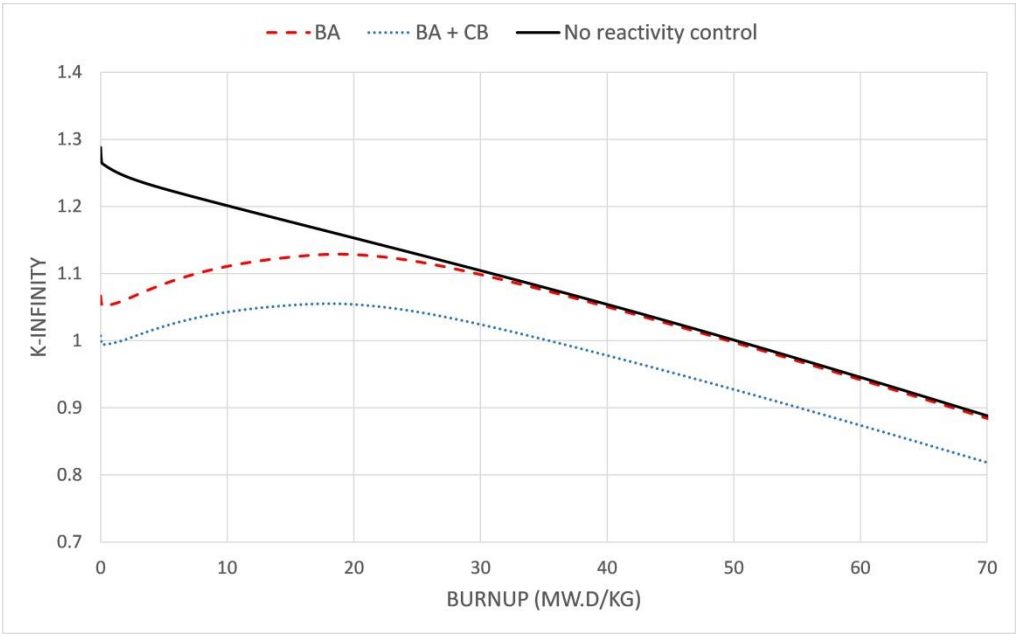

Figure 5 k_{inf} as function of burnup with and without reactivity systems

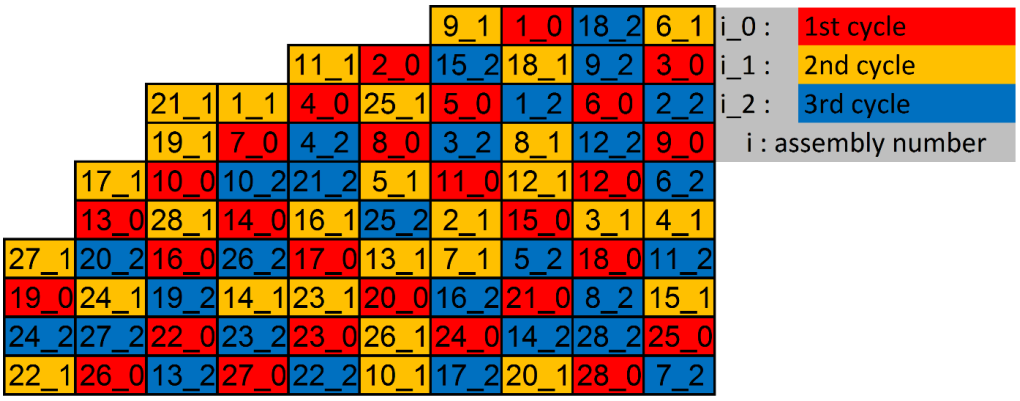

Figure 6 New 3-batch refuelling scheme

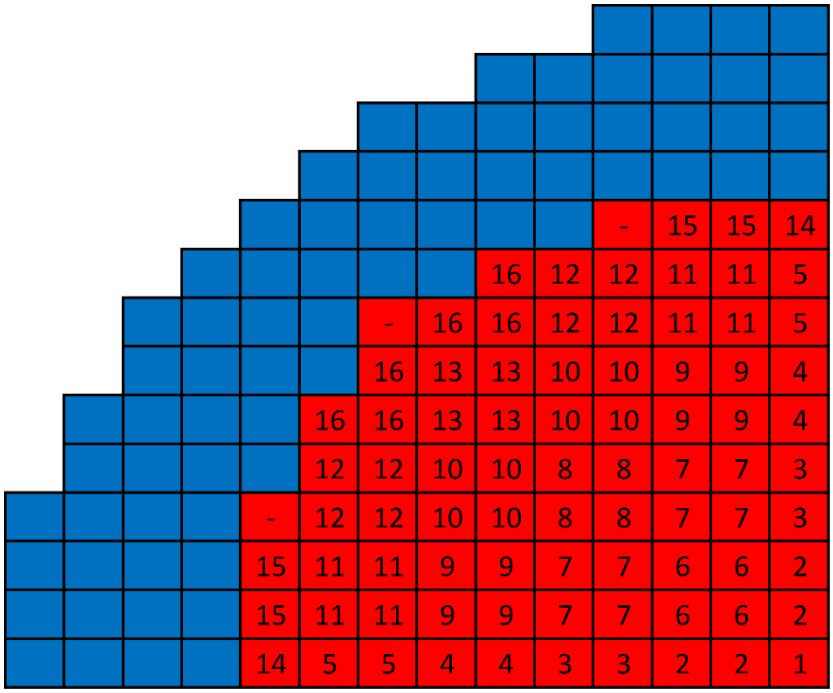

Figure 7 Control blades bank numbers (Red cells = fuel assembly ; Blue cells = reflector)

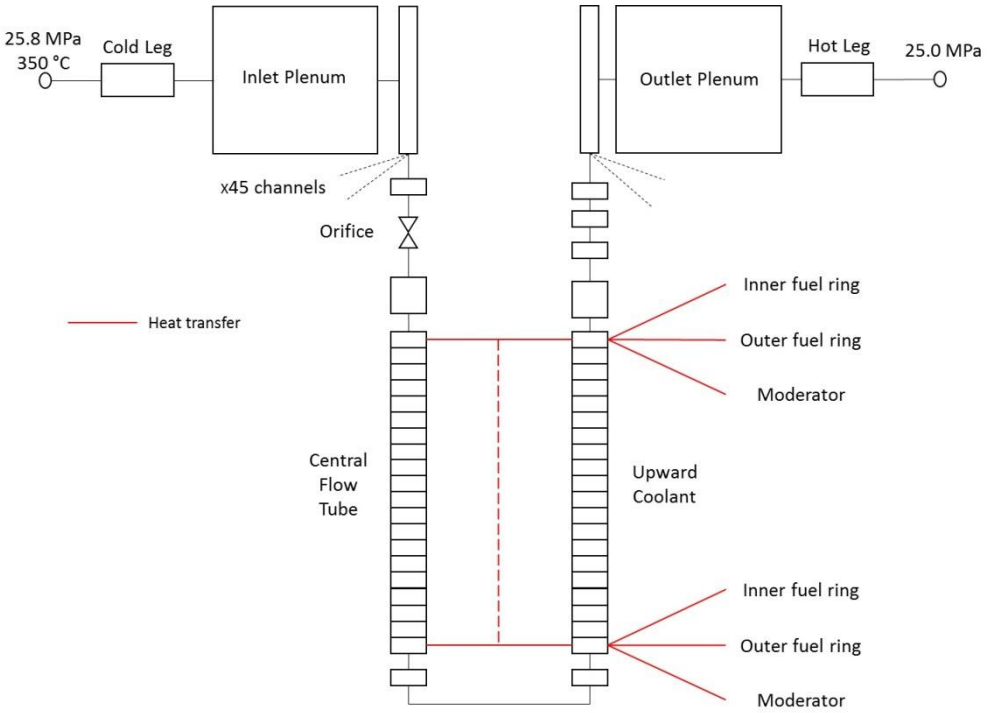

Figure 8 Thermal-hydraulic model of the Canadian SCWR in RELAP5/MOD4

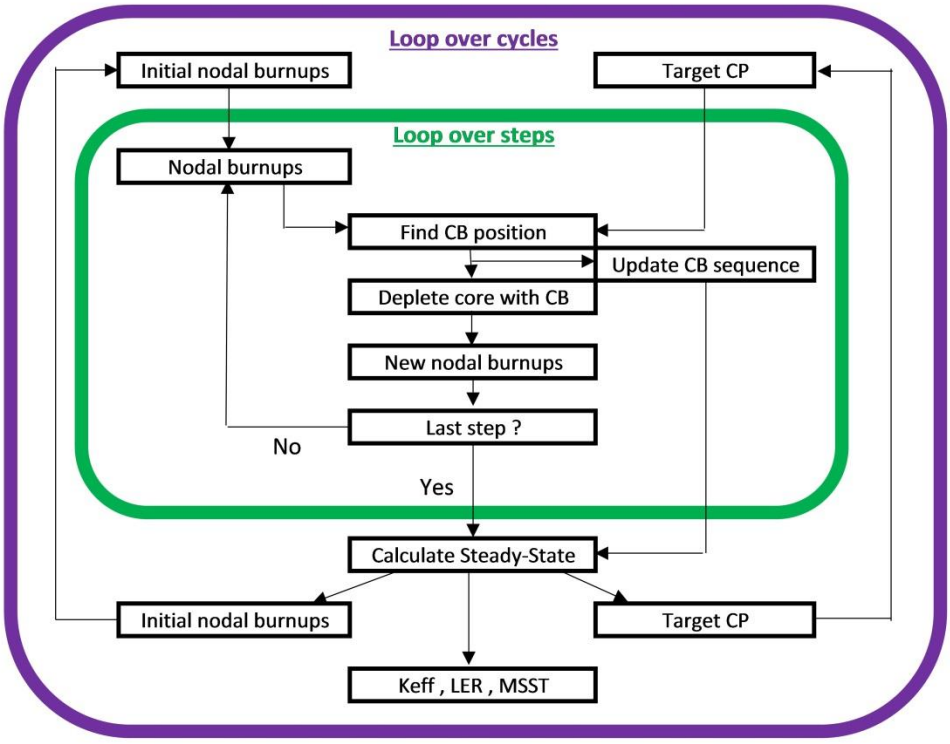

Figure 9 Control blade sequence optimization diagram

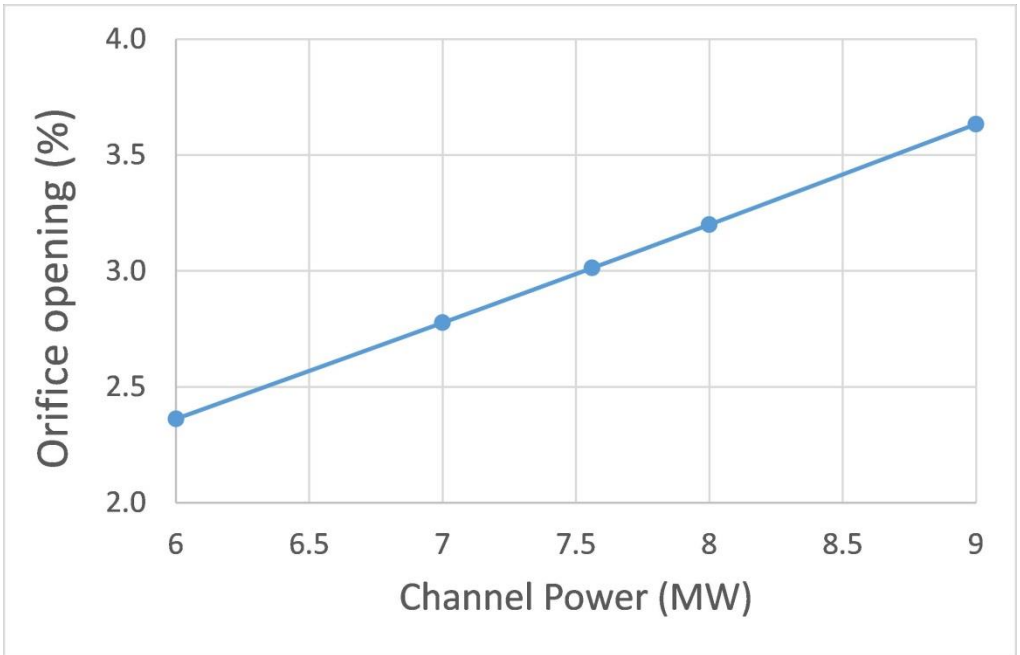

Figure 10 Orifice opening of the fuel channel as function of channel power

					1.03	1.01	0.86	0.98	
				1.11	1.06	0.86	1.05	0.91	1.15
			1.07	1.1	1.09	1.03	1.03	0.95	1.15	0.98
			1.1	0.99	0.82	0.97	0.85	1.1	0.95	1.15
		1.11	1.09	0.82	0.78	0.95	1.05	1.12	1.15	0.93
		1.06	1.03	0.97	0.95	0.92	1.1	1.07	1	0.98
	1.03	0.86	1.03	0.85	1.05	1.1	1.1	0.89	0.98	0.81
	1.01	1.05	0.95	1.1	1.12	1.07	0.89	1.09	0.92	0.98
	0.86	0.91	1.15	0.95	1.15	1	0.98	0.92	0.92	1.02
	0.98	1.15	0.98	1.15	0.93	0.98	0.81	0.98	1.02	0.86

Figure 11 Reference channel power distribution

				0.5	0.49	0.46	0.37	
			0.78	0.73	0.58	0.54	0.52	0.56
		0.95	1.01	0.86	0.55	0.67	0.47	0.65	0.37
		1.01	0.77	0.41	0.28	0.33	0.74	0.42	0.78
	0.78	0.86	0.41	0.4	0.23	0.37	0.67	0.55	0.42
	0.73	0.55	0.28	0.23	0.39	0.54	0.43	0.3	0.4
0.5	0.58	0.67	0.33	0.37	0.54	0.55	0.33	0.36	0.3
0.49	0.54	0.47	0.74	0.67	0.43	0.33	0.59	0.52	0.33
0.46	0.52	0.65	0.42	0.55	0.3	0.36	0.52	0.43	0.61
0.37	0.56	0.37	0.78	0.42	0.4	0.3	0.33	0.61	0.44

Figure 12 Standard deviation of the 84 channel powers throughout the cycle, with respect to their individual power target [MW]

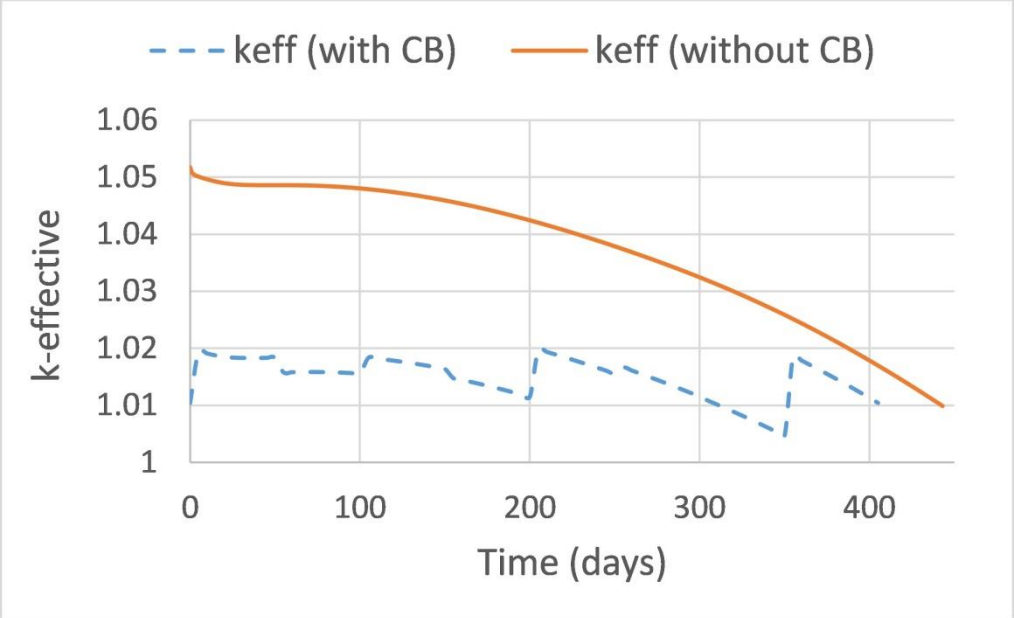

Figure 13 Multiplication constant (k_{eff}) over the cycle with and without the use of control blades

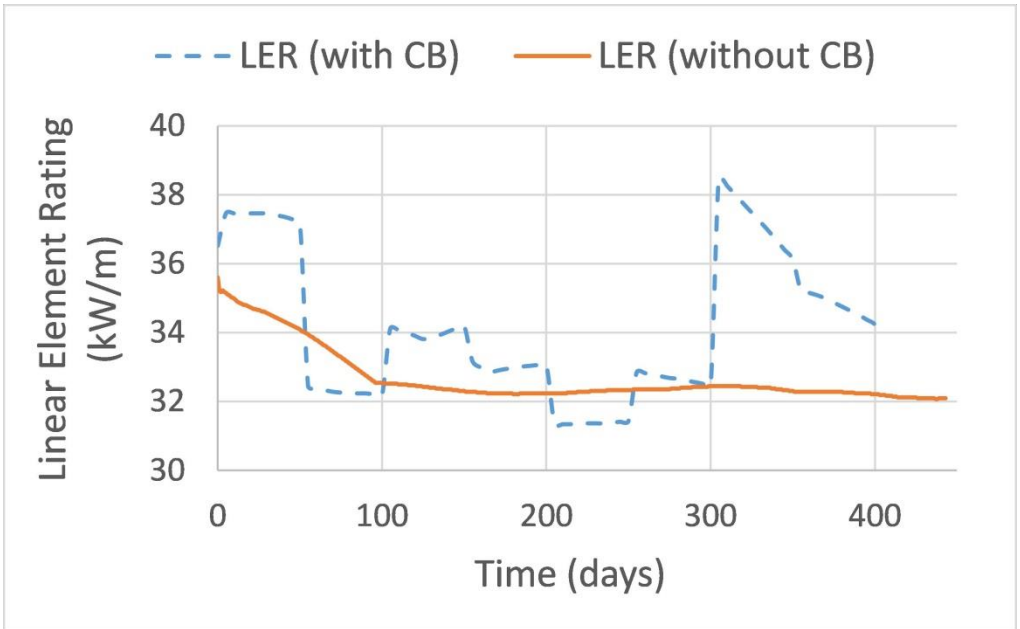

Figure 14 Linear element rating during the cycle with and without the control blades

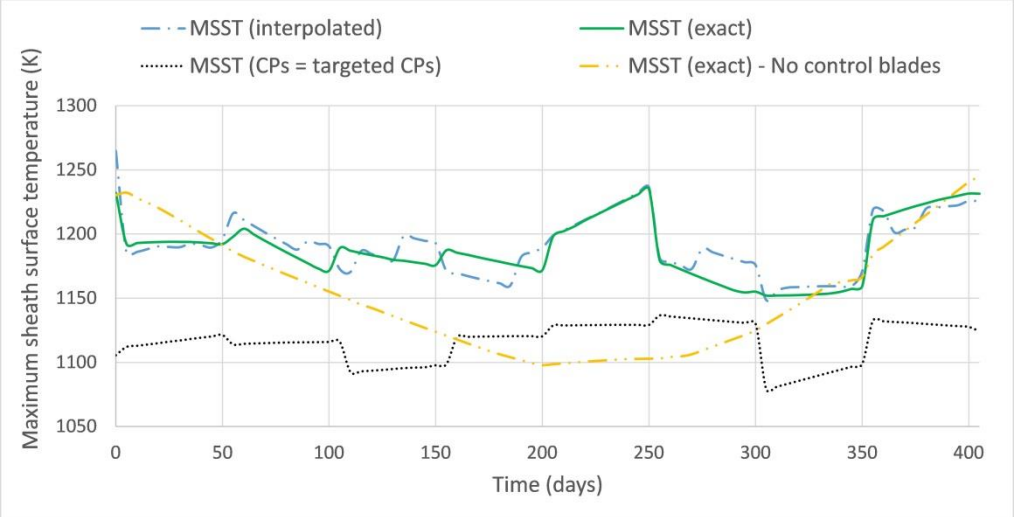

Figure 15 MSST before and after control blade sequence optimization

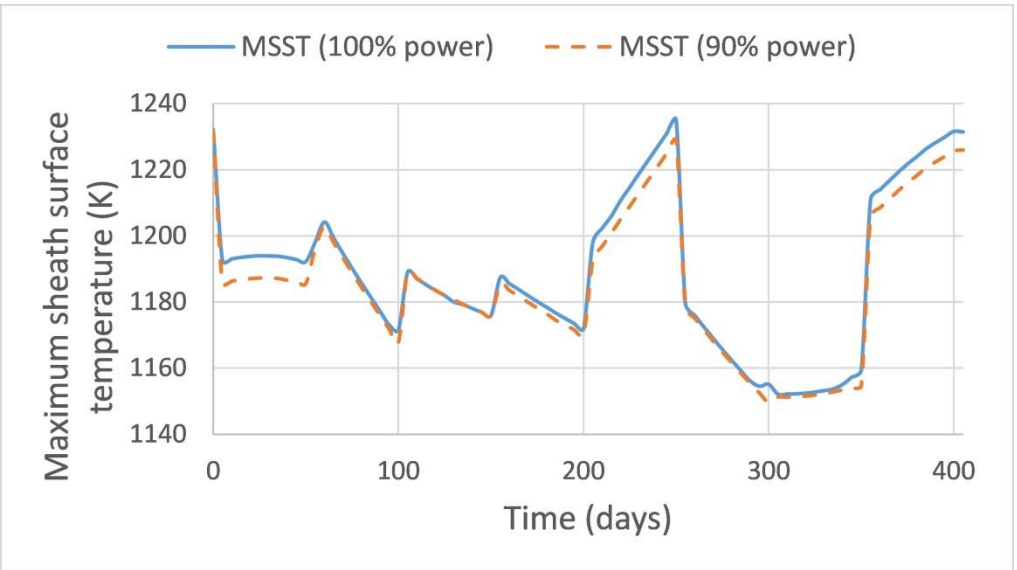

Figure 16 Maximum sheath surface temperature at 100% and 90% full power

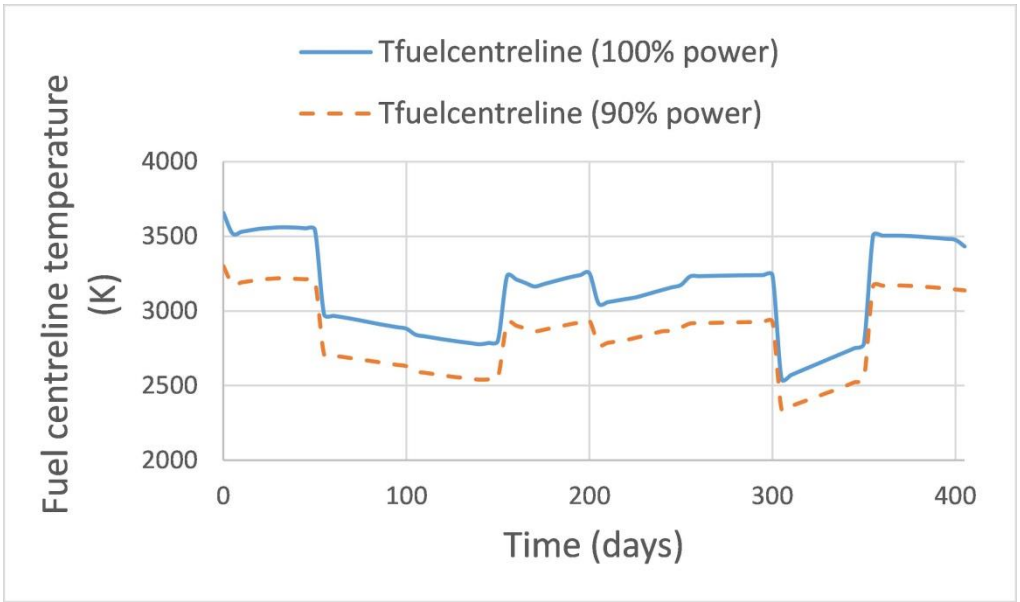

Figure 17 Fuel centerline temperature at 100% and 90% full power

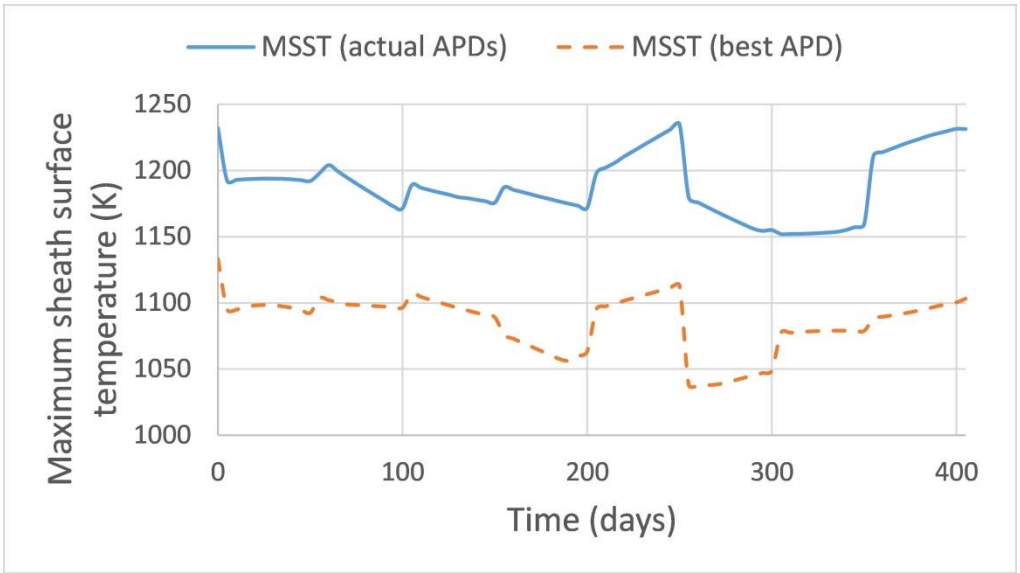

Figure 18 Maximum sheath surface temperature with the actual power distribution and the axial power distribution minimizing the MSST

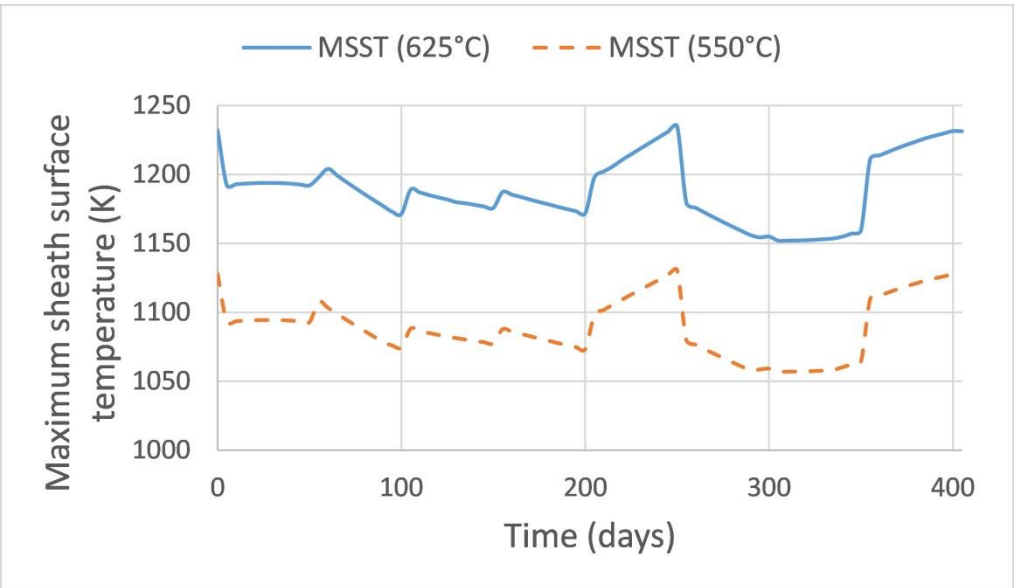

Figure 19 Maximum sheath surface temperature for a coolant outlet temperature of 625°C and 550°C

List of Tables

Table 1 Canadian SCWR fuel lattice cell dimensions and composition

Component	Dimension	Material	Composition [wt%]	Density [g.cm^{-3}]
Centre Tube Coolant	4.6 cm radius	Light Water	100% H2O	Variable
Centre Flow Tube	4.60 cm inner radius ; 0.1 cm thick	Zr-modified 310 Stainless Steel	C: 0.034; Si: 0.51; Mn: 0.74; P: 0.016; S: 0.002; Ni: 20.82; Cr: 25.04; Fe: 51.738; Mo: 0.51; Zr: 0.59	7.9
Inner Fuel Pins (32)	0.415 cm radius; 5.4 cm pitch radius	15 wt% PuO_2 in ThO_2	Pu: 13.23; Th: 74.7; O: 12.07	9.91
Outer Fuel Pins (32)	0.44 cm radius; 6.575 cm pitch radius	12 wt% PuO_2 in ThO_2	Pu: 10.59; Th: 77.34; O: 12.08	9.87
Cladding	0.06 cm thick	Zr-modified 310 Stainless Steel	As above	7.9
Coolant		Light Water	100% H2O	Variable
Liner Tube	7.2 cm inner radius; 0.05 cm thick	Zr-modified 310 Stainless Steel	As above	7.9
Insulator	7.25 cm inner radius; 0.55 cm thick	Yttria Stabilized Zirconia	Zr: 66.63; Y: 7.87; O: 25.5	5.37
Outer Liner Tube	7.8 cm inner radius; 0.05 cm thick	Excel Alloy	Sn: 3.5; Mo: 0.8; Nb: 0.8; Zr 94.9	6.52
Pressure Tube	7.85 cm inner radius; 1.2 cm thick	Excel Alloy	As above	6.52
Moderator	25 cm square lattice pitch	Heavy Water	99.833 D2O; 0.167 H2O	1.0851
Plutonium Isotopics		Reactor Grade Plutonium	Pu238: 2.75; Pu239: 51.96; Pu240: 22.96; Pu241: 15.23; Pu242: 7.10	

Table 2 Materials temperatures and densities in the Canadian SCWR fuel lattice cell

Position (mm)	Upward Coolant Density	Upward Coolant Temperature	Cladding Temperature	Liner Temperature	Insulator Temperature
4875	0.068	898.22	1027.86	868.77	678.80
4625	0.071	874.76	1015.29	846.94	665.38
4375	0.074	849.19	995.60	822.77	650.51
4125	0.079	822.58	969.50	797.80	635.14
3875	0.084	796.23	940.27	773.34	620.04
3625	0.091	771.03	909.17	750.17	605.84
3375	0.099	747.67	877.38	729.00	592.80
3125	0.108	726.72	845.01	710.29	581.20
2875	0.119	708.63	813.50	694.45	571.33
2625	0.133	693.64	783.80	681.62	563.33
2375	0.149	681.79	756.30	671.80	557.17
2125	0.170	672.97	732.66	664.82	552.79
1875	0.195	666.80	712.63	660.28	549.94
1625	0.226	662.80	696.70	657.67	548.31
1375	0.263	660.35	685.40	656.27	547.43
1125	0.309	658.78	678.51	655.37	546.87
875	0.364	657.34	679.99	653.71	545.82
625	0.424	655.07	684.69	650.74	543.96
375	0.483	650.88	689.28	645.52	540.68
125	0.536	644.19	684.35	637.83	535.83

Table 3 Materials temperatures and densities in the Canadian SCWR fuel lattice cell

Position (mm)	Pressure Tube Temperature	Downward Coolant Temperature	Downward Coolant Density	Fuel Temperature	Center Tube Temperature
4875	453.89	624.65	0.621	1625.88	761.44
4625	449.98	626.29	0.616	1676.94	750.53
4375	445.60	627.74	0.611	1700.69	738.47
4125	441.01	629.00	0.606	1691.88	725.79
3875	436.44	630.08	0.602	1666.43	713.15
3625	432.10	631.00	0.599	1631.85	701.01
3375	428.05	631.77	0.596	1594.48	689.72
3125	424.40	632.42	0.593	1551.57	679.57
2875	421.27	632.96	0.591	1507.90	670.79
2625	418.72	633.41	0.589	1465.39	663.53
2375	416.74	633.79	0.588	1420.62	657.79
2125	415.32	634.11	0.586	1381.78	653.54
1875	414.40	634.40	0.585	1345.72	650.60
1625	413.86	634.66	0.584	1312.25	648.73
1375	413.58	634.90	0.583	1285.71	647.62
1125	413.40	635.13	0.582	1262.89	646.96
875	413.06	635.34	0.581	1249.20	646.34
625	412.45	635.52	0.580	1234.12	645.30
375	411.37	635.66	0.580	1201.29	643.27
125	409.77	635.73	0.579	1136.85	639.96

Table 4 Fuel-integrated burnable absorber specifications

	Inner fuel ring	Outer fuel ring
Pins per ring	8	8
Angular offset	$\pi/8$ (evenly spaced)	0 (evenly spaced)
Pin radius (cm)	Pin radius : 0.415 cm	Pin radius : 0.44 cm
Pitch circle radius (cm)	Pitch circle radius : 5.4 cm	Pitch circle radius : 6.575 cm
Materials (wt%)	Th232: 72.458 O16: 12.103 Pu238: 0.353 Pu239: 6.670 Pu240: 2.947 Pu241: 1.955 Pu242: 0.911	Th232: 75.015 O16: 12.113 Pu238: 0.282 Pu239: 5.336 Pu240: 2.358 Pu241: 1.564 Pu242: 0.729
Density ($g.cm^{-3}$)	9.82	9.79

Table 5 Control blade specifications

	Control Blade
Half span	24.2 cm
Thickness	1 cm
CB material (wt%)	Sn:3.5; Mo:0.8; Nb:0.8; Zr:94.9
Length of absorber	15 cm
Thickness of absorber	0.4 cm
Absorber material	Stainless Steel 304
Density	7.94 $g \cdot cm^{-3}$

Table 6 Power fraction generated in the inner fuel ring (conservative values)

Axial Position (mm)	125	375	625	875	1125	1375	1625	1875	2125	2375
Power fraction generated in the innerfuel ring (%)	52.91	52.87	52.82	52.77	52.73	52.7	52.69	52.67	52.66	52.66

Table 7 Power fraction generated in the inner fuel ring (conservative values) (cont'd)

Axial Position (mm)	2625	2875	3125	3375	3625	3875	4125	4375	4625	4875
Power fraction generated in the innerfuel ring (%)	52.66	52.66	52.67	52.67	52.68	52.69	52.7	52.71	52.72	52.74

Table 8 Orifice opening as function of channel power and impact of the axial power distribution on the orifice opening

Channel power (MW)	6	7	7.56	8	9
Average orifice opening (%)	2.36	2.78	3.01	3.20	3.63
Standard deviation due to the axial power distribution	5.31E-05	1.15E-04	1.61E-04	2.03E-04	3.24E-04

Chapter 5

Optimization of the Canadian SCWR Using 3D coupled Reactor Physics and Thermal-hydraulics Calculations

5.1 Preface

Given that the reference design for the SCWR analyzed in Chapter 4 did not meet some of the required safety criteria, the objective of the paper in Chapter 5 was to optimize the design such as to obtain acceptable MCST and MFCLT throughout the batch cycle. PARCS and RSM4 were coupled to evaluate the exact power distribution and thermal-hydraulic conditions and demonstrate that these key limits can be achieved.

An introductory literature review on the modifications made to SCWR concepts to improve the MCST and MFCLT was performed in this paper. It showed that while most of the other SCWR designs meet the limits on sheath and fuel temperatures, the reference Canadian SCWR design showed excessively high cladding and fuel temperatures. Moreover, most of the concepts analyzed in literature did not include control rods which tend to distort the flux shape and negatively impact the cladding and fuel temperatures.

The paper presented in Chapter 5 assesses many potential design changes for the Canadian SCWR including:

- Axially graded fuel enrichment
- Axially graded fuel-integrated burnable poison
- Reduced core power leading to lower fuel enrichment

- 4-batch fueling scheme resulting in a shorter batch length
- Lower control rod's reactivity worth

The first two design changes involve axially grading the fuel enrichment and burnable absorber such as to shift the peak power from the downstream end of the core (where the coolant temperature is highest) towards more upstream locations. Such changes directly reduce the peak cladding temperatures. The third change, while influencing the sheath temperature to some degree, aims at lowering the fuel centerline temperatures. Finally, the last two modifications aim at reducing the power swings caused by fueling and reduce the power changes cause by rod movement, respectively.

The genetic algorithm was used to determine the optimal control rod sequence throughout the batch cycle similar to that done in Chapter 4; however, in this case both the MCST and MFCLT were minimized. A unique surface response for the MFCLT – similar to the MCST's - was created to accelerate the optimization. Further validation between the response surfaces and actual simulations was also performed.

The results of this optimization showed considerable improvement in all metrics, although the limit on MCST was not met for the latter third of the cycle. The MFCLT is now in the acceptable range throughout the cycle. Given the stong improvement obtained in this study, a more exhaustive optimization including number of fuel channels, core power, enrichment and FIBA schemes may produce lower MCST.

The optimization results using thermal hydraulic response surfaces were benchmarked against fully coupled thermalhydraulic and 3D-neutron physics simulations. The results show good agreement with the MCST and MFCLT predicted by the surface responses throughout the cycle.

Finally, the study demonstrates the viability of control rods inserted from the bottom of the core for bulk reactivity control and spatial power distribution. While the issue of bulk and spatial control was also assessed by CNL for their horizontal control rod system, the integrated effects on cycle length, thermal-hydraulics, and local power distribution over an entire cycle length was not analyzed. Therefore this work represents the only assessment of the Canadian SCWR control system behavior at a full core and time dependent level.

The background work, simulations, data analysis, scripts and writing of the manuscript were performed by the main author (F. Salaun). Dr. David Novog was consulted on many occasions for advice, guidance, and expertise.

F. Salaun and D.R. Novog, "Optimization of the Canadian SCWR Core Using Coupled 3D Reactor Physics and Thermal-hydraulics Calculations", Nuclear Engineering and Radiation Science (In production) DOI: 10.1115/1.4038557

5.2 Publication 2

Optimization of the Canadian SCWR Core Using Coupled 3D Reactor Physics and Thermal-hydraulics Calculations

F. Salaun[1] and D.R. Novog[1]
[1]McMaster University, 1280 Main Street West, Hamilton, ON L8S 4L8

Abstract

The Canadian SuperCritical Water-cooled Reactor (SCWR) design is part of Canada's Generation IV reactor development program. The reactor uses batch fueling, light water above the thermodynamic critical point as a coolant and a heavy water moderator. The design has evolved considerably and is currently at the conceptual design level. As a result of batch fueling a certain amount of excess reactivity is loaded at the beginning of each fueling cycle. This excess reactivity must be controlled using a combination of burnable neutron poisons in the fuel, moderator poisons and control blades interspersed in the heavy water moderator. Recent studies have shown that the combination of power density, high coolant temperatures, and reactivity management can lead to high maximum cladding surface temperatures (MCST) and maximum fuel centerline temperatures (MFCLT) in this design. This study focuses on improving both the MCST and the MFCLT through modifications of the conceptual design including changes from a 3 to 4 batch fueling cycle, a slightly shortened fuel cycle (although exit burnup remains the same), axial graded fuel enrichment, fuel-integrated burnable neutron absorbers, lower reactivity control blades, and lower reactor thermal powers as compared to the original conceptual design. The optimal blade positions throughout the fuel cycle were determined such as to minimize the MCST and MFCLT using a genetic algorithm and the reactor physics code PARCS. The final design was analyzed using a fully coupled PARCS-RELAP5/SCDAPSIM/MOD4.0 model to accurately predict the MCST as a function of time during a fueling cycle.

1. Introduction

Canada is developing the SuperCritical Water-cooled Reactor (SCWR) as part of its Generation IV advanced reactor development program [1]. The core is composed of 336 High-Efficiency Re-entrant Channels (HERC) producing a total thermal power of 2540 MW with an approximate thermal efficiency of 48% [2]. In each fuel channel, the 350°C inlet light water coolant passes through the 64 $(Pu,Th)O_2$ fuel pins and exits the channel at an average temperature of 625°C. The 25 MPa coolant in the channel is separated from the 0.3 MPa heavy water moderator by a series of liners, ceramic insulator and zirconium-based pressure tube (Fig. 1 [3]).

Many SCWR concepts have been developed and in each design, the elevated coolant temperature associated with the low coolant density and low heat transfer coefficients towards the end of the channel greatly challenge the cladding surface temperature. As a consequence, studies were performed to evaluate the maximum cladding surface temperature (MCST) during normal operations to demonstrate the viability of each of these concepts. The High Performance Light Water Reactor, the Japanese SCWR, the high temperature super Light Water Reactor, the SCWR mixed spectrum, the Simplified SCWR, the Korean SCWR and the Chinese SCWR have almost all managed to maintain the MCST below their respective thermal limit [4-13]. Many of these designs have implemented a multi-core pass configuration with intermediate coolant mixing in order to satisfy cladding constraints [7,8,10,14]. Axially graded fuel enrichment was also adopted as it modulates the axial power depressing the power at the channel outlets where MCST limits dominate. Finally, the number of refueling batches can be increased to help reduce the MCST as well as to increase the discharge burnup similar to that done by Oka et al [4]. Increasing the number of fueling batches reduced the channel power fluctuations over a fueling cycle, hence minimizing the difference between the reference power used to size each channel's orifice and the operating channel power.

To maintain criticality throughout a fuel cycle a certain excess reactivity is introduced to compensate for fissile depletion and fission products/actinide absorption. A combination of fuel-integrated neutron burnable absorbers (FIBAs) and adjustable control rods are used in many reactor designs to manage this excess reactivity [15]. All concepts have implemented FIBAs to flatten the pin power distribution and remove part of the core total excess reactivity. However, few studies have been performed on the impact of using control rods to manage the large excess reactivity in SCWR designs. The insertion of control rods distorts the axial power distribution and may modify individual channel powers either closer or farther from their reference values. Such deviations in channel power with control rod positions and core wide depletion cause deviations in flow from the reference conditions used to size the inlet orifices. The combination of channel power deviation from its reference value and alterations in the axial shape can have a significant impact on the cladding temperature. It is therefore very important to evaluate the MCST over the representative operating cycle including the effects of all reactivity control systems. Sakurai et al. [9] demonstrated that the cladding temperatures remained below 700 C but no information was given regarding the position of the control rods during the operating cycle or the optimization of the channel's orifice size through each batch cycle. In the Korean concept [13] the position of the control rods is optimized in order to minimize the power peaking factor and an orifice has been introduced to allow for different mass flow rates in each channel, however, the MCST was not evaluated.

Relatively few studies have been performed to evaluate the MCST for the Canadian SCWR as a function of time during an equilibrium batch fueling cycle. One of the first studies by Ahmad et al [16] noticed a very high MCST

at both beginning of cycle (BOC) and end of cycle (EOC). Subsequent changes to the number of fuel pins, refueling scheme, and central flow tube radius reduced the MCST considerably. Hummel et al [17] used the updated concept and implemented orifices at each channel inlet which led, after optimization, to a MCST of ~900°C. No reactivity control mechanisms were included in that study, and hence the MCST in a more realistic case with reactivity suppression would have demonstrated even higher MCST values. More recently, Salaun et al incorporated fuel-integrated burnable absorbers and adjustable control blades for reactivity management [18]. Core-follow simulations for an equilibrium fuel cycle were used to optimize the control blades' position throughout the batch cycle. The MCST was found to be approximately 100°C higher than the design requirements and the Maximum Fuel CenterLine Temperature (MFCLT) reached unreasonable values.
The current study investigates multiple design changes which can be implemented to ensure the MCST and MFCLT are within acceptable limits throughout an equilibrium fuel cycle while maintaining criticality. The combination of power density and fuel thermal conductivity leads to unacceptably high MFCLT values; as such the first design change was to reduce the core thermal power by 20%. Other design options such as increasing the number of fuel pins in the core (e.g., by incorporating fuel into the central flow tube of the channel or increasing the number of fuel channels) and use of higher thermal conductivity accident tolerant fuels were also explored. Axial enrichment and axial-graded FIBA were also included in order to manage the axial power profile throughout the fuel cycle. A lower reactivity worth of the control blades and a 4-batch refueling scheme were also adopted to obtain a better control over the power of the channels over the batch cycle. Finally, the fuel cycle length was decreased and the number of batches increased in order to minimize the power peaking factors throughout each cycle and to maintain the channel powers closer to the reference values used for orifice sizing. A genetic algorithm was then used to find the position of the control devices throughout the operation cycle by minimizing both the MCST and the MFCLT. The equilibrium core was evaluated with fully coupled neutron-physics/thermal-hydraulics to validate the optimization results.

2. Methodology

The current study utilizes 4 codes to calculate the parameters of interest. The 2-group condensed and homogenized cross-sections are evaluated using SCALE 6.1.3 [19]. GenPMAXS [20] is then used to convert the output from SCALE 6.1.3 to the PARCS [21] format which evaluates the 3-dimensional core power distribution. The thermal-hydraulic conditions are calculated by a full-core model designed in RELAP/SCDAPSIM/MOD4.0 (RSM4) [22]. The details of these models are described in this section.

2.1 Cross-sections calculation

SCALE 6.1.3 is a package of modules developed at Oak Ridge National Laboratory. The NEWT module solves the multi-group transport equation with a 238 energy group library based on ENDF/B-VII.0 to generate problem-specific few-group cross-sections. The adequacy of SCALE to accurately model the Canadian SCWR fuel lattice cell was proven in a benchmark study [23] by comparing the results to, amongst others, MCNP. ORIGEN module is then used to deplete the fuel materials based on the fluxes obtained from the transport solution.
The meshing and materials of the fuel lattice cell used in this study are shown in Fig. 2 and Fig. 3. The geometry details and materials information are listed in Table 1. The coolant undertakes a significant change in temperature/density along the channel. As a consequence, the neutron physics is substantially impacted and the 2-group condensed and homogenized cross-sections were evaluated separately at 20 axial positions using the expected materials' averaged thermal-hydraulic conditions at each location (Table 2 and 3). The same temperatures and densities as in [24] were used except for the fuel temperatures which were re-evaluated at the lower core power (2032 MW[1]) using the RSM4 core model [18]. A previous study demonstrated the need for a higher energy cut-off than the usual 0.625eV due to the high coolant temperature [25]; therefore, 2.57 eV was chosen as the limit between the fast and thermal group. The author, however, mentioned that even if the 2-group model with higher energy cut-off might be sufficient, verification and validation should be performed in the future.
Reflective boundary conditions were applied on each side on the lattice cell. The self-shielding calculation utilizes Dancoff factors which need to be evaluated through the MCDancoff module due to the irregular pin distribution. Therefore, the Dancoff factors were calculated separately at each of the 20 axial positions based on the recommendations in [26].

The 2-group homogenized cross-sections for the reference fuel lattice cell – without the control blades – were first calculated for 60 burnup steps at each elevation. The fuel composition at each burnup step was then used in a branch calculation with the control blade inserted in the lattice cell. Additional branches for each important feedback coefficient were also performed at each elevation and several burnup steps (see section 3.3).
The core is surrounded by a 1-meter thick heavy-water reflector. A multi-cell model was built to evaluate the 2-group homogenized cross-sections for the reflector. More details can be found in [18].

2.2 Full-Core diffusion model

The output from the lattice calculations is first processed into PARCS format using GenPMAXS. The 2 energy-group diffusion equation is solved by

[1] Channel orifices were adjusted to keep a coolant outlet temperature of 625 °C

PARCS to evaluate the three-dimensional core power distribution. A special treatment of the assemblies located near the reflector should be performed to enhance the solution of the diffusion model [27, 28]; however, this model is only based on infinite lattice calculations due to the intensive computational requirements that would be involved in solving the transport equation in a multi-cell geometry in NEWT. The fuel assemblies in contact with the reflector would be primarily affected leading to an expected bias of 10-15% regarding those channel powers. Nevertheless, the approach carried out in this study remains valid but could be enhanced in the future with the use of more accurate modeling techniques.
The 336 fuel channels are modeled as 84 parallel fuel assemblies using symmetry. Each channel was divided into 20 geometrically identical positions with each of these 20 elevations using the appropriate cross-sections from the fuel lattice calculations. 75 cm thick axial and 100 cm thick radial reflectors were also simulated in the core model. The PARCS model is described further in section 2.3.

2.3 Thermal-hydraulic model

RSM4 was used to represent the thermal hydraulic behavior in the core. Innovative Systems Software combined US Nuclear Regulatory Commission codes RELAP5/MOD3.3 [29] and SCDAP/RELAP5/MOD3.2 [30] with advanced techniques while also improving fluid supercritical conditions [31]. For instance, the fluid properties now use the National Institute of Standards and Technology (NIST) formulation over the ASTM-1967 formulation to obtain more accurate fluid properties, especially around the pseudo-critical line. The transition through the (pseudo) critical point was also improved by implementing new numerical techniques due to the multiple errors encountered by users [31]. Finally, an updated version of the current RSM4 was used since the water thermal conductivity above the critical temperature was inexact in the original MOD4.0 release [32]. Indeed, Lou [32] updated the source code to obtain the thermal conductivity based on the 2011 International Association for Properties of Water and Steam formulation [33]. The new thermal conductivity predictions were evaluated and compared to the NIST 23 database which validated its proper implementation.
The thermal-hydraulic model is composed of a cold and hot leg, inlet and outlet plena and fuel channels with their orifice. The Canadian SCWR core is $1/8^{th}$ symmetric hence only 46 channels were represented to obtain the thermal-hydraulic properties of each fuel channel. Each of the 46 average channels in RSM4 was mapped to the corresponding physical location in the PARCS model. Boundary conditions are applied at the inlet of the cold leg (25.8 MPa, 350°C) and outlet of the hot leg (25 MPa) and are assumed constant over a fueling cycle. The hydrodynamic components of the system are depicted in Fig. 4. The moderator system is also modeled as a constant temperature thermal reservoir which receives heat via convection from the outer surface of the pressure tube. More details can be found in [18].

Convective heat transfer from the fuel sheath to the coolant was modeled using the Dittus-Boelter correlation. While this correlation has been proven to poorly predict the heat transfer coefficient in the vicinity of the pseudo-critical point [34, 35, 36], the following points have to be kept in mind:
The Dittus-Boelter correlation performs fairly well away from the pseudo-critical point. Therefore, the heat transfer coefficient is only poorly predicted for approximately 20°C while the coolant undergoes a 275°C temperature change
The transition through the pseudo critical point is located at the bottom of the channel (inlet temperature: 350°C and transition is around 380-400°C). However, the limiting temperatures (cladding and fuel) are located towards the top of the channel and therefore far from the inaccurate region.
The use of the Dittus-Boelter correlation is then deemed acceptable for the current work but more research has to be carried out in order to enhance the accuracy of heat transfer at supercritical conditions as mentioned in the previously referenced studies.

3. Design improvements

3.1 Fuel temperature

The maximum fuel centerline temperature is directly linked to the fuel's power density and the fuel thermal conductivity. While accident tolerant fuels (ATF) would improve the fuel thermal conductivity this option is out-of-scope for the current study [37,38]. To reduce the fuel's power density the reactor power can be lowered or the volume of fuel in the reactor can be increased. The latter implies either increasing the number of fuel channels or the number/size of the fuel pins. The fuel lattice cell has already undertaken several geometrical optimizations [39] and even if the fuel lattice cell geometry could be further optimized in the future, the choice was made to make no further modifications for this work. The diameter of the current reactor vessel (12 m) cannot be increased due to manufacturing limits and as a consequence, the number of channels cannot be increased. Hence while ATF designs and or further geometrical optimization would also lead to lower fuel temperatures this work examines an equivalent reduction in temperature driven by a reduction in core power.

3.2 Axially graded fuel enrichment and burnable poison

The previous Canadian SCWR reactor concepts had uniform fuel enrichment/FIBAs and as a consequence, the axial power distribution of the Canadian SCWR is not optimum. One objective of the present work was to improve the axial power distribution throughout the burnup cycle with a particular focus on how the MCST can be lowered by suppressing power at the outlet of each channel. The 5-meter channel was divided into 3 zones with distinct fuel enrichments and FIBA concentrations as depicted in Fig. 5. Table 4 shows the detailed fuel composition where the plutonium uses the same

isotopic distribution as in Table 1. While further subdivisions of the fuel assembly and finer distinctions in enrichment and FIBAs may provide additional benefit, the segmentation used here was deemed sufficient for demonstrating the impact of axial fuel gradients on MCST.

The equilibrium core with a 3-batch refueling scheme [40] has been evaluated for the Canadian Nuclear Laboratories (CNL) reference concept with a uniform composition and the improved concept with an axially graded fuel enrichment/FIBAs concentration. The equilibrium core for the new axially graded fuel was generated by repeating a fuel cycle simulation and refueling sequence a sufficient number of times such that the nodal burnups are invariant from cycle to cycle (less than 0.1 MW·d/kg change at the beginning of cycle for each subsequent batch cycle). Figure 6 depicts the core-averaged axial power distribution (APD) for the two concepts at BOC, middle of cycle (MOC) and EOC after an equilibrium cycle has been generated. The shape at BOC for the reference case is quite similar to the graded cases since the lower FIBA concentration compensates for the lower fuel enrichment at the top of the core. At MOC, the power increases towards the top of the core as the FIBAs burn out. The FIBAs are exhausted at EOC and the power shifts towards the bottom of the core due to the higher fuel enrichment in the graded case. The APD has also been plotted for the axially graded fuel enrichment/FIBAs concentration using the new 4-batch fueling scheme described in section II.d as the 3-batch one is only used for comparison to the CNL concept. A significant observation for the graded cases examined here is that they typically involve higher peaking factors than the ungraded case, albeit such peaks located away from the channel exit. Such a result is particularly important near the end of cycle conditions where typically MCST are the highest.
Figure 7 shows the evolution of the MCST as a function of time during a fueling cycle for the reference case and the axially graded case. At EOC conditions, the MCST benefits from the strong changes in the core averaged axial profile such that power in the upper portion of the core is reduced.

3.3 Control blade design

SCWR design previously analyzed considered control blades with an approximate reactivity of 60 mk [18]. In order to reduce the impact of blade movements and the subsequent channel power changes across the core, the sensitivity to rod worth on MCST has been investigated in this work. The new design and its specifications can be found in Fig. 3 and Table 1, respectively. The control blades are grouped into 16 banks and inserted from the bottom of the core similar to [18]. The banks maintain the symmetry of the core and their numeration is shown in Fig. 8.

3.4 Refuelling scheme

The coolant mass flow rate is dictated by a static orifice to obtain a coolant outlet temperature of 625°C based upon assumed reference channel powers. Ideally, the channel power should be constant at these reference powers throughout the batch cycle to maintain the 625°C outlet temperature and hence minimize the changes in MCST. However, the channel powers deviate from their reference as the fuel depletes and the neutron poison is consumed as well as from the changes in powers caused by control rod positional changes. These deviations are most significant at BOC and EOC as the channels tend to match relatively closely their reference values at MOC [18]. As a consequence, a shorter cycle length can mitigate these deviations and a 4-batch refueling scheme was adopted to maintain acceptable fuel exit burnup. The refueling scheme used is shown in Fig. 9 and the cycle length decreased from 405 days to 325 days with an average exit burnup of 50 MW·d/kg. The APD of the new equilibrium cycle at BOC, MOC, and EOC is plotted in Fig. 6 using the axially graded fuel enrichment/FIBAs concentration and the 4-batch fueling scheme.

4. Control blade sequence optimization

The final design change involves optimization of the control rod insertion sequence utilizing the lower reactor power, fuel grading, the reduced cycle length and the new fueling scheme. The optimization was performed using DAKOTA's genetic algorithm over a search space of 21 discrete insertion positions for each of the 16 control banks at 17 burnup stages. DAKOTA is developed at Sandia National Laboratories and is a toolkit providing an interface between simulation codes and a wide range of numerical techniques such as optimization methods, uncertainty quantifications, and sensitivity analyses [41]. DAKOTA optimization utilizes the PARCS physics code to calculate the core power distribution and determines the corresponding MCST and MFCLT using multi-dimensional response surfaces based on RSM4 simulations of the reactor thermal-hydraulics. Once the optimum is found, the entire burnup/rod-sequence is re-simulated with a fully coupled 3D PARCS and RSM4 simulation and the results compared to those obtained in the optimization calculations using the thermal-hydraulic response surfaces. Details of the calculations are provided in the following sections.

4.1 Optimization process

4.1.1 Setup

The objective of the optimization is to determine the position of the 16 banks of control rods as a function of time during a fueling cycle that minimizes the MCST and MFCLT throughout the cycle. This optimization process is a multi-step, multi-cycle problem that requires around 10^6 function evaluations. While a PARCS simulation requires less than 2 seconds, RSM4 execution is on the

order of 1 minute making MCST and MFCLT evaluation impractical within the optimization framework. In order to reduce computational overhead, response surfaces were used in the evaluation of the MCST and MFCLT during the optimization process. The response surfaces went through rigorous validation prior to optimization and independent direct RSM4 simulations were performed after the optimization to independently confirm the MCST results. Each response surface has 3 independent inputs:
Channel reference power: imposed by the orifice at the channel's inlet to reach a coolant outlet temperature of 625°C. The higher the channel power the higher the power density and the higher the fuel centerline temperature will be.
Channel power deviation from the reference power: if the power increases from the reference power, the coolant outlet temperature will increase and so will the cladding surface temperature and fuel centerline temperature.
APD: a set of APDs was generated a priori which covers the different shapes that could be encountered.
The response surfaces were constructed using a single-channel model in RSM4 and independently varying each input. The potential for cross correlation between the inputs was also considered. Finally, each surface was validated against a large body of independently generated inputs where both the response surface predictions and RSM4 single channel models results were available. More details can be found in [18].

4.1.2 Genetic algorithm

To find the optimized position of the control blades for each state in the burnup cycle, the optimization process calls a multi-objective genetic algorithm in DAKOTA. The MCST and MFCLT are being minimized while k_{eff} and the maximum linear heat generation rate (MLHGR) are constrained. K_{eff} is maintained between 1 and 1.01 while the MLHGR has to be kept below 40 kW/m. A random initial population of individuals is first generated (1 individual corresponds to a set of positions for each of the control blade banks). For each individual, a PARCS simulation is performed to predict the 3D core power distribution. Channel powers and channel power axial distributions are extracted and the corresponding MCST and MFCLT are determined from the response surfaces. Crossovers and mutations are then applied to the population to try finding a better individual. The best individuals are then kept and the process is repeated until convergence or until the maximum number of evaluations is reached.

4.1.3 Cycle optimization

The optimization starts from the burnup distribution obtained for the beginning of the equilibrium cycle without any control blades inserted. The genetic algorithm is called for day 0 and each control blade bank can assume

an optimized position from fully out to fully inserted[2]. To initiate the genetic algorithm a random set of positions (i.e., a seed) is adopted and the algorithm then searches at that burn-up step for an acceptable solution. Once the optimized positions are found, the core is burned until the next time step within the burn-up cycle. At this point, the optimization is repeated and a new set of positions is determined. The process continues until the end of the fuel cycle is reached at which point the core is refueled by moving and replacing the appropriate assemblies according to the fuel loading pattern described earlier. Since the initial fuel burn-up distribution on day 0 was not based on bundle irradiations using the updated control rod positions, the next fuel cycle and rod positions will differ from the initial optimal values. Therefore the optimization is repeated 3 times to allow for the fueling cycle to reach near equilibrium with consistent control rod movements from batch to batch. Cycle 4 follows the same principle but at each burnup step, new initial rod position seeds may be re-selected if the criteria are not satisfied during the search process. Such resetting of the seed positions is recommended by the DAKOTA developers for large and discontinuous search spaces such as this problem in order to avoid local minimum. The preceding simulation of 4 cycles then provides a near optimal condition. Finally, additional cycles are performed to ensure that a self-consistent set of irradiations and rod positions is determined for an equilibrium cycle. Within these additional cycles, optimization is performed but additional criteria are placed to limit rod movement to within 2 positions from the previous cycle. The combination of additional cycles and small rod movements refines the blade positions and forms a suitable equilibrium core within another 5 to 10 cycle simulations[3].

5. Coupling procedure for steady-state

The preceding section used 3-dimensional neutronic calculations coupled to thermal-hydraulic response surfaces. The use of response surfaces greatly improved the efficiency of the optimization method but introduces additional uncertainties into the calculation stemming from the limited number of inputs and discrete nature of the response surfaces. Earlier SCWR studies pointed out the need for neutron physics/thermal-hydraulics coupling to accurately simulate the SCWR core [31-34]. Therefore, PARCS and RSM4 have been chosen to carry out the coupling. PARCS is widely used to model light water reactors (LWRs) and a SCWR can be seen as a combination of a pressurized water reactor due to the single phase flow and a boiling water reactor because of the large density variation along the fuel assembly. PARCS is also the code that was chosen for the US SCWR neutronic framework [46]. PARCS is then considered a very good candidate for the Canadian SCWR studies. Moreover, PARCS and RELAP5/Mod3.3 have already been coupled and used to evaluate

[2] The control blade moves by steps of 25 cm which allow 20 in-core positions and 1 out-of-the-core position

[3] An addition set of cycles was also performed where rod movement was not constrained to only 20 positions but rather each bank allowed to move ±25 cm from the previous cycles optimum by step of 5 cm.

LWRs response to various transient scenarios [47, 48]. More recently, PARCS was linked to RSM4 through an interface (NIRK3D) and its performance was evaluated against a LWR benchmark case which showed good agreements [49]. However, the interface only allows for a limited number of reactivity feedback dedicated to LWRs studies which is inapplicable for the Canadian SCWR. Finally, RSM4 was also run with a point kinetics model for a wide range of loss-of-coolant accidents (LOCAs). The results showed good agreement for steady-state and transients simulations in comparison with the thermal-hydraulics code CATHENA [50] under development for SCWR studies. PARCS and RSM4 are then promising for SCWR safety analyses and have been coupled through a series of external scripts to provide a fully coupled 3-dimensional power distribution and thermal-hydraulic prediction. The coupled simulations are then used to confirm the accuracy of the response surface predictions.

5.1 Methodology

The coupling process begins from an initial steady-state core physics calculation generated by PARCS. An external script extracts the nodal powers and transfers them to the RSM4 input file at the corresponding thermal-hydraulics node[4]. RSM4 simulations are performed for a set duration and the corresponding nodal temperatures and densities (see section 3.3 for more details) are extracted from the output file. Those thermal-hydraulic conditions are transferred to the PARCS routines which perform the cross-section interpolation for each node. PARCS simulations are performed to obtain an updated power distribution and the process iterates until convergence of the nodal powers and thermal-hydraulic conditions. The coupling process is shown in Fig. 10.

5.2 Reactivity feedback coefficients

The change in cross-sections due to changes in each of the thermal-hydraulic parameters, namely the temperature and density of the coolant in the central flow tube, the temperature and density of the coolant going upwards between the fuel pins and the temperature of the fuel, are determined through separate lattice physics calculations. The feedback from the low-pressure low-temperature moderator fluid is not considered in this work. For the 20 axial positions and for several burnup steps the thermal-hydraulic parameters are independently changed in the SCALE model to a higher and lower value from the reference state at each axial position. Table 5 shows the values used to calculate the first order derivatives (1). The end result of these lattice physics calculations are the estimated first derivatives for each branch calculation at each axial position which can be used with the corresponding changes in local thermal-hydraulics parameters to determine the suitable cross sections (2, 3). The change in cross-section due to the control rod is assumed linear in each

[4] A 1 to 1 nodal mapping is used between PARCS and RSM4

node. Therefore, the variable "c" represents the fraction of the inserted rod in equation (2). The impact of each thermal-hydraulic parameter is also evaluated by a weighted sum of the two partial derivatives relative to the parameter. Based on the notations in equation (2), "x_1" and "x_2" would be the lower and higher value of the parameter, respectively (see Table 5). "x" and "x_{ref}" are the current and reference value thermal-hydraulic parameter, respectively.

$$\frac{\partial \Sigma}{\partial x} = \frac{\Sigma_{branch} - \Sigma_{ref}}{x_{branch} - x_{ref}} \tag{1}$$

$$\Sigma = \Sigma_{ref} + c\frac{\partial \Sigma}{\partial Cr} + \sum_{i=1}^{5}\left[\left(x - x_{ref}\right) \times \left(w_1 \frac{\partial \Sigma}{\partial x_1} + (1 - w_1)\frac{\partial \Sigma}{\partial x_2}\right)\right] \tag{2}$$

Where

$$w_1 = \frac{x - x_2}{x_1 - x_2} \tag{3}$$

The interpolation scheme was verified for each thermal-hydraulic parameter, at two burnups (0.2 and 30.0 MW·d/kg), and at the bottom and top of the assembly (0.125 and 4.875 m). The change in k-infinity was evaluated for multiple values of each thermal-hydraulic parameter with SCALE (exact results) and with the interpolation scheme. The results are shown in figure 11. The legend of figure 11 is made of three variables where the first one is the thermal-hydraulic parameter studied, the second is the fuel burnup, and the last variable can either be "c" for calculated (exact) value or "i" for interpolated value. The black box shows the approximate range of interest for each thermal-hydraulic parameter. From these graphs, the accuracy of the interpolation scheme is considered sufficient to evaluate the variation induced by local thermal-hydraulic changes.

6. Results

The MCST and MFCLT throughout the batch cycle from the surface responses and for the fully coupled 3D reactor physics/ RSM4 calculations are plotted in Fig. 12 and Fig. 13, respectively. Close agreement between the results from the optimization steps and the fully coupled models is observed. The control blade sequence maintains the reactivity effectively throughout the entire cycle (Fig. 14).

While the MCST exceeds the 1123 K (850°C [51]) design limit towards the EOC, the improvement is considerable compared to cases without graded fuel properties, alterations in batch cycle and control blade worth (Fig. 12). While further optimization may be required the duration of the cycle outside of the acceptance criteria, as well as the peak deviation, are significantly improved.

The MFCLT is within the acceptance criteria for the full cycle, largely resulting from the reduction in core power (Fig. 13). Finally, the MLHGR is always far below the limit of 40 kW/m [52] (Fig. 15).

7. Conclusion and discussion

By examining the reference SCWR with reactivity control over an entire fuel cycle it was determined that the limits on fuel and sheath temperatures were not met. The purpose of this work was to evaluate the potential design changes which can further improve the SCWR performance. The core power was first reduced from 2540 MW to 2032 MW to help to reduce the excessively high fuel temperatures. Moreover, the fuel enrichment and the fuel-integrated burnable absorber have been axially graded to lower the power at the top of the core where the MCST tends to occur. The refueling scheme has evolved from 3 to 4 batches to reduce the cycle length while maintaining a similar exit fuel burnup. As a consequence, channel powers deviate less from their reference power. Finally, the reactivity worth of the control blades has been decreased to provide finer bulk and spatial reactivity control.

The control blades' position throughout the batch cycle was evaluated through an optimization process using a multi-objective genetic algorithm. The MCST and MFCLT were the 2 objectives being minimized while the MLHGR had to be kept below 40 kW/m and k_{eff} maintained close to 1. The optimization used PARCS and a multidimensional thermal-hydraulic response surface. The results obtained with the optimization were verified with coupled reactor physics/thermal-hydraulics calculations. A comparison of the methodologies used in the optimization process and the fully coupled models showed the MCST is within 10°C, the MFCLT within 100°C, the MLHGR within 2 kW/m and k_{eff} are comparable.

The change in fuel lattice cell k-infinity, or reactivity, was evaluated for the five main thermal-hydraulic parameters over their range of variation. This study was carried out at two fuel burnups at the bottom and top of the core. As the interpolation scheme in PARCS only uses a lower and upper value from the reference condition to evaluate the cross-sections at any thermal-hydraulic conditions, discrepancies are expected to arise from the interpolation. The interpolation technique was, however, proven to perform very well, especially close to the reference conditions for the steady-state. Even though larger discrepancies can be observed further away from the reference conditions, the interpolation scheme reproduces the reactivity change fairly well. Transient scenarios could, therefore, be simulated with a similar branch structure. More branches could enhance the results and reduce the uncertainties generated through cross-sections interpolation, however.

In terms of the design changes significant improvements were obtained, although some deviation from the limits may require further fuel or core optimization. The MFCLT is within limits over the entire cycle due to the lower core power. While the reduction in power is significant, the use of advanced fuel materials such as those being considered as accident tolerant fuels, may restore acceptable centerline temperatures at higher power levels. The changes in batch cycle, rod worth, fuel profiling and rod optimization

produce maximum cladding temperatures which are below acceptable limits for 2/3 of the fuel cycle and with a maximum deviation from the allowable value of 40°C. While the burnable absorber and enrichment grading was selected based on existing SCWR concepts from other jurisdictions, optimization of such values could potentially lower the cladding temperatures to within acceptable values. In the end, this work strengthens the viability of this Canadian SCWR design which is expected to meet the safety requirements with further design refinements. It has to be noted that the code validation for SCWR simulations is still an ongoing area of research and since the cladding and fuel temperature limits do not account for the uncertainties in code predictions (for instance heat transfer coefficients), such optimization studies need to focus on achieving clad and fuel temperature low enough to accommodate these uncertainties.

Acknowledgements
This work was funded by Natural Resources Canada (NRCAN) through the office of Energy Research and Development, Canadian Nuclear Laboratories (CNL) and Natural Sciences and Engineering Research Council of Canada (NSERC). The authors are also very grateful to Innovative System Software (ISS) for providing the software and support for RSM4.

Nomenclature

Acronyms and Abbreviations

APD	Axial Power Distribution
ATF	Accident Tolerant Fuel
BOC	Beginning Of Cycle
BWR	Boiling water Reactor
CNL	Canadian Nuclear Laboratories
EOC	End Of Cycle
FIBA	Fuel-Integrated Burnable Absorber
HERC	High-Efficiency Re-entrant Channel
K_{eff}	Effective multiplication constant
LOCA	Loss Of Coolant Accident
LWR	Light Water Reactor
MCST	Maximum cladding Surface Temperature
MFCLT	Maximum Fuel Centerline Temperature
MLGHR	Maximum Linear Heat Generation Rate
MOC	Middle Of Cycle
NIST	National Institute of Standards and Technology
RSM4	RELAP5/SCDAPSIM/MOD4.0
SCWR	SuperCritical Water-cooled Reactor

Greek Letters

Σ	Nuclear cross-section

Subscripts and Superscripts

ref	Reference
branch	Thermal-hydraulic branch

References

[1] Leung, L. K. H., Yetisir, M., Diamond, W., Martin, D., Pencer, J., Hyland, B., Hamilton, H., Guzonas, D., and Duffey, R., 2011, "A Next Generation Heavy Water Nuclear Reactor with Supercritical Water as Coolant", International Conference on Future of Heavy Water Reactors, Ottawa, Canada.

[2] Pencer, J., Bromley, B., and Nava-Dominguez, A., 2012, "Fuel Channel Assembly and Fuel Bundle for a Nuclear Reactor", Canadian Patent CA 2881784 A1, June 13.

[3] Hummel, D. W., and Novog, D. R., 2016, "Coupled 3D neutron kinetics and thermalhydraulics characteristics of the Canadian supercritical water reactor", Nucl. Eng. Des. 298, pp. 78-89

[4] Wu, J., and Oka, Y., 2014, "Improved single pass core design for high temperature Super LWR", Nucl. Eng. Des. 267, pp.100-108.

[5] Monti, L., Starflinger, J., and Schulenberg, T., 2011, "Development of a coupled neutronic/thermal-hydraulic tool with multi-scale capabilities and applications to HPLWR core analysis", Nucl. Eng. Des. 241, pp.1579-1591.

[6] Schulenberg, T., Starflinger, J., Marsault, P., Bitterman, D., Maraczy, C., Laurien, E., Lycklama a Nijeholt, J.A., Anglart, H., Andreani, M., Ruzickova, M., and Toivonen, A., 2011, "European supercritical water cooled reactor", Nucl. Eng. Des. 241, pp.3505-3513.

[7] Liu, Q., and Oka, Y., 2014, "Improvements of two-pass core design for super fast reactor", Annals of Nuclear Energy 69, pp.108-115.

[8] Reiss, T., Csom, Gy., Fehér, S., and Czifrus, Sz., 2010, "The Simplified Supercritical Water-Cooled Reactor (SSCWR), a new design", Progress in Nuclear Energy 52, p.177-189.

[9] Sakurai, S., Yamada, K., Higuchi, S., Ishiwatari, Y., Xiong, Z., and Kito, K., 2011, "Japanese SCWR fuel and core design study", The 5th International Symposium on Supercritical Water-cooled Reactors (ISSCWR-5), Vancouver, British Columbia, Canada, March 13-16.

[10] Liu, X.J., and Cheng, X., 2010, "Coupled thermal-hydraulics and neutron-physics analysis of SCWR with mixed spectrum core", Progress in Nuclear Energy 52, pp.640-647.

[11] Wu, J., and Oka, Y., 2014, "Improved single pass core design for high temperature Super LWR", Nucl. Eng. Des. 267, pp. 100-108

[12] Li, H., Yang, J., Fu, X., Lu, D., Wang, F., Zhang, J., and Zhang, Y., 2013, "Research and Development of Supercritical Water-cooled Reactor in CGNPC", The 6th International Symposium on Supercritical Water-cooled Reactors (ISSCWR-6), Shenzhen, Guangdong, China, March 03-07.

[13] Bae, Y., Jang, J., Kim, H., Yoon, H., Kand, H., and Bae, K., 2007, "Research activities on a supercritical pressure water reactor in Korea", Nuclear Engineering and Technology, 39 (4).

[14] Schulenberg, T., Starflinger, J., and Heinecke, J., 2008, "Three pass core design proposal for a high performance light water reactor", Progress in Nuclear Energy 50, pp. 526-531.

[15] McDonald, M., Colton, A., and Pencer, J., 2015, "Power flattening and reactivity suppression strategies for the Canadian Supercritical Water Reactor concept", 35th Annual Conference of the Canadian Nuclear Society, Saint John, New Brunswick, Canada, May 31 – June 3.

[16] Ahmad, A., Cao, L., and Wu, H., 2014, "Coupled analysis and improvements for Canadian-SCWR core design", Nucl. Eng. Des. 268, pp.104-112.

[17] Hummel, D.W., and. Novog, D.R, 2014, "Optimized channel inlet orifice sizing for the pressure tube type supercritical water-cooled reactor", The 19th Pacific Basin Nuclear Conference (PBNC), Vancouver, British Columbia, Canada

[18] Salaun, F., and Novog, D.R., 2016, "Spatial and bulk reactivity systems design and optimization for the Canadian Supercritical Water Reactor", Canadian Nuclear Laboratories Nuclear Review, 5(2), pp. 285-298

[19] Oak Ridge National Laboratory, 2011, SCALE: A comprehensive modeling and simulation suite for nuclear safety analysis and design, ORNL/TM-2005/39 Version 6.1

[20] Downar, T., Xu, Y., and Seker, V., 2013, PARCS v3.0 U.S. NRC Core Neutronics Simulator, USER MANUAL draft (05/29/2013).

[21] Ward, A., Xu, Y., and Downar, T., 2013, GenPMAXS – v6.1.2dev, Code for Generating the PARCS Cross Section Interface File PMAX

[22] Allison, C. M., and Hohorst, J.K., 2010, "Role of RELAP5/SCDAPSIM in Nuclear Safety", Science and Technology of Nuclear Installations, Volume 2010, Article ID 425658.

[23] Sharpe, J.R., Salaun, F., Hummel, D.W., Moghrabi, A., Nowak, M., Pencer, J., Novog, D.R., and Buijs, A., 2015, "A Benchmark Comparison of the Canadian Supercritical Water-cooled Reactor (SCWR) 64-element Fuel Lattice Cell Parameters using Various computer Codes", 35th Annual Conference of the Canadian Nuclear Society, Saint John, New-Brunswick, Canada

[24] Hummel, D.W., 2015, "Transient neutronic-thermalhydraulic coupling in a PT_SCWR", Ph.D. dissertation, McMaster University, Hamilton, Ontario, Canada.

[25] Moghrabi, A., and Novog, D.R., 2017, "Optimization approach of energy group structure for the Canadian pressure tube supercritical water reactor", 37th Annual Conference of the Canadian Nuclear Society, Niagara Falls, Ontario, Canada.

[26] Moghrabi, A., and Novog, D.R., 2016, "Investigation of reactor physics phenomena in the Canadian Supercritical-water reactor", Canadian Nuclear Laboratories Nuclear Review, 5(2), pp. 253-268

[27] Salaun, F., Hummel, D.W., and Novog, D.R., 2014, "The Impact of the Radial Reflector on the 8-group Cell-Averaged Cross-Sections for the SCWR 62-element Lattice Cell, Canada-China Conference on Advanced Reactor Development (CCCARD-2014), Niagara Falls, Ontario, Canada.

[28] Shen, W., 2012, "Assessment of the traditional neutron-diffusion core-analysis method for the analysis of the Super Critical Water Reactor", Annals of Nuclear Energy, (45), pp.1-7.

[29] USNRC Relap5/Mod3.32 Code Manual, Volumes I to VIII. NUREG/CR-5535/Rev 1, 2001

[30] USNRC SCDAP/RELAP5/MOD3.2 Code Manual, NUREG/CR6150, INEL-96/0422, July 1998

[31] Allison, C.M., Wagner, R.J., Hohorst, J.K., Perez-Ferragut, M., Martinez-Quiroga, V., Freixa, J., Mas de les Valls, E., Fu, Z., Lin, H-C., and Lou, M.,2016, "The development of RELAP/SCDAPSIM/MOD4.0 for fluid systems design analysis", NUTHOS-11: The 11th International Topical Meeting on Nuclear Reactor Hydraulics, Operation and Safety, Gyeongju, Korea

[32] Lou, C., 2016, "Loss of coolant accident simulation for the Canadian supercritical water-cooled reactor using RELAP5/MOD4", Master dissertation, McMaster University, Hamilton, Ontario, Canada.

[33] The international Association for Properties of Water and Steam, Release on the IAPWS Formulation 2011 for the Thermal Conductivity of Ordinary water Substance, September 2011

[34] Mokry, S., Pioro, I., Kirillov, P., and Gospodinov, Y., 2010, "Supercritical-water heat transfer in a vertical bare tube", Nucl. Eng. Des. 240, pp.568-576

[35] Pioro, I. L., Khartabil, H. F., and Duffey, R. B., 2004, "Heat transfer to supercritical fluids flowing in channels – empirical correlations (survey)", Nucl. Eng. Des. 230, pp.69-91

[36] Cheng, X., and Schulenberg, T., 2001, "Heat transfer at supercritical pressures – Literature review and application to an HPLWR", Institut fur Kern und Energietechnik, Programm Nukleare Sicherheitsforschung, Forschungszentrum Karlsruhe GmbH, Karlhube

[37] Ammirabile, L., 2010, "Studies on supercritical water fuel assemblies using the sub-channel code COBRA-EN", Nucl. Eng. Des. 240(10), pp. 3087-3094

[38] Chaudri, K., Tian, W., Su, Y., Zhao, H., Zhu, D., Su, G., and Qiu, S., 2013, "Coupled analysis for a new fuel design using UN and UC for SCWR", Progress in Nuclear Energy 63, pp. 57-65.

[39] Pencer, J., and Colton, A., 2013, "Progression of the Lattice Physics Concept for the Canadian Supercritical Water Reactor", 34th Annual Conference of the Canadian Nuclear Society, Toronto, Ontario, Canada.

[40] Pencer, J., Watts, D., Colton, A., Wang, X., Blomeley, L., Anghel, V., and Yue, S., 2013, "Core neutronics for the Canadian SCWR Conceptual Design", The 6th International Symposium on Supercritical Water-Cooled Reactors (ISSCWR-6), Shenzhen, China.

[41] Dakota, A Multilevel Parallel Object-Oriented Framework for Design Optimization, Parameter Estimation, Uncertainty Quantification and Sensitivity Analysis, Version 5.4 Reference Manual released December 2009 and updated November 2013, Sandia National Laboratories.

[42] Adouki, P., and Marleau, G., 2012, "Neutronics/Thermalhydraulics coupling in a CANDU SCWR", The 3rd China-Canada Joint Workshop on Supercritical Water-Cooled Reactors, CCSC-2012, Xian, China.

[43] Waata, C., Schulenberg, T., cheng, X., and Laurien, E., 2005, "Coupling of MCNP with a subchannel code for analysis of a HPLWR fuel assembly", NURETH-11, Avignon, France (paper 021).

[44] Chaudri, K., Su, Y., Chen, R., Tian, W., Su, G. and Qiu, S., 2012, "Development of sub-channel code SACoS and its application in coupled neutronics/thermal-hydraulics system for SCWR", Annals of Nuclear Energy 45, pp.37-45.

[45] Monti, L., and Schulenberg, T., 2009, "Coupled ERANOS/TRACE system for HPLWR 3 pass core analyses", International Conference on Mathematics, Computational Methods & Reactor Physics (M&C), New-York, USA.

[46] Hu, P., and Wilson, P., 2014, "Code Development in coupled PARCS-RELAP5 for SCWR', Science and Technology of Nuclear Installations, Volume 2014, Article ID 286434

[47] Miro, R., Verdu, G., Soler, A., Gomez, A., Ortego, A., and Martinez-Murillo, J.C., 2008, "Analysis of a rod withdrawal in a PWR core with the neutronic-thermalhydraulic coupled code RELAP/PARCS", International Conference on the Physics of Reactors 2008 (PHYSOR 08), Interlaken, Switzerland

[48] Vedivi, J., Bousbia Salah, A., Ivanov, K., Galassi, G.M., and D'Auria, F., 2002, "OECD/NRC BWR turbine trip benchmark: analysis and sensitivity studies of exercise 2 using RELAP/PARCS", Transaction of the American Nuclear Society

[49] Martinez-Quiroga, V., Allison, C. M., Wagner, R.J., Aydogan, F., and Akbas, S., 2016, "NIRK3D and 3DKIN: General description and current status of the new 3D kinetics capabilities of RELAP5/SCDAPSIM/MOD4.0", NUTHOS-11: The 11th International Topical Meeting on Nuclear Reactor Hydraulics, Operation and Safety, Gyeongju, Korea

[50] Wang, D.F., and Wang, S., 2013, "A preliminary CATHENA thermalhydraulic model of the Canadian SCWR for safety analysis", CNL Nuclear Review 3(01), pp. 9-16

[51] Xu, S., and Amirkhiz, S., 2016, "Mechanical Properties of Fuel Cladding Candidate Alloys for Canadian SCWR Concept", Journal of the Minerals, metals, and Materials society, 68(2), pp. 469-474

[52] McDonald, M. H., Hyland, B., Hamilton, H., Leung, L. K. H., Onder, N., Pencer, J., and Xu, R., 2011, "Pre-conceptual Fuel Design Concepts For The Canadian Super Critical Water-cooled Reactor", The 5th

International Symposium on Supercritical Water-Cooled Reactors (ISSCWR-5), Vancouver, Canada.

List of Figures

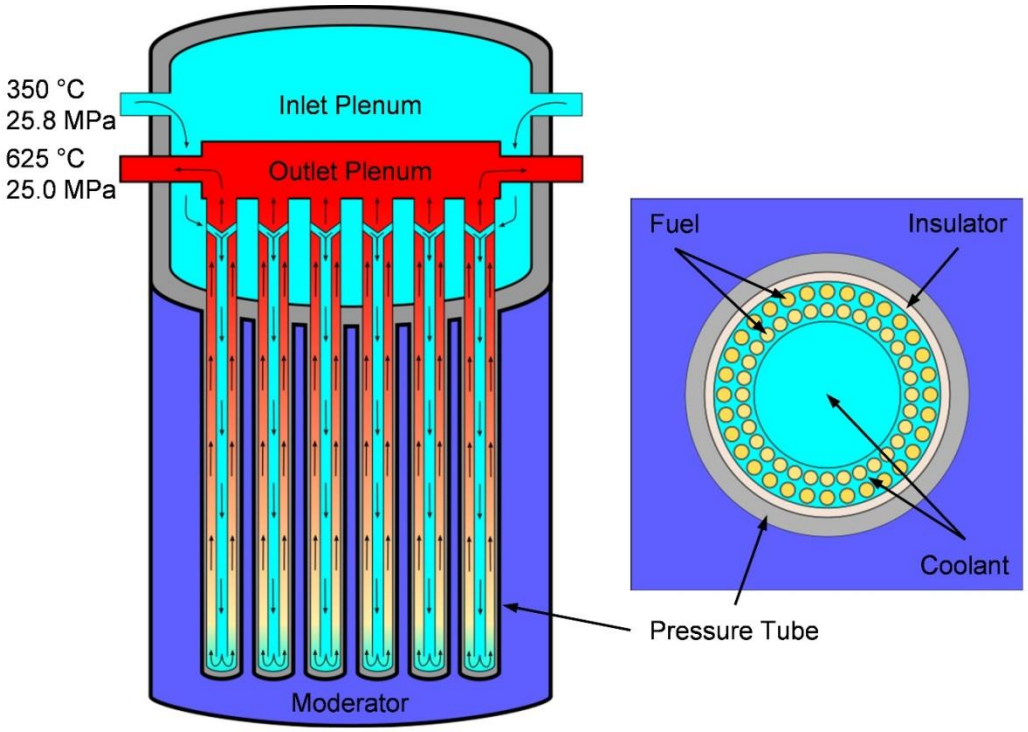

Figure 1 Canadian SCWR core and HERC concept

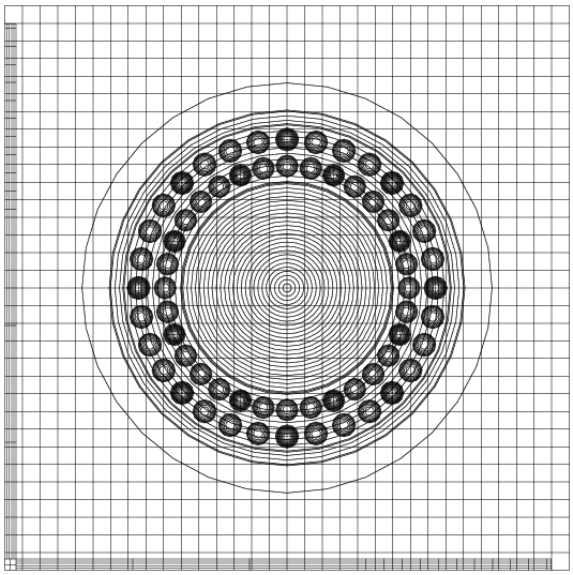

Figure 2 Meshing of the fuel lattice cell

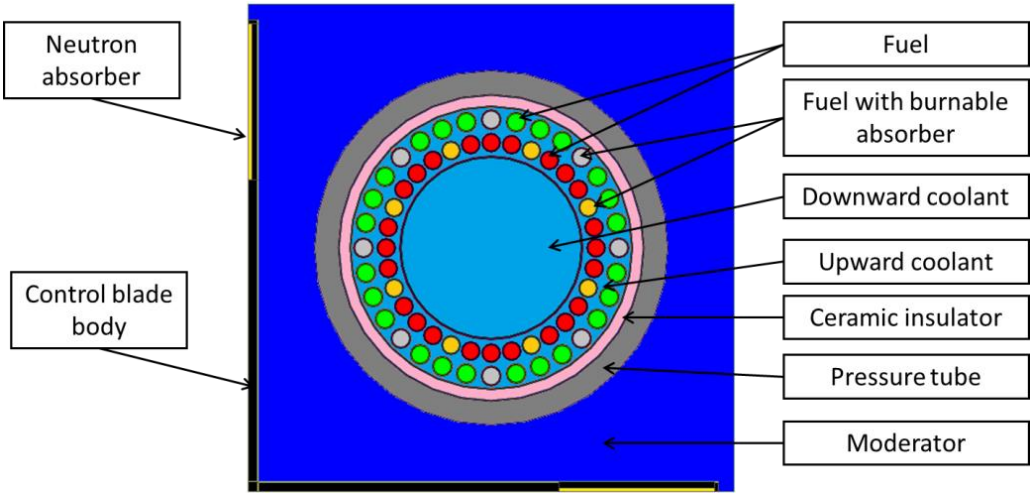

Figure 3 Fuel lattice concept with the control blade inserted

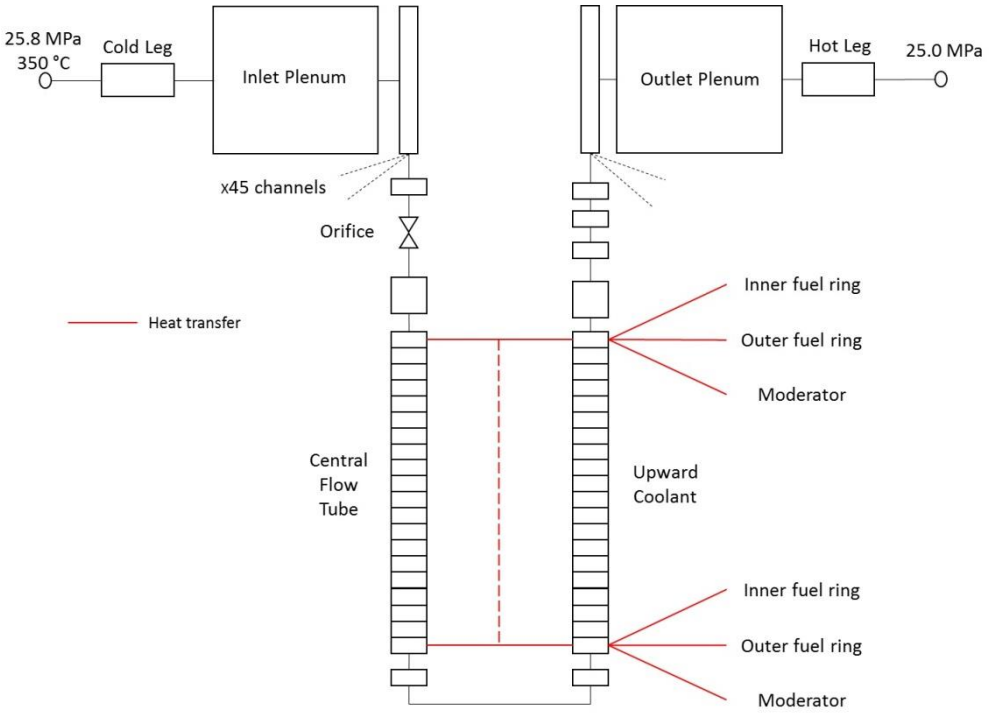

Figure 4 RELAP/SCDAPSIM/MOD4 model

Channel	Number of nodes	Burnable absorber (in wt% in (Pu,Th)O2)	Fuel enrichment Inner ring (wt%)	Fuel enrichment Outer ring (wt%)
Top 1 m	4	2	11.5	9.2
1 m	4	2	12.3	9.84
3 m Bot	12	3	12.8	10.24

Figure 5 Fuel enrichment and burnable absorber concentration along the fuel channel

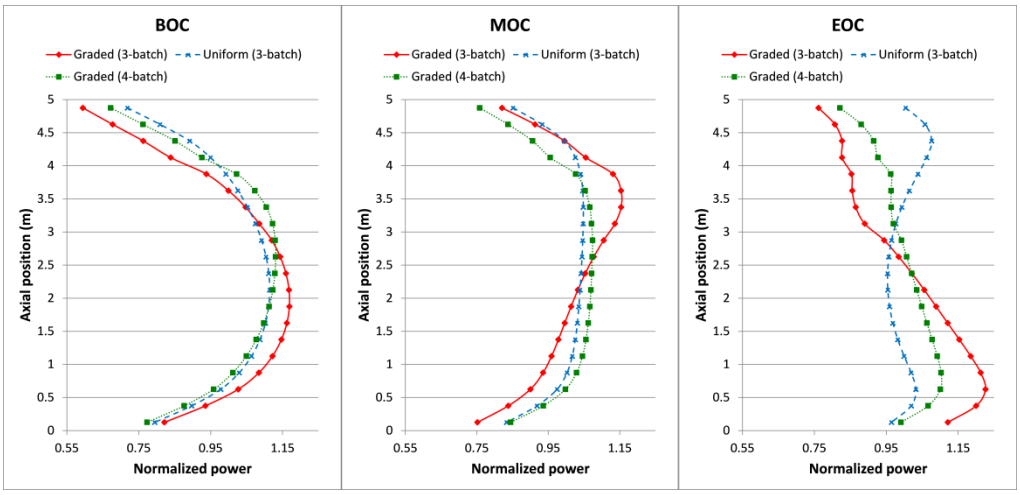

Figure 6 Core-averaged axial power distribution at BOC, MOC, and EOC

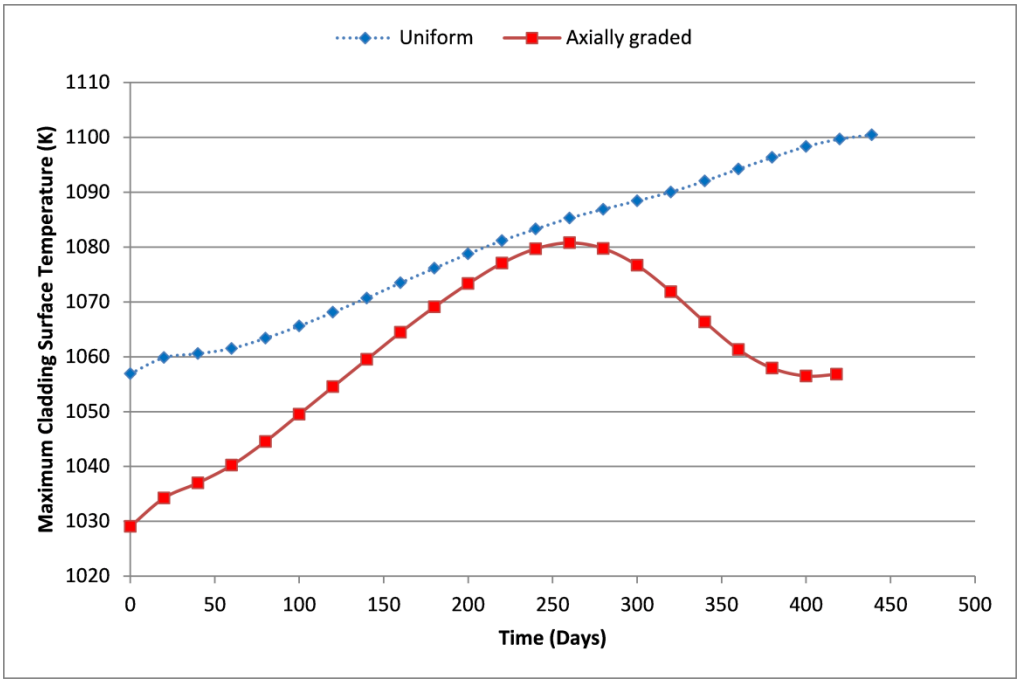

Figure 7 Improvement of the MCST over the equilibrium cycle without control blades

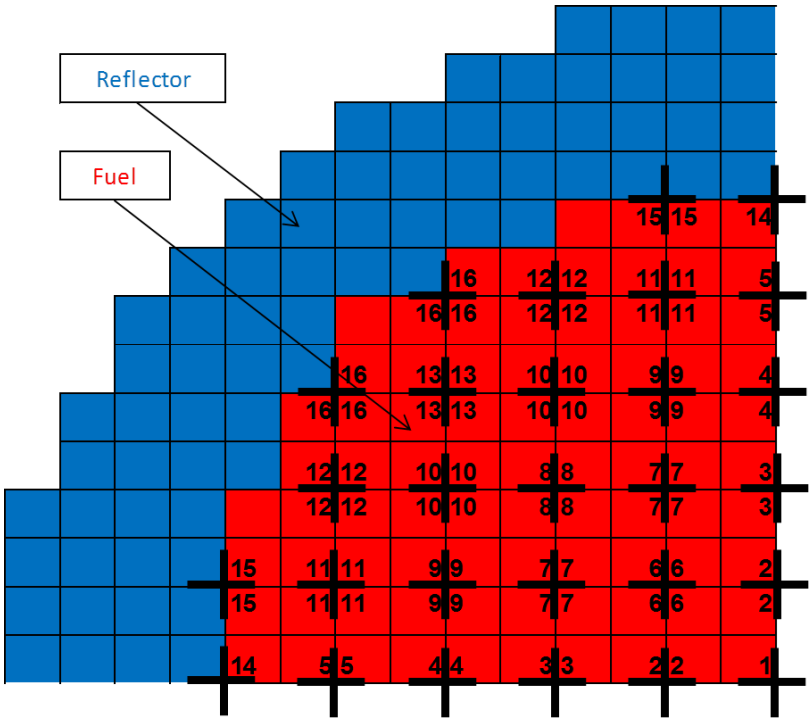

Figure 8 Control blade banks numeration

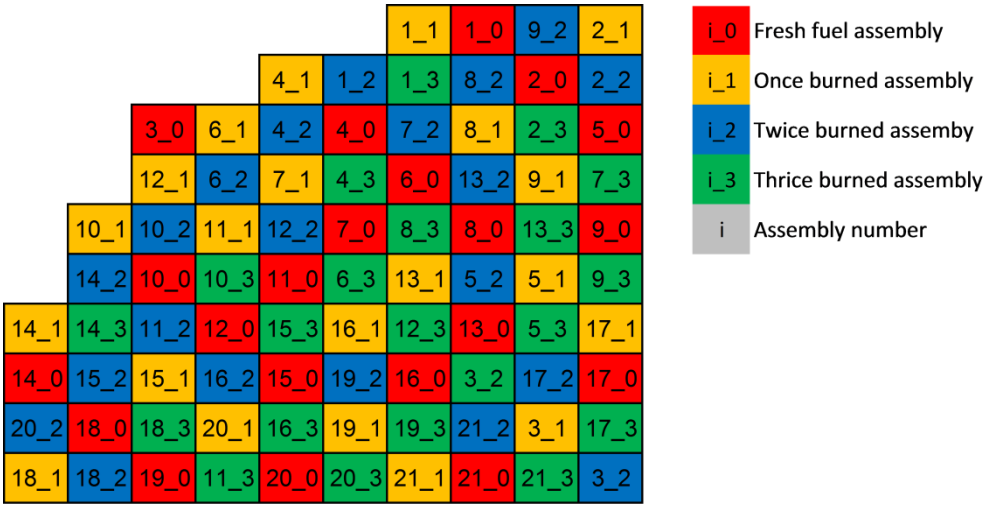

Figure 9 4-batch refueling scheme

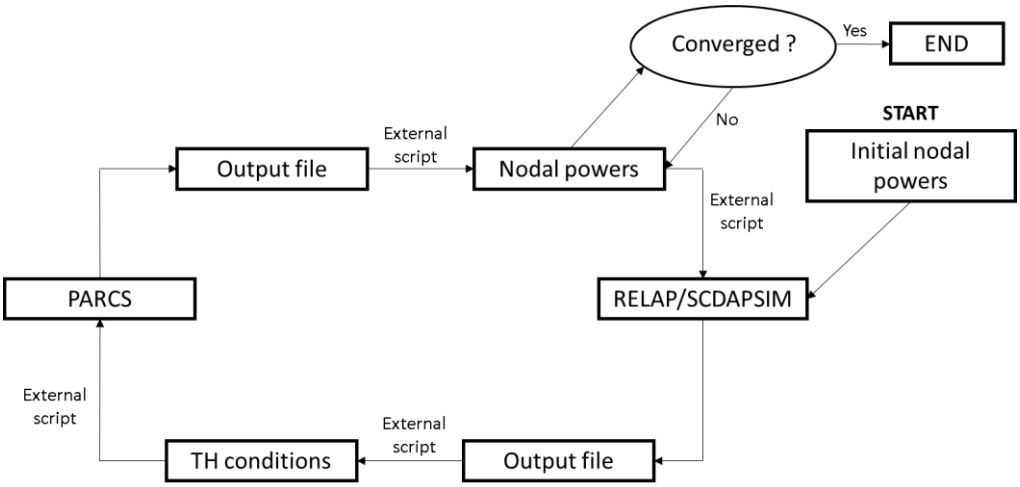

Figure 10 Neutronics/Thermal-hydraulics coupling process

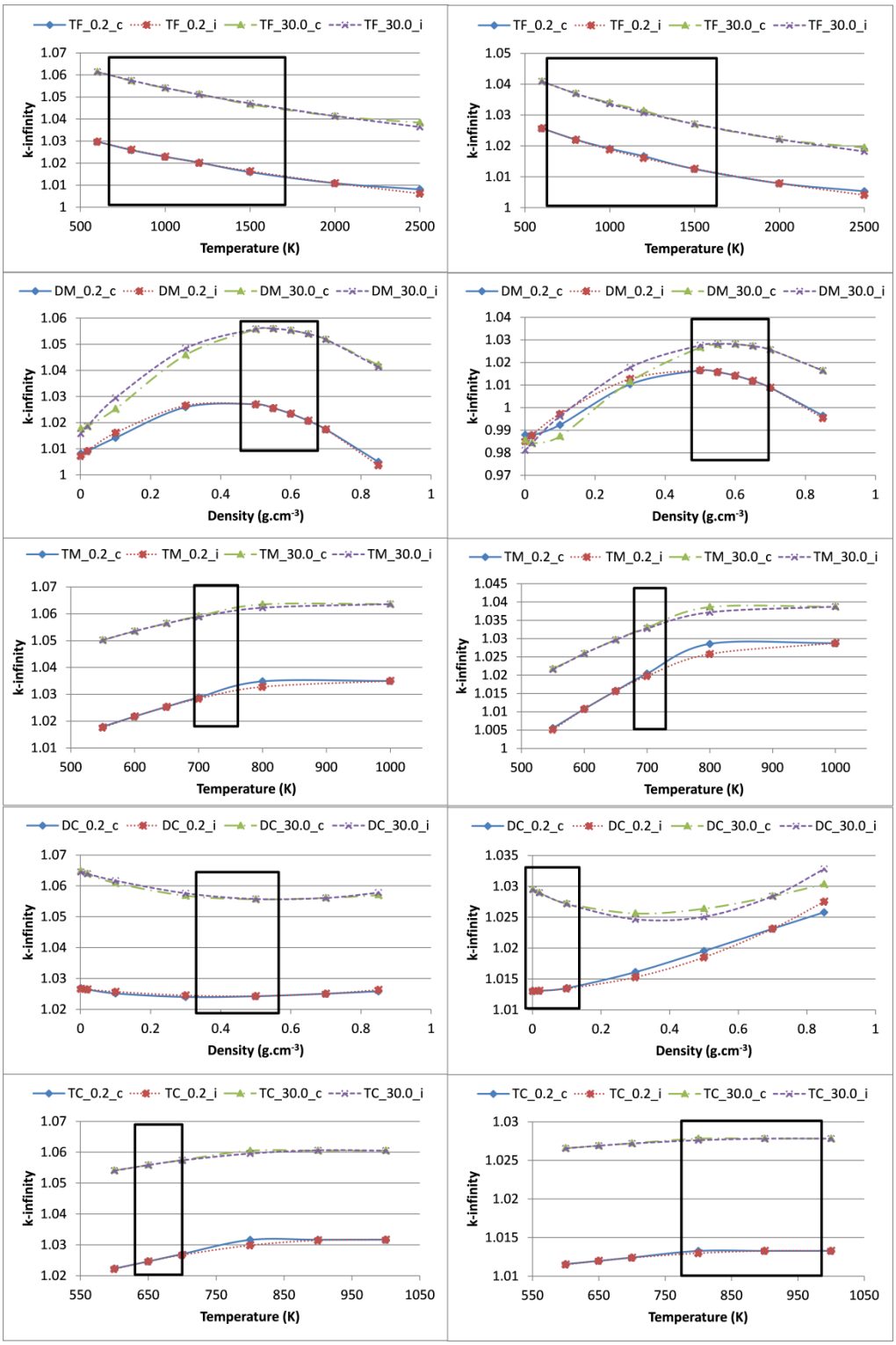

Figure 11 Impact of the variation of the thermal-hydraulic parameters and validation of the interpolation scheme at the bottom (left) and top (right) of the core

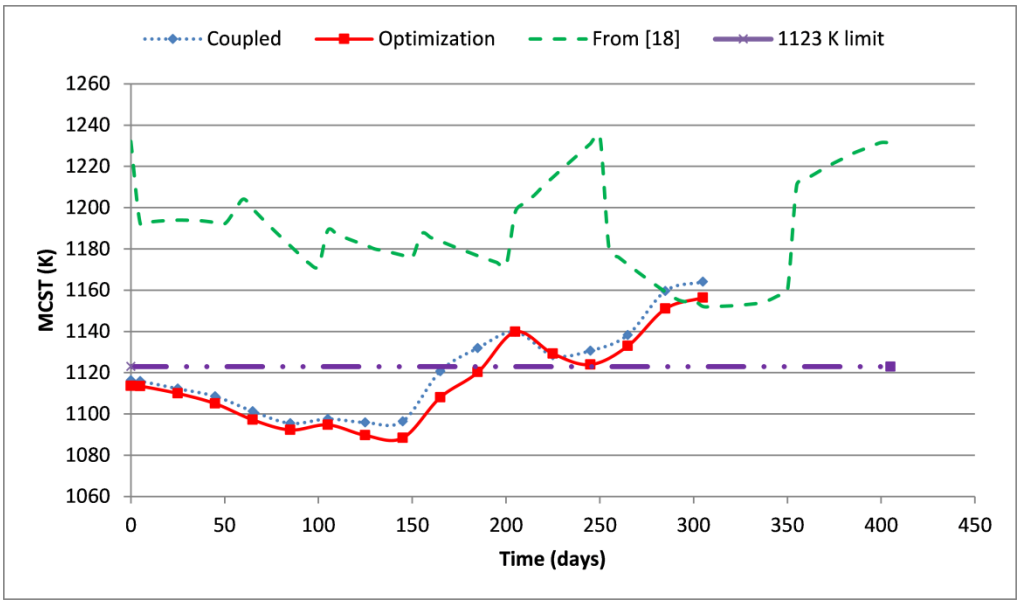

Figure 12 Improved MCST throughout the batch cycle

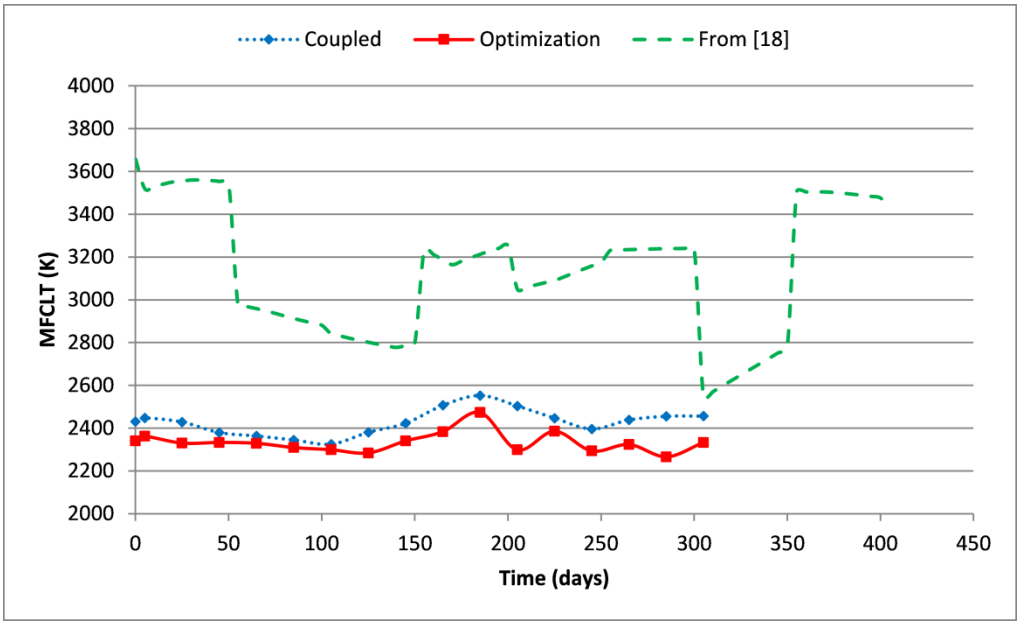

Figure 13 Improved MFCLT throughout the batch cycle

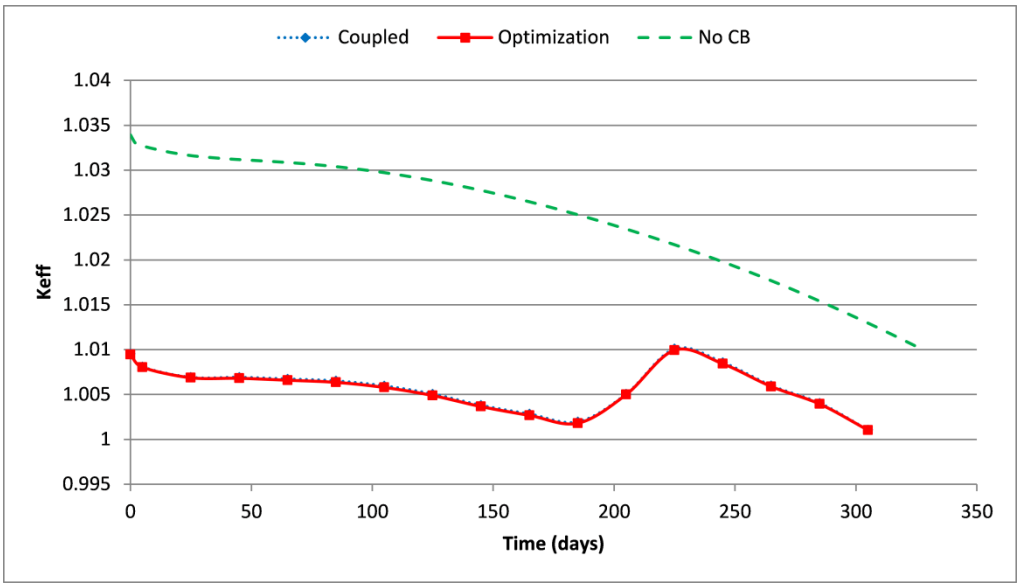

Figure 14 k_{eff} during the batch cycle before and after the insertion of the control blades

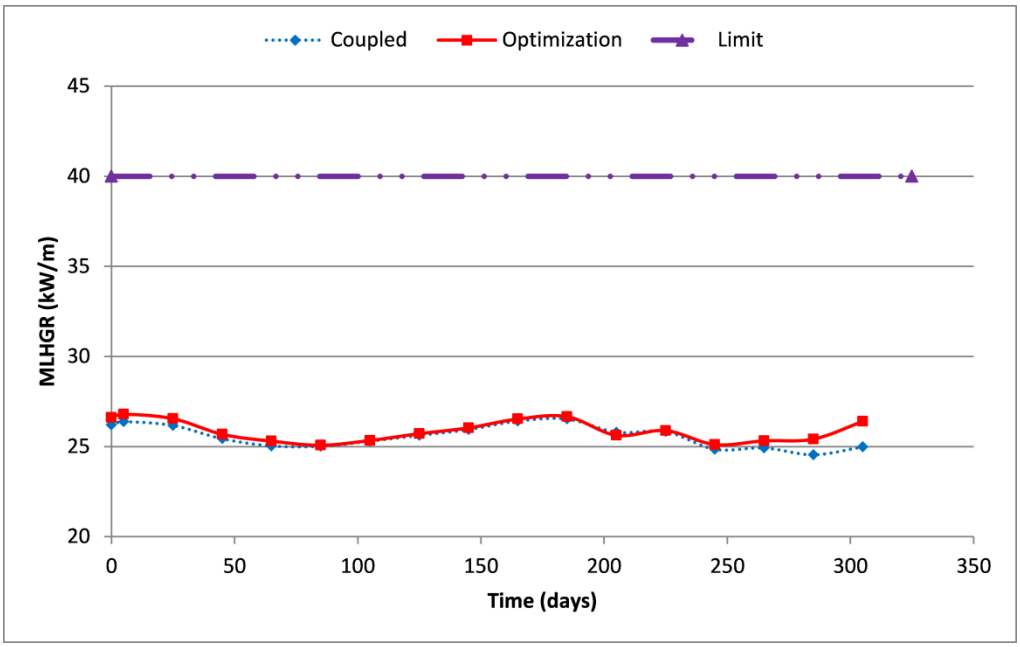

Figure 15 MLHGR over the batch cycle

List of Tables

Table 1 Geometry and materials specifications

Component	Dimension	Material	Composition [wt%]	Density [g.cm^{-3}]
Centre Tube Coolant	4.6 cm radius	Light Water	100% H2O	Variable
Centre Flow Tube	4.60 cm inner radius ; 0.1 cm thick	Zr-modified 310 Stainless Steel	C: 0.034; Si: 0.51; Mn: 0.74; P: 0.016; S: 0.002; Ni: 20.82; Cr: 25.04; Fe: 51.738; Mo: 0.51; Zr: 0.59	7.9
Inner Fuel Pins (24)	0.415 cm radius; 5.4 cm pitch radius	0-3m | 12.8 wt% PuO_2 in ThO_2	Pu: 11.293; Th: 76.632; O: 12.075	9.91
		3-4m | 12.3 wt% PuO_2 in ThO_2	Pu: 10.851; Th: 77.072; O: 12.077	
		4-5m | 11.5 wt% PuO_2 in ThO_2	Pu: 10.146; Th: 77.775; O: 12.079	
Outer Fuel Pins (24)	0.44 cm radius; 6.575 cm pitch radius	0-3m | 10.24 wt% PuO_2 in ThO_2	Pu: 9.034; Th: 78.882; O: 12.084	9.87
		3-4m | 9.84 wt% PuO_2 in ThO_2	Pu: 8.682; Th: 79.233; O: 12.085	
		4-5m | 9.20 wt% PuO_2 in ThO_2	Pu: 8.117; Th: 79.796; O: 12.087	
Inner Fuel Pins with burnable absorber (8)	0.415 cm radius; 5.4 cm pitch radius (evenly spaced, π/8 angular offset)	0-3m | 12.8 wt% PuO_2 in ThO_2 ; 3 wt% Gd_2O_3 in PuO_2/ThO_2	Pu: 10.954; Th: 74.333; O: 12.11 ; Gd: 2.603	9.82
		3-4m | 12.3 wt% PuO_2 in ThO_2 ; 2 wt% Gd_2O_3 in PuO_2/ThO_2	Pu: 10.635; Th: 75.53; O: 12.10 ; Gd: 1.735	9.85
		4-5m | 11.5 wt% PuO_2 in ThO_2 ; 2 wt% Gd_2O_3 in PuO_2/ThO_2	Pu: 9.943; Th: 76.219; O: 12.103 ; Gd: 1.735	9.85
Outer Fuel Pins with burnable absorber (8)	0.44 cm radius; 6.575 cm pitch radius (evenly spaced, no angular offset)	0-3m | 10.24 wt% PuO_2 in ThO_2 ; 3 wt% Gd_2O_3 in PuO_2/ThO_2	Pu: 8.764; Th: 76.515; O: 12.118 ; Gd: 2.603	9.79
		3-4m | 9.84 wt% PuO_2 in ThO_2 ; 2 wt% Gd_2O_3 in PuO_2/ThO_2	Pu: 8.508; Th: 77.649; O: 12.108 ; Gd: 1.735	9.81
		4-5m | 9.20 wt% PuO_2 in ThO_2 ; 2 wt% Gd_2O_3 in PuO_2/ThO_2	Pu: 7.955; Th: 78.20; O: 12.11 ; Gd: 1.735	9.81
Cladding	0.06 cm thick	Zr-modified 310 Stainless Steel	As above	7.9
Coolant		Light Water	100% H2O	Variable
Liner Tube	7.2 cm inner radius; 0.05 cm thick	Zr-modified 310 Stainless Steel	As above	7.9
Insulator	7.25 cm inner radius; 0.55 cm thick	Yttria Stabilized Zirconia	Zr: 66.63; Y: 7.87; O: 25.5	5.37
Outer Liner Tube	7.8 cm inner radius; 0.05 cm thick	Excel Alloy	Sn: 3.5; Mo: 0.8; Nb: 0.8; Zr 94.9	6.52
Pressure Tube	7.85 cm inner radius; 1.2 cm thick	Excel Alloy	Sn: 3.5; Mo: 0.8; Nb: 0.8; Zr 94.9	6.52
Moderator	25 cm square lattice pitch	Heavy Water	99.833 D2O; 0.167 H2O	1.0851
Plutonium Isotopics		Reactor Grade Plutonium	Pu238: 2.75; Pu239: 51.96; Pu240: 22.96; Pu241: 15.23; Pu242: 7.10	
Control blade body	Span 48.4 cm ; Thickness 1cm ;	Excel Alloy	Sn:3.5; Mo:0.8; Nb:0.8; Zr:94.9	6.52
Control blade absorber	Position on the blade's arm: 16-24 cm ; Thickness 0.8 cm	Stainless Steel 304		7.94

Table 2 Materials' local averaged temperature and density as function of the axial position

Position (mm)	Upward Coolant Density	Upward Coolant Temperature	Cladding Temperature	Liner Temperature	Insulator Temperature
4875	0.068	898.22	1027.86	868.77	678.8
4625	0.071	874.76	1015.29	846.94	665.38
4375	0.074	849.19	995.6	822.77	650.51
4125	0.079	822.58	969.5	797.8	635.14
3875	0.084	796.23	940.27	773.34	620.04
3625	0.091	771.03	909.17	750.17	605.84
3375	0.099	747.67	877.38	729	592.8
3125	0.108	726.72	845.01	710.29	581.2
2875	0.119	708.63	813.5	694.45	571.33
2625	0.133	693.64	783.8	681.62	563.33
2375	0.149	681.79	756.3	671.8	557.17
2125	0.170	672.97	732.66	664.82	552.79
1875	0.195	666.8	712.63	660.28	549.94
1625	0.226	662.8	696.7	657.67	548.31
1375	0.263	660.35	685.4	656.27	547.43
1125	0.309	658.78	678.51	655.37	546.87
875	0.364	657.34	679.99	653.71	545.82
625	0.424	655.07	684.69	650.74	543.96
375	0.483	650.88	689.28	645.52	540.68
125	0.536	644.19	684.35	637.83	535.83

Table 3 Materials' local averaged temperature and density as function of the axial position (cont'd)

Position (mm)	Pressure Tube Temperature (K)	Downward Coolant Temperature (K)	Downward Coolant Density ($kg.m^{-3}$)	Fuel Temperature (K)	Center Tube Temperature (K)
4875	454	625	621.1	1437	761
4625	450	626	615.6	1443	751
4375	446	628	610.5	1437	738
4125	441	629	606.0	1410	726
3875	436	630	602.1	1371	713
3625	432	631	598.6	1328	701
3375	428	632	595.6	1284	690
3125	424	632	593.1	1242	680
2875	421	633	590.9	1200	671
2625	419	633	589.1	1159	664
2375	417	634	587.6	1120	658
2125	415	634	586.2	1083	654
1875	414	634	585.1	1053	651
1625	414	635	584.0	1033	649
1375	414	635	582.9	1017	648
1125	413	635	582.0	1006	647
875	413	635	581.1	995	646
625	412	636	580.3	976	645
375	411	636	579.7	947	643
125	410	636	579.4	907	640

Table 4 Fuel composition before and after design changes

	Uniform				Axially graded			
	Fuel		Fuel with burnable absorber		Fuel		Fuel with burnable absorber	
	Inner ring	Outer ring	Inner ring	Outer ring	Inner ring	Outer ring	Inner ring	Outer ring
4-5m	Pu: 13.23; Th:74.70; O: 12.07	Pu: 10.59; Th:77.34; O: 12.08	Pu: 12.836; Th:72.458; O: 12.103; Gd:2.603	Pu: 10.269; Th:75.015; O: 12.113; Gd:2.603	Pu: 10.146 ; Th:77.775; O: 12.079	Pu: 8.117 ; Th:79.796; O: 12.087	Pu: 9.943 ; Th:76.219; O: 12.103; Gd:1.735	Pu: 7.955 ; Th:78.20; O: 12.11; Gd:1.735
3-4m					Pu: 10.851 ; Th:77.072; O: 12.077	Pu: 8.682 ; Th:79.233; O: 12.085	Pu: 10.635 ; Th:75.53; O: 12.10; Gd:1.735	Pu: 8.508 ; Th:77.649; O: 12.108; Gd:1.735
0-3m					Pu: 11.293 ; Th:76.632; O: 12.075	Pu: 9.034 ; Th:78.882; O: 12.084	Pu: 10.954 ; Th:74.333; O: 12.11; Gd:2.603	Pu: 8.764 ; Th:76.515; O: 12.118; Gd:2.603

Table 5 Branches calculated with SCALE

	CB	DC	TF	TC	DM	TM
Reference	0	Ref_DC*	Ref_TF*	Ref_TC*	Ref_DM*	Ref_TM*
Branch 1	1	-	-	-	-	-
Branch 2	0	0.02	-	-	-	-
Branch 3	0	0.7	-	-	-	-
Branch 4	0	-	600	-	-	-
Branch 5	0	-	2000	-	-	-
Branch 6	0	-	-	650	-	-
Branch 7	0	-	-	1000	-	-
Branch 8	0	-	-	-	0.02	-
Branch 9	0	-	-	-	0.7	-
Branch 10	0	-	-	-	-	600
Branch 11	0	-	-	-	-	1000

* Depending on the axial position, the reference thermal-hydraulic conditions vary

Chapter 6

Analysis of Control Rod Drop Accidents for the Canadian SCWR Using Coupled 3-Dimensional Neutron Kinetics and Thermalhydraulics

6.1 Preface

The work carried out in this publication is the culmination of the development of the coupled 3D neutronics and thermalhydraulics development, the control system design, and optimized fuel loading and assess the impact of control rod accidents. To date there have been no published comprehensive studies of the Canadian SCWR safety characteristics during a reactivity device failure. Given that a main requirement of the GEN IV designs is an improvement in safety, this work forms an important basis for additional design optimization and indicates that under bounding reactivity transients, acceptable performance is demonstrated for cases where shut down system intervention is credited.

The steady-states reached at beginning and end of cycle for the equilibrium cycle with control rods are used as initial conditions to perform transient calculations. In the coupled algorithm, PARCS uses the cross-sections and kinetics parameters calculated by SCALE and thermalhydraulic parameters are simulated each time step. Five separate types of thermal-hydraulic feedbacks were considered and individually tested to verify their proper implementation. Three of them were found to act as a positive feedback (coolant density in the fuel region, coolant temperature, and moderator temperature). The coolant

density in the central tube is a negative feedback; however, the time delay due to the heat transfer leads to small power oscillations which decay to a new steady-state. Finally, the Doppler effect is a strong negative feedback, fast acting, and consequently very stabilizing. The delayed neutron fraction of the Canadian SCWR was also found to be relatively low due to the high plutonium content. While smaller than traditional CANDU designs, the combination of delayed fraction and device reactivities preclude prompt-criticality from a rod drop event.

The CRDA was simulated at BOC and EOC for each of the control rods inserted. In addition, the study was carried out with and without reactor scram to evaluate the effectiveness of SDS action. As soon as the control rod drops, the total core power increases and the power redistributed to the affected region. The power excursion is, however, limited by the thermal-hydraulic feedback dominated by the Doppler effect. If the reactor trips, the power rapidly decreases and limits the MCST and MFCLT increase without challenging the safety margins. However, in one case the overpower signal of 115% full power was not reached leading to fuel melting. Therefore, a different detection technique or detector arrangement should be considered such as local neutron power protection. For cases where SDS action is not credited, there are a number of cases where fuel melting may occur.

Finally, a parametric study was performed on the time step, scram delay, control rod falling speed, and overpower set point. The MCST and MFCLT were found fairly insensitive to these parameters.

The background work, simulations, data analysis, and writing was performed by the main author (F. Salaun). Dr. David R. Novog was consulted many times for advice and brainstorming. The paper was submitted and accepted to *Science and Technology of Nuclear Installations*.

6.2 Publication 3

Analysis of Control Rod Drop Accidents for the Canadian SCWR Using Coupled 3-Dimensional Neutron Kinetics and Thermalhydraulics

Frederic Salaun[1] and David R. Novog[1]

[1]McMaster University, 1280 Main Street West, Hamilton, Ontario L8S 4L8, Canada

Corresponding author: salaunf@mcmaster.ca

Other author: novog@mcmaster.ca

Abstract

The Canadian SuperCritical Water-cooled Reactor (SCWR) is a proposed GEN IV reactor design with improved sustainability, economics and safety characteristics. It is a hybrid of the well-established CANDU™ design and a direct-cycle Boiling Water Reactor with coolant conditions above the thermodynamic critical point of water. The reactor design is batch fueled and utilizes a low pressure heavy water moderator, a separate supercritical water coolant, and a Pu-Th fuel mixture. Given the batch fueled design a large number of control rods are used to manage the reactivity throughout the fuel cycle. This paper examines the consequences of a control rod drop accident (CRDA) for the Canadian SCWR. The asymmetry generated by the dropped rod requires an accurate 3-dimensional neutron kinetics calculation coupled to a detailed thermal-hydraulic model. The implementation of the 3D reactivity feedback was first verified through a series of separate effect simulations. The CRDA was then simulated with and without reactor SCRAM and various sensitivity studies were performed. This work demonstrates that the proposed safety systems for the SCWR core are capable of terminating the CRDA sequence prior to exceeding maximum sheath and centerline temperatures. In one instance involving a rod on the periphery of the core the reactor the proposed trip setpoint (115%FP) was not exceeded and a new steady state was reached. Therefore it is recommended that the design also include provisions for a high-log rate, high-linear rate and/or local Neutron Overpower Protection (NOP) trips, similar to existing CANDU™ designs such that reactor shutdown can be assured for such spatial anomalies.

Keywords: Control rod drop accident, Coupling, Neutron kinetics, Thermalhydraulics

1. Introduction

The Canadian Supercritical Water-cooled Reactor (SCWR) design is the result of the fusion of a CANDU^{TM} reactor and a Boiling Water Reactor (BWR) [1]. The vertical orientation of the core and large light water density variation along the channel resemble the latter while the pressure-tube technology and separate low-pressure (0.3 MPa) heavy water moderator is inspired from the CANDU™ design (Figure 1). It is important to note that the light water coolant (25 MPa, 350°C inlet) is in the supercritical condition and therefore there is no phase change as the coolant heats up along the channel (625°C outlet). The batch refueling design necessitates a large excess reactivity at beginning of cycle; therefore two reactivity control systems were designed for the Canadian SCWR. A burnable absorber (Gd_2O_3) was integrated into a selected number of fuel pins and 89 adjustable cruciform control rods can be inserted from the bottom of the core into the low-pressure moderator [2]. The core is composed of 336 fuel assemblies which generate a thermal power of 2032 MW leading to approximately 1000 MW_{el} (~48% efficiency).

Nuclear reactors can be subjected to a wide variety of conditions ranging from normal operations to postulated accidents. As a consequence, safety analyses are performed to evaluate the impact of such transients, the performance of the special safety systems, and to ensure that safety limits are not exceeded. Evaluation of the conceptual designs of several GEN IV SCWRs has been performed as outlined below.

The High Performance Light Water Reactor (HPLWR), a European design, has already been subjected to extensive analyses of turbine trips, loss of coolant accidents (LOCAs), and loss of flow accidents (LOFAs) [3]. The transient created by a turbine trip/load rejection was expected to be relatively severe, however the detailed analysis showed large margins. Analysis of LOCA scenarios demonstrated cladding temperatures up to 849°C which is well below the 1204°C safety limit. Finally, LOFAs without reactor SCRAM did not show any issues as the thermal limits were not exceeded; however, the author recommended a 3D kinetics model in future studies to confirm the validity of the point kinetics model. All these thermal-hydraulic driven accidents showed acceptable consequences but more challenging results were observed during reactivity initiated accidents (RIAs). Uncontrolled withdrawal of control rods and control rod ejections without SCRAM were investigated in [3,4]. The maximum allowed cladding and fuel temperature were not exceeded however the margins in some cases were very small. Additional studies of uncontrolled withdrawal of control rods without SCRAM, loss of feedwater heating, and control rod malfunction [5] showed that the last two transients have large margins to the safety limits, however the control rod withdrawal leads to fuel melting and emphasizes the importance of RIAs analyses. Finally, potential xenon oscillations also have to be investigated despite being a much

slower transient [6]. Xenon stability analysis was then performed for the HPLWR and concluded that xenon oscillations are non-existent [7].

The Super Light Water Reactor (Super LWR), a Japanese SCWR concept, evaluated the impact of a small and large LOCA, a LOFA, a loss of turbine flow, a pressure control system failure, and an uncontrolled CR withdrawal at normal operation [8]. While the maximum cladding surface temperature (MCST) always remained within the acceptable range, the maximum fuel centerline temperature (MFCLT) wasn't evaluated [9]. Given the importance of MFCLT in RIA transients it is difficult to assess the performance under these conditions. A mixed spectrum SCWR (SCWR-M) proposed by Cheng et al [10] investigated LOFAs and met the safety criteria as long as few design features were respected [11]. In addition, LOCAs were carried out for many break sizes and in the most detrimental case, the MCST largely exceeded the safety criterion which will lead to further core optimization [12].

Thus far only thermal-hydraulic driven accident scenarios (LOCA, LOFA) have been investigated for the Canadian SCWR. While the CVR for the design was negative, studies demonstrate a positive reactivity insertion under non-equilibrium voiding conditions [13,14]. As can be seen in Figure 1, the coolant enters at the top of the core from the inlet plenum through channel specific orifices and travels downwards in the central tube. When the coolant reaches the bottom of the channel it turns arounds and travels upwards picking up the heat from the 64 $(Pu,Th)O_2$ fuel pins. The positive reactivity insertion happens when the coolant first voids around the fuel pins and was studied using coupled 3D neutron kinetics and thermal-hydraulic simulations for thermal-hydraulic driven transients [15]. The inlet LOCA resulted in a flow reversal leading first to a coolant density decrease around the fuel which generated a power pulse before being terminated by the fuel Doppler effect as well as the large central tube coolant density feedback. An inlet LOCA with loss of emergency core cooling systems was also investigated in [16] and evaluated a MCST up to 1278°C which is just above the 1260°C safety limit.

The work carried out in this study presents the first reactivity initiated accidents for the Canadian SCWR. Given the importance of RIA in the literature review of the HPLWR, it is important that such accidents be analyzed for the Canadian design. Such accidents may involve highly localized phenomena and reactivity feedbacks thus necessitating a 3-dimensional neutron kinetics analysis coupled to thermalhydraulics simulations. A very fast control rod ejection is not considered for the Canadian SCWR as the control rods are inserted in the low pressure moderator which is different from Light Water Reactor (LWR) technologies where the rods are surrounded by high pressure coolant. However, a control rod can fall under the action of gravity and lead to a control rod drop accident (CRDA). The initiating event, which is the separation of a control rod from its driving

mechanism, is considered identical to a BWR's as the control rod design is similar [17]. The incident can occur at any time of the fuel cycle, and for any control rod, leading to a local reduction in neutron absorption which in turn increases the fission rate causing a fast and localized power excursion in the reactor core. Such local phenomena cannot be assessed using point-kinetics approximations. Moreover, neutron physics and thermal-hydraulic parameters are intrinsically coupled and play an important role during the transient by providing reactivity feedback mechanisms [18,19,20]. As a consequence, a 3D neutron kinetics model was built in PARCS [21] and has been coupled to RELAP/SCDAPSIM/MOD4 [22] through a series of external python scripts to provide a comprehensive prediction of the transient core response during RIA events.

2. Canadian SCWR core modelling

This section presents the reactor physics and thermal-hydraulics models built to simulate the Canadian SCWR.

2.1 Lattice physics modelling

2.2.1 Fuel cell lattice

The fuel channel geometry and materials specifications for the Canadian SCWR lattice are summarized in Table1. A total of 64 (Pu,Th)O_2 fuel pins are surrounded by a supercritical light water coolant contained in a pressure tube sitting in the heavy-water moderator. TRITON [23] was used to simulate the fuel lattice cell with depletion using the model shown in Figure 2. Reflective boundary conditions were applied on the sides of the cell and the 238 energy group neutron transport equation was solved to obtain the flux distribution within the cell. Using a flux weighting process, the cross-sections were homogenized and condensed in 2 energy groups with an energy cut-off of 2.57 eV [24, 25]. The fuel materials were then depleted with ORIGEN [23] and this entire process was repeated until a burnup of approximately 70 MW.d/kg. Given the fuel enrichment and burnable absorber grading in the axial direction as well as changing thermalhydraulic conditions along the channel, fuel lattice calculations were performed at 20 axial elevations (see Table 2, Table3 and Table 4). The thermalhydraulic conditions (coolant temperature and properties, material temperatures and properties) were taken from [26]. Finally, the kinetics parameters (neutron velocity, delayed neutron fractions and lambdas) were evaluated at each depletion step for the 20 elevations as recommended in [27] hence providing the model with locally varying kinetics parameters. These runs represent the reference state of the lattice calculations. Additional sensitivity calculations were performed to assess the impact of lattice cell meshing to ensure accurate lattice cell cross sections are determined.

Branch calculations have also been performed to evaluate the sensitivity of the reference lattice homogenized cross sections to important thermalhydraulic and control system perturbations. The branches listed in Table 4 were simulated at every axial elevation and several burnup steps by perturbing the reference thermal-hydraulic parameter (see Table 2 and Table 3) as well as simulating the insertion or removal of the control rod. It has to be noted that even though the coolant in the central tube and between the fuel pins is the same, their impact on the lattice physics phenomena is very different [14]. Since non-equilibrium voiding transients may occur each coolant region is treated separately by having separate branches for the inner and outer coolant regions. These branch calculations were used by PARCS to interpolate new cross-sections depending on the local thermal-hydraulic conditions calculated by RELAP/SCDAPSIM/MOD4, and based on control rod positions.

Finally, the reflector cross-sections were generated through a multi-cell geometry as shown in Figure 3. Sensitivity studies demonstrated that the fuel type and thermal-hydraulic conditions of the four fuel assemblies did not significantly change the reflector properties. Therefore, the reflector's cross sections were evaluated using the fuel assembly's thermal-hydraulic conditions at the bottom of the core and for fresh fuel. Moreover, it was found that homogenizing the entire reflector region in the multi-cell to generate the reflector's cross-sections and applying it to every reflector cell in the diffusion model was also a good approximation.

2.1.2 Full-core diffusion model

The 336 fuel channels are surrounded by a 100 cm thick radial reflector and 75 cm axial reflector at the top and bottom of the core. The fuel channel is divided into 20 axial positions using the corresponding 2-group cross-sections evaluated at the lattice level (Figure 3). Zero incoming current boundary conditions were applied on the edge of the reflector. The control rods are inserted through the bottom of the core similar to a BWR and their location is depicted in Figure 4 (for $1/8^{th}$ of the core due to the symmetry). A separate module, VERAview [28], was used for visualization of the transients result.

2.2 Thermal-hydraulic model

The original RELAP/SCDAPSIM/MOD4 (RSM4) [22] source code was previously modified to correct for the water properties at supercritical conditions in [29]. Each of the 336 fuel channels is simulated in this work; however due to limitations in RSM4 not all channels are simulated simultaneously. Therefore the core was divided into eight identical zones and RSM4 simulations were performed for each of the eight regions successively (Figure 5). Each of the eight separate RSM4 models has a fixed inlet boundary condition (25.8 MPa, 350°C), an inlet plenum, 46 parallel channels with individual static orifices, an outlet plenum and a 25 MPa fixed outlet boundary

condition (Figure 6). The power in each channel was split between the two fuel rings using a constant ratio (53% and 47% for the inner and outer ring, respectively) based on fuel lattice calculations over the fuel cycle. While this ratio varies with burnup, the values were selected such that the peak power occurs on the limiting elements and hence it is conservative for the MCST and MFCLT calculations. The power imbalance within a fuel ring due to the presence of burnable absorbers in few pins has not been considered here. As a consequence, the MFCLT is not completely conservative.

The conductivity and heat capacity for the inner ring fuel, outer ring fuel, cladding/central tube material, liners, insulator, and pressure tube was taken from [30]. This work used the Dittus-Boelter correlation for convective heat transfer, however many studies have examined that its error may be very large in the vicinity of the pseudo-critical temperature. To observe the sensitivity of the MCST to the convective heat transfer coefficients three separate sensitivity studies were performed. IN all sensitivity studies, a null-change transient was performed until the diffusion and thermalhydraulic models converged to a new steady-state. In the first test the convective heat transfer was reduced uniformly by 10% across the entire core and an increase of 20°C was observed. In the second study, the heat transfer coefficient was reduced by 50% for all RSM4 nodes where the coolant temperature was near the pseudocritical point (where deterioration may occur) and the resultant MCST only increases by 1°C. Finally, the conductivity and heat capacity of the fuels were increased by 10% and resulted in a 160°C decrease in MFCLT.

2.3 Control rod optimization

A genetic algorithm was used to optimize the insertion depth of the control rods during the batch cycle similar to the optimization performed in [26]. The goal was to obtain an equilibrium cycle with a near-critical core while minimizing the MCST and the MFCLT. The simulations assume a four batch fueling scheme and a shuffling pattern and thermalhydraulic response surface similar to [26] are used. A series of successive fuel cycles is simulated with the rod optimization performed at each burnup step in each successive fuel cycle. The iterations are terminated when the control rod pattern is constant from cycle to cycle. The insertion of the control rods at beginning of cycle (BOC) and end of cycle (EOC) for the equilibrium case are shown in Figure 7.

A coupled steady-state between PARCS and RSM4 was then evaluated at BOC and EOC to obtain a consistent 3D power distribution with the thermal-hydraulic conditions and these coupled states are used as the initial conditions for the transients below.

2.4 PARCS/RSM4 coupling for transient simulation

The synchronization in time between PARCS and RSM4 is of prime importance during a fast transient. A quasi-static process involving very small time steps was used where thermalhydraulic conditions are assumed constant during a PARCS time step and conversely, the local powers are assumed constant during a RSM4 time step.

The neutronic simulation leads the coupling as it will initiate the reactivity transient so PARCS is first run for a small time step and the new 3D power distribution is extracted. Then, RSM4 simulations are performed for the updated 3D power distribution for the same small time step and the new 3D thermal-hydraulic conditions are extracted. In fact 8 RSM4 simulations are performed for the time step each with 46 channels so that no channel averaging is needed. The extracted powers are then used by PARCS to update all cross-sections based on the partial derivatives in each branch calculation done in SCALE (see section 2.1.1). A diagram of the coupling process is shown in Figure 8. Sensitivity simulations were performed for time steps ranging from 0.005 to 0.1s with no observed impact on the conclusions.

The control rod drop accident is a localized and fast power excursion transient. Therefore, every fuel channel had to be simulated in RSM4 to obtain accurate predictions in the entire core. Channel grouping is not used in the thermal-hydraulic simulations [31].

3. Control rod drop accident

3.1 Transient set-up

The fully inserted, or close to full insertion, control rods at BOC and EOC have been fully removed one by one to calculate their reactivity worth (Table 5). Conversely, the control rods sitting out of the core or barely inserted have been fully inserted one by one to find to highest worth rod (red cell in Table 6). The most-effective rod is assumed stuck during simulations where reactor trip is credited as per the International Atomic Energy Agency (IAEA) standards [32].

The drop time of the control rod was evaluated based on its weight and the small pressure difference between the moderator (0.3 MPa) and the containment (atmospheric pressure of 0.1 MPa). The control rod's weight was calculated to be 334 kg based on its dimensions and material properties. The drop time was evaluated to be 0.8s using Newton's second law of motion (the hydraulic resistance due to viscosity was neglected in order to provide a conservative estimate on the drop time). The sensitivity to rod drop was assessed by changing the drop time by 50%.

The safety limits of interest are the integrity of the cladding (T < 1533 K [29]) and the fuel (T < 3100 K). The melting point of thorium-plutonium fuels can be estimated from earlier studies which evaluated the melting point of such fuels using different molar fraction ratios. Fresh fuel's melting point can be estimated to be around 3400K but will likely decrease as the fuel gets irradiated [33]. Hence 3100 K is used as a conservative estimate of the fuel melting temperature.

3.2 Transients results

A null transient was performed to ensure that the coupled initial steady-state kinetics and thermal-hydraulics simulations were converged.

3.2.1 Reactivity feedback verification

The control rod drop accident (CRDA) of the central control rod (number 1 in Figure 4) was investigated for several cases to ensure the feedback models were properly implemented. The CRDA was first simulated without reactivity feedback; and then simulated with each of the five types of reactivity feedbacks separately. Finally all feedbacks are included such that the integrated response can be assessed. Figure 9 shows the relative power change for each case.

When no reactivity feedback are modeled the prompt jump can be initially observed followed by a slow power increase which is expected as no phenomena are included to alter the power trajectory and the power will end up increasing exponentially. The impact of each reactivity feedback is then evaluated individually and they can be classified in two categories: negative feedback (fuel temperature and inner coolant density) or positive feedback (outer coolant density/temperature and the inner coolant temperature).

- The fuel temperature Doppler effect shows a strong negative feedback and is near-instantaneous. For the case where the fuel temperature is included as a feedback the reactor power rapidly decreases and stabilizes to approximately 2% higher than the steady-state power.
- The central tube coolant density feedback also introduces a negative reactivity as shown in Figure 9 although the feedback is smaller and at a slower rate than the fuel temperature case. Here the power oscillates before converging to a power 14% higher than the steady-state power. These oscillations are due to the heat transfer phenomena which are proceeding at a slower time scale than the initial rod perturbation. The heat generated in a fuel pin needs to be transferred through the pin, the cladding, the coolant between the fuel pins and the central tube, before finally reaching the central tube coolant and causing a perturbation. This delay causes the power transient to initially exceed its new-steady

state power during the portions of the transients where power is increasing and vice versa for periods of decreasing power.

- The central flow tube temperature feedback is positive as higher temperature moderators tend to up-scatter neutrons into the low-energy Pu fission resonances. This feedback is slightly delayed relative to the two other positive mechanisms due to the time delay involved in the heat transfer from the fuel pins through the central flow liner and to the central coolant (similar to the time delay involved in the central density feedback).
- The coolant in the fuel region also has a positive feedback contribution due to its propensity to up scatter neutrons into the low-lying Pu fission resonances, although the feedback has an earlier onset since the thermal lag to the coolant in this region is less than that to the central flow tube.
- Finally the fuel region coolant density feedback is also strongly positive and on a time scale similar to coolant temperature changes in this region of the channel.

These results are consistent with the benchmark study in [14] and confirm the proper implementation of the reactivity feedback.

3.2.2 CRDA with SCRAM

All the fully inserted, or near full insertion, control rods were considered for rod drop analyses at both BOC and EOC (Table 7). A minimum time step of 0.1s (maximum time step of 0.5s) was used during these transients based on a parametric study presented below (Table 8). Each control rod starts dropping two seconds after the beginning of the simulation from its initial position and is removed until the out-of-the-core position in 0.8s (simulation time reaching 2.8s) by assuming a constant speed fall. The reactor trip signal occurs when the total power reaches 115% full power (FP) and the reactor SCRAM delay is 0.6s, consistent with LWR studies [34,35]. During the reactor SCRAM, all the control rods (no shutoff rods were modeled) are linearly inserted into the core in 3s (approximately speed of 1.6 m/s) with the exception of the rod dropped and the assumed unavailable rod (the most effective rod). A typical transient for the changes in relative power, MCST, and MFCLT as a function of time for the drop of control rod 15 at BOC have been plotted in Figure 10. Note that the MCST and MFCLT were normalized relative to the hot zero power condition (623 K) and slowly converge towards it as the power converges to zero. The normalized radial power distribution has also been plotted before the accident and when the core reaches its maximum power (0.8s after the beginning of the drop) (Figure 11). The local power excursion near the dropped control rod can be clearly observed with the relative assembly power going from 1.08 up to 1.86 for assembly number 50 (see Figure 3 for assembly numeration). Figure 12 is an axial cut of row 4 at four different times during

the transient. At 2.4s, half of the control rod is still inserted into the core leading to a distorted power distribution towards the top of the core, especially where the control rod is removed (column P and Q). It can be noted that the normalized power remains locally high after the SCRAM (t=10s) because the dropped rod and the most effective rod are assumed stuck; however, the core total power is significantly reduced with the SCRAM (6.7% FP). Figure 13 shows an axial cut of row 4 for the cladding and fuel centerline temperature at steady-state and when they reach their highest value. A slight increase and asymmetry can be observed.

At BOC condition a CRDA involving control rod number 6 never reaches the overpower signal of 115% full power. Therefore, the reactor trip does not register and the core reaches a new steady-state with excessively high cladding and fuel temperature. Further analysis of such cases is provided in the next section which considers cases where reactor trip is unavailable.

For all other CRDA cases the safety limits were met. The maximum reactivity insertion was 0.3$ (see Table 5) therefore supercriticality is avoided. The power excursion can be terminated by the reactivity feedback alone but the reactor SCRAM safely shut down the reactor and limits the MCST increase to 10-30°C and the MFCLT rise to 80-150°C.

Parametric studies on the minimum time step, control rod drop time, overpower signal, and SCRAM delay were carried out to evaluate the sensitivity of the results to those parameters. The CRDA for control rod 15 at BOC was simulated with the modified parameters and the results are shown in Table 8.

Cases 0, 1, and 5 demonstrate the minimal impact of the time step on the studied parameters. A higher time step tends to overestimate the MCST, MFCLT and maximum power albeit only to a small extent. Therefore any time step between 0.005s and 0.1s is considered acceptable. Increasing the SCRAM signal from 115% to 120% full power also has negligible effects on the transient. The MCST and MFCLT are more sensitive to the time delay associated with the SCRAM signal, but they remain far below the safety limits. Finally, the sensitivity to rod drop timing was examined by decreasing the drop time by 50% and showed that the power increase is more substantial but the MCST and MFCLT are not significantly affected.

3.2.3 CRDA without SCRAM

The CRDAs discussed above were reexamined assuming a rod drop without SCRAM. Such events involve changes in power, fuel temperature, coolant properties etc. over the full core. In all cases the power was redistributed within the core and a new steady-state power was reached. The MCST, and MFCLT were evaluated to assess the performance of the core and the results

summarized in Table 9. For almost all cases the fuel centerline limit was exceeded, hence reactor SCRAM is required for this accident scenario.

The relative core power, MCST, and MFCLT change for the drop of control rod 15 at BOC are presented in Figure 14. This scenario presents the highest cladding temperature increase as well as the highest power increase.

The normalized radial power distribution has been plotted for three states: before the accident (0s), at maximum core power (2.8s), and when the MFCLT reached the melting point of 3100K (9.1s). As the two first states are identical to the transient without SCRAM they are not plotted here again and only the latter state is shown in Figure 15. After reaching a maximum at 2.8s, the radial power tilt decreases due to the reactivity feedback. For instance, the relative assembly power in assembly 50 increases from 1.08 to 1.86 before decreasing to 1.61.

A vertical slice of row 4 of the core was used to plot the normalized axial power distribution at 4 specific times of the transient (Figure 16): before the accident (0s), half-way through the rod drop (2.4s), rod reaching the out-of-the-core position (2.8s), and when the MFCLT reached the assumed melting point (9.1s). The cladding and fuel centerline temperature were also plotted before the transient and at 9.1s. The power decreases after the positive reactivity insertion due to the negative power coefficient and stabilizes to a new level (104% FP in this case).

Initially, the MCST is located in this vertical slice (column Q in Figure 17 or assembly 51) but the MFCLT is in assembly 163. The MCST remains in the same location as the transient progresses because the MCST is already located around the failing rod. However, the MFCLT location changes to assembly 50 (column P in Figure 17) two seconds after the initiation of the transient.

4. Conclusion

A system capable of simulating coupled neutron physics and thermal-hydraulic transients for the Canadian Supercritical Water-cooled Reactor has been developed with PARCS, RELAP/SCDAPSIM/MOD4, and external python scripts for data exchange. Control rod drop accidents have not previously been assessed for this core design and given these accidents are localized, fast and asymmetric, there is a need for fully coupled 3D neutron kinetic and thermal-hydraulic analysis. The PARCS spatial kinetics model was built using the cross-sections and kinetics parameters evaluated as function of burnup and axial elevation at the lattice level and the RSM4 model includes all of the 336 fuel assemblies.

Five types of feedback were considered in addition to the effect of the rod drop. In order to verify the coupled model a series of separate effect feedback analyses were performed where each feedback was considered in isolation.

The strong fuel Doppler effect was found to be very stabilizing and quickly terminated the transient. The coolant density in the central tube also limits the power excursion but oscillations were observed due to the differences between neutronic and heat transfer time scales. While the three other feedbacks are positive, the power coefficient remains strongly negative.

The reactivity worth of each rod was evaluated at BOC and EOC when dropped. Even though the delayed neutron fraction is low (beta ~ 0.3%) due to the high plutonium content, the reactivity insertion remains less than prompt criticality for all drop scenarios. The first set of transients assumed an operational reactor trip when the core power exceeded 115% full power. After a delay of 0.6 second, all the control rods except the failed one and the highest reactivity worth rod were introduced from their current position to a fully inserted position using a conservative insertion characteristic time. All transients but one activated the reactor trip and safely shutdown without challenging the safety margins. Moreover, a parametric study was carried out on the minimum time step, overpower trip set point, SCRAM delay and control rod drop time. The maximum relative power, MCST, and MFCLT were found to be fairly insensitive to those parameters. However, while the case which did not trip reached a new steady-state and the MCST remained below the safety limit, fuel melting occurred in the assemblies around the dropped rod. As a consequence, other detection techniques and trip parameters are needed. For example, the local Neutron Power Protection (NOP) system utilized in the existing CANDU™ fleet could be considered for this design.

While unacceptable from a consequence standpoint (i.e., fuel melting), cases without reactor SCRAM are interesting to assess the overall core properties. The study shows that almost all the transients reached a MFCLT above 3100 K; therefore, fuel melting would occur in most cases and show the necessity for reactor SCRAM demonstrating the need for special safety system action for these events.

Acknowledgement

The author would like to thank Andrew Ward from the University of Michigan for his help regarding PARCS. This work was funded by Natural Resources Canada (NRCAN) through the Office of Energy Research and Development, Canadian Nuclear Laboratories (CNL) and Natural Sciences and Engineering Research Council of Canada (NSERC).

References

[1] L. K. H. Leung, M. Yetisir, W. Diamond, D. Martin, J. Pencer, B. Hyland, H. Hamilton, D. Guzonas and R. Duffey, "A Next Generation Heavy Water Nuclear Reactor with Supercritical Water as Coolant," in International Conference on Future of Heavy Water Reactors, Ottawa, 2011.

[2] F. Salaun and D. Novog, "Spatial and bulk reactivity systems design and optimization for the Canadian Supercritical Water Reactor," Canadian Nuclear Laboratories Nuclear Review, vol. 5, no. 2, pp. 285-298, 2016.

[3] M. Andreani, D. Bittermann, P. Marsault, O. Antoni, A. Kereszturi, M. Schlagenhaufer, A. Manera, M. Seppäla and J. Kurki, "Evaluation of a preliminary safety concept for the HPLWR," Progress in Nuclear Energy, vol. 55, pp. 68-77, 2012.

[4] C. Maraczy, A. Kereszturi, I. Trosztel and G. Hegyi, "Safety analysis of reactivity initiated accidents in a HPLWR reactor by the coupled ATHLET-KIKO3D code," Progress in Nuclear Energy, vol. 52, pp. 190-196, 2010.

[5] G. Hegyi, A. Kereszturi, C. Maraczy and I. I. Trosztel, "Reactivity Initiated Accident Analysis of the HPLWR Three Pass Core with Ascending Gap Flow Using the KIKO3D-ATHLET Code," in International Conference Nuclear Energy for New Europe , Portoroz, Sloven, 2010.

[6] C. Jeong and H. Choi, "Xenon transient analysis for direct use of spent pressurized water reactor fuel in CANDU reactor (DUPIC)," Annals of Nuclear Energy, vol. 27, pp. 269-278, 2000.

[7] T. T. Reiss, S. Feher and S. Czifrus, "Xenon oscillations in SCWRs," Progress in Nuclear Energy, vol. 53, pp. 457-462, 2011.

[8] Y. Ishiwatari, K. Silva, Z. Xiong, S. Sakurai and R. Hamazaki, "Safety analysis of JSCWR," in The 5th International Symposium on Supercritical Water Reactor (ISSCWR-5), Vancouver, British Columbia, Canada, March 2011.

[9] N. Tamiya, Susanto and Y. Oka, "Safety analysis of a Super LWR with double tube water rods," Nuclear Engineering and Design, vol. 266, pp. 129-136, 2014.

[10] X. Cheng, X. Liu and Y. Yang, "A mixed core for supercritical water-cooled reactor," Nuclear Engineering and Technology, vol. 40, no. 2, pp. 117-126, 2008.

[11] Z. Z. Xu, D. Hou, S. Fu, Y. Yang and X. Cheng, "Loss of flow accident and its mitigation measures for nuclear systems with SCWR-M," “Loss of flow accident and its mitigation measures for nuclear systems with SCWR-M”, Annals of Nuclear Energy 38 (2011), p.2634-2644, vol. 38, pp. 2634-2644, 2011.

[12] X. Liu, S. Fu, Z. Xu, Y. Yang and X. Cheng, "LOCA analysis of SCWR-M with passive safety system," Nuclear Engineering and Design, vol. 259, pp. 187-197, 2013.

[13] P. Schwanke and E. Nichita, "Preliminary space-kinetics simulation of a coolant voiding-induced transient for a supercritical water cooled reactor with re-entrant fuel channels," in The 19th Pacific Basin Nuclear Conference (PBNC 2014), Vancouver, British Columbia, 2014.

[14] J. Sharpe, F. Salaun, D. Hummel, A. Moghrabi, M. Nowak, J. Pencer, D. Novog and A. Buijs, "A Benchmark Comparison of the Canadian Supercritical Water-cooled Reactor (SCWR) 64-element Fuel Lattice Cell Parameters Using Various Computer Codes," in The 35th Annual Canadian Nuclear Society Conference, Saint John, New Brunswick, 2015.

[15] D. Hummel and D. R. Novog, "Coupled 3D neutron kinetics and thermalhydraulics charasteristics of the Canadian supercritical water reactor," Nuclear Engineering and Design, vol. 298, pp. 78-89, 2016.

[16] P. Wu, J. Shan, J. Gou, L. Leung, B. Zhang and B. Zhang, "Heat transfer effectiveness for cooling of Canadian SCWR fuel assembly under the LOCA/LOECC scenario," Annals of Nuclear Energy, vol. 81, pp. 306-319, 2015.

[17] C. Shih, A. Ho, J. Wang, H. Lin and S. Chiang, "Analysis of the Control Rod Drop Accident (CRDA) for Lungmen ABWR," US Nuclear Regulatory Commission, Washington DC, 2015.

[18] P. Adouki and G. Marleau, "Neutronics/Thermalhydraulics coupling in a CANDU SCWR," in The 3rd China-Canada Joint Workshop on Supercritical Water-Cooled Reactors, CCSC-2012, Xian, China, 2012.

[19] M. Hursin and T. Downar, "PWR control rod ejection analysis with MOC code DeCART," in Joint International Workshop: Nuclear Technology and Society, Berkeley, California, USA, 2008.

[20] H. Cheng and D. J. Diamond, "Analyzing the rod drop accident in a boiling water reactor," Nuclear Technology, vol. 56, pp. 40-54, 1982.

[21] T. Downar, Y. Xu and V. Seker, "PARCS v3.0 U.S. NRC Core Neutronics Simulator, USER MANUAL draft," 2013.

[22] C. Allison and J. Hohorst, "Role of RELAP5/SCDAPSIM in Nuclear Safety," Science and Technology of Nuclear Installations, vol. 2010, 2010.

[23] SCALE: A comprehensive modelling and simulation suite for nuclear safety analysis and design, Oak Ridge National Laboratory, 2011.

[24] J. Duderstadt and L. Hamilton, Nuclear Reactor Analysis, Canada: John Wiley & Sons, 1976.

[25] L. Massimo, Physics of High Temperature Reactors, NY: Pergamon Press, 1976.

[26] F. Salaun and D. Novog, "Optimization of the Canadian SCWR Core Using 3D Reactor Physics and Thermal-hydraulics Calculations," Nuclear Engineering and Radiation Science, 2017.

[27] J. Pencer, M. McDonald and V. Anghel, "Parameters for transient response modeling for the Canadian SCWR," in The 19th Pacific Basin Nuclear Conference (PBNC-2014), Vancouver, British Columbia, 2014.

[28] A. Godfrey and R. Lee, "VERAview User's Guide. CASL-U-2016-1058-000," Oak Ridge National Laboratory, Oak Ridge, Tennessee, March, 2016.

[29] C. Lou, "Loss of coolant accident simulation for the Canadian supercritical water-cooled reactor using RELAP5/MOD4," Hamilton, Ontario, Canada, 2016.

[30] D. Hummel, "Transient neutronic-thermalhydraulic coupling in a PT-SCWR," Ph.D. Dissertation, McMaster University, Hamilton. Ontario, Canada, 2015.

[31] T. Barrachina, M. Garcia-Fenoll, F. Ánchel, R. Miró, G. Verdú, C. Pereira, C. da Silva, A. Ortego and J. Martinez-Murillo, "REA 3D-dynamic analysis in Almaraz NPP with RELAP5/PARCS v2.7 and SIMTAB cross sections tables," Progress in Nuclear Energy, vol. 53, pp. 1167-1180, 2011.

[32] C. B. E. Allison, F. D'Auria, M. Jankowski, J. Misak, C. Munhoz-Camargo, S. Salvatores and V. Snell, "Accident Analysis for Nuclear Power Plants with Pressurized Water Reactors," International Atomic Energy Agency, 1999.

[33] P. Ghosh, N. Kuganathan, C. Galvin, A. Arya, G. Dey and B. Dutta, "Melting behavior of (Th,U)O2 and (Th,Pu)O2 mixed oxides," Journal of Nuclear Materials, vol. 479, pp. 112-122, 2016.

[34] D. Diamond, B. Bromley and A. Aronson, "Studies of the rod ejection accident in a PWR," Brookhaven National Laboratory, New-York, 2002.

[35] T. Barrachina, R. Miro, G. Verdu, A. Ortego and J. Martinez-Murillo, "Rod ejection accident 3D-dynamic analysis in Trillo NPP with RELAP5/PARCS v2.7," in 1st International Nuclear and Renewable Energy Conference (INREC10), Amman, Jordan, 2010.

List of Figures

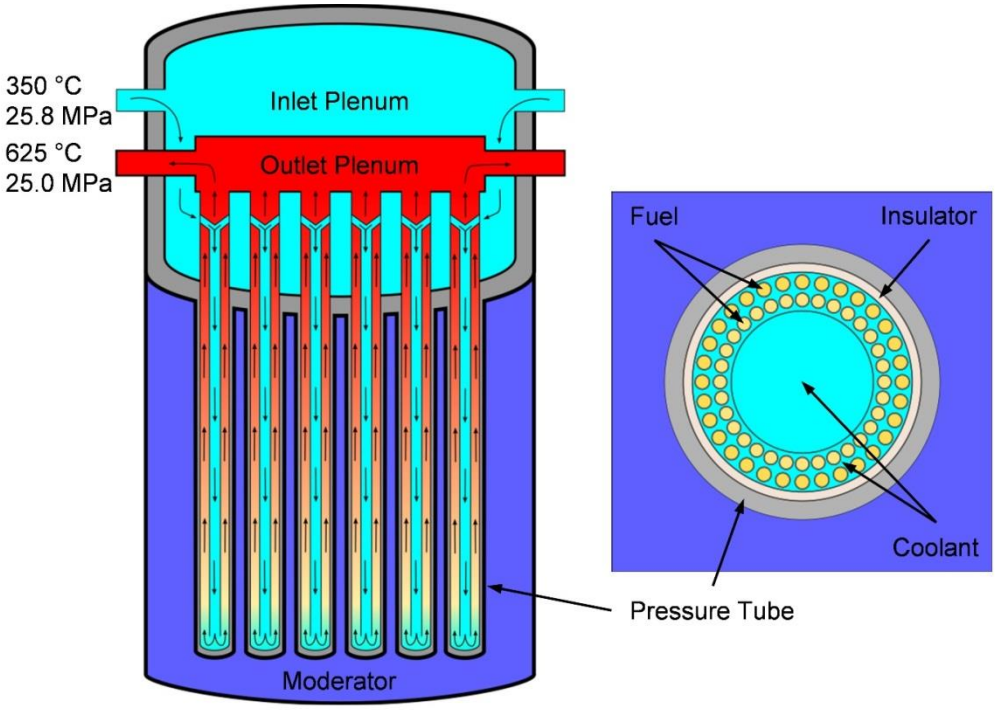

Figure 1 Canadian SCWR concept

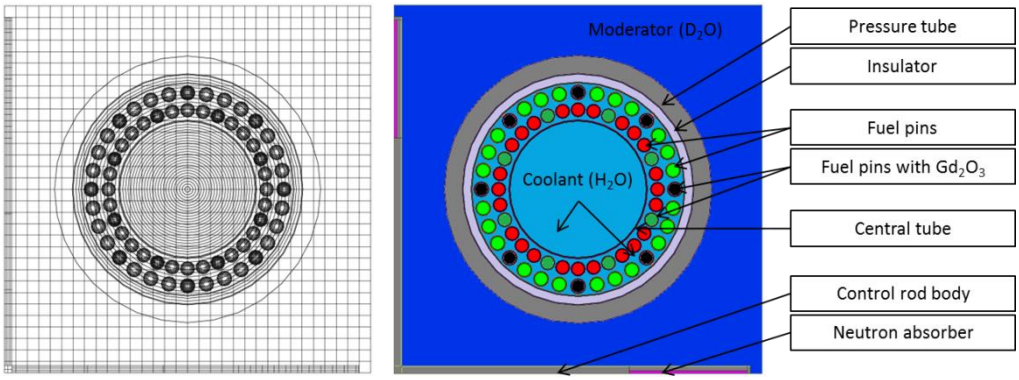

Figure 2 Fuel lattice cell meshing (left) and materials (right)

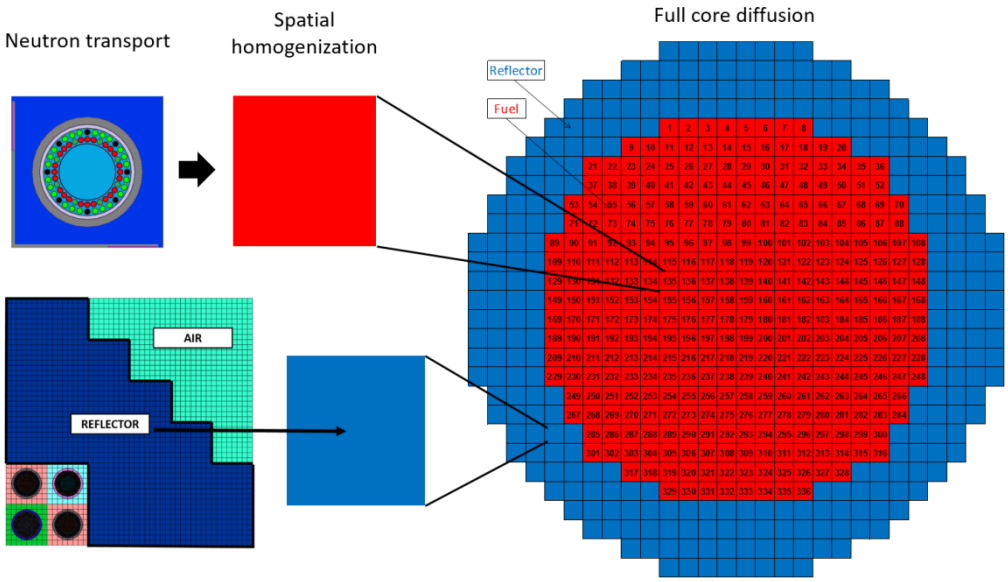

Figure 3 Reactor physics modelling process (2D view)

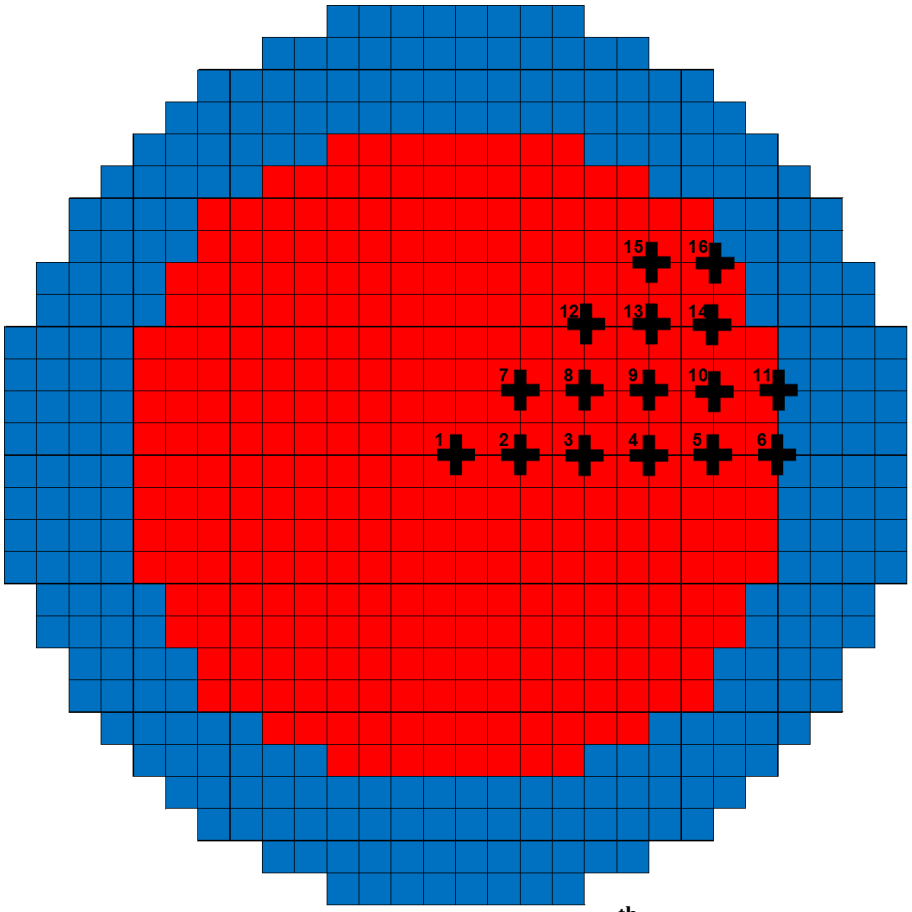

Figure 4 Control rods location (1/8th symmetric)

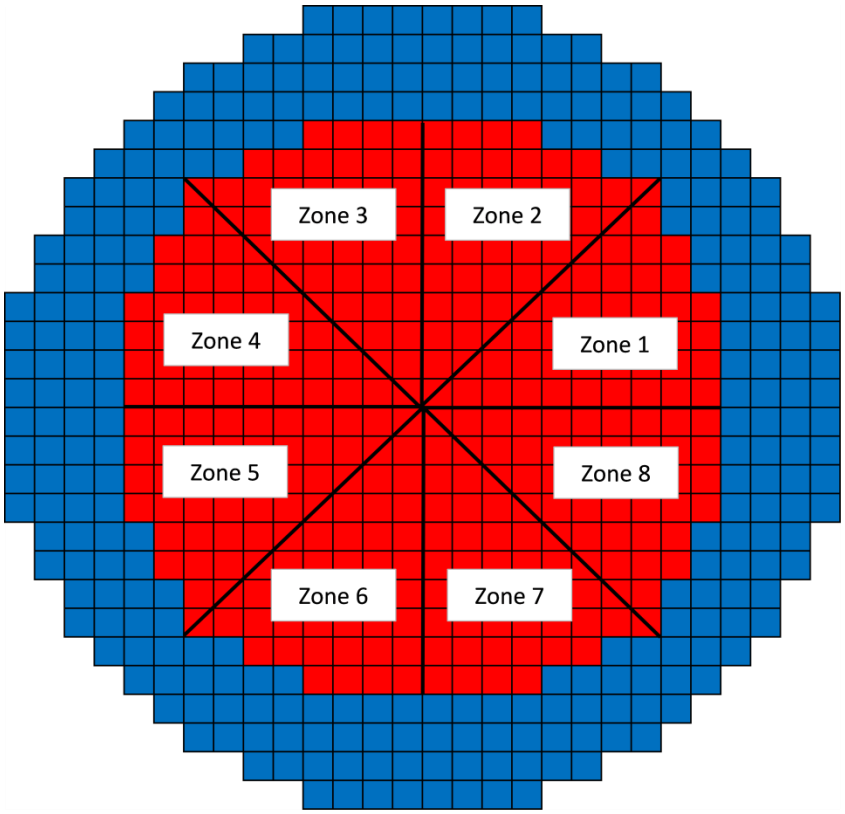

Figure 5 Channels splitting for RSM4

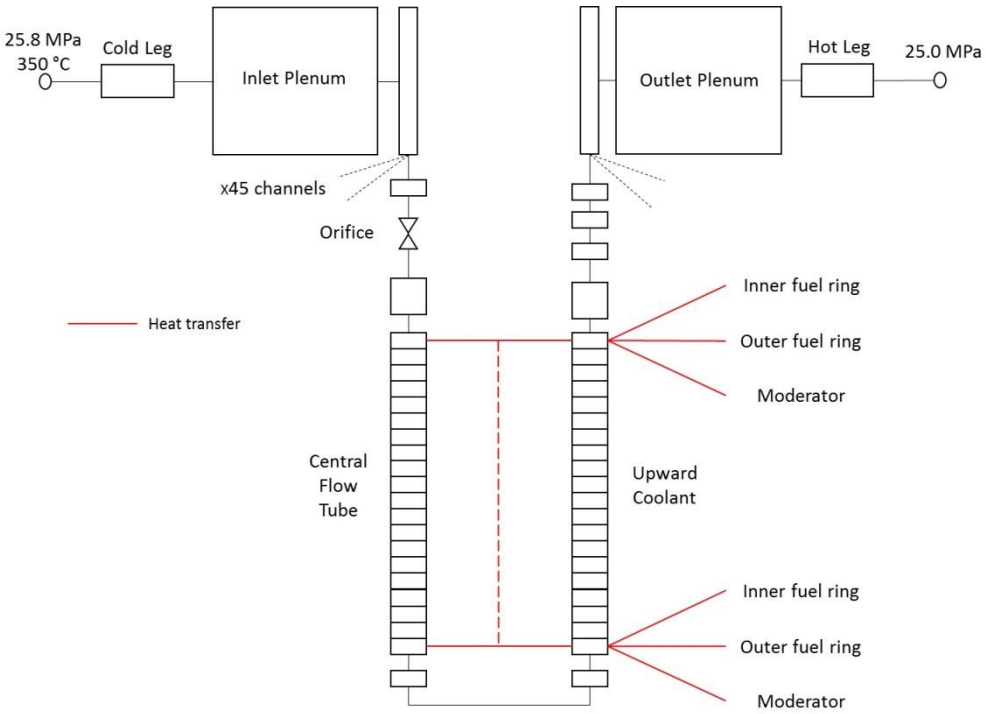

Figure 6 Canadian SCWR model for thermal-hydraulic studies in RSM4

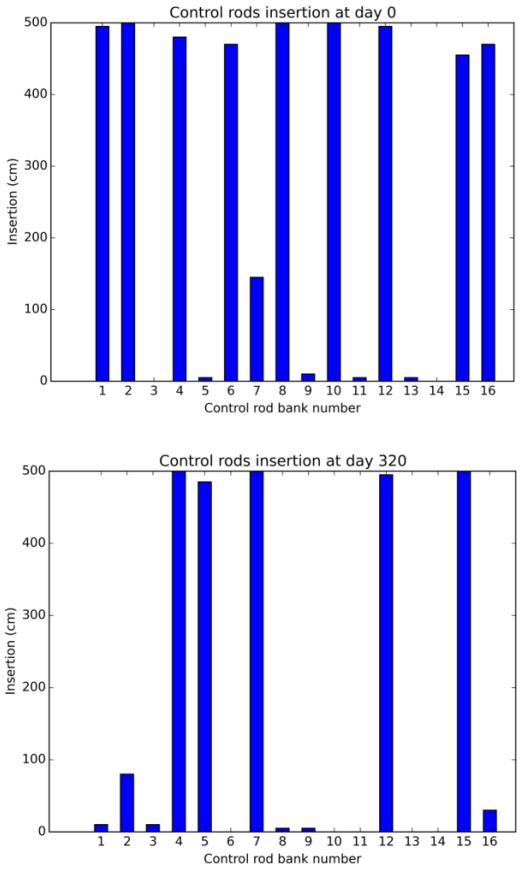

Figure 7 Control rods insertion at BOC (left) and EOC (right)

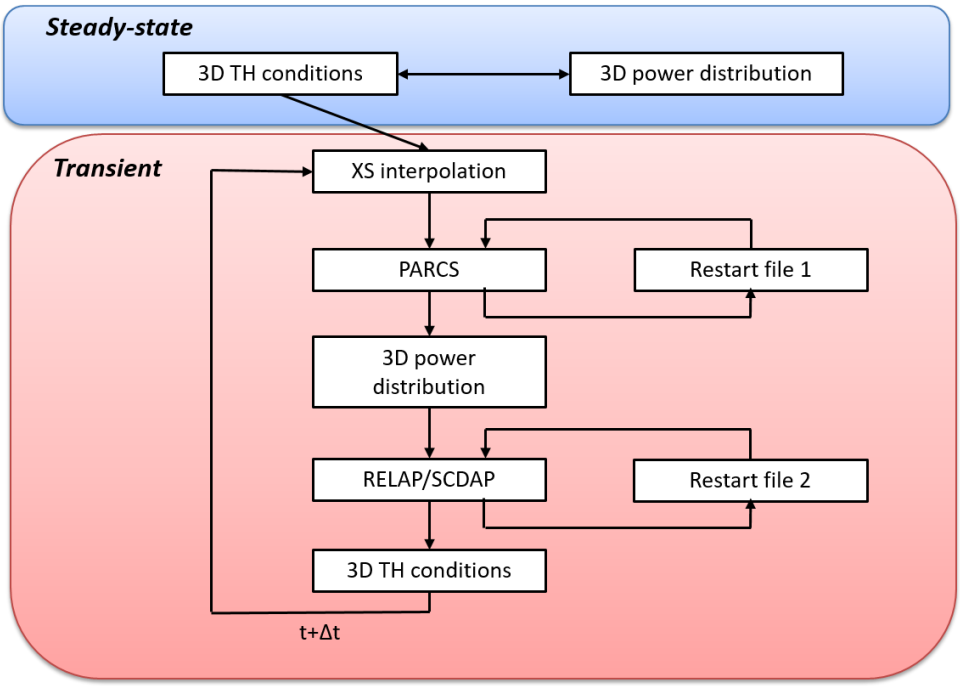

Figure 8 Coupling process for transients simulation

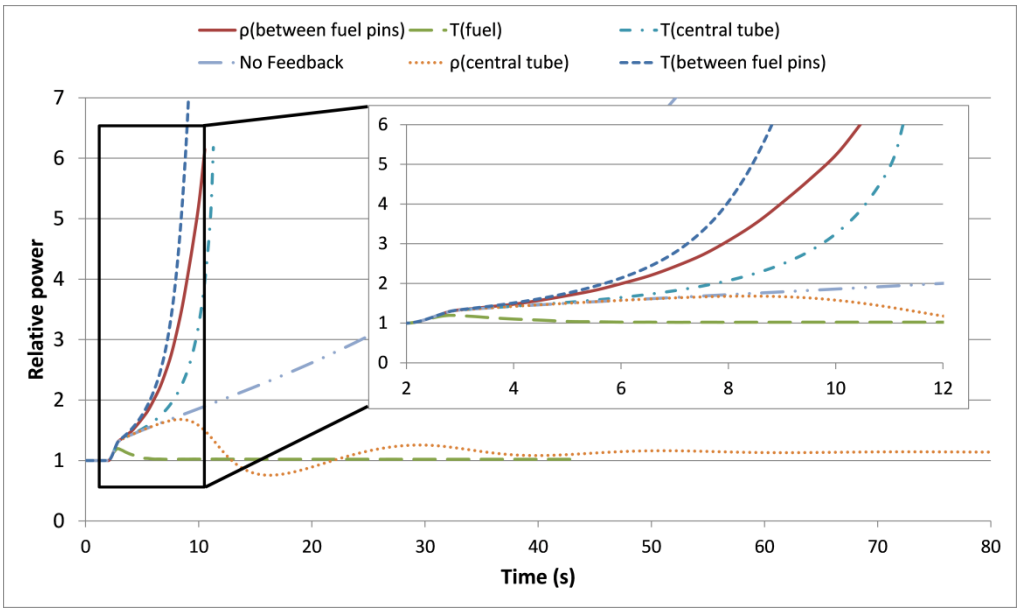

Figure 9 Impact of individual reactivity feedback on the power during a control rod drop accident

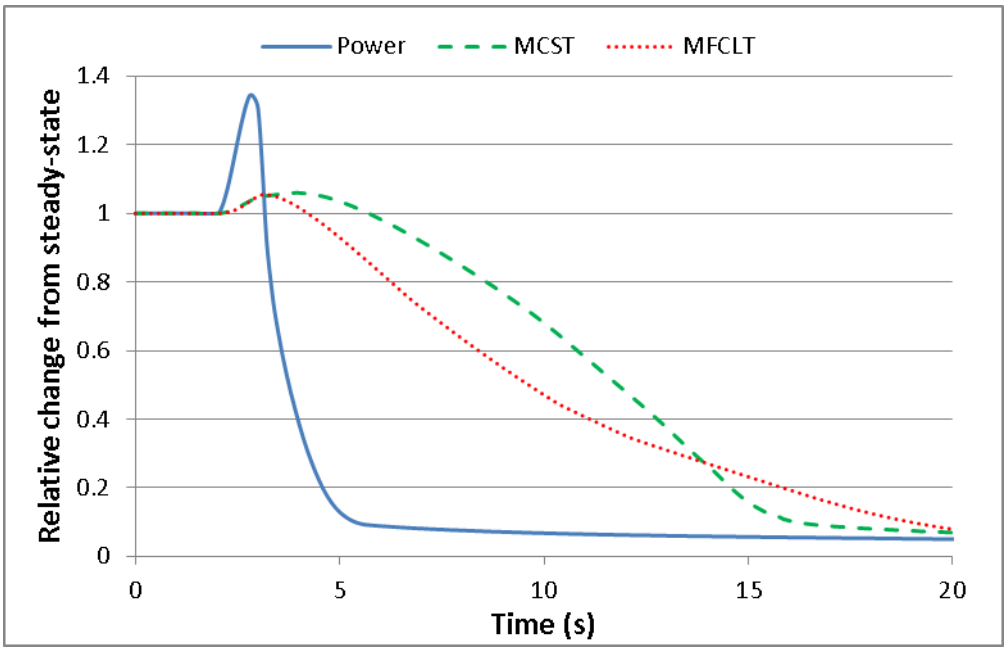

Figure 10 Relative power, MCST, and MFCLT evolution during the CRDA of control rod 15

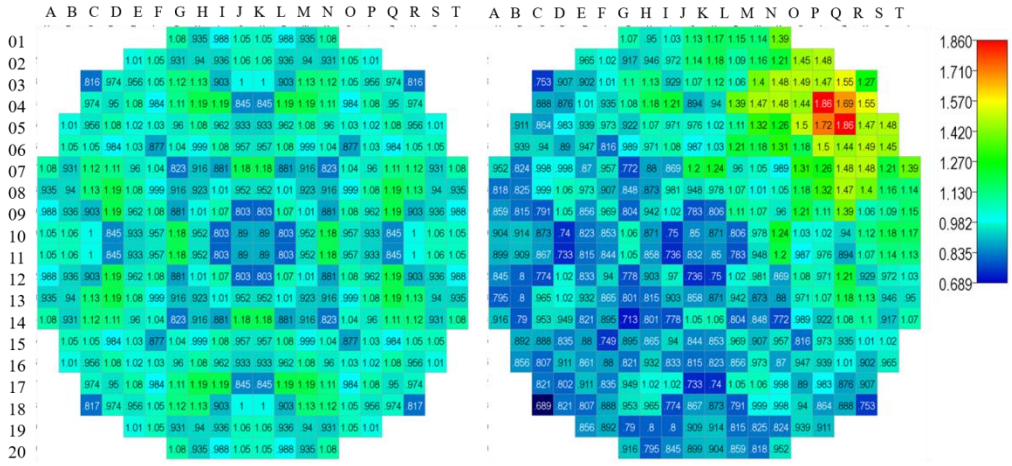

Figure 11 Normalized assembly power distribution before the accident (left) and at core maximum power (right) during the CRDA of CR 15

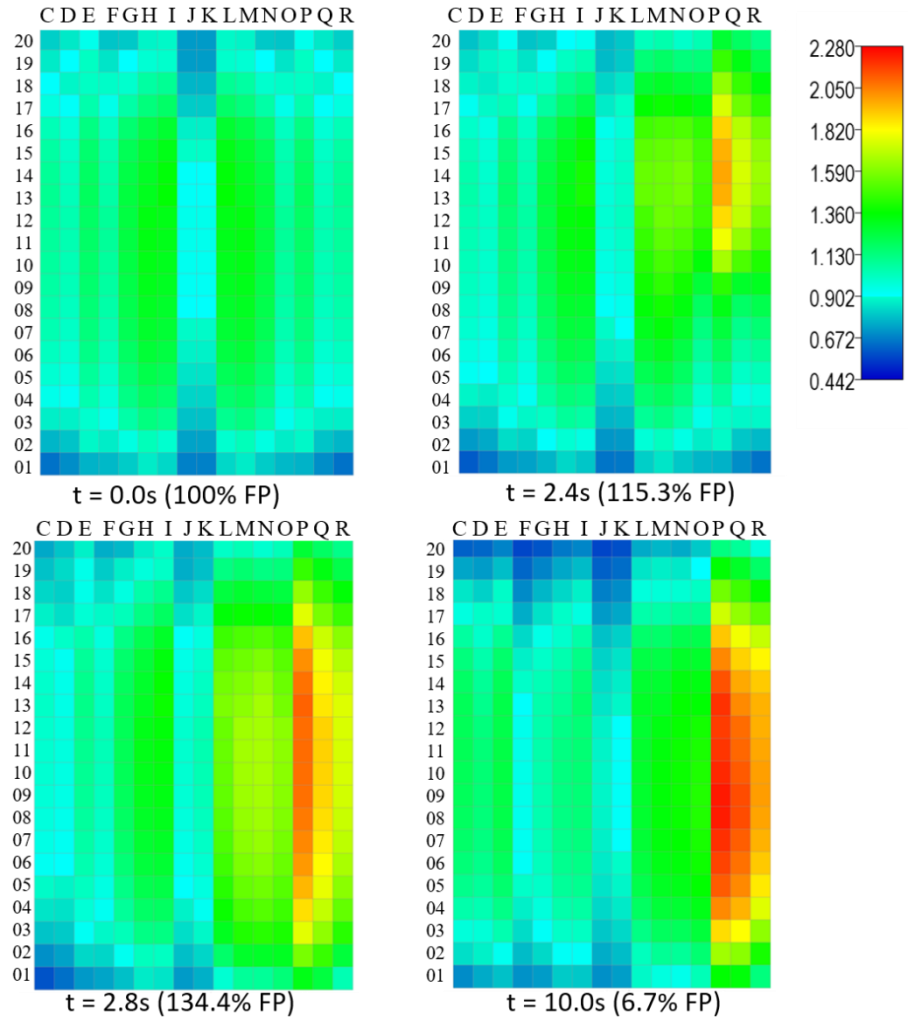

Figure 12 Snapshots of the axial power distribution of row 4 for the CRDA of CR15 with reactor SCRAM

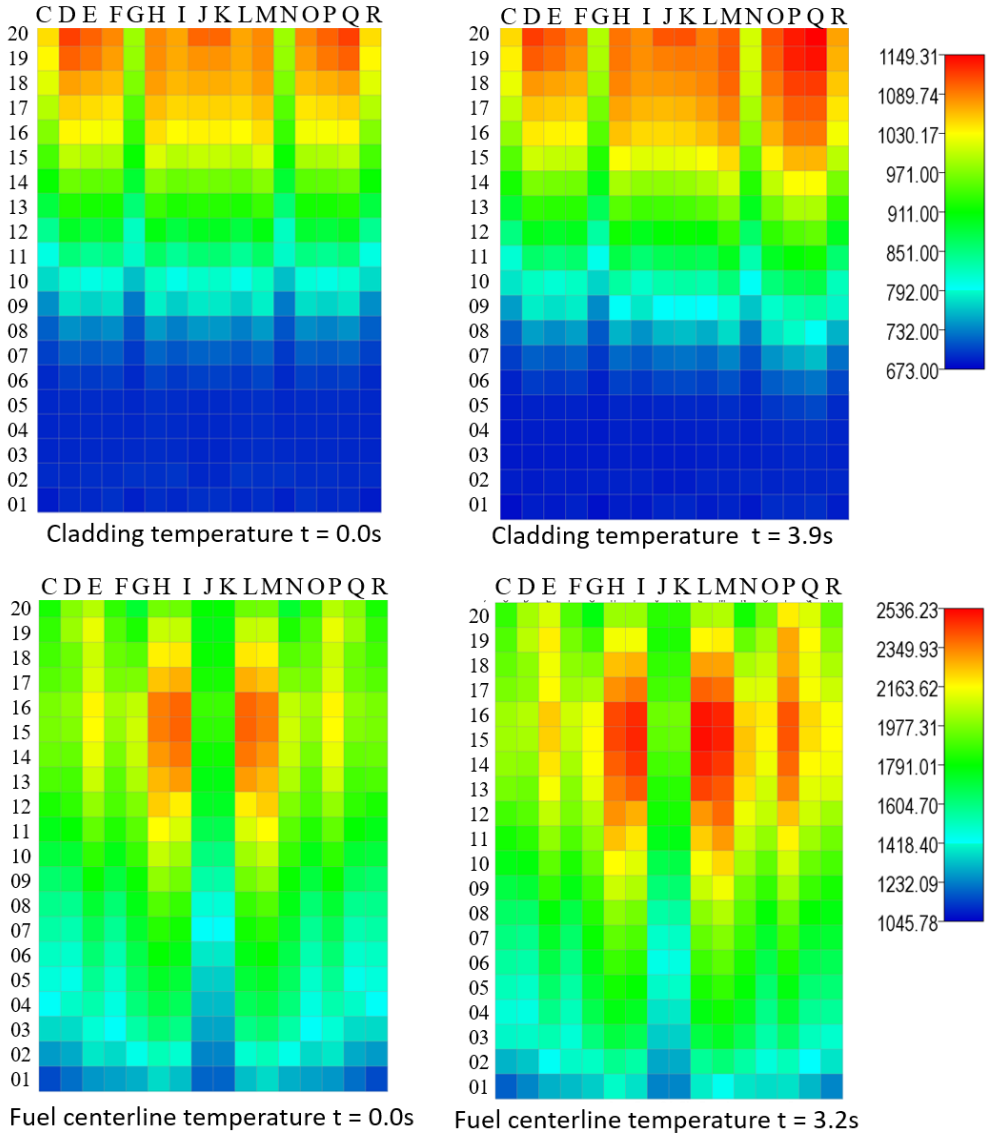

Figure 13 Snapshots of the cladding and fuel centerline temperature for the CRDA of CR15 with reactor SCRAM

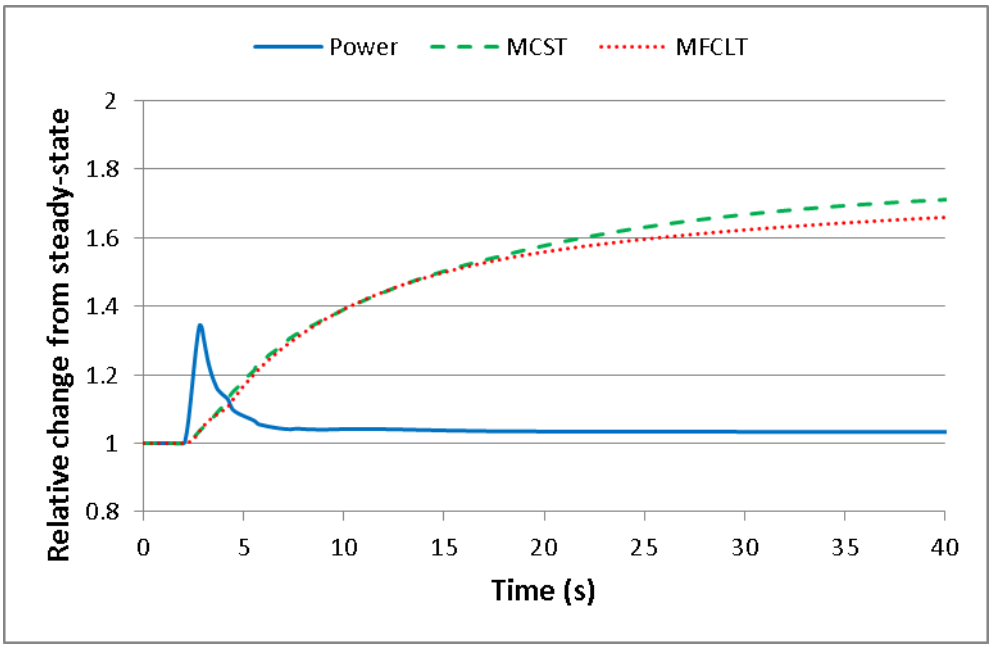

Figure 14 Normalized power, MCST, and MFCLT evolution during the control rod 15 drop without SCRAM

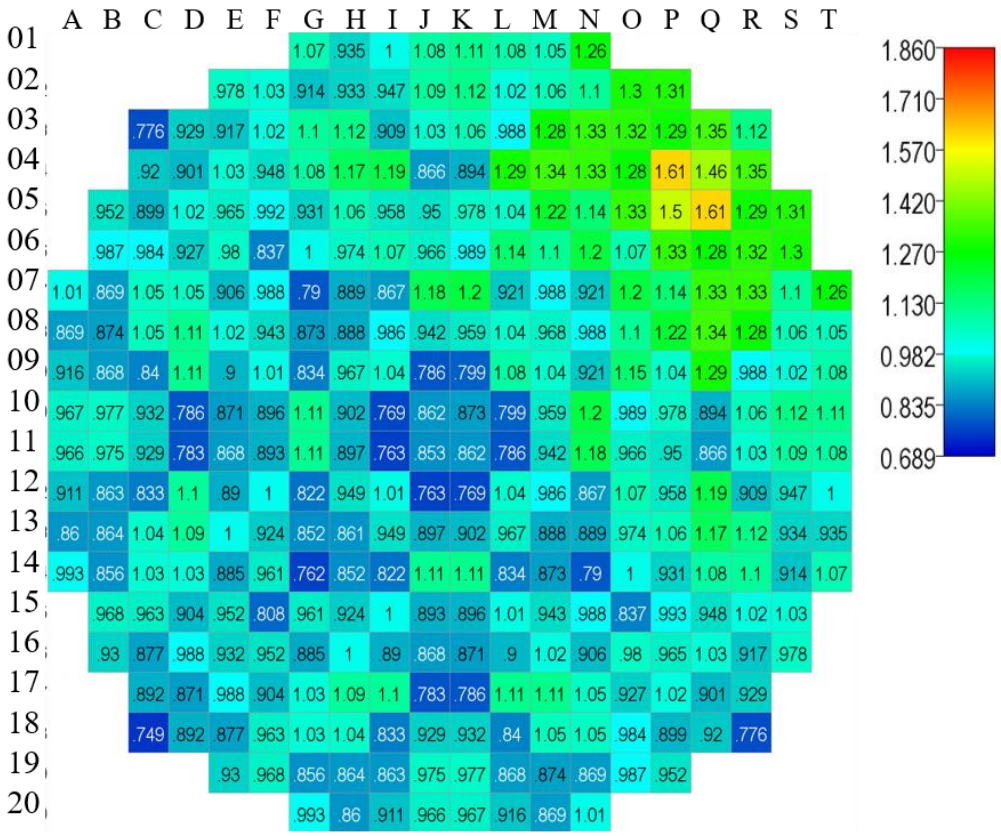

Figure 15 Normalized radial power distribution reached at t=9.1s without SCRAM

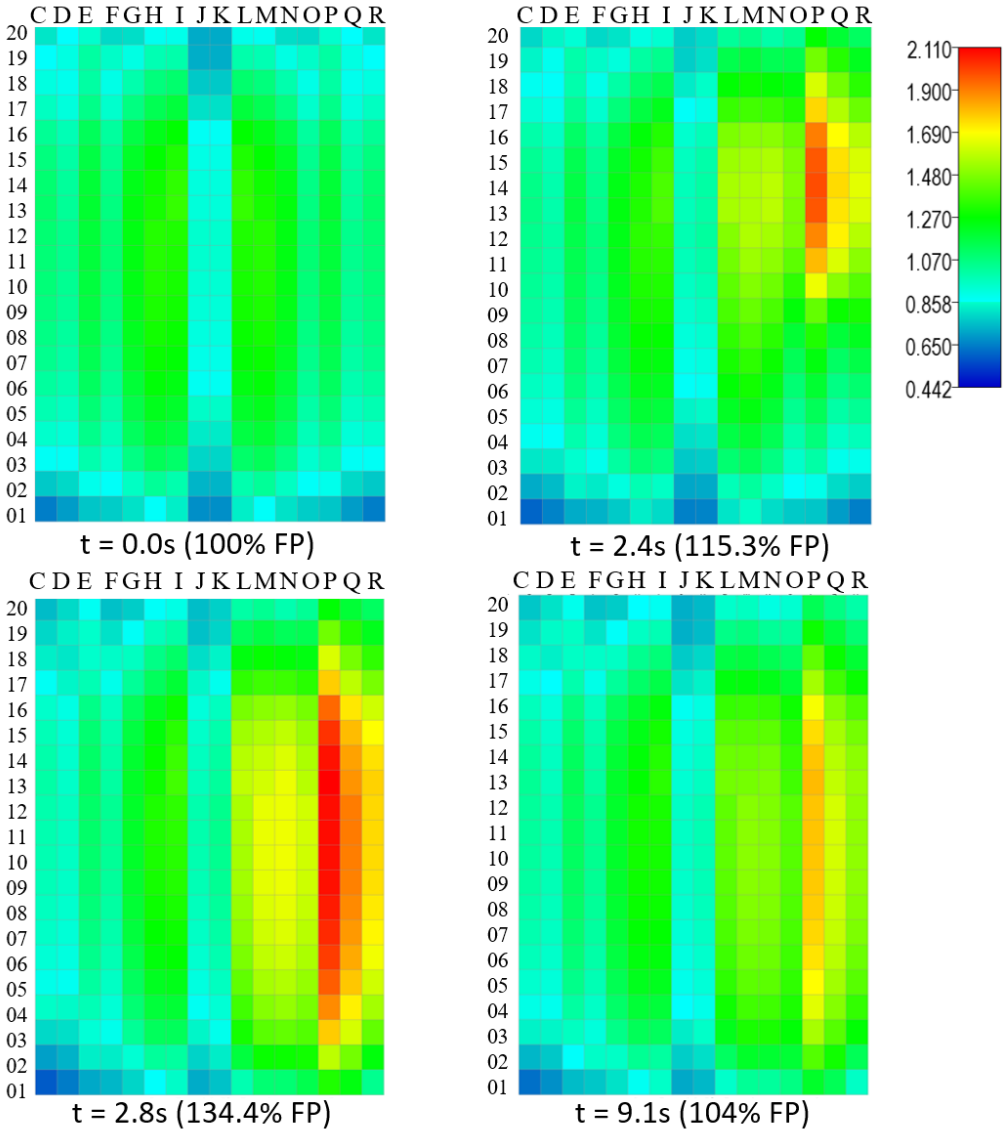

Figure 16 Snapshots of the normalized axial power distribution of row 4 during the CRDA of CR15 without reactor SCRAM

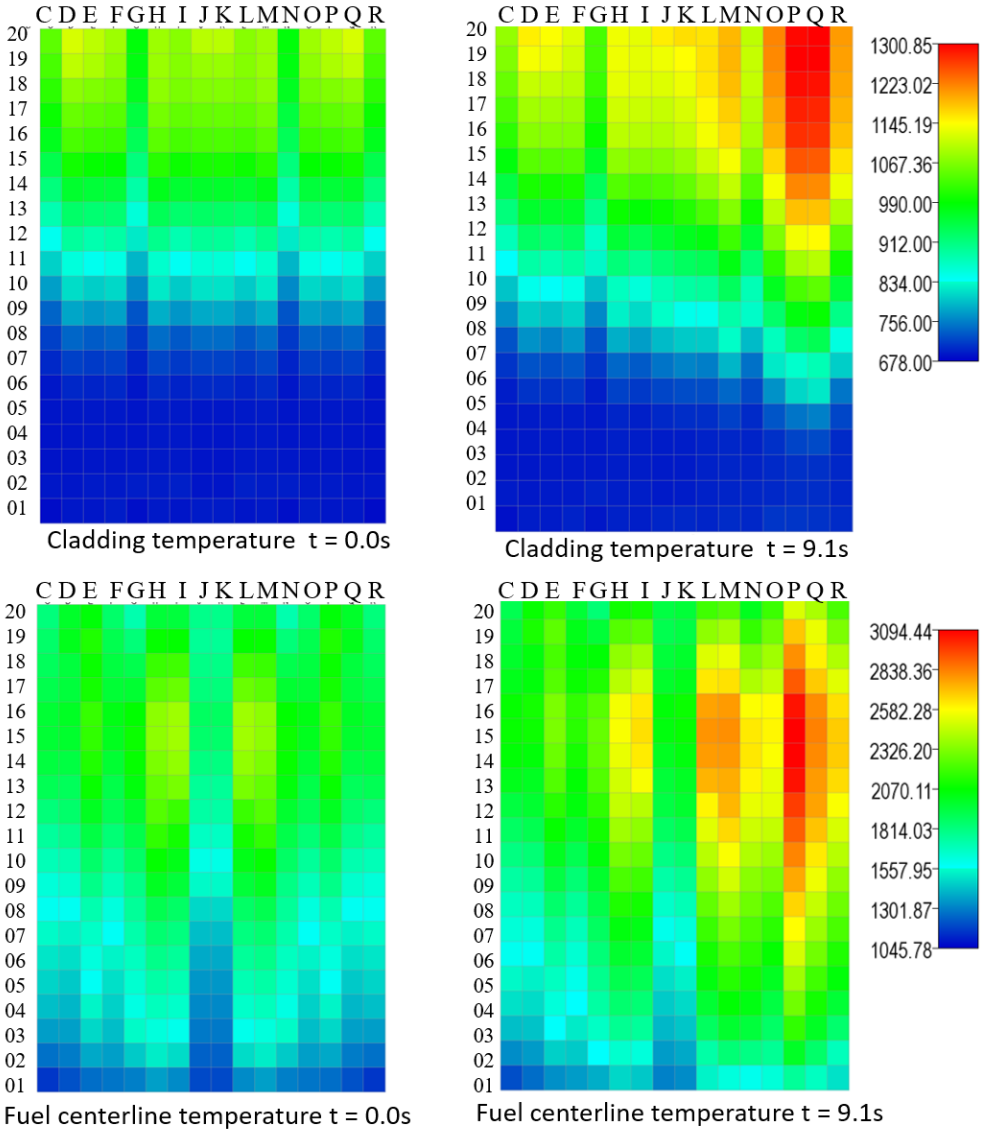

Figure 17 Snapshot of the cladding (top) and fuel centerline (bottom) temperature of row 4 during the CRDA of CR15 without reactor SCRAM

List of Tables

Table 1 Fuel lattice cell specifications

Component	Dimension	Material	Composition [wt%]	Density [g.cm^{-3}]
Centre Tube Coolant	4.6 cm radius	Light Water	100% H2O	Variable
Centre Flow Tube	4.60 cm inner radius ; 0.1 cm thick	Zr-modified 310 Stainless Steel	C: 0.034; Si: 0.51; Mn: 0.74; P: 0.016; S: 0.002; Ni: 20.82; Cr: 25.04; Fe: 51.738; Mo: 0.51; Zr: 0.59	7.9
Inner Fuel Pins (24)	0.415 cm radius; 5.4 cm pitch radius	0-3m | 12.8 wt% PuO_2 in ThO_2	Pu: 11.293; Th: 76.632; O: 12.075	9.91
		3-4m | 12.3 wt% PuO_2 in ThO_2	Pu: 10.851; Th: 77.072; O: 12.077	
		4-5m | 11.5 wt% PuO_2 in ThO_2	Pu: 10.146; Th: 77.775; O: 12.079	
Outer Fuel Pins (24)	0.44 cm radius; 6.575 cm pitch radius	0-3m | 10.24 wt% PuO_2 in ThO_2	Pu: 9.034; Th: 78.882; O: 12.084	9.87
		3-4m | 9.84 wt% PuO_2 in ThO_2	Pu: 8.682; Th: 79.233; O: 12.085	
		4-5m | 9.20 wt% PuO_2 in ThO_2	Pu: 8.117; Th: 79.796; O: 12.087	
Inner Fuel Pins with burnable absorber (8)	0.415 cm radius; 5.4 cm pitch radius (evenly spaced, π/8 angular offset)	0-3m | 12.8 wt% PuO_2 in ThO_2 ; 3 wt% Gd_2O_3 in PuO_2/ThO_2	Pu: 10.954; Th: 74.333; O: 12.11 ; Gd: 2.603	9.82
		3-4m | 12.3 wt% PuO_2 in ThO_2 ; 2 wt% Gd_2O_3 in PuO_2/ThO_2	Pu: 10.635; Th: 75.53; O: 12.10 ; Gd: 1.735	9.85
		4-5m | 11.5 wt% PuO_2 in ThO_2 ; 2 wt% Gd_2O_3 in PuO_2/ThO_2	Pu: 9.943; Th: 76.219; O: 12.103 ; Gd: 1.735	9.85
Outer Fuel Pins with burnable absorber (8)	0.44 cm radius; 6.575 cm pitch radius (evenly spaced, no angular offset)	0-3m | 10.24 wt% PuO_2 in ThO_2 ; 3 wt% Gd_2O_3 in PuO_2/ThO_2	Pu: 8.764; Th: 76.515; O: 12.118 ; Gd: 2.603	9.79
		3-4m | 9.84 wt% PuO_2 in ThO_2 ; 2 wt% Gd_2O_3 in PuO_2/ThO_2	Pu: 8.508; Th: 77.649; O: 12.108 ; Gd: 1.735	9.81
		4-5m | 9.20 wt% PuO_2 in ThO_2 ; 2 wt% Gd_2O_3 in PuO_2/ThO_2	Pu: 7.955; Th: 78.20; O: 12.11 ; Gd: 1.735	9.81
Cladding	0.06 cm thick	Zr-modified 310 Stainless Steel	As above	7.9
Coolant		Light Water	100% H2O	Variable
Liner Tube	7.2 cm inner radius; 0.05 cm thick	Zr-modified 310 Stainless Steel	As above	7.9
Insulator	7.25 cm inner radius; 0.55 cm thick	Yttria Stabilized Zirconia	Zr: 66.63; Y: 7.87; O: 25.5	5.37
Outer Liner Tube	7.8 cm inner radius; 0.05 cm thick	Excel Alloy	Sn: 3.5; Mo: 0.8; Nb: 0.8; Zr 94.9	6.52
Pressure Tube	7.85 cm inner radius; 1.2 cm thick	Excel Alloy	Sn: 3.5; Mo: 0.8; Nb: 0.8; Zr 94.9	6.52
Moderator	25 cm square lattice pitch	Heavy Water	99.833 D2O; 0.167 H2O	1.0851
Plutonium Isotopics		Reactor Grade Plutonium	Pu238: 2.75; Pu239: 51.96; Pu240: 22.96; Pu241: 15.23; Pu242: 7.10	
Control blade body	Span 48.4 cm ; Thickness 1cm ;	Excel Alloy	Sn:3.5; Mo:0.8; Nb:0.8; Zr:94.9	6.52
Control blade absorber	Position on the blade's arm: 16-24 cm ; Thickness 0.8 cm	Stainless Steel 304		7.94

Table 2 Thermal-hydraulic conditions for fuel lattice simulation

Position (mm)	Upward Coolant Density	Upward Coolant Temperature	Cladding Temperature	Liner Temperature	Insulator Temperature
4875	0.068	898.22	1027.86	868.77	678.8
4625	0.071	874.76	1015.29	846.94	665.38
4375	0.074	849.19	995.6	822.77	650.51
4125	0.079	822.58	969.5	797.8	635.14
3875	0.084	796.23	940.27	773.34	620.04
3625	0.091	771.03	909.17	750.17	605.84
3375	0.099	747.67	877.38	729	592.8
3125	0.108	726.72	845.01	710.29	581.2
2875	0.119	708.63	813.5	694.45	571.33
2625	0.133	693.64	783.8	681.62	563.33
2375	0.149	681.79	756.3	671.8	557.17
2125	0.170	672.97	732.66	664.82	552.79
1875	0.195	666.8	712.63	660.28	549.94
1625	0.226	662.8	696.7	657.67	548.31
1375	0.263	660.35	685.4	656.27	547.43
1125	0.309	658.78	678.51	655.37	546.87
875	0.364	657.34	679.99	653.71	545.82
625	0.424	655.07	684.69	650.74	543.96
375	0.483	650.88	689.28	645.52	540.68
125	0.536	644.19	684.35	637.83	535.83

Table 3 Thermal-hydraulic conditions for fuel lattice simulation (cont'd)

Position (mm)	Pressure Tube Temperature	Downward Coolant Temperature	Downward Coolant Density	Fuel Temperature	Center Tube Temperature
4875	453.89	624.65	0.621	1437.34	761.44
4625	449.98	626.29	0.616	1442.78	750.53
4375	445.6	627.74	0.611	1437.4	738.47
4125	441.01	629	0.606	1410.09	725.79
3875	436.44	630.08	0.602	1371.13	713.15
3625	432.1	631	0.599	1327.81	701.01
3375	428.05	631.77	0.596	1284.33	689.72
3125	424.4	632.42	0.593	1242.09	679.57
2875	421.27	632.96	0.591	1200.04	670.79
2625	418.72	633.41	0.589	1159.12	663.53
2375	416.74	633.79	0.588	1120.16	657.79
2125	415.32	634.11	0.586	1083.33	653.54
1875	414.4	634.4	0.585	1053.46	650.6
1625	413.86	634.66	0.584	1032.7	648.73
1375	413.58	634.9	0.583	1017.2	647.62
1125	413.4	635.13	0.582	1005.77	646.96
875	413.06	635.34	0.581	995.09	646.34
625	412.45	635.52	0.580	976.3	645.3
375	411.37	635.66	0.580	946.84	643.27
125	409.77	635.73	0.579	907.14	639.96

Table 4 Branches definitions for cross-sections interpolation

	Control Rod	Central Tube		Fuel	Coolant around fuel pins	
Branches	0 = out 1 = in	Density ($g.cm^{-3}$)	Temperature (K)	Temperature (K)	Density ($g.cm^{-3}$)	Temperature (K)
0 (reference)	0	ρ_{ref_cool1}	T_{ref_cool1}	T_{ref_fuel}	ρ_{ref_cool2}	T_{ref_cool2}
1	1	-	-	-	-	-
2	0	0.02	-	-	-	-
3	0	0.70	-	-	-	-
4	0	-	600	-	-	-
5	0	-	1000	-	-	-
6	0	-	-	600	-	-
7	0	-	-	2000	-	-
8	0	-	-	-	0.02	-
9	0	-	-	-	0.70	-
10	0	-	-	-	-	650
11	0	-	-	-	-	1000
12	1	0.02	-	-	-	-
13	1	0.70	-	-	-	-
14	1	-	600	-	-	-
15	1	-	1000	-	-	-
16	1	-	-	600	-	-
17	1	-	-	2000	-	-
18	1	-	-	-	0.02	-
19	1	-	-	-	0.70	-
20	1	-	-	-	-	650
21	1	-	-	-	-	1000

Table 5 Control rod reactivity worth when fully removed from the core

Control rod removal	BOC (beta = 2.959 mk)								
Control rod number	1	2	4	6	8	10	12	15	16
Reactivity worth (mk)	0.64	0.59	0.60	0.37	0.76	0.84	0.75	0.89	0.55
Reactivity worth ($)	0.21	0.20	0.20	0.12	0.25	0.28	0.25	0.30	0.18

Control rod removal	EOC (beta = 3.153 mk)				
Control rod number	4	5	7	12	15
Reactivity worth (mk)	0.69	0.82	0.67	0.74	0.83
Reactivity worth ($)	0.23	0.27	0.22	0.25	0.28

Table 6 Control rod reactivity worth when fully inserted into the core

Control rod insertion	BOC (beta = 2.959 mk)						
Control rod number	3	5	7	9	11	13	14
Reactivity worth (mk)	-0.54	-0.44	-0.40	-0.54	-0.20	-0.47	-0.46
Reactivity worth ($)	-0.18	-0.15	-0.13	-0.18	-0.07	-0.16	-0.15

Control rod insertion	EOC (beta = 3.153 mk)										
Control rod number	1	2	3	6	8	9	10	11	13	14	16
Reactivity worth (mk)	-0.43	-0.45	-0.52	-0.25	-0.52	-0.55	-0.50	-0.24	-0.54	-0.46	-0.32
Reactivity worth ($)	-0.14	-0.15	-0.17	-0.08	-0.17	-0.18	-0.17	-0.08	-0.18	-0.15	-0.11

Table 7 MCST, MFCLT, and maximum relative power during the CRDA with reactor SCRAM

BOC	Initial	CR1	CR2	CR4	CR6	CR8	CR10	CR12	CR15	CR16
MCST (K)	1119.7	1129.0	1133.7	1129.8	1334.0	1136.6	1141.6	1137.1	1149.3	1142.5
MFCLT(K)	2436.9	2516.5	2549.2	2530.0	3307.9	2570.5	2578.9	2533.5	2536.2	2512.5
Max relative power	1.0	1.208	1.194	1.202	1.121	1.261	1.321	1.261	1.344	1.191

EOC	Initial	CR4	CR5	CR7	CR12	CR15
MCST (K)	1168.9	1187.0	1186.4	1190.8	1187.9	1185.8
MFCLT(K)	2447.8	2536	2534	2552	2535	2528
Max relative power	1.0	1.229	1.293	1.214	1.250	1.302

Table 8 Parametric study on the CRDA of control rod 15 at BOC

CR15 at BOC	Time step (s)	Scram signal (%FP)	Scram delay (s)	Drop time (s)	Max relative power	MCST (K)	MFCLT (K)
Case 0 : Reference	0.02	115	0.6	0.8	1.332	1148.7	2535.6
Case 1 : Time step decrease	0.005	115	0.6	0.8	1.331	1147.6	2533.1
Case 2 : Scram signal	0.02	120	0.6	0.8	1.332	1152.4	2544.4
Case 3 : Scram delay	0.02	115	1.2	0.8	1.332	1173.2	2587.5
Case 4 : Drop time	0.02	115	0.6	0.4	1.3893	1148.4	2540.1
Case 5 : Time step increase	0.1	115	0.6	0.8	1.344	1149.3	2536.2

Table 9 Results for CRDAs without SCRAM

BOC	Initial	CR1	CR2	CR4	CR6	CR8	CR10	CR12	CR15	CR16
MCST (K)	1119.7	1363	1358	1369	1333	1397	1450	1411	1493	1431
MFCLT(K)	2436.9	2855	3139	3097	3307	3478	3787	3379	3735	3577
Max relative power	1.0	1.203	1.189	1.198	1.119	1.255	1.312	1.256	1.333	1.189
New relative steady-state power	-	1.031	1.030	1.029	1.018	1.035	1.034	1.034	1.033	1.024

EOC	Initial	CR4	CR5	CR7	CR12	CR15
MCST (K)	1168.9	1429	1450	1364	1400	1458
MFCLT(K)	2447.8	3233	3400	3122	3100	3350
Max relative power	1.0	1.223	1.285	1.209	1.243	1.295
New relative steady-state power	-	1.037	1.037	1.037	1.038	1.038

Chapter 7

Conclusion and Future work

7.1 Summary of the work

The Canadian Supercritical Water-cooled Reactor was designed by Canadian Nuclear Laboratories and is aligned with the goals of the Generation IV (GEN-IV) International Forum. The design is supposed to meet the goals of the next generation of nuclear reactors: improved economics, enhanced safety, increased proliferation resistance, and become more sustainable. Throughout the last decade, the SCWR concept was subjected to modifications to improve its performance towards the GEN-IV goals. The latest design, however, was lacking reactivity control systems. Moreover, the cladding temperature was shown to exceed the safety margins when the batch cycle was modeled with static orifices at the inlet of the channels. In fact, up to now, there has not been a comprehensive study of fuel cladding temperatures for each channel as a function of burnup and with static orifices. A major contribution of this work was to design a credible control system which, when considered with a set of static orifices, provides acceptable fuel and fuel cladding temperatures over each batch cycle.

In this work a set of existing codes was applied for the first time to the Canadian SCWR to model its behavior. The utilized codes include SCALE/TRITON, PARCS, and RSM4. SCALE/TRITON was selected due to its wide application to LWR physics analysis. A benchmark study was carried out and proved the adequacy of TRITON to simulate the Canadian SCWR lattice cell. The 3D core power distribution calculated in PARCS was compared to previous work and showed good agreement; hence validating its capability of simulating the Canadian SCWR core. Finally, RSM4 was selected as it has been recently modified to include trans-critical and super-critical water modelling capabilities.

Chapter 4 presented two mechanisms designed to control reactivity throughout the batch cycle: gadolinia as a fuel-integrated burnable absorber and a

cruciform control rod in the low-pressure moderator. An optimization process based on a genetic algorithm was utilized to find the control rods' position throughout the equilibrium cycle. The optimization minimized the MCST while constraining k_{eff} and the linear element rating. A unique response surface was created to evaluate the MCST solely based on PARCS calculations to speed up the optimization. The work performed in Chapter 4 led to a new equilibrium cycle which includes the reactivity control systems with a set of static orifices. Unfortunately, the design could not meet the safety limit regarding the MCST. Furthermore, the MFCLT was found to be excessively high and, as a consequence, modifications were needed.

Chapter 5 focused on improving the reactor design to reduce both the MCST and MFCLT. The changes involved axially graded fuel enrichment and fuel-integrated burnable absorber concentration to shape the axial power distribution over the cycle. The core thermal power was lowered by 20% down to 2032 MW to reduce the core power density and fuel temperature. This modification led to a reduction of the overall fuel enrichment to maintain a similar cycle length/average fuel exit burnup. The fueling scheme evolved from a 3-batch to a 4-batch scheme to shorten the cycle length, but the assemblies stay in the core for four cycles leading to a similar fuel exit irradiation. The shorter fuel cycle allowed for easier control of the assembly powers from beginning to end of cycle. Finally, the reactivity worth of the control rod was reduced to obtain finer control over the assembly powers. Unique response surfaces were once again used for the fast evaluation of the MCST and MFCLT. The new optimization process minimized both the MCST and MFCLT while keeping the same constraints as those discussed in Chapter 4. The new design showed a large improvement with an acceptable MFCLT throughout the cycle and a MCST meeting the safety margins for two third of the cycle and exceeded the limit by only 40°C at most. PARCS and RSM4 were also coupled through external scripts to match power distribution/thermal-hydraulic conditions in the core. The optimization results were verified against the coupled results and showed good agreement, hence validating the use of response surfaces for the evaluation of the MCST and MFCLT.

Chapter 6 made use of the new equilibrium cycle with the control rod pattern to evaluate the impact of control rod drop accidents (CRDAs). PARCS and RSM4 interfaced through a series of external scripts to obtain a 3D neutron kinetics/thermal-hydraulics coupled system. PARCS's native branch structure had to be circumvented to perform the necessary cross-sections interpolation based on the local thermal-hydraulic conditions. Due to the asymmetrical nature of CRDAs, the 336 fuel assemblies have been individually modeled in PARCS and RSM4 resulting in the first toolset capable of simulating coupled 3D neutron kinetics/thermal-hydraulics reactivity initiated accidents for the Canadian SCWR. The CRDAs were evaluated for every control rod at BOC

and EOC. In each case, a power pulse was generated by the positive reactivity insertion and a localized power excursion was observed around the dropped rod. In the first phase of the analysis, reactor SCRAM was assumed operational, and all the scenarios but one activated the reactor trip. When tripped, the reactor safely shuts down without exceeding any thermal limits. In the second phase, the reactor SCRAM was not available and the negative power coefficient stabilized the core to a new power level. However, local fuel melting occurred during most of the transients making the reactor SCRAM a requirement for this type of accident. The one particular scenario which did not reach the trip set point led to recommendations related to in-core and local flux measurements similar to the ROP/NOP system in a CANDU.

7.2 Discussion and recommendation for future work

Based on the work performed in this thesis, the author would like to emphasize the conclusions, potential research areas for further improvement and point out the limitations of the work.

7.2.1 Reactivity control systems design

This dissertation proved that the combination of fuel-integrated burnable absorbers and cruciform control rods can achieve both bulk and spatial reactivity control throughout the batch cycle. While the MCST and MFCLT were initially found to be unreasonably high, they were significantly improved after refining the core design. Few suggestions are presented to further improve the Canadian SCWR design:

- The axial assembly design could be divided in more than three enrichment/poison zones. A further optimized graded fuel enrichment/burnable poison concentration along the assembly would lead to a better axial power distribution throughout the batch cycle.
- Consideration for part-length fuel rods and control assemblies, similar to BWR designs, should be made.
- The optimization of the fueling scheme in conjunction with the control rod pattern should be performed and should improve the safety margins throughout the cycle.
- The economics could be improved as the control rods are not fully withdrawn at EOC. Therefore, the cycle length could be extended or the overall fuel enrichment reduced.
- Advanced fuel types such as accident tolerant fuels or a larger fuel volume could lower the fuel temperature, and the core thermal power could be potentially increased.
- The power imbalance within each ring of fuel pins due to the presence of FIBA has not been taken into account. Such imbalance will not

likely change the conclusions of this work, however it would provide more accurate fuel and cladding temperatures.

The genetic algorithm with thermalhydraulic response surfaces provides a fast tool to find optimized control rod pattern and should therefore be considered in future work to evaluate the adequacy of subsequent designs.

The design proposed in this study is promising and should be further investigated. The insertion of control rods parallel to fuel assemblies provides better control over the assembly powers. Consequently, the deviation of the assembly powers from their reference power, imposed by the static orifice, can be more easily minimized leading to lower cladding temperatures. As compared to rod insertion orthogonally to the channels (i.e., horizontally as originally proposed by CNL) there is a potential for local channel power adjustment. Furthermore, the axial control assembly design can shape the axial power distribution throughout the batch cycle and help to reduce the MCST and MFCLT.

7.2.2 Control rod drop accidents

The consequences of a control rod dropping out of the core were evaluated for the Canadian SCWR. The importance of the reactor SCRAM was clearly observed and should be noted, not to stop the power increase but to avoid fuel melting in the fuel assemblies around the dropped rod. Even without SCRAM, the negative power coefficient limits the power excursion and even though the lower coolant density in the vicinity of the fuel pins inserts a positive amount of reactivity, the Doppler effect was found to be very stabilizing and completely negates this undesired positive reactivity insertion.

The low reactivity worth of an individual rod (< 0.3$) combined with the insertion in the low-pressure moderator (i.e., gravity driven drop as opposed to high pressure rod ejection in a PWR) results in a safe transient, assuming the availability of the reactor SCRAM. Even if CRDA events are sensitive to the drop speed and SCRAM delay, the safety margins are far from being challenged.

To ensure the reactor SCRAM in the event of a CRDA, different detection techniques should be investigated such as rate of power change, zone power imbalance or high local neutron flux, as is normal is existing CANDU reactor designs.

7.2.3 Modeling techniques

Due to the lack of information or to avoid excessive computational time, the assumptions were applied to simplify the computations. The few assumptions and approximations utilized are listed below and should be taken into consideration in future work.

- The multi-group transport solution from SCALE was condensed into two energy groups for subsequent use in PARCS. While the energy cut-off was increased to 2.57 eV to take into account the high temperatures in the Canadian SCWR from the usual 0.625 eV for LWRs, the optimum number of energy groups to be used and their lower/upper range should be assessed.
- PARCS diffusion model only uses infinite lattice cross-sections for the fuel assemblies. Errors, especially on the edge of the core, are introduced in the model regarding the actual assembly powers.
- A full-core model of the Canadian SCWR should be built in a stochastic code such as MCNP or SERPENT to provide a reference core.
- The Dittus-Boelter convective heat transfer correlation was used in RSM4. A dedicated heat transfer correlation for supercritical water should be used to increase the confidence in the calculated temperature.
- Radiative heat transfer has not been included in the work performed and should be added for increased fidelity.
- The fixed boundary conditions in RSM4 should be replaced by all the necessary components such as the pumps, steam generators, and condenser.
- The feedback database did not include covariant terms for the thermal-hydraulic variables. If two, or more, thermal-hydraulic variables have a significant influence on other variables, more branches should be added to the database.
- The PARCS interpolation scheme for cross-sections based on the local thermal-hydraulic conditions was shown to perform well for this work. However, the non-linearity of the reactivity change as a function of certain thermal-hydraulic variables has to be carefully dealt with. Transients with important fluid properties variations would require a more specific attention.
- Finally, PARCS source could be modified to extend its branch module to add other feedbacks such as the moderator density or moderator temperature coefficients.

Improving the simulation models would help to increase fidelity and to reduce the uncertainties during transient calculations. Ultimately, the data such as convective heat transfer correlation, fuel conductivity, and fuel melting point should be compared to experimental data to increase confidence in the results.

7.3 Conclusions

In this section, the author provides conclusions based on his analysis of the design over the last several years. Strengths and weaknesses of the design are emphasized as well as the grey areas where the large uncertainties could potentially have a significant effect on the predictions.

As of this writing, the Canadian SCWR has been evaluated as safe when subjected to many different accident scenarios. LOCAs, LOFAs, and now CRDAs have been investigated using various safety codes. Peak fuel and cladding temperatures did not exceed the safety margins, even in the most limiting cases.

However, some transients were shown to be quite sensitive to certain parameters. So far, the most noticeable parameter is the cladding emissivity, which led to unacceptable cladding temperatures in a LOCA scenario when decreased from 0.8 to less than 0.5 [102]. This is due to the radiation being the dominant heat transfer mechanism when there is little to no flow in the channel, and therefore the determination of an accurate value for the cladding emissivity is of high importance. Radiative heat transfer was not included for CRDAs in this study, but is not expected to significantly impact the outcome. Because reactivity initiated events, such as a rod drop, involve sustained coolant flow, they are challenged more by the fuel temperature than the cladding temperature.

The SCWR's negative power coefficient of reactivity results in a stable reactor over all of the transients considered both in this thesis and in all other literature. Moreover, the positive outer coolant void coefficient of reactivity has not been found to be problematic during any transients in existing literature [30, 49]. This is due to outer coolant voiding not occurring in isolation; voiding of the coolant in the outer flow tube is accompanied by a rise in fuel temperature and/or voiding in the coolant of the inner flow tube. This rapidly leads to a strong negative reactivity insertion which counterbalances the relatively small positive reactivity insertion. These effects, when considered as a whole, result in a well-designed fuel bundle.

Although the Canadian SCWR performs as desired under abnormal conditions, very little focus has been given to normal conditions. In the work documented in this thesis (Paper #1) it is clear that some design changes are needed in order to achieve acceptable normal operating margins.

A combination of fuel-integrated burnable absorbers and adjustable control rods were suitable to control the bulk of the reactivity throughout the batch cycle (Paper #2). The use of control blades inserted from the bottom of the core provides a high degree of channel power control because the effect is largely localized to the rod's neighboring channels. However, bottom insertion tends to force the axial power peak to the top of the core where the

coolant temperatures are the highest, thereby increasing the cladding temperatures to undesirable levels.

Alternative designs using horizontal control rods would provide better axial power shape control, but have relatively poor individual channel power control [8]. Given that no design has been shown to be universally preferred, the reactivity management of the Canadian SCWR still needs more research. Fine reactivity control is crucial to the SCWR and it cannot utilize coolant based absorbers (similar to boron in a PWR), hence fuel integrated absorbers, such as those analyzed in this thesis, are needed. Partial length fuel rods may also help limit reactivity and provide some form of spatial power shaping, but exceeded the scope of this thesis.

Aside from reactivity control systems, one of the SCWR's major issues is the high fuel centerline temperature. Even though the peak fuel centerline temperature was successfully reduced to acceptable values, the core power had to be reduced to 20% below the reference design. This is a matter that should be rectified at the design level by increasing the number of fuel assemblies or modifying the fuel assembly geometry to lower power density. Such a low margin between normal and limit fuel temperatures makes the design sensitive to reactivity induced accidents as shown in Paper #3. Alternatively, some Accident Tolerant Fuel (ATF) concepts could be deployed to significantly reduce the normal operating fuel temperatures, providing more operating room and enabling the reactor power to remain at the reference level.

Conceptual changes are also needed to deal with high cladding surface temperatures. While the work performed in this thesis was generally as conservative as possible, margins for uncertainties and operation were not taken into consideration. The 850°C operating sheath temperature limit was not achieved over the entire batch cycle in this work, even considering the changes in reactor design.

Comparatively, all other SCWR concepts have a cladding surface temperature limit of 600-650°C. If the Canadian concept was to align its MCST objective to the more widely accepted 650°C, the 625°C coolant outlet temperature would have to be lowered to approximately 500°C. Given that the reactor efficiency is linked to the coolant outlet temperature, this change would be accompanied by a decrease in efficiency. However, the MCST would be considerably improved due to the very low convective heat transfer coefficient between 500°C and 625°C. Subsequently, the 350°C inlet coolant temperature should also be modified to approximately 250°C to keep a similar coolant enthalpy rise along the assembly.

At this stage in the design evolution, computer codes are not yet fully validated for application to these reactors due to the relatively recent interest in supercritical water coolant. However given that there are no trans-critical

transients in this work, it is likely that the code performs reasonably well. While the thermalhydraulic correlations require further improvement, large changes (i.e., 30 to 50%) are unlikely to have significant impact on the conclusions of this work since i) under normal operations there is still a portion of the batch cycle with unacceptable sheath temperatures (so that any changes in heat transfer would only affect the percentage of acceptable batch cycle performance) and ii) under rod-drop events acceptable fuel temperatures require in-core flux and spatial neutronic protection (with such protection all rod drop sequences would be terminated with a large margin to fuel melting).

Finally, optimization techniques such as heuristic algorithms should be widely utilized when evaluating potential designs in future works. Such algorithms are time efficient and can explore a large searching space with decreased need for computing resources. While the optimization of current reactors is restricted by their geometry, future concepts offer a lot of flexibility and allow for multi-variate optimization. Thus, heuristic algorithms are ideally suited to explore improvements to the safety and economics of GEN IV reactor concepts.

References

[1] World Nuclear Association, "Plans For New Reactors Worldwide," [Online]. Available: http://www.world-nuclear.org/information-library/current-and-future-generation/plans-for-new-reactors-worldwide.aspx.

[2] "GEN IV International Forum," [Online]. Available: https://www.gen-4.org/gif/jcms/c_9502/generation-iv-goals.

[3] B. Gates. [Online]. Available: https://www.ted.com/talks/bill_gates/discussion?language=en.

[4] [Online]. Available: http://bigpicture.unfccc.int/#content-the-paris-agreemen.

[5] R. Pachauri and L. Meyer, "IPCC, 2014: Climate Change 2014: Synthesis Report. Contribution of Working Groups I, II and III to the Fifth Assessment Report of the Intergovernmental Panel on Climate Change," Geneva, Switzerland, 2014.

[6] M. McDonald, B. Hyland, H. Hamilton, L. Leung, N. Onder, J. Pencer and R. Xu, "Preconceptual fuel design concepts for the Canadian SCWR," in *The 5th International Symposium on Supercritical Water-cooled Reactors*, Vancouver, British Columbia, Canada, 2011.

[7] M. Magill, J. Pencer, R. Pratt, W. Young, G. Edwards and B. Hyland, "Thorium Fuel Cycles in the CANDU Supercritical Water Reactor," in *The 5th International Symposium on Supercritical Water-cooled Reactors (ISSCWR-5)*, Vancouver, British Columbia, Canada, 2011.

[8] M. McDonald, A. Colton and J. Pencer, "Power flattening and reactivity suppression strategies for the Canadian Supercritical Water Reactor concept," in *35th Annual Conference of the Canadian Nuclear Society*, Saint John, New-Brunswick, Canada, 2015.

[9] D. Hummel, "Transient neutronic-thermalhydraulic coupling in a PT-SCWR," Hamilton, Ontario, Canada, 2015.

[10] D. Rozon, Introduction to Nuclear Reactor Kinetics, Montreal: Polytechnic International Press, 1992.

[11] J. Duderstadt and L. Hamilton, Nuclear Reactor Analysis, John Wiley and Sons, Inc, 1976.

[12] Laby and Kaye, "Table of Physical and Chemical Constants, Sec 4.7.1. Nuclear Fission," [Online]. Available: http://www.kayelaby.npl.co.uk/atomic_and_nuclear_physics/4_7/4_7_1.html.

[13] "Nuclear Data Center Japan Atomic Energy Agency: Fission product yields," [Online]. Available: http://wwwndc.jaea.go.jp/cgi-bin/FPYfig?iso=nPu239&typ=g1&yld=i&zlog=unset.

[14] J. Briesmeister, "MCNP - A general Monte-Carlo N-Particle Transport, Version 4C," 2000.

[15] J. Shultis and R. Faw, Fundamentals of Nuclear Science and Engineering, CRC Press, 2008.

[16] "National Nuclear Data Center," [Online]. Available: http://www.nndc.bnl.gov/exfor/endf00.jsp.

[17] Oak Ridge National Laboratory, "NEWT: a new transport algorithm for two-dimensional discrete-ordinates analysis in non-orthogonal geometries, ORNL/TM-2005/39 Version 6.1 Sect. F.21," Oak Ridge, Tennessee, 2011.

[18] G. Marleau, A. Hebert and R. Roy, "A User Guide for DRAGON 3.06," Institut de genie nucleaire, Departement de genie physique, Ecole Polytechnique de Montreal, Montreal, 2008.

[19] "HELIOS Documentation," Studsvik Scandpower, 2000.

[20] Y. Oka, Nuclear Reactor Design, Tokyom Japan: Ohmsha Ltd, 2010.

[21] N. Greene, "BONAMI: Resonance self-shielding by the bondarenko method. ORNL/TM-2005/39 Version 6.1 Sect. F1," Oak Ridge National Laboratory, Oak Ridge, Tennessee, 2011.

[22] Oak Ridge National Laboratory, "SCALE: A comprehensive Modelling and Simulation Suite for Nuclear Safety Analysis and Design. ORNL/TM-2005/39 Version 6.1," ORNL/TM-2005/39 Version 6.1, Oak Ridge, Tennessee, 2011.

[23] S. Goluoglu, D. Hollenbach, N. Landers, L. Petrie, J. Bucholz, C. Weber and C. Hopper, "The material information processor for SCALE. ORNL/TM-2005/39 Version 6.1 Sect. M7," Oak Ridge National Laboratory, Oak Ridge, Tennessee, 2011.

[24] Oak Ridge National Laboratory, "ORIGEN-S: Depletion module to calculate neutron activation, actinide transmutation, fission product generation, and radiation source terms. ORNL/TM-2005/39 Version 6.1 Sect. F7.," Oak Ridge, Tennessee, 2011.

[25] C. M. Allison and J. Hohorst, "Role of RELAP5/SCDAPSIM in Nuclear Safety," *Science and Technology of Nuclear Installations,* vol. 2010, 2010.

[26] B. Hanna, "CATHENA: a thermalhydraulics code for CANDU analysis," *Nuclear Engineering and Design,* vol. 180, pp. 113-131, 1998.

[27] P. Wu, J. Gou, J. Shan, Y. Jiang, J. Yang and B. Zhang, "Safety analysis code SCTRAN development for SCWR and its application to CGNPC SCWR," *Annals of Nuclear Energy,* vol. 56, pp. 122-135, 2013.

[28] U.S.NRC, "TRACE V5.840 User's Manual," 2014.

[29] C. Allison, R. Wagner, J. Hohorst, M. Perez-Ferragut, V. Martinez-Quiroga, J. Freixa, E. Mas de les Valls, Z. Fu, H.-C. Lin and M. Lou, "The development of RELAP/SCDAPSIM/MOD4.0 for advanced fluid systems design analysis," in *NUTHOS-11: The 11th International Topical Meeting on Nuclear Reactor Thermal Hydraulics, Operation and Safety*, Gyeongju, Korea, 2016.

[30] C. Lou, "Loss of coolant accident simulation for the Canadian supercritical water-cooled reactor using RELAP5/MOD4," Hamilton, Ontario, Canada, 2016.

[31] N. Todreas and M. Kazimi, Nuclear Systems Vol.1, Boka Raton, Florida: CRC Press Taylor & Francis Group, 2012.

[32] "RELAP5/MOD3.3 Code Manual Volume 1: Code Structure, System Models, and Solution Models," Information Systems Laboratories, Inc, October 2010.

[33] J. Shan, W. Chen, B. Rhee and L. Leung, "Coupled neutronics/thermal–hydraulics analysis of CANDU–SCWR fuel channel," *Annals of Nuclear*

Energy, vol. 37, pp. 58-65, 2010.

[34] J. Pencer, "SCWR 78-element bundle reference model," AECL internal report 217-123700-REPT-001, 2011.

[35] D. Hummel, S. Langton, M. Ball, D. Novog and A. Buijs, "Description and Preliminary Results of a Two-Dimensional Lattice Physics Code Benchmark for the Canadian Pressure Tube Supercritical Water-cooled Reactor (PT-SCWR)," in *The 6th International Symposium on Supercritical Water-Cooled Reactors (ISSCWR-6)*, Shenzhen, Guangdong, China, 2013.

[36] J. Pencer, W. D., Colton.A., X. Wang, L. Blomeley, V. Anghel and S. Yue, "Core Neutronics for the Canadian SCWR Conceptual Design," in *The 6th International Symposium on Supercritical Water-Cooled Reactors*, Shenzhen, Guangdong, China, 2013.

[37] A. Dominguez, N. Onder, J. Pencer and D. Watts, "Canadian SCWR Bundle Optimization for the New Fuel Channel Design," in *The 6th International Symposium on Supercritical Water-cooled Reactors (ISSCWR-6)*, Shenzhen, Guangdong, China, 2013.

[38] J. Pencer and A. Colton, "Progression of the Lattice Physics Concept for the Canadian Supercritical Water Reactor," in *34th Annual Conference of the Canadian Nuclear Society*, Toronto, Ontario, Canada, 2013.

[39] G. Harrisson and G. Marleau, "Simulation Strategy for the Evaluation of Neutronic Property of Canadian SCWR fuel channel," *Science and Technology of Nuclear Installations*, vol. 2013, 2013.

[40] Oak Ridge National Laboratory, "MCDANCOFF Data guide ORNL/TM-2005/39 Version 6.1 Section M.24," Oak Ridge, Tennessee, 2011.

[41] J. Valko, S. Feher, J. Hoogenboom and J. Slobben, "Calculation of the void reactivity of CANDU lattices using the SCALE code system," *Nuclear Engineering and Design*, vol. 159, pp. 225-231, 1995.

[42] H. Raouafi and G. Marleau, "Monte Carlo Simulation of Inclined Reactivity Control Rod and Boron Poisoning for the Canadian-SCWR Supercell," *Journal of Nuclear Engineering and Radiation Science*, vol. 2, 2016.

[43] B. Ade, "SCALE/TRITON Primer: A primer for Light Water Reactor Lattice Physics Calculations," U.S NRC, NUREG/CR-7041 ORNL/TM-2011/21,

2012.

[44] X. Wang, "Investigation of neutron absorbers for reactivity control and shutdown systems for the Canadian Super Critical Water Reactor (SCWR). 217-123700-440-008 Revision 0.," AECL, 2013.

[45] L. Massimo, Physics of High Temperature Reactors, NY: Pergamon Press, 1976.

[46] A. Moghrabi and D. Novog, "Optimization approach of energy group structure for the Canadian pressure tube supercritical water reactor," in *37th Annual Conference of the Canadian Nuclear Society*, Niagara Falls, Ontario, Canada, 2017.

[47] F. Salaun and D. Novog, "The Impact of the Radial Reflector on the 8-group Cell-Averaged Cross-Sections for the SCWR 62-element Lattice Cell," in *Canada-China conference on Advanced Reactor Development (CCCARD-2014)*, Niagara Falls, Ontario, Canada, 2014.

[48] W. Shen, "Assessment of the traditional neutron-diffusion core-analysis method for the analysis of the Super-Critical Water Reactor," *Annals of Nuclear Energy,* vol. 45, pp. 1-7, 2012.

[49] D. Hummel and D. Novog, "Coupled 3D neutron kinetics and thermalhydraulic characteristics of the Canadian supercritical water reactor," *Nuclear Engineering and Design,* vol. 298, pp. 78-89, 2016.

[50] J. Sharpe and A. Buijs, "Practical environment-corrected discontinuity factors and homogenized parameters for improved PT-SCWR neutron diffusion solutions," *Annals of Nuclear Energy,* vol. 111, pp. 101-117, 2018.

[51] T. Downar, Y. Xu and V. Seker, "PARCS v3.0 U.S. NRC Core Neutronic Simulator User Manual," 2013.

[52] A. Ward, Y. Xu and T. Downar, "GenPMAXS v6.1.2: Code for Generating the PARCS Cross Section Interface File PMAXS," 2013.

[53] E. Varin, A. Hebert, R. Roy and J. Koclas, "A User Guide for DONJON Version 3.01," Institut de genie nucleaire, Departement de genie physique, Ecole Polytechnique de Montreal, Montreal, 2005.

[54] D. Wang and S. Wang, "A preliminary CATHENA thermalhydraulic model of the Canadian SCWR for safety analysis," *Atomic Energy of Canada*

Limited Nuclear Review, vol. 3, no. 1, pp. 9-16, 2014.

[55] X. Cheng and T. Schulenberg, "Heat Transfer at Supercritical Pressures - Literature Reveiw and Application to an HPLWR," Institut fur Kern und Energietechnik Programm Nukleare Sicherheitsforschung, Karlsruhe, Germany, 2001.

[56] C. Darwin, On the origin of species, London, England: John Murray, 1859.

[57] J. Holland, "Genetic Algorithms," *Scientific American,* vol. 267, pp. 66-72, 1992.

[58] B. Adams, M. Ebeida, M. Eldred, J. Jakeman, L. Swiler, W. Bohnhoff, K. Dalbey, J. Eddy, K. Hu, D. Vigil, L. Bauman and P. Hough, "Dakota, A Multilevel Parallel Object-Oriented Framework for Design Optimization, Parameter Estimation, Uncertainty Quantification, and Sensitivity Analysis. Version 5.4 Reference Manual," Sandia National Laboratories, Livermore, CA, 2013.

[59] B. Adams, M. Ebeida, M. Eldred, J. Jakeman, L. Swiler, W. Bohnhoff, K. Dalbey, J. Eddy, K. Hu, D. Vigil, L. Bauman and P. Hough, "Dakota, A Multilevel Parallel Object-Oriented Framework for Design Optimization, Parameter Estimation, Uncertainty Quantification, and Sensitivity Analysis. Version 5.4 User's Manual," Sandia National Laboratories, Livermore, CA, 2013.

[60] R. Kolisch and S. Hartmann, "Heuristic Algorithms for the Resource-Constrained Project Scheduling Problem: Classification and Computational Analysis," in *Project Scheduling: Recent Models, Algorothms and Applications*, Berlin, Kluwer Academic Publishers, 1999, pp. 147-178.

[61] H. Eiselt and C. Sandblom, "Heuristic Algorithms," in *Integer Programming and Network Models*, Springer PRess, 2000, pp. 229-258.

[62] L. Davis, Handbook of Genetic Algorithms, New York: Van Nostrand Reinhold, 1991.

[63] D. Goldberg, "Genetic Algorithms," in *Search, Optimimization and Learning Machine,* Reading, MA, Addison-Wesley, 1989.

[64] J. Francois, C. Martin del Campo, R. Francois and L. Morales, "A practical optimization procedure for radial BWR fuel lattice design using tabu search with a multiobjective function," *Annals of Nuclear Energy,* vol. 30, pp. 1213-

1229, 2003.

[65] J. Casillo-Mendez, V. Jauregui Chavez, J. Ortiz-Servin, J. Montes-Tadeo, R. Perusquia and L. Morales, "A statistical analysis in the BWR fuel lattice design," *Annals of Nuclear Energy*, vol. 90, pp. 83-92, 2016.

[66] A. Castillo, C. Martin del Campo, J. Montes-Tadeo, J. Francois, J. Ortiz-Servin and R. Perusquia del Cueto, "Comparison of heuristic optimization techniques for the enrichment and gadolinia distribution in BWR fuel lattices and decision analysis," *Annals of Nuclear Energy*, vol. 63, pp. 556-564, 2014.

[67] C. Lin and T.-H. Lin, "Automatic fuel lattice design in a boiling water reactor using a particle swarm optimization algorithm and local search," *Annals of Nuclear Energy*, vol. 47, pp. 98-103, 2012.

[68] J. Ortiz, A. Castillo, J. Montes, R. Perusquia and J. Hernandez, "Nuclear Fuel Lattice Optimization Using Neural Networks and a Fuzzy Logic System," *Nuclear Science and Engineering*, vol. 162, no. 2, pp. 148-157, 2009.

[69] J. Ortiz-Servin, J. Cadenas, D. Pelta, A. Castillo and J. Montes-Tadeo, "Nuclear fuel lattice performance analysis by data mining techniques," *Annals of Nuclear Energy*, vol. 80, pp. 236-247, 2015.

[70] T. Rogers, J. Ragusa, S. Schultz and R. St Clair, "Optimization of PWR fuel assembly radial enrichment and burnable poison location based on adaptive simulated annealing," *Nuclear Engineering and Design*, vol. 239, pp. 1019-1029, 2009.

[71] Y. Hirano, K. Hida, K. Sakurada and M. Yamamoto, "Optimization of Fuel Rod Enrichment Distribution to Minimize Rod Power Peaking throughout Life within BWR Fuel Assembly," *Nuclear Science and Technology*, vol. 34, no. 1, pp. 5-12, 1997.

[72] C. Martin del Campo, J. Francois and L. Morales, "Boiling Water Reactor Fuel Assembly Axial Design Optimization Using Tabu Search," *Nuclear Science and Engineering*, vol. 142, no. 1, pp. 107-115, 2002.

[73] J. Francois, C. Martin del Campo, L. Morales and M.-A. Palomera, "Development of a Scatter Search Optimization Algortihm for Boiling Water Reactor Fuel LAttice Design," *Nuclear Science and Engineering*, vol. 155, no. 3, pp. 367-377, 2007.

[74] W.-H. Tung, T.-T. Lee, W.-S. Kuo and S.-J. Yaur, "Fuel lattice design in a boiling water reactor using a knowledge-based automation system," *Nuclear Engineering and Design,* vol. 293, pp. 63-74, 2015.

[75] C. Martin del Campo, J. Francois, R. Carmona and I. Oropeza, "Optimization of BWR fuel lattice enrichment and gadolinia distribution using genetic algorithms and knowledge," *Annals of Nuclear Energy,* vol. 34, pp. 248-253, 2007.

[76] S. Yilmaz, K. Ivanov, S. Levine and M. Mahgerefteh, "Genetic Algorithm to Optimize the UO2/Gd2O3 Fuel Pin Designs in a Pressurized Water Reactor," *Nuclear Technology,* vol. 156, no. 2, pp. 168-179, 2006.

[77] K. Bjork, "A BWR fuel assembly design for efficient use of plutonium in thorium-plutonium fuel," *Progress in Nuclear Energy,* vol. 65, pp. 56-63, 2013.

[78] J. Washington and J. King, "Optimization of plutonium and minor actinide transmutation in an AP1000 fuel assembly via a genetic search algorithm," *Nuclear Engineering and Design,* vol. 311, pp. 199-212, 2017.

[79] V. Lattarulo, B. Lindley and G. Parks, "Application of the MOAA for the optimization of CORAIL assemblies for nuclear reactors," in *IEEE Congress on Evolutionary Computation (CEC)*, Beijing, China, 2014.

[80] D. Hummel and D. Novog, "Fuel composition optimization in a 78-element fuel bundle for use in a pressure tube type supercritical water-cooled reactor," in *The 3rd China-Canada Joint Workshop on Supercritical Water-Cooled Reactors, CCSC-2012*, Xi'an, China, 2012.

[81] C. Martin del Campo, J. Francois, A. Barragan and M. Palomera, "Boiling water reactor fuel lattice enrichment distribution optimization using tabu search and fuzzy logic," *Nuclear Technology,* vol. 157, no. 3, pp. 251-260, 2007.

[82] C. Martin del Campo, J. Francois and H. Lopez, "AXIAL: a system for boiling water reactor fuel assembly axial optimization using genetic algorithms," *Annals of Nuclear Energy,* vol. 28, pp. 1667-1682, 2001.

[83] W.-H. Tung, T.-T. Lee, W.-S. Kuo and S.-J. Yaur, "Optimization of axial enrichment distribution for BWR fuels using scoping libraries and block coordinate descent method," *Nuclear Engineering and Design,* vol. 313, pp.

84-95, 2017.

[84] T. Yang, X. Liu and X. Cheng, "Optimization of multilayer fuel assemblies for supercritical water-cooled reactors with mixed neutron spectrum," *Nuclear Engineering and Design,* vol. 249, pp. 159-165, 2012.

[85] W. Raza and K.-Y. Kim, "Shape Optimization of 19-Pin Wire-Wrapped Fuel Assembly of LMR Using Multiobjective Evolutionary Algorithm," *Nuclear Science and Engineering,* vol. 161, no. 2, pp. 245-254, 2009.

[86] F. Khoshahval, A. Zolfaghari and H. Minuchehr, "A new method for multi-objective in core fuel management optimization using biogeography based algorithm," *Annals of Nuclear Energy,* vol. 73, pp. 294-303, 2014.

[87] M. DeChaine and M. Feltus, "Nuclear fuel management optimization using genetic algorithms," *Nuclear Technology,* vol. 111, pp. 109-114, 1995.

[88] N. Poursalehi, A. Zolfaghari and A. Minuchehr, "A novel optimization method, Effective Discrete Firefly Algorithm, for fuel reload design of nuclear reactors," *Annals of Nuclear Energy,* vol. 81, pp. 263-275, 2015.

[89] C.-H. Chen and C.-H. Wu, "Development of an automatic tool for BWR loading pattern optimization by utilizing genetic algorithm," in *PHYSOR 2010 - Advances in Reactor Physics to Power the Nuclear Renaissance*, Pittsburgh, Pennsylvania, USA, 2010.

[90] Z. Gong, K. Wang and D. Yao, "Loading pattern optimization cooperatively using two new algorithms," in *PHYSOR 2010 - Advances in Reactor Physics to Power the Nuclear Renaissance*, Pittsburgh, Pennsylvania, USA, 2010.

[91] H. Lee, H. Shim and C. Kim, "Parallel Computing Adaptive Simulated Annealing Scheme for Fuel Assembly Loading Pattern Optimization in PWRs," *Nuclear Technology,* vol. 135, no. 1, pp. 39-50, 2001.

[92] J.-M. Do, J.-J. Lautard, A.-M. D. S. Baudron and G. Arnaud, "Use of Meta-Heuristics for Design of Fuel Loading Pattern in light water Reactor comprising some Radial and Axial Heterogeneities," in *IEEE International Parallel and Distributed Processing Symposium*, Anchorage, AK, USA, 2011.

[93] C.-D. Wang and C. Lin, "Automatic boiling water reactor control rod pattern design using ant colony optimization algorithm," *Nuclear Technology,* vol.

176, pp. 72-82, 2010.

[94] C.-D. Wang and C. Lin, "Automatic boiling water reactor control rod pattern design using particle swarm optimization algorithm and local search," *Nuclear Engineering and Design,* vol. 255, pp. 273-279, 2013.

[95] J. Ortiz and I. Requena, "Azcatl-CRP: An ant colony-based system for searching full power control rod pattern in BWRs," *Annals of Nuclear Energy,* vol. 33, pp. 30-36, 2005.

[96] J. Montes, J. Ortiz, I. Requena and R. Perusquia, "Searching for full power control rod patterns in a boiling water reactor using genetic algorithms," *Annals of Nuclear Energy,* vol. 31, pp. 1939-1954, 2004.

[97] J.-L. Francois, C. Martin del Campo and A. Tavares, "Development of a BWR control rod pattern design system based on fuzzy logic and knowledge," *Annals of Nuclear Energy,* vol. 31, pp. 343-356, 2004.

[98] J. Ortiz-Servin, J. Castillo and D. Pelta, "GreeNN: A hybrid method for the coupled optimization of the axial and radial design of BWR fuel assemblies," *Progress in Nuclear Energy,* vol. 52, pp. 249-256, 2010.

[99] A. Castillo, J. Ortiz, J. Montes and R. Perusquia, "Fuel loading and control rod patterns optimization in a BWR using tabu search," *Annals of Nuclear Energy,* vol. 34, pp. 207-212, 2007.

[100] C.-H. Chen, P.-F. Lin and Y.-N. Huang, "PLAYGO: Program for BWR LP-CRP Automatic Yielding by using GA Optimization," *Nuclear Engineering and Design,* vol. 322, pp. 427-443, 2017.

[101] J. Ortiz-Servin, J. Castillo and D. Pelta, "BWR fuel cycle optimization using neural networks," *Nuclear Engineering and Design,* vol. 241, pp. 3729-3735, 2011.

[102] P. Wu, J. Shan, J. Gou, L. Leung, B. Zhang et B. Zhang, «Heat transfer effectiveness for cooling of Canadian SCWR fuel assembly under the LOCA/LOECC scenario,» *Annals of Nuclear Energy,* vol. 81, pp. 306-319, 2015.

Appendix A

Pin-wise Dancoff factors for the Canadian SCWR lattice cell

	Pin number (Inner ring)																	
Axial position (mm)	**1**	**2**	**3**	**4**	**5**	**6**	**7**	**8**	**9**	**10**	**11**	**12**	**13**	**14**	**15**	**16**	**17**	**Average**	**Std Dev**
125 (bottom)	0.3299	0.3311	0.3359	0.3345	0.3350	0.3345	0.3358	0.3354	0.3355	0.3337	0.3308	0.3357	0.3297	0.3308	0.3331	0.3349	0.3361	**0.3337**	2.2E-03
375	0.3412	0.3425	0.3473	0.3459	0.3465	0.3460	0.3472	0.3468	0.3468	0.3451	0.3422	0.3471	0.3411	0.3421	0.3444	0.3463	0.3475	**0.3451**	2.3E-03
625	0.3549	0.3563	0.3612	0.3598	0.3603	0.3599	0.3610	0.3607	0.3606	0.3590	0.3560	0.3610	0.3549	0.3559	0.3582	0.3601	0.3613	**0.3589**	2.3E-03
875	0.3698	0.3714	0.3763	0.3749	0.3755	0.3750	0.3761	0.3758	0.3756	0.3741	0.3711	0.3760	0.3700	0.3708	0.3732	0.3751	0.3764	**0.3739**	2.3E-03
1125	0.3844	0.3861	0.3911	0.3896	0.3902	0.3898	0.3908	0.3905	0.3902	0.3889	0.3858	0.3907	0.3847	0.3855	0.3879	0.3898	0.3910	**0.3886**	2.3E-03
1375	0.3976	0.3994	0.4044	0.4029	0.4036	0.4032	0.4041	0.4038	0.4034	0.4022	0.3991	0.4040	0.3981	0.3987	0.4011	0.4030	0.4043	**0.4019**	2.3E-03
1625	0.4091	0.4111	0.4160	0.4145	0.4153	0.4149	0.4158	0.4155	0.4149	0.4139	0.4108	0.4157	0.4098	0.4103	0.4128	0.4147	0.4159	**0.4136**	2.3E-03
1875	0.4191	0.4212	0.4261	0.4246	0.4253	0.4250	0.4258	0.4255	0.4249	0.4240	0.4209	0.4257	0.4199	0.4203	0.4228	0.4247	0.4259	**0.4236**	2.3E-03
2125	0.4275	0.4298	0.4347	0.4331	0.4339	0.4336	0.4344	0.4341	0.4334	0.4326	0.4294	0.4343	0.4285	0.4288	0.4313	0.4332	0.4345	**0.4322**	2.3E-03
2375	0.4347	0.4370	0.4419	0.4403	0.4412	0.4408	0.4416	0.4413	0.4405	0.4398	0.4367	0.4415	0.4357	0.4360	0.4385	0.4404	0.4416	**0.4394**	2.3E-03
2625	0.4407	0.4431	0.4480	0.4464	0.4473	0.4469	0.4477	0.4474	0.4465	0.4459	0.4427	0.4475	0.4418	0.4421	0.4446	0.4465	0.4477	**0.4455**	2.4E-03
2875	0.4458	0.4483	0.4531	0.4515	0.4524	0.4521	0.4528	0.4525	0.4516	0.4510	0.4479	0.4526	0.4470	0.4471	0.4497	0.4516	0.4528	**0.4506**	2.4E-03
3125	0.4500	0.4526	0.4574	0.4558	0.4567	0.4564	0.4571	0.4568	0.4559	0.4553	0.4522	0.4569	0.4513	0.4514	0.4540	0.4559	0.4570	**0.4549**	2.4E-03
3375	0.4536	0.4562	0.4610	0.4594	0.4604	0.4601	0.4607	0.4604	0.4594	0.4590	0.4558	0.4606	0.4549	0.4550	0.4577	0.4595	0.4606	**0.4585**	2.4E-03
3625	0.4566	0.4593	0.4640	0.4624	0.4634	0.4631	0.4638	0.4634	0.4625	0.4620	0.4588	0.4636	0.4580	0.4581	0.4607	0.4626	0.4637	**0.4615**	2.4E-03
3875	0.4592	0.4619	0.4666	0.4650	0.4660	0.4657	0.4663	0.4660	0.4650	0.4646	0.4614	0.4662	0.4606	0.4606	0.4633	0.4652	0.4662	**0.4641**	2.4E-03
4125	0.4614	0.4641	0.4688	0.4672	0.4682	0.4679	0.4685	0.4682	0.4672	0.4668	0.4636	0.4684	0.4628	0.4628	0.4655	0.4674	0.4684	**0.4663**	2.4E-03
4375	0.4632	0.4659	0.4707	0.4690	0.4701	0.4698	0.4704	0.4700	0.4690	0.4686	0.4655	0.4702	0.4647	0.4646	0.4673	0.4692	0.4702	**0.4681**	2.4E-03
4625	0.4647	0.4674	0.4722	0.4705	0.4716	0.4713	0.4719	0.4716	0.4705	0.4702	0.4670	0.4717	0.4662	0.4661	0.4688	0.4707	0.4717	**0.4696**	2.4E-03
4875 (top)	0.4659	0.4687	0.4734	0.4717	0.4728	0.4725	0.4731	0.4728	0.4717	0.4714	0.4682	0.4729	0.4674	0.4674	0.4700	0.4719	0.4729	**0.4709**	2.4E-03

	Pin number (Outer ring)																	
Axial position (mm)	**1**	**2**	**3**	**4**	**5**	**6**	**7**	**8**	**9**	**10**	**11**	**12**	**13**	**14**	**15**	**16**	**17**	**Average**	**Std Dev**
125 (bottom)	0.2711	0.2716	0.2680	0.2724	0.2676	0.2680	0.2723	0.2711	0.2700	0.2729	0.2689	0.2709	0.2686	0.2721	0.2724	0.2714	0.2698	**0.27054**	1.7E-03
375	0.2834	0.2839	0.2802	0.2847	0.2798	0.2802	0.2846	0.2835	0.2822	0.2852	0.2811	0.2832	0.2807	0.2844	0.2847	0.2837	0.2822	**0.2828**	1.8E-03
625	0.2983	0.2990	0.2950	0.2996	0.2947	0.2949	0.2996	0.2986	0.2970	0.3002	0.2958	0.2982	0.2955	0.2994	0.2996	0.2987	0.2972	**0.29772**	1.8E-03
875	0.3147	0.3153	0.3112	0.3158	0.3110	0.3110	0.3160	0.3150	0.3131	0.3165	0.3119	0.3146	0.3116	0.3157	0.3158	0.3150	0.3136	**0.31398**	1.9E-03
1125	0.3306	0.3314	0.3270	0.3316	0.3269	0.3267	0.3320	0.3311	0.3289	0.3324	0.3276	0.3306	0.3273	0.3317	0.3316	0.3310	0.3296	**0.32988**	2.0E-03
1375	0.3450	0.3459	0.3413	0.3460	0.3413	0.3410	0.3465	0.3457	0.3432	0.3467	0.3418	0.3451	0.3416	0.3461	0.3460	0.3454	0.3441	**0.34427**	2.0E-03
1625	0.3577	0.3586	0.3538	0.3586	0.3539	0.3535	0.3592	0.3584	0.3557	0.3593	0.3542	0.3579	0.3540	0.3587	0.3585	0.3581	0.3568	**0.35688**	2.1E-03
1875	0.3686	0.3695	0.3647	0.3694	0.3648	0.3643	0.3702	0.3695	0.3665	0.3702	0.3650	0.3689	0.3648	0.3696	0.3694	0.3691	0.3678	**0.36777**	2.2E-03
2125	0.3779	0.3789	0.3739	0.3786	0.3741	0.3735	0.3795	0.3789	0.3757	0.3794	0.3741	0.3783	0.3740	0.3789	0.3786	0.3784	0.3772	**0.37704**	2.2E-03
2375	0.3857	0.3867	0.3817	0.3864	0.3819	0.3813	0.3874	0.3868	0.3835	0.3872	0.3819	0.3862	0.3817	0.3867	0.3864	0.3863	0.3851	**0.38487**	2.2E-03
2625	0.3923	0.3934	0.3882	0.3930	0.3885	0.3878	0.3941	0.3935	0.3900	0.3938	0.3884	0.3929	0.3882	0.3933	0.3930	0.3929	0.3917	**0.39148**	2.3E-03
2875	0.3979	0.3990	0.3938	0.3986	0.3941	0.3933	0.3997	0.3991	0.3956	0.3993	0.3939	0.3985	0.3937	0.3989	0.3985	0.3985	0.3973	**0.39703**	2.3E-03
3125	0.4026	0.4037	0.3984	0.4032	0.3987	0.3980	0.4044	0.4039	0.4002	0.4039	0.3985	0.4033	0.3983	0.4036	0.4032	0.4032	0.4021	**0.40171**	2.3E-03
3375	0.4065	0.4077	0.4024	0.4072	0.4027	0.4019	0.4084	0.4079	0.4041	0.4078	0.4024	0.4073	0.4022	0.4075	0.4071	0.4072	0.4061	**0.40566**	2.4E-03
3625	0.4099	0.4110	0.4057	0.4105	0.4060	0.4052	0.4117	0.4113	0.4075	0.4112	0.4057	0.4106	0.4055	0.4108	0.4104	0.4105	0.4094	**0.409**	2.4E-03
3875	0.4127	0.4139	0.4085	0.4133	0.4089	0.4081	0.4146	0.4142	0.4103	0.4140	0.4085	0.4135	0.4083	0.4137	0.4132	0.4134	0.4123	**0.41183**	2.4E-03
4125	0.4151	0.4163	0.4109	0.4157	0.4113	0.4105	0.4170	0.4166	0.4127	0.4163	0.4108	0.4160	0.4107	0.4161	0.4156	0.4158	0.4147	**0.41423**	2.4E-03
4375	0.4171	0.4183	0.4129	0.4177	0.4133	0.4125	0.4190	0.4186	0.4147	0.4184	0.4128	0.4180	0.4127	0.4181	0.4176	0.4178	0.4167	**0.41625**	2.4E-03
4625	0.4188	0.4200	0.4146	0.4194	0.4150	0.4141	0.4207	0.4203	0.4163	0.4200	0.4145	0.4197	0.4143	0.4197	0.4193	0.4195	0.4184	**0.41792**	2.4E-03
4875 (top)	0.4201	0.4214	0.4159	0.4207	0.4163	0.4155	0.4221	0.4217	0.4177	0.4213	0.4158	0.4211	0.4156	0.4211	0.4206	0.4209	0.4198	**0.41927**	2.4E-03